DOTTORATO DI RICERCA IN INGEGNERIA CIVILE PER L'AMBIENTE ED IL TERRITORIO

XII Ciclo - Nuova Serie (2011-2013)

DIPARTIMENTO DI INGEGNERIA CIVILE, UNIVERSITÀ DEGLI STUDI DI SALERNO

ANALYSIS OF DInSAR DATA IN URBAN AREAS AFFECTED BY SUBSIDENCE OR SLOW-MOVING LANDSLIDES

(ANALISI DI DATI DInSAR IN AREE URBANE AFFETTE DA SUBSIDENZA O FRANE A CINEMATICA LENTA)

ING. LIVIA ARENA

Relatore:
PROF. ING. LEONARDO CASCINI

Coordinatore
PROF. ING VINCENZO BELGIORNO

Correlatori:
PROF. ING. SETTIMIO FERLISI
DOTT. ING. DARIO PEDUTO
DOTT. ING. GIANFRANCO FORNARO

ANALYSIS OF DInSAR DATA IN URBAN AREAS AFFECTED BY SUBSIDENCE OR SLOW-MOVING LANDSLIDES

To the people of my life

INDEX

INDEX OF FIGURES

INDEX OF TABLES

ABSTRACT

Subsidence and slow-moving landslides systematically cause social, economic and environmental impacts all over the world. For this reason studies aimed at both the characterization of subsidence and slow-moving landslides and the analysis of the consequences on the exposed elements interacting with them are of great interest for the scientific and the technical community.

These studies, to be useful in land use planning and management, need a huge number of displacement measurements within and on the boundary of the affected areas. Recently the scientific community has shown an increasing interest in the potential of using satellite observation techniques and, in particular, interferometric methods of Synthetic Aperture Radar (DInSAR) image processing.

The literature review on DInSAR applications highlights the possibility of further researches pursuing the exploitation of DInSAR potentiality in studies at different scales and the development of procedures for the proper use of interferometric data and their validation with reference to well documented case studies.

To this end, this PhD Thesis is aimed at developing original procedures for the analysis of the interferometric measurements specifically devoted to pursue two main objectives: the characterization of the phenomena of interest and the prediction of consequences to buildings interacting with them. The conceived procedures were tested, in sample areas of the Campania region (southern Italy) following a multi-scale approach. With reference to subsidence phenomena, the studies at small-scale involved the entire region and were mainly aimed at detecting subsiding macro-areas; within these latter, more detailed studies at medium scale were carried out and the most affected municipalities were individuated. At large scale, focusing on one of these municipalities, studies dealing with the analysis of parameters whose variation leads to the generation of the damage were carried out. Finally, at the scale of the single building the interferometric data were interpreted according to damageability criteria adopted in engineering practice.

As for slow-moving landslides, the joint use of interferometric measurements and damage surveys allowed the updating of landslide

inventory maps at medium scale and the analysis of the consequences through the generation of fragility and vulnerability curves within a test area including 21 municipalities of Benevento Province. At large-scale studies were performed on a landslide-affected area within the municipality of Ascea (Salerno Province) in order to follow the evolution - in space and time - of the analyzed phenomenon as well as to deepen its kinematic behavior, in turn useful for zoning purposes.

The obtained results highlight that the conceived procedures can valuably integrate the current practice for land use planning and as well as for the selection of the most suitable management strategy.

SOMMARIO

Nel mondo si registrano sistematicamente danni sociali, economici e ambientali indotti da subsidenza o fenomeni franosi a cinematica lenta.

Per tale ragione appaiono di indubbio interesse sia per la Comunità scientifica che Tecnica, studi rivolti alla caratterizzazioni di tali fenomeni e all'analisi delle conseguenze delle suddette fenomenologie sugli elementi esposti

Per rendere proficui tali studi, nell'ambito d'iniziative mirate ad una corretta pianificazione e gestione del territorio, sono, in ogni caso, indispensabili misure accurate degli spostamenti di punti della superficie topografica ricadenti all'interno o sul contorno delle aree affette dai fenomeni in questione. Negli ultimi anni la comunità scientifica operante nel settore del rischio idrogeologico ha manifestato un notevole e crescente interesse verso le potenzialità d'impiego di tecniche di osservazione da satellite e, in particolare, dei metodi interferometrici che si avvalgono d'immagini acquisite con Radar ad Apertura Sintetica (SAR).

Da una analisi della letteratura scientifica sulle applicazioni di queste tecniche allo studio di subsidenze o frane a cinematica lenta appaiono evidenti sia gli ampi margini di approfondimento e, quindi, i nuovi sviluppi della ricerca per un pieno sfruttamento delle potenzialità delle tecniche DInSAR in problemi da affrontare a diverse scale di riferimento, sia la necessità di definire adeguate e condivise procedure di analisi e di interpretazione dei dati satellitari per evitare che un uso poco accorto e non del tutto consapevole ne limiti le enormi potenzialità di impiego.

In tale ambito si inquadra il presente lavoro di Tesi che si propone di fornire procedure originali mirate al perseguimento di due obiettivi principali, ovvero la caratterizzazione dei fenomeni di interesse e la previsione delle conseguenze agli edifici che con essi interagiscono. Le procedure proposte sono state testate, sulla base di un approccio multi-scalare in aree campione della Regione Campania.

Con particolare riferimento ai fenomeni di subsidenza, le attività svolte a piccola scala hanno riguardato l'intero territorio regionale e sono state volte all'individuazione delle macro-aree che risultano sede di fenomeni di subsidenza; all'interno di queste, si sono quindi individuati a media scala i Comuni il cui urbanizzato è maggiormente affetto dai fenomeni di interesse e per i quali, pertanto, sono necessari studi a grande scala per l'analisi dei parametri la cui variazione prelude alla generazione del danno; infine, alla scala del singolo edificio i dati interferometrici sono stati interpretati alla luce di criteri di danneggiabilità convalidati dall'esperienza. Con riferimento alle frane a cinematica lenta e a 21 Comuni della Provincia di Benevento, l'analisi congiunta delle misure interferometriche e del rilievo del danno è stata impiegata, da un lato, per l'aggiornamento dello stato di attività e l'individuazione di fenomeni non cartografati nella documentazione ufficiale; dall'altro, per la generazione di curve di fragilità e di vulnerabilità su base empirica. A grande scala, con riferimento a fenomeni franosi singoli ricadenti nel Comune di Ascea in Provincia di Salerno, sono stati condotti studi che hanno consentito di seguire l'evoluzione spazio-temporale dei fenomeni franosi e la loro zonazione in base a differenti campi di velocità/spostamento.

Gli studi condotti aprono scenari di sicuro interesse applicativo nel settore della pianificazione territoriale oltre che nella scelta delle più opportune strategie di gestione del rischio
.
.

ACKNOWLEDGEMENTS

Siamo come nani sulle spalle di giganti,
così che possiamo vedere più cose di loro e più lontane,
non certo per l'altezza del nostro corpo,
ma perché siamo sollevati e portati in alto dalla statura dei giganti.

Bernardo di Chartres

Alea iacta est!!! Non me ne voglia Giulio Cesare se ho deciso di involargli la sua più celebre frase: certo non siamo nel 49 a.C. ed io non sono il dittatore romano! Eppure, è come se anch'io avessi oltrepassato un piccolo "Rubicone". Giunta al termine di questa "impresa" desidero esprimere la mia riconoscenza nei confronti di tutti i coloro che, in modi diversi, mi sono stati vicini e hanno permesso e incoraggiato sia le mie ricerche che la realizzazione e stesura di questa Tesi.

Innanzitutto l'intero Collegio dei Docenti e in particolare il *prof. Leonardo Cascini* per avermi saputo guidare e indirizzare in questa attività di ricerca. Grazie anche per i rimproveri, a volte stimolo a fare di più e meglio. Desidero comunicargli inoltre tutta la mia gratitudine per avermi dato la possibilità di frequentare la scuola Laram e di vivere un'entusiasmante esperienza di ricerca in Olanda presso l'Università di Twente.

Un ringraziamento veramente speciale è rivolto al *dott. ing. Dario Peduto*, per avermi fatto intravedere questa stimolante opportunità, per i preziosi suggerimenti e per la costante attenzione con la quale mi ha seguito nel lavoro di Tesi. Ringrazio *Dario* per l'amicizia dimostratami.

Un sentito ringraziamento va al *prof. Settimio Ferlisi* per la qualità del tempo che mi ha dedicato e le sue parole di incoraggiamento, sempre donate nel momento e nel modo giusto.

Ringrazio il *dott. ing. Gianfranco Fornaro* e l'IREA C.N.R. di Napoli, per la necessaria quanto stimolante interazione.

Grazie al *dott. ing. Giovanni Pisciotta* per le lunghe consulenze telefoniche, per la disponibilità e la cordialità.

Ringrazio l'Autorità di Bacino Liri Garigliano e Volturno nella persona della *dott.ssa Vera Corbelli*, il Ministero dell'Ambiente e della Tutela del Territorio e del Mare nella persone del *dott. Salvatore Costabile* e il Settore

ABOUT THE AUTHOR

Livia Arena si laurea in Ingegneria Civile per l'Ambiente e il Territorio, presso l'Università di Salerno con votazione 110/110 e lode. Nel Febbraio 2011 supera l'esame di ammissione al Dottorato di Ricerca in Ingegneria Civile per l'Ambiente ed il Territorio (XII ciclo Nuova Serie) presso l'Università degli Studi di Salerno. Durante il Corso di Dottorato sviluppa ricerche sull'interferometria differenziale e sulle sue applicazione allo studio di subsidenze e frane a cinematica lenta. Allo scopo di approfondire tali tematiche segue numerosi seminari e corsi nell'ambito di Scuole di Alta Formazione, svolgendo parte dell'attività di studio e ricerca presso la facoltà di Geo-Information Science and Earth Observation dell'Università di Twente in Enschede, Olanda. Alcuni risultati ad oggi conseguiti, sono stati oggetto di pubblicazioni su riviste internazionali e nazionali, nonché in contributi di atti di Convegni.

Livia Arena graduated in February 2010 in Civil Environmental Engineering at the University of Salerno with 110/110 cum laude. In February 2011 she passed the admission exam for the PhD course in Civil and Environmental Engineering (XII cycle- New Series) at the University of Salerno. During the PhD Course she developed her research on Differential Interferometry Synthetic Aperture Radar and on its application to the study of subsidence and landslide phenomena. To deepen these themes, she attended several seminars and courses within PhD International Schools, undertaking part of her study and research activities at the Faculty of Geo-Information Science and Earth Observation of the University of Twente in Enschede, Netherlands. Some of the obtained result have been already published on both International and National journals and presented in Conference.

1 INTRODUCTION

Subsidence and landslide phenomena are among the most damaging geohazards in terms of both their worldwide distribution and their related effects on structure and infrastructures. The number of events significantly grew in the last decades and they are expected to increase for many reasons, such as the increased demographic pressure and climate changes (EEA, 2012). Studies addressed to damage prediction devoted to reduce socio-economic impact represent an urgent need and they call for a deep knowledge of both phenomena (e.g. extension and intensity) and exposed elements, as well as the interaction among them. These studies to be useful need a huge number of displacement measurements, in space and time, that can turn out to be expensive and time consuming especially over large areas, via conventional monitoring technique. In the last decades the Scientific Community has shown an increasing interest towards satellite technique, such as those involving data achieved by space-borne Synthetic Aperture Radar (SAR). Among these, the Differential SAR Interferometry (DInSAR) is a very promising tool. This growing interest results from several advantages offered by widely developing DInSAR-based techniques, namely: the high spatial coverage of SAR images; the possibility of measuring ground surface displacements with subcentimetric accuracy by exploiting large datasets of images acquired over about 20 years; the cost-effectiveness of monitoring which, conversely, can turn out to be not affordable, if carried out via conventional in-situ techniques, due to the wide extension of the affected areas as well as the large number of the involved facilities. This PhD Thesis aims to provide a further contribution towards both the proper interpretation, in terms of reliability and confident use at different scales of analysis, of DInSAR data and the forecast of damage to structures.

In particular, Chapter 2 offers an overview of subsidence and slow-moving landslide phenomena in terms of general features, kinematics and diffusion over the world.

Chapter 3 provides a state of the art of available methods for the prevision of damage induced by subsidence and slow-moving landslides, highlighting the advantages and limitations of each method.

Chapter 4 focuses on DInSAR techniques synthesizing their basics, limitations and potentiality as well as most advanced application, available in scientific literature, to subsidence and slow-moving landslides.

In Chapter 5, first of all a multidisciplinary general framework for the proper use of DInSAR data is introduced; then original procedures for the confident and reliable interpretation of DInSAR data at different scales for both subsidence phenomena and slow-moving landslides are described.

Chapter 6 deals with the application at different scale of the proposed procedures to some case studies of subsidence phenomena in the Campania Region (southern Italy). In particular, referring to the whole Campania Plain critical areas are mapped at small scale in order to furnish a preliminary interpretation of phenomena; then, the analyses carried out at medium scale within the Campanian Plain allowed the detection and ranking of subsidence-affected municipal territories in which more detailed analyses need to be carried out; the analyses at municipal scale to zone the portions of the municipal territory in which damage to structure/infrastructure is likely to occur; finally, at detailed scale to detect buildings in which damage of different severity is likely to occur.

In Chapter 7 the proposed procedure to update landslide inventory map at medium scale, based on combination of DInSAR data and damage survey, is applied in an area of 557 km^2, located in Campania region . At the same scale of analysis an example of vulnerability function is presented.

Finally Chapter 8 deals with some remarks on the obtained results discussing the necessary research developments to further improve the forecast and prevention of damages induced by subsidence phenomena and slow-moving landslides.

2 THE ANALYSED PHENOMENA

> "Any fool can know. The point is to understand."
>
> *Einstein*

The knowledge and understanding of both predisposing and triggering factors as well as of features and kinematics of a given phenomenon are fundamental steps for a proper analysis of the consequences to exposed elements owing to the same phenomenon. This Chapter offers an insight into subsidence and slow-moving landslide phenomena.

2.1 SUBSIDENCE

Subsidence refers to ground surface displacements – with prevailing vertical component - owing to natural or anthropogenic causes.

Natural subsidence is generally very slow and it could develop also in geological periods; it can be induced essentially by tectonic movement, natural consolidation or modification of physical and chemical soil properties.

Anthropogenic subsidence is more rapid than natural subsidence and its effects are more evident in the short term; it can be induced essentially by withdrawals of fluids, mining or removal of solids (e.g. tunneling).

Fluids withdrawal from subsoil is the more widespread cause of anthropogenic subsidence. Pumping fluids are generally water, oil or gas. The parameters that mainly influence the entity and surface distribution of settlements are: soil stratigraphy, geotechnical soil properties; hydraulic conditions; withdrawal characteristics.

Subsidence can be also induced by mining which can lead sudden sinking or slow settlements. The involved areas are generally coincident with the excavation zone. A number of factors control the extent of mining subsidence. The main influencing factors are (Jones and Bellamy, 1973): seam thickness, depth of working, mine geometry, total amount of

mining, angle of draw, seam inclination, geological conditions, time, direction and rate of advance of the face and method of working.

Another cause of anthropogenic subsidence is tunneling. It is well recognized (Peck, 1969) that the deformations caused by tunneling (and the consequent potential damage to adjacent and overlying services and structures) will depend on: (i) the ground and groundwater conditions; (ii) the tunnel depth and diameter and, most importantly, (iii) the construction details.

However, sometimes different concurrent causes can originate a subsidence phenomenon, thus making it difficult to individuate the role played by each of them; consequently, it may be not easy to relate causes and consequence effects. Construction of cities on unconsolidated soils is just an example of subsidence induced by both natural and anthropogenic causes. Unconsolidated sediments (essentially clays, silts, peats and sands) are relevant predisposing factors to subsidence while building cities are the triggering cause for several reasons, such as: the compaction of sediments due to the weight of civil engineering works; the lowering of the water table because of drainage in the construction area; water exploitation for industrial and human need. Also the construction of levees and dams – often built to prevent or control flooding – could be a triggering cause of subsidence. These constructions shuts off the natural supply of new sediment to the area. In a natural setting sedimentation resulting from floods helps replenish the sediment that subsides and, thus, builds new material over the subsiding sediment, decreasing the overall rate of subsidence. When the sediment supply is cut off, the replenishment does not occur and the rate of subsidence in enhanced (Nelson, 2012).

Subsidence is an extensive worldwide phenomenon affecting large areas and important cities. In this regard, Table 2.1 synthesizes some case studies with the indication of their main cause and maximum recorded settlement. It is worth noting that most of cities reported in Table 2.1 are coastal cities like London, Houston, and Venice, or are built on river flood plains and deltas, like New Orleans, Baton Rouge, and the San Joaquin Valley of central California; accordingly it can be inferred that subsidence phenomena, in some particular areas, could result in a increase of the flood risk. Mexico City is somewhat different in that it was built in a former lake.

Table 2.1 Case studies od subsidence (modified after Nelson, 2012)

City	Maximum settlment [m]	Area (km²)	Cause	Some References
Los Angeles, U.S.A.	9	50	Petroleum withdrawal and tectonic activity	Allen and Mayuga, 1969
New Orleans, LA	2	175	Compactation of river sediments	Tornqvist et al., 2008
Houston, USA	2.7	12100	Coastal sediments	Gabrysch, 1984
San Joaquin Valley,U.S.A.	8.8	13500	Groundwater withdrawal	Ireland et al., 1984 Prokopovich, 1983
Mexico City	8.5	225	Filled lake	Booker et al., 1985 Bell, 1994 Ovando-Shelley et al., 2003 López-Quiroz et al., 2009
Tokyo, Japan	4.5	3000	Groundwater withdrawal from unconsolidated coastal sediments and tectonic activity	Konogai et al., 2012
Niigata, Japan	3	500	Groundwater withdrawal from unconsolidated coastal sediments	Okumura et al., 1969
Shanghai, China	2.63	121	Ground water withdrawal	Shi et al., 2008
Bangkok, Thailand	1	800	Groundwater withdrawal from unconsolidated river sediments	Phien-wej et al., 2005
Venice, Italy	0.22	150	Groundwater withdrawal from unconsolidated coastal sediments	Ricceri, 2007
Bologna	4	225	Groundwater withdrawal	Modoni et al., 2013
Ripon, England	30	300	Dissolution of Gypsum	Cooper et al., 2008

2.1 SLOW-MOVING LANDSLIDES

Slow-moving landslides are not clearly defined as a "class" in any of existing classification systems (see Appendix A). Anyway, referring to Varnes' classification (1978), for the purposes of this work they can be mainly identified with the following types involving earth soils: rotational slides (Figure 2.1); translational slides (Figure 2.2); flows (Figure 2.3) or complex phenomena. Furthermore, deep seated gravitational slope deformations (Zischinskik, 1969) and creep phenomena (Hutchinson, 1988) are also taken into account.

As for the selected typologies, rotational slides are characterized by curvilinear (concave upward) sliding surfaces; moreover, they are generally deep compared with their length (Skempton, 1953). On the contrary, translational slides are characterized by sliding surfaces essentially parallel to the existing ground surface; furthermore they are generally shallower than rotational slides. Flows are characterized by a displaced mass strongly deformed internally that behaves as a viscous fluid. It is worth observing that many slope failure begin as slide and propagate as flows.

Creep, according to Hutchinson (1988) and Sharpe (1938), means any extremely slow movements which are imperceptible except through long period measurements. It is possible distinguish mass creep and superficial creep. Mass creep occur under essential constant stress and the resulting displacements tend to be diffuse rather than concentrated upon discernible slip surface. Superficial creep is confined to the surface layers of the ground which suffered seasonal changes in volume, through changes in water content and temperature, and through freeze-thaw of the soil moisture.
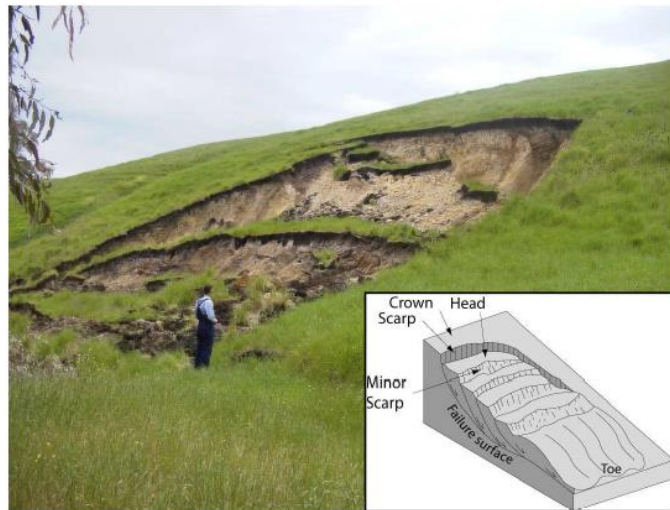
Figure 2.1 An example of rotational earth slide, Sheoaks (Australia), november 2001 (http://www.ccma.vic.gov.au).

Figure 2.2 An example of translational earth slide, Ireland (http://www.qub.ac.uk).
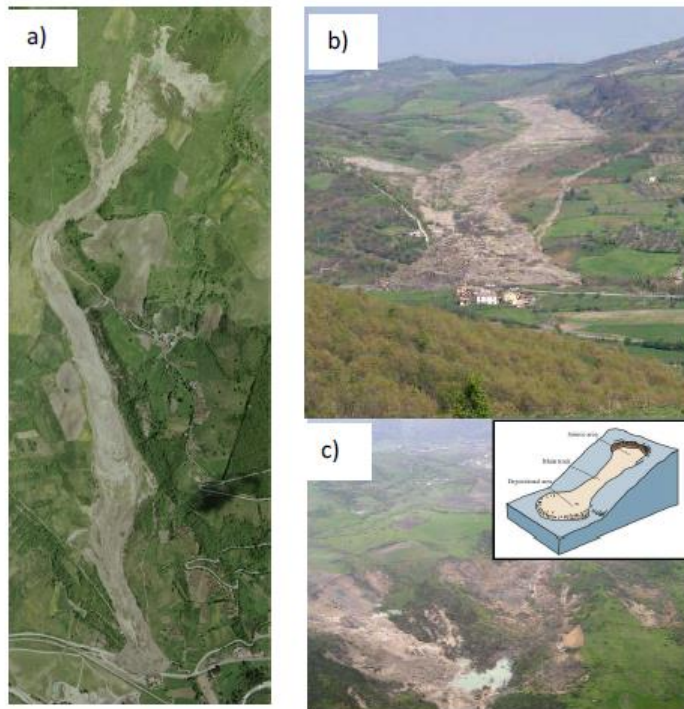
Figure 2.3 An example of earth flow: a) orthophoto of Montaguto earthflow (Avellino, Italy, Avio Riprese); b) photo of the toe of the landslide taken in January 2006 (source: Department of National Civil Protection); c) photo of the head of the landslide taken in January 2006 (source: Department of National Civil Protection) (modified after Cascini et al., 2012).

As far as the typical rate-of-displacement values are concerned, slow-moving landslides fall in the velocities classes provided by Cruden and Varnes (1996), ranging between "slow" (until 13 m/year) and "extremely slow" (until 16 mm/year) (Figure 2.5 b).

Referring to the general framework proposed by Leroueil et al. (1996) for the geotechnical characterization of a slope movement, slow-moving landslides are phenomena either at pre-failure stage or moving along one or several preexisting slip surfaces (Cascini et al., 2010b). The first case includes all the deformation processes leading to failure. These processes determine a relatively small displacement rate that increases when approaching failure, as a consequence of the gradual formation and propagation of a shear zone in the soil mass. In the last case they are defined as "reactivations" and can exhibit active or occasional

reactivation style, which have to be studied using different approaches. In particular, active slow-moving landslides show seasonal variations (Figure 2.5d) of the rate of movement that are controlled, both in the accelerating and decelerating phases, by pore-water pressure fluctuations that are, in turn, strictly correlated to the net rainfall regime and/or snowmelt. The occasional reactivations (Figure 2.5d) refer to episodic movements that are not controlled by the seasonal fluctuations of the pore-water pressures and must be related to a different specific and episodic triggering factor.

Further insight on slow-moving landslides were provided by Iaccarino et al. (1995) who defined the evolution stages of the earth flows that affect a territory of the Basilicata region, southern Italy (Figure 2.4). On the basis of geomorphological evidences the Authors distinguish four evolution stages named A', B', C', D'. During the stage A' the mobilized material moves from the source zone, through the track zone as a viscous flow with velocity varying from moderate to very rapid (Cruden and Varnes, 1996). During the stage B' the shape of three parts of the landslide is still noticeable, as for stage A', but the rate of movement decreases from moderate to slow. The stage C' may last tens of years and it is characterized by rate of movements within the very slow to extremely slow classes (Cruden and Varnes, 1996). Compared to the previous stage of movement, the shape of three main zones of the landslide is not clearly distinguishable from the stable area and the landslide body shows an undulated ground surface and rounded boundaries. During the last stage of movement, D', the boundaries of the landslide are almost undistinguishable from the stable area and the undulate behavior of the ground surface becomes less visible. This stage of activity lasts tens of years and the rate of movement falls within the extremely slow class (Cruden and Varnes, 1996) or goes down to null values.
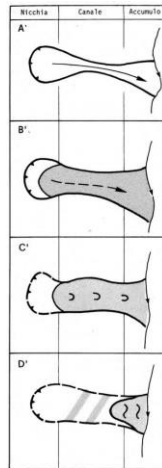
Figure 2.4 Geomorphologic evolutionary stages proposed by Iaccarino et al. (1995).

Slow-moving landslides are widespread in many geological contexts. Focusing on the Italian territory, according to the IFFI project (2007) the earth slides represent about 33% of landslides while earth flows about 16%. Clear examples of diffusion of these phenomena within the Italian territory are testified by more than 17,500 slow-moving landslides mapped at 1:25,000 scale within the territory of National Basin Authority of "Liri-Garigliano and Volturno rivers" (central-southern Italy) (Cascini, 2002) or around 32,000 phenomena mapped at 1:25,000 scale in the Emiliano-Romagnolo Apennine (northern Italy) (Bertolini et al., 2005).

Some interesting case studies, well-documented in the scientific literature, are shown in the Table 2.2.

a)

TYPE OF MOVEMENT		TYPE OF MATERIAL		
		BEDROCK	ENGINEERING SOILS	
			Predominantly coarse	Predominantly fine
FALLS		Rock fall	Debris fall	Earth fall
TOPPLES		Rock topple	Debris topple	Earth topple
SLIDES	ROTATIONAL	Rock slide	Debris slide	Earth slide
	TRANSLATIONAL			
LATERAL SPREADS		Rock spread	Debris spread	Earth spread
FLOWS		Rock flow (deep creep)	Debris flow (soil creep)	Earth flow
COMPLEX		Combination of two or more principal types of movement		

b)

Velocity Class	Description	Velocity (mm/sec)
7	Extremely Rapid	
6	Very Rapid	5×10^{3}
5	Rapid	5×10^{1}
4	Moderate	5×10^{-1}
3	Slow	5×10^{-3}
2	Very Slow	5×10^{-5}
	Extremely SLOW	5×10^{-7}

c)

d)

Figure 2.5 (a) Types of slow-moving landslides according to Varnes (1978); (b) velocity of slow-moving landslide according to Cruden and Varnes (1996); (c) involved materials according to Leroueil et al. (1996); (d) activity stage according to Leroueil et al. (1996).

Table 2.2 Selected slow-moving landslides in Italy (modified after Grimaldi, 2008)

Place	Typology	Main references
Porta Cassia (Orvieto, Italy)	Earth slides	Tommasi et al., 2006
Fosso San Martino (Teramo, Italy)	Earth slides	Bertini et al., 1986
Bomba (Arezzo, Italy)	Earth slides	Lanzo and D'Elia, 1997
Piagge (Arezzo, Italy	Earth slides	Lanzo and D'Elia, 1997
Lioni (Avellino, Italy)	Earth slides	Cotecchia, 1989
San Pietro in Guarano	Earth slides	Cascini et al., 1992a,b; 1994; Antronico et al., 2003
Masseria de Nicola (Potenza. Italy)	Earth flow	Pellegrino et al., 2004
Torrente Miscano (Benevento, Italy)	Earth flow	Pellegrino et al., 2004
Averà (Belluno, Italy)	Earth flow	Angeli et al, 1989
Montaguto (Avellino)	Earth flow	Cascini et al., 2012
Cerzeto	Earth flow	Iovine et al., 2006
Ancona	Rotational slide	Cotecchia, 2006, Agostini 2013

3 CONSEQUENCE ANALYSIS

"Chance and coincidence were invented to express the known effects of the unknown causes"

Voltaire

The consequences induced by slow-moving landslides and subsidence may have a relevant socio-economic impact. In this Chapter, after a short overview of damages induced by subsidence and slow-moving landslides in the world, the main methods to predict damages are discussed.

3.1 DAMAGES INDUCED BY SUBSIDENCE OR SLOW-MOVING LANDSLIDES

Land subsidence may cause severe damages to facilities (pipelines, linear infrastructures, buildings), induce seawater intrusion and flood, and consequently, lead to huge economic losses all over the world.

As far as Asian countries are concerned, land subsidence has become one of the most challenging issues in China. In Shanghai, for example, the phenomenon has caused economic losses summing up to more than US$ 13 billion (100 billion RMB) (China Daily, Feb. 14, 2007) and for the first decade of 21st century (Feng et al., 2008) the economic loss is estimated to be about US$ 3.3 billion.

As for United States, the National Research Council (1991) estimated that annual costs deriving from flooding and structural damage caused by land subsidence exceeded $125 million. Moreover, the assessment of other costs related to land subsidence is complicated thus the total cost of subsidence is probably significantly larger than the current best estimate (Galloway et al., 1999).

Europe is witnessing a dramatic increase in property damage as a result of soil subsidence. A new loss model developed by Swiss Re and the Swiss Federal Institute of Technology (ETH Zurich) suggests that soil subsidence will worsen and spread in Europe, with some areas seeing a

more than 50% rise in future losses (Swiss Re, 2011). In France alone, subsidence-related losses have increased by more than 50% within two decades, costing affected regions an average of € 340 million per year (Swiss Re, 2011). In the UK, figures from the Association of British Insurers (ABI) posted on the Internet indicate that building damage, as a result of subsidence, cost about £500 millions over the dry summers of 1975–1976, and £400 millions in 2003 (Professional Broking, 2007). Other figures from the ABI (Dlugolecki, 2004) suggest that with the effects of climate change, by 2050 the costs could be as much as £600 million in a normal year and £1.2 billion in a bad year (at 2004 prices). In many Countries most household insurance policies cover loss or damage caused by subsidence. They do not cover the cost of preventing further subsidence, this means that the cost of repairing damage (such as cracks) to the building's superstructure is covered but is not covered the cost of stopping the building from moving in the future.

In Italy an economical evaluation of damage related to subsidence doesn't exist; however, a study carried out by the Istituto Superiore per la Protezione e la Ricerca Ambientale (ISPRA, 2006) demonstrated that about 10% of Italian municipalities (747 out of 8,101) are affected by this phenomenon (Figure 3.1). Among these, evacuation ordinances (Ordinance no. 253 23/09/2010) and a system of tax allowance have been implemented in Guidonia (Roma Province, Lazio Region).

Generally, case studies reported in technical and scientific literature show that subsidence affects different facilities in different ways. Focusing on buildings, the severity of the damage to the superstructures is to a great extent controlled by the structural typology as well as by the soil-footing relative stiffness. For instance, a masonry building resting on high deformable shallow footings can be affected by ground movements more than a reinforced concrete building with very stiff shallow footings. Furthermore, it must be taken into account that – in some situations - vertical components of the ground displacements may coexist with horizontal ones, thus inducing (Cooper, 2008) concave upward bending (hogging) or convex bending (sagging) mode of deformation (Figure 3.2). Each movement type – including footing extension or support loss (Figure 3.2) – imposes a different combination of stresses upon a building, though damage is often concentrated upon corners or stress concentrators such as door or window areas (National Coal Board, 1975; Institution of Structural Engineers, 1994; Audell, 1996).

.
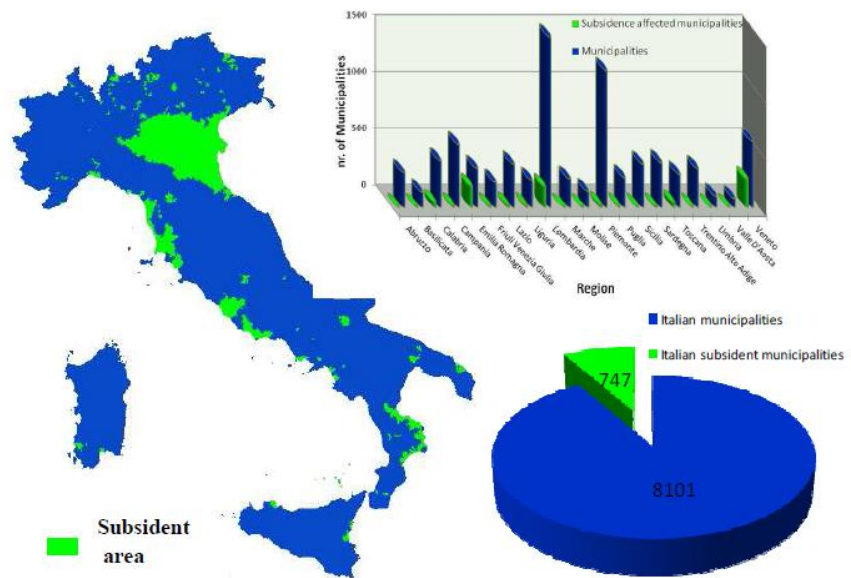
Figure 3.1 Map of subsiding area (a), number of Municipalities affected by subsidence for each Italian region (modified after ISPRA, 2006)(b), number of subsiding municipalities in Italy.
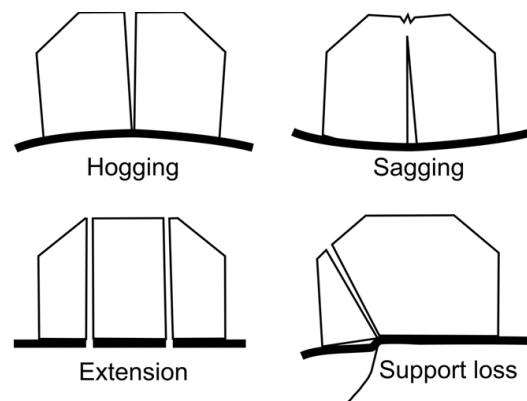
Figure 3.2 Schematic illustration of building damage associated with various types of subsidence movement, some of which may occur together (Cooper, 2008).

15

Figure 3.3 a) Hogging mode of failure with loss of support to the right of the picture Calatayud, Spain (Cooper, 1998); b) Sagging building damage Princess Road, Ripon (Cooper, 1998); c) Damage to road (Tivoli Terme, Italy) d) A row of buildings, showing effects of land subsidence (Credit: Chris Earle) e)settlement and titlting of a building in Bangkok; f) An 18 mm crack in the wall of a house at Hutton Conyers near Ripon,UK (Cooper, 1998);g) building at the Everglades Experiment Station originally constructed at the land surface; latticework and stairs were added after substantial land subsidence (http://water.usgs.gov); h) damage to Cathedral in Mexico City.

As far as landslides are concerned, available information on related economic losses deals with all types of phenomena. In this regard, the annual economic losses in Italy, Austria, Switzerland and France are estimated as USD 1–5 billion while United States exceed USD 3.5 billion (Kjekstad and Highland 2009). Also the impact on natural environment, such as on morphology, forest and fauna is considerable (Schuster 2007). Focusing on buildings, it is generally admissible that damage resulting from the impact with fast-moving landslides – such as debris flows and rock falls – is generally the highest as it may corresponds to the collapse of the whole superstructure or of a part of it. However, slow-moving landslides may also have adverse effects on affected facilities that sometimes could be underestimated in decision making processes(Safeland Deriverable 2.5, 2011).

Generally, the damageability of facilities to slow-moving landslides may depend on several factors. Among them, some of the most relevant are: (a) the hazard level; (b) the rate of movement (relative slow to extremely slow moving landslides); (c) the triggering mechanism (intense rainfall, earthquake, erosion, construction activities etc); (d) the specific strength and stiffness characteristics of the exposed elements and (e) their position in relation to the potential sliding surface, and (f) the type of materials controlling the movement (Safeland Deliverable 2.5, 2011).

Mansour et al. (2011) reviewed more than 50 cases of slow-moving landslides causing damage of different severity to facilities in many countries in the world such as: Canada (Clementino et al.2008; Moore et al. 2006), USA (Esser, 2000), Australia (Jworchan et al., 2008), New Zealand (Gillon and Saul, 1996), United Kingdom (Nichol and Lowman, 2000), Switzerland (Bonnard et al. 2008), Greece (Topal and Akin,2008), China (Zhou , 2000), Japan (Fujisawa et al. 2007), Malaysia (Malone et al., 2008). They revealed that buildings and residential houses may sustain higher slide velocities and total displacements than the other facilities before experiencing serious damage while bridges were found to be the most damageable elements.

In Italy, among the case studies reported in the scientific literature a significant example is that of Ancona, a coastal town of Central-Eastern Italy, where a reactivated rotational slide involving an area of about 300 hectares occurred in 1982 (Crescenti et al., 1983). According to the National Research Council, the landslide caused extensive damage to buildings and infrastructures. In detail, the phenomenon damaged the University Medical Faculty and two hospitals, damaged or completely

destroyed 280 buildings, for a total of 865 dwellings. In addition, the Adriatic railway and the Flaminia road were shifted laterally 10 m toward the sea.

Figure 3.4 Ancona landslide: damage to man-made structures caused by the landslide (Cotecchia, 2006).

Another significant example is the landslide that occured in a little town in southern Italy, San Pietro in Guarano, in the Province of Cosenza. This is a typical reactivation of the Western Sila massif affecting the intensely weathered gneiss rocks (Cascini et al., 1992a,b; 1994; 2006).

Many buildings were so severely damaged to be demolished or evacuated. For instance, a primary school mainly suffered cracks in the beam, pillar and partitions, but also detached sections of wall plugging (Figure. 3.5); a secondary school presented diagonal cracks in the wall plugging as associated with the rigid body rotation of horizontal

structures (Figure 3.6); finally, a private building mainly suffered widespread cracking in the masonry walls (Figure 3.6) (Antronico et al., 2003).
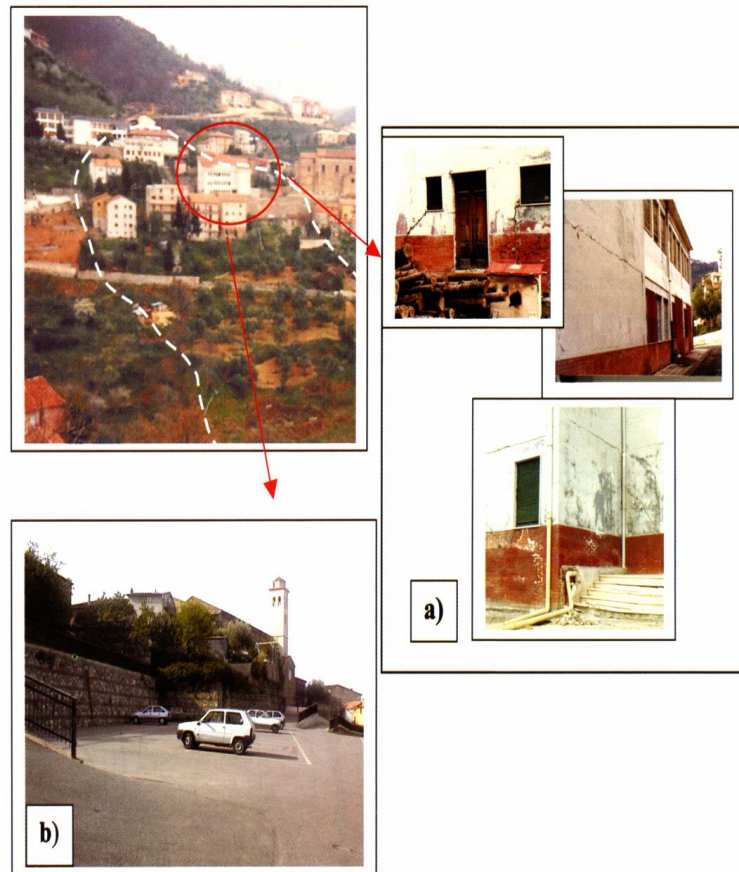
Figure 3.5 A primary school San Pietro in Guarano (Cosenza Province, Italy): a) effects after reactivation 1981; b) area after demolition (Antronico et al., 2003).
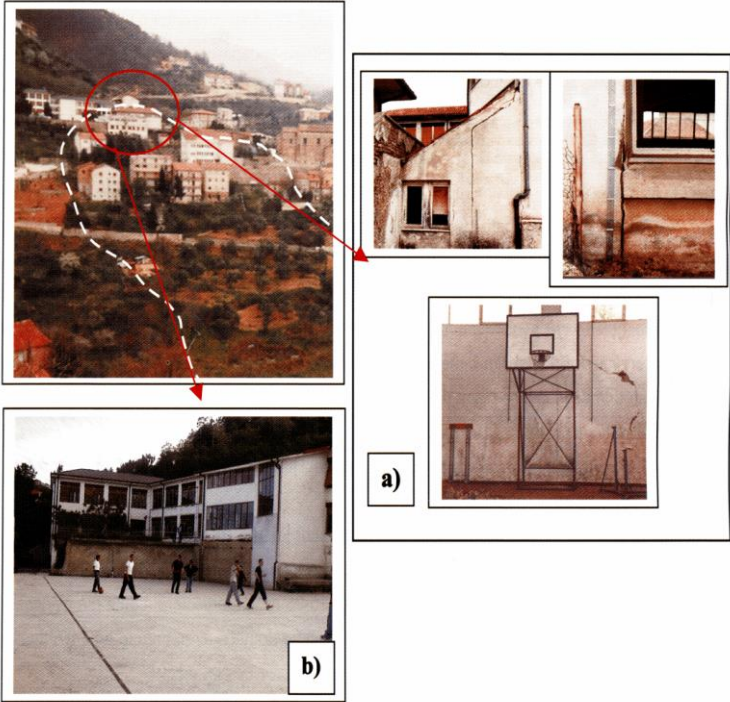
Figure 3.6 A secondary school in San Pietro in Guarano (Cosenza Province, Italy) (Antronico et al., 2003): a) effect after reactivation 1981; b) area after demolition.

Figure 3.7 San Pietro in Guarano (Cosenza Province, Italy): damages to private houses (Antronico et al., 2003).

More recently a vast reactivated complex landslide occurred in the early morning of March 7th 2005, after a period of prolonged rainfall combined with snowfall, in Cavallerizzo in Calabria region (Italy). In total, thirty buildings were severely damaged or destroyed by the landslide, and the provincial road (locally called Emigranti Street) connecting the hamlet of Cavallerizzo to the main village of Cerzeto, and to Mongrassano was disrupted. About 310 inhabitants had to be evacuated to nearby villages (Iovine et al., 2006).
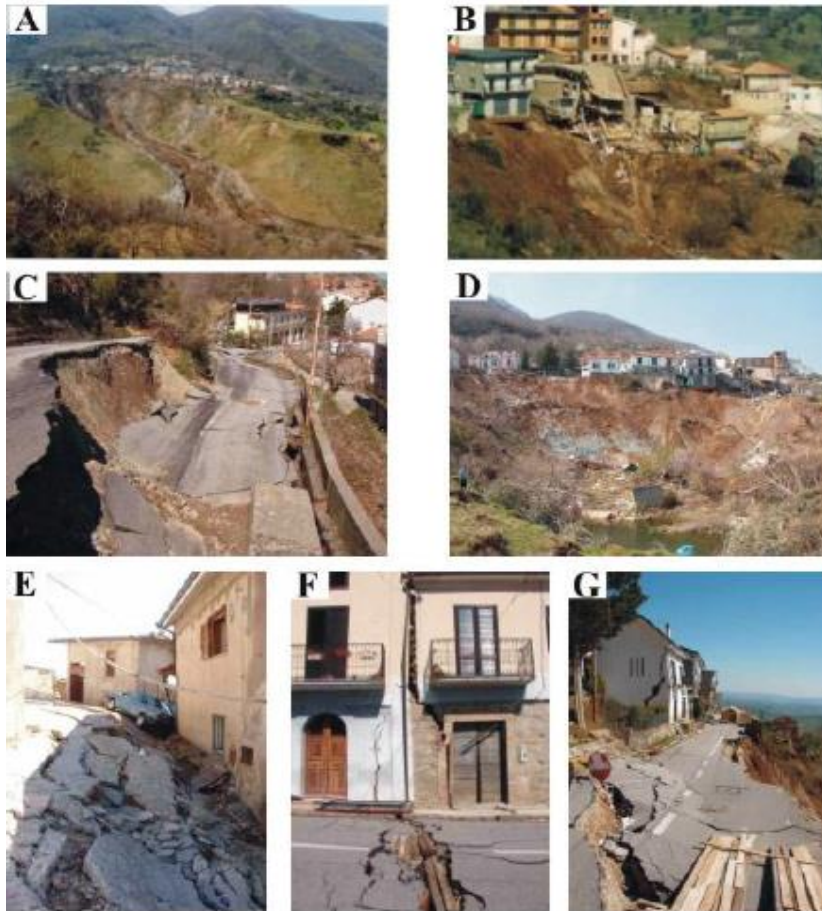
Figure 3.8 Some photographs of the March 2005 landslide at Cavallerizzo.: a) a panoramic view of the village (in foreground, the main earth flow); b) view of buildings damaged along the crown; c) view of damage to the provincial road; d) view of the main scarp (in foreground, the landslide lake); e-g) view of damage to the urbanized area, along the main scarp (Iovine et al, 2006).

Another interesting case study is reported by Fruzzetti and Scarpelli (2004) referring to a slide in the urban area of Camerata Picena (An). The Authors describe the damage, numerous cracks with a prevailing inclination of 45°, suffered by a four-stored building on shallow foundation built on overconsolidated clay.
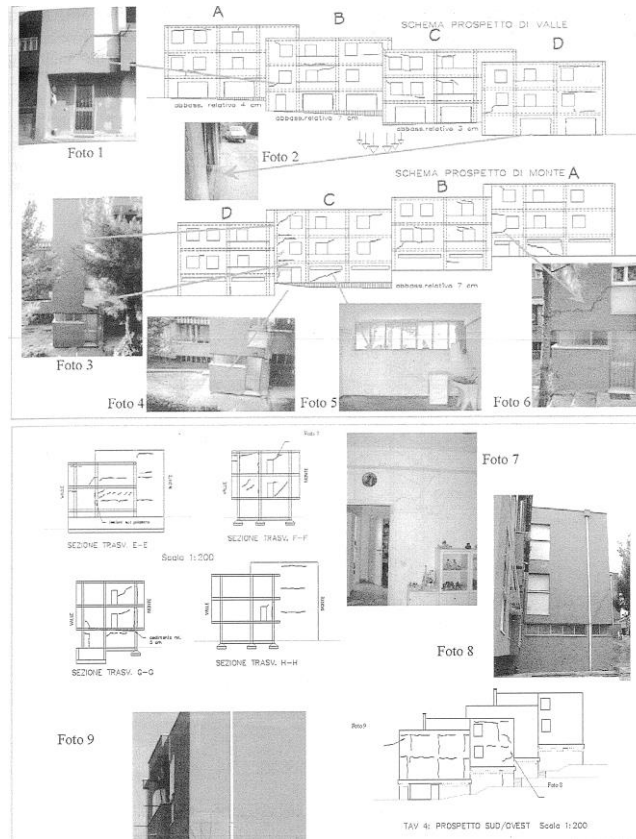
Figure 3.9 Damage to buildings with prevailing systems of cracks (Fruzzetti and Scarpelli, 2004).

Generally, the case studies reported in the scientific literature show that absolute horizontal movements – also of several centimeters – can be tolerated by buildings, especially if differential deformations are small. On the other hand, differential displacement of the same order of intensity can lead to severe damage and impose evacuation. However, a rational criterion it is necessary to adequately assess the acceptability of displacements caused by slope movements (Picarelli and Russo, 2004). In the next Section the most widely used methods in geotechnical engineer to predict damage induced by displacements are presented.

3.2 VISIBLE DAMAGE AND ITS CHARACTERIZATION

Assessment of building damage can be conditioned by factors such as: local experiences; caution of professional engineer; occupancy type, market value and saleability of the property (Burland, 2008). Of course, damage usually relates to the existence of cracks that generally concentrate in correspondence of weak Sections of the affected superstructure (BRE, 1995).

According to Audell (1996), crack patterns are diagnostic indicators which implicate specific structural movements relative to a particular geologic hazard. The Author suggests a crack classification system based on (Figure 3.10):

- ground movements;
- cracks orientation;
- type of stress;
- type of feature.

Ground movements are defined as: normal (N), reverse (R), pull-apart (P), seismic (S) and undefined or non-geologic (U). Normal movement is downward, vertical settlement, such as from soil subsidence. Reverse movement is upward vertical heave, such as from swelling expansive soils. Pull-apart movement is horizontal separation which may be associated with landsliding, slope creep or lateral drift from expansive clays. The three senses of movement (normal, reverse and pull-apart) may be realized by a fourth: earthquake ground shaking. A single geologic hazard or a combination of geologic hazards may affect localized or widespread parts of the building.

Crack orientations in walls are defined as: vertical (V), diagonal (D) and horizontal (H). Crack orientations in slabs are defined as: oblique (0), parallel (P) and radial (R). Vertical cracks, commonly found at mid-wall areas and oriented normal to the foundation. Diagonal cracks, commonly found at the corner wall areas and oriented at some angle to the foundation. Horizontal cracks, commonly found anywhere along the height of the wall and oriented parallel to the foundation. These cracks exhibit a preferred orientation because of the applied stress caused by ground movement.

The types of stress are defined as: tension (T), compression (C) and shear (S). Tension cracks are commonly found with open separations. Shear cracks are commonly found closed or with very narrow separations accompanied by lateral surface displacements (denoted by

hatchure patterns across the crack). Compression cracks are commonly found closed with characteristic bulging. Ground movement and seismic shaking can generate one or all three types of stress in buildings. The type of feature may be a crack (C) or a gap (G). Cracks are breaks in brittle building materials which include stucco, plaster, drywall and concrete. Gaps are separations which develop in building materials at construction joints.
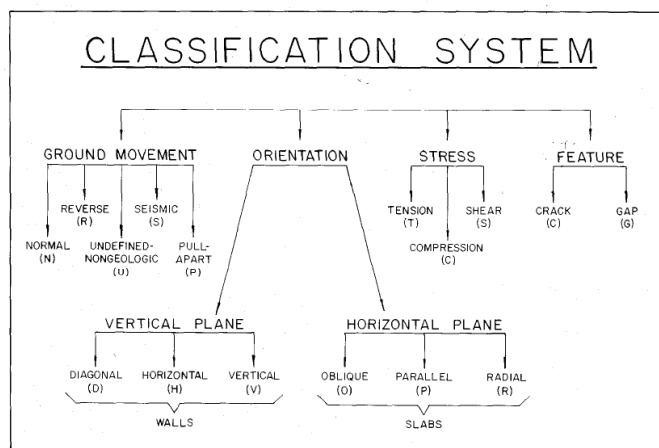
Figure 3.10 The "Crack Classification System" for crack patterns in buildings (Audell, 1996).

One of the first, widely used schemes for recording building damage in Britain was that of the UK National Coal Board (NCB) (Table 3.1) based on the NCB approach detailed in the Subsidence Engineers Handbook (National Coal Board, 1975). The scheme is based on the change in the length of the structure related to the length of the actual structure.

Change in length of structure (m)	Class of damage	Description of typical damage
≤0.03	1: very slight or negligible	Hairline cracks in plaster, perhaps isolated slight fracture in the building, not visible from the outside
0.03–0.06	2: slight	Several slight fractures showing inside the building. Doors and windows may stick slightly. Repairs to decoration probably necessary
0.06–0.12	3: appreciable	Slight fractures showing on outside of building (or one main fracture). Doors and windows sticking. Service pipes may fracture
0.12–0.18	4: severe	Service pipes disrupted. Open fractures requiring rebonding and allowing weather into the structure. Window and door frames distorted; floors sloping noticeably; walls leaning or bulging noticeably. Some loss of bearing in beams. If compressive damage, overlapping of roof joints and lifting of brickwork with open horizontal fractures
>0.18	5: very severe	As above, but worse and requiring partial or complete rebuilding. Roof and floor beams lose bearing and need shoring up. Windows broken with distortion. Severe slopes on floors. If compressive damage, severe buckling and bulging of the roof and walls

Table 3.1 Ranking of damage categories used by the UK NCB (National Coal Board 1975)

Because Table 3.1 is based on change of length rather than crack width, it was also applicable to compressive stresses in the sagging mode. However, it requires detailed measurements and does not lend itself to quick surveys based on crack widths.

Burland et al. (1977) summarized several approaches to quantify building damage. They distinguished between three criteria when considering building damage:

1. visual appearance;
2. serviceability or function;
3. stability.

They proposed a system of damage categories based on the ease of repair (Figure 3.11), so to classify visible damage is necessary, when carrying out the survey, to assess the type of work necessary to repair the damage both externally and internally. This defines six categories of damages, numbered 0 to 5 in increasing severity. Normally categories 0, 1, 2 related to aesthetic damage, 3 and 4 to serviceability damage and 5 damage affecting stability. The Authors also noted that:

- the classification relates only to the visible damage at a given time and not its cause or possible progression, which are separate issues.
- The strong temptation to classify damage solely on crack width must be resisted. It is the case of repair that is the key factor in determining the category of damage.
- The classification was developed for brickwork or blockwork and stone mansory could be adapted for other forms of cladding. It is

not intended to apply to reinforced concrete structural elements. More stringent criteria may be necessary when damage may lead to corrosion, penetration or leakage of harmful liquids and gases or structural failure

Category of damage	Normal degree of severity	Description of typical damage (Ease of repair is printed *italic*) Note: Crack width is only one factor in assessing category of damage and should not be used on its own as a direct measure of it
0	Negligible	Hairline cracks less than about 0.1 mm
1	Very Slight	*Fine cracks which are easily treated during normal decoration.* Damage generally restricted to internal wall finishes. Close inspection may reveal some cracks in external brickworks or masonry. Typical crack widths up to 1 mm.
2	Slight	*Cracks easily filled. Re-decoration probably required. Recurrent cracks can be masked by suitable linings.* Cracks may be visible externally and *some repointing may be required to ensure weathertightness.* Doors and windows may stick slightly. Typical crack width up to 5 mm.
3	Moderate	*The cracks require some opening up and can be patched by mason. Repointing of external brickwork and possibly a small amount of brickwork to be replaced.* Doors and windows sticking. Service pipes may fracture. Weathertightness often impaired. Typical crack widths are 5 to 15 mm or several up to 3 mm.
4	Severe	*Extensive repair work involving breaking-out and replacing sections of walls, especially over doors and windows.* Windows and door frames distorted, floor sloping noticeably[1]. Walls leaning[1] or bulging noticeably, some loss of bearing in beams. Service pipes disrupted. Typical crack widths are 15 to 25 mm but also depends on the number of cracks.
5	Very severe	*This requires a major repair job involving partial or complete rebuilding.* Beams lose bearing, walls lean badly and require shoring. Windows broken with distortion. Danger of instability. Typical crack widths are greater than 25 mm but depends on the number of cracks.

[1] Note: Local deviation of slope, from the horizontal or vertical, of more than 1/100 will normally be clearly visible. Overall deviations in excess of 1/150 are undesirable.

Figure 3.11 Classification of visible damage to walls with particular reference to ease of repair of plaster and brickwork masonry (Burland, 1977).

3.3 METHODS FOR DAMAGE FORECAST

3.3.1 Damageability criteria

Predicting building damage due to ground movements is an important task for territory management in order to reduce socio-economical effect. A study of the literature reveals a wide variety of confusing symbols and terminology describing foundation movements.

Burland and Wroth (1974) proposed a consistent set of definitions based on the displacements (either measured or calculated) of a number of discrete points on the foundations of a building later widely accepted, to define building distortion (Figure 3.12).
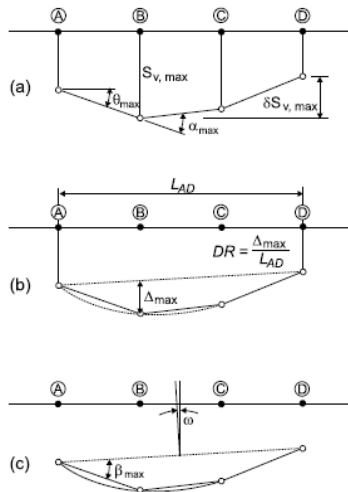
Figure 3.12 Definition of building deformation: a) settlement, differential settlement; b) relative deflection, deflection ratio, c) tilt, relative rotation (After Burland, 1995).

The following deformation parameters, shown in Figure 3.12, are defined:

1. *Settlement defines the vertical movement of a point. Positive values indicate downwards movement.*

2. *Differential or relative settlement δS_v is the difference between two settlement values.*

3. Rotation or slope θ *describes the change in gradient of the straight line defined by two reference points embedded in the structure.*

4. Angular strain produces sagging or upward concavity when positive, while hogging or downward concavity is described by a negative value.

5. Relative deflection Δ *describes the maximum displacement relative to the straight line connecting two reference points with a distance L.*

6. Deflection ratio DR is defined as the quotient of relative defection and the corresponding length: $DR = \Delta/L$.

7. Tilt ω *describes the rigid body rotation of the whole superstructure or a well defined part of it. It is difficult to determine as the structure normally flexes itself.*

8. Relative rotation or angular distortion β *is defined as the rotation of the straight line joining two reference points relative to the tilt.*

9. Average horizontal strain ε_h *develops as a change in length* δL *over the corresponding length L:* $\varepsilon_h = \delta L /L$.

The above definitions only describe `in-Plain' deformation. Three-dimensional behavior such as twisting is not included.

In literature there are several methods to predict damages ranging from empirical methods to detailed finite element calculations (Figure 3.13).

Type of method	Limiting parameter	Limiting value	Applicability	Reference
Empirical	β	1/150	Structural damage	Skempton and MacDonald (1956)
	β	1/300	Cracking in walls and partitions	
Empirical	δ/l	1/500	Steel and reinforced concrete frames	Polshin and Tokar (1957)
Deep beam model of building	$\Delta/(L\varepsilon_{crit})$	$f(L/H, E/G,$ neutral axis location)	Load bearing wall (E/G=2.6), frame structures (E/G=12.5), and masonry building (E/G=0.5) assuming no lateral strain	Burland and Wroth (1975)
Extended deep beam model	β, ε_h	Chart	L/H=1 and assumption horizontal ground and building strains are equal	Boscardin and Cording (1989)
Detailed analysis of structure	Crack width	$\varepsilon_p, \varepsilon_t$	General procedure that considers bending and shear stiffness of building sections, distribution of ground movements, slip between foundation and grade and building configuration	Boone (1996)

Figure 3.13 Damage Criteria (Finno et al., 2005).

According to Negulescu and Foerster (2010) it is possible distinguish three categories of methods:
– empirical methods (e.g. Skempton and MacDonald, 1956; Polshin and Tokar, 1957; Sowers, 1962; Bjerrum,1963; Rusch and Mayer, 1964; Beeby and Miles, 1969), which aim at establishing criteria of serviceability by relating the deformation observed from field surveys to

the damage generally induced by settlements due to the own weight of the structure.

– methods using structural engineering principles (Burland and Wroth, 1974; Boscardin and Cording, 1989; Boone, 1996; Finno et al., 2005; Bird et al., 2005a,b).

– methods based on numerical modelling (e.g. see Burd et al., 2000).

The first attempts to derive recommendations on allowable settlements of structures based on empirical methods were made by Skempton and MacDonald (1956) and Polshin and Tokar (1957).

Recommendations from Skempton and MacDonald (1956) are obtained by treating data collected from settlements and damage observations on 98 buildings from which 40 showed signs of damages. The damage criterion that they used is the "angular distortion" defined as the ratio of the differential settlements and the distance between two points after eliminating the influence of the tilt of the building. Based on their observations, they reported a range of limit values depending on the type of building or foundation, to determine the magnitude of differential foundation movement that will cause cosmetic, i.e. architectural damage to structures, or more seriously, structural damage. For instance, they propose a limit value of 1/300 for "angular distortion" corresponding to a threshold for crack initiation in walls and finishes. They note also that a value greater than 1/150 would cause structural damage. Polshin and Tokar (1957) recognize different modes of deformation for different types of buildings, so that they treat separately unreinforced load bearing walls and frame structures. They define some limit criteria which depend on the "slope" (difference of settlement of two adjacent supports relative to the distance between them), the "relative deflection" (ratio of deflection to the deflected part length) and the average settlement under the building. These criteria are in concordance with the values proposed by Skempton and Mc-Donald (1956) and are also in agreement with the results obtained later by Burland and Worth (1974).

The observation of the settlement of structures and possible consequent damage, according to Ricceri et al. (1985) is undoubtedly a valid method of evaluating the limits within which certain types of structures may accept deformation without weakness which may jeopardize o restrict their use. Undoubtedly the criteria that has been formulated from a set of data, must be used for other buildings with great caution, because of the extremely complexness of the soil/structure interaction influenced by a high number of parameters.

As for methods based on structural engineering principles, the most emblematic and widely used literature study on settlement-induced damage is the one published by Burland and Wroth in 1974. In their paper, they analyze the damage due to the foundation movement, as well as the interaction between the structure and the underlying ground.

They propose a new fundamental approach for building damage assessment, in which they replace a simple structure by an equivalent uniform, weightless, elastic beam of length L, height H, and unit thickness (the Deep Beam Method) (Figure 3.14).
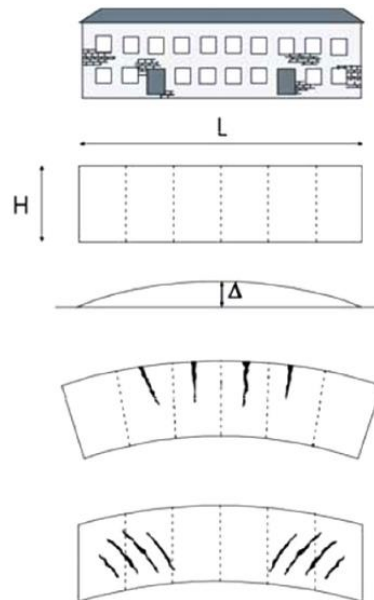
Figure 3.14 Illustration of the equivalent Deep Beam Method, used to replace an actual building by a uniform, weightless, elastic beam of unit thickness (Burland and Wroth, 1974).

Then, they define a criterion for initial cracking based on the calculation of tensile strains developing in the beam. In order to assess the factors related to soil-structure interactions, they first evaluate the ground settlements at an equivalent site with no overlying building (so called 'greenfield' settlements) and setting lateral strains to zero. Then, they impose the obtained displacements on a structural model of the building in order to assess the expected damage.

The Figure 3.14 shows two extreme modes of deformation: in bending cracking is caused by direct tensile strain while in shear diagonal cracks appear, caused by diagonal tensile strains. For a centrally loaded beam subjected to both shear and bending deformation the total central deflection is given by Timoshenko (1955):

$$\Delta = \frac{PB^3}{48EI}(1+\frac{18EI}{L^2HG}) \tag{1}$$

where E is the Young's modulus and G is the shear modulus. P is the point load which is applied at the centre of the beam. For an isotropic elastic material $E/G = 2(1 + \nu)$. Assuming a Poisson's ratio of $\nu = 0,3$ it can be derived $E/G = 2.6$. In the case where the neutral axis is in the middle of the beam, Burland and Wroth (1974) expressed in terms of deflection ratio Δ/L and the maximum extreme fibre strain $\varepsilon_{b;max}$:

$$\frac{\Delta}{L} = (0.167\frac{L}{H} + 0.165\frac{H}{L})\varepsilon_{b,max} \tag{2}$$

and for the maximum diagonal strain $\varepsilon_{d,max}$:

$$\frac{\Delta}{L} = (0.25\frac{L^2}{H^2})\varepsilon_{d,max} \tag{3}$$

Both equations are plotted in Figure 3.15. It is obvious that for L/H < 0,5 the diagonal strain is critical. As L/H increases above this value bending becomes the more critical mode of deformation. For the equations plotted in Figure 3.15a it was assumed that the neutral axis was in the middle of the beam. In real buildings, however, the foundations offer a significant restraint to their deformation.

Therefore, it may be more realistic to assume the neutral axis to be at the lower extreme fibre. With this assumption Burland and Wroth (1974) changed Equations:

$$\frac{\Delta}{L} = (0.083\frac{L}{H} + 1.3\frac{H}{L})\varepsilon_{b,max} \tag{4}$$

$$\frac{\Delta}{L} = (0.064\frac{L^2}{H^2})\varepsilon_{d,max} \tag{5}$$

As the neutral axis is at the lower extreme fibre, Equation 3 only applies for a hogging deformation mode. In the case of sagging there are no tensile strains. Equations 4 and 5 are plotted in Figure 3.15. Comparing Figure 3.15b) with Figure3.15 a) shows that for any given value of $\Delta/L\varepsilon_{lim}$ the value of Δ/L in Figure 3.15 b) is twice that in Figure 3.15 a).
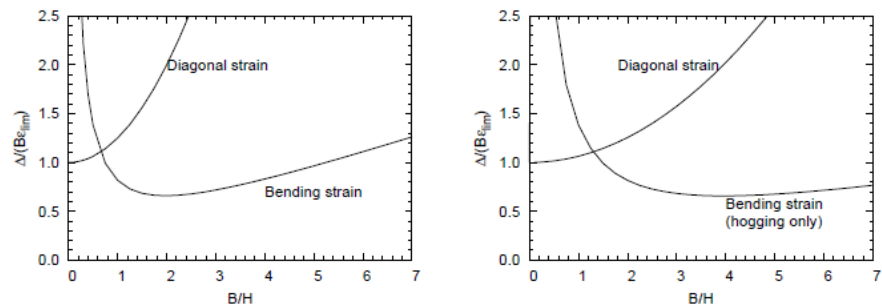
Figure 3.15 a) Relationship between D/Le_{crit} and L=H for rectangular beams deflecting due to combined bending and shear. Neutral axis in the middle. b) Relationship $\Delta/L\varepsilon_{crit}$ between and L=H for rectangular beams defecting due to combined bending and shear. Neutral axis at the bottom. (after Burland & Wroth, 1974).

Boscardin and Cording (1989) have complemented Burland and Wroth's concepts by including the effect of horizontal strain developing in the ground due to settlements. They note that this effect depends on the lateral stiffness of the structure. For instance, a frame structure would be more affected by horizontal ground strains than a structure with reinforced concrete walls supported by continuous footings or with stiff floor systems. Based on the results of their studies, they define categories of damage by developing relationships between the horizontal strain and the angular distortion (Figure 3.16).
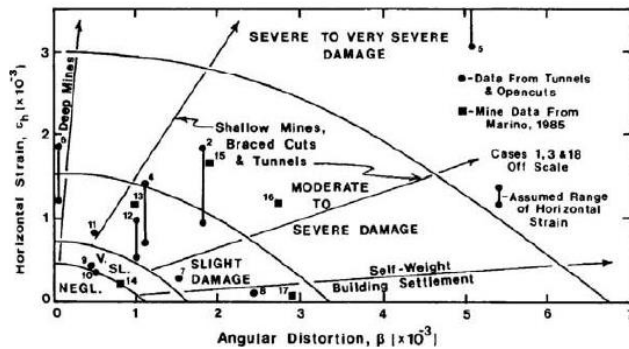
Figure 3.16 Interaction diagram relating angular distortion and horizontal strain for different categories of damage (Boscardin and Cording, 1989).

This approach is interesting as it relies on sound theoretical backgrounds for damage induced by ground movements, which was new with regards to the previous works based on empirical observations only. However, a main issue concerns the difficulty to provide guidance on the selection of the equivalent beam features (e.g. equivalent rigidity), especially when dealing with a multi-story structure.

In the last years more sophisticated methods, such as finite elements (FE), in order to estimate settlement-induced damages are developing. They are undoubtedly complex and they may lead to results that are signicantly more realistic than those obtained using conventional methods (Burd et al., 2000).

Among them it is possible to distinguish uncoupled and coupled approaches. Uncoupled approaches study the soil and the structure separately, on the other hand coupled approaches model structure interactions (SSI), but they are more complex and time consuming. Burd et al.(2000) developed procedures based on a three-dimensional finite element method, in which the building, the ground and the tunnelling processes are combined in a single numerical model using coupled and uncoupled approaches. The purpose of the coupled analyses was to investigate the general mechanisms of soil structure interaction that occur in this type of problem while the uncoupled analyses were intended to investigate the shortcomings of methods in which soil structure interaction effects are not considered. Depending on the building deformation mode (e.g. sagging or hogging), SSI effects may be more or less important, as lateral restraint provided by the ground may reduce the extent of tensile stresses in the building. For buildings

subjected to sagging deformations it is seen that an uncoupled approach is likely to be excessively conservative. Soil structure interaction effects when the building deforms in a hogging mode, although important, are less significant than for buildings subjected to sagging. For buildings subjected to hogging, therefore, it is possible that a conventional uncoupled approach may give useful results.

Different approaches with varying level of details have been used to represent the building including: deep beam model and 3D modeling, of structure.

The deep beam model is similar to the approach adopted by Burland and Wroth(1974). The structure is represented by an elastic beam with bending stiffness (EI) and axial stiffness (EA) representing the overall stiffness of the structure. The deformation can be imposed on the beam by incorporating it into a FE analysis using a coupled approach (either 2D or 3D) or by pre-describing the displacement of the beam (uncoupled approach). The advantages of this method are, especially when used in 2D conditions, the small amount of computational resources required and, therefore, the ability to perform extensive parametric studies.

Losacco (2011) proposed a simplified building model, called "equivalent solid", useful especially when many buildings have to be analyzed. The equivalent solid used in the study has the same footprint and the same height as the embedded part of the structure it is meant to represent. The adopted equivalence criterion is based on the agreement between the distributions of vertical reactions caused by a displacement field applied at the base of both the full and the simplified building model in uncoupled three-dimensional FE analyses.

3.3.2   Fragility and vulnerability curves

In the last few decades, a dramatic increase in the losses caused by natural catastrophes has been observed worldwide.

The vulnerability of buildings and territories to natural hazards (earthquake, landslide, tsunami etc.) are often addressed with fragility and vulnerability curves because they represent a good compromise between the accuracy of the results and the amount of time and money required for the studies. Fragility curves provide the probability of reaching or exceeding a given damage state as a function of the intensity of the natural event, and they are usually modeled by lognormal functions. A

very important point is that fragility curves clearly take into account that not all buildings of the same type will suffer the same level of damage for a given event intensity. Vulnerability curves are relationships between the mean amount of damage for a given type of building and the value of the event intensity. An example of these curves is shown in Figure 3.17 (from Saedi et al., 1999) for a massive stone masonry building (Lagomarsino and Giovinazzi, 2006). In particular, Figure 3.17(a) shows the damage distribution for this type of building for an earthquake EMS-98 intensity equal to 11. After calculating these damage distributions for all intensity levels, fragility curves can be generated (Figure 3.17 (b)). Then all this material is combined to calculate a mean damage value, for each intensity level, so that the vulnerability curves can be plotted (Figure 3.17(c)).
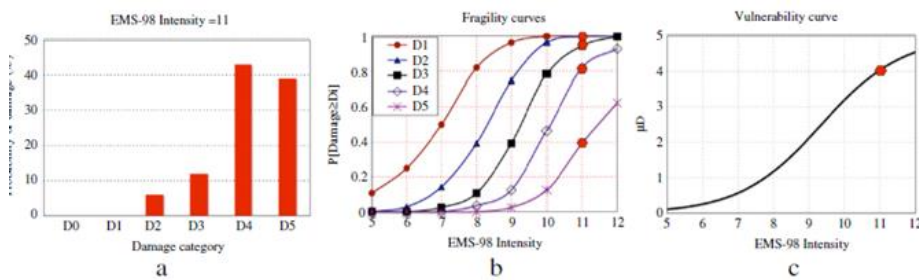
Figure 3.17 (a) Damage distribution, (b) fragility curves and (c)vulnerability curves for M4 building type, according to EMS-98 (Saeidi et al., 2009).

The various methods available to derive fragility and vulnerability curves can be distinguished in four main categories: empirical, engineering judgmental, analytical and hybrid, based on the scale of the study area, the availability and quality of input data and the local technology in construction practice (SafeLand Deliverable 2.5, 2011).

Empirical methods are based on observational data from post-events surveys; generally empirical vulnerability curves should be inherently more realistic compared to other categories, since they are based on the observed damage of actual structures subjected to real event. The most common problem when applying a purely empirical approach is the unavailability of (sufficient and reliable) necessary data; moreover the exportability of results need great caution.

Engineering judgmental fragility relationships resort to expert opinion.

The reliability of judgment-based curves is questionable due to their dependence on the individual experience of the experts consulted.

On the other hand, analytical fragility vulnerability curves are based on numerical modeling, so they can be extremely computationally intensive and time consuming and thus the curves cannot be easily developed for different areas or countries with diverse construction characteristics.

Hybrid relationships attempt to compensate for the scarcity of observational data, subjectivity of judgmental data and modeling deficiencies of analytical procedures by combining observed data and analytical estimations

Anyway in order to develop vulnerability and fragility curves three main types of input data are used:

1. damage scale;
2. building typology;
3. an intensity criterion.

The damage scale are generally based on threshold on global and local parameters of the structure.

Building typology must be defined according to the most important parameters relevant to resistance of the buildings against the considered hazard. For instance, the building materials (concrete, wood, masonry, etc.), the age and the quality of construction, the type of foundations (shallow or deep) and the global stiffness of the building.

Intensity of a given event can be expressed in different ways depending on the phenomena; for example, commonly used intensity parameter for landslides are absolute or differential displacement, velocity, kinetic energy, volume of the landslide deposit, impact force, etc.

Various methods for vulnerability assessment have been proposed in seismic engineering. Sabetta et al. (1998) used post-earthquake surveys of approximately 50,000 buildings damaged by destructive Italian earthquakes in order to derive vulnerability curves. The database was sorted into three structural classes and six damage levels according to the MSK macroseismic scale. A mean damage index, calculated as the weighted average of the frequencies of each damage level, was derived for each municipality where damage occurred and each structural class. Empirical fragility curves with a binomial distribution were derived as a function of PGA, Arias Intensity and effective peak acceleration. Rota et al. (2006) have also used data obtained from post-earthquake damage surveys carried out in various municipalities over the past 30 years in Italy in order to derive typological fragility curves for typical building

classes (e.g., seismically designed reinforced concrete buildings of 1-3 storeys). Rosetto et al. (2003) derived vulnerability functions for European-type RC structures based on observational data of 99 post-earthquake damage distributions observed in 19 earthquakes. Singhal and Kiremidjian (1996) developed fragility (or vulnerability) curves and damage probability matrices for three categories of reinforced concrete frame structures using Monte Carlo simulation. The probabilities of structural damage were determined using nonlinear dynamic analysis with an ensemble of ground motions. Dumova-Jovanoska (2004) produced vulnerability curves/damage probability matrices for reinforced concrete buildings built in the Skopje region. These earthquake damage-intensity relationships were derived by analytically modelling the representative RC buildings and by running the dynamic nonlinear analysis with a set of 240 synthetic earthquake records.

In scientific literature there are not so many case of generation of fragility or vulnerability function for subsidence (Saedi et al. 2009, 2012) and slow-moving landslides (Pitilakis et al., 2006a and b; Fotopoulou et al., 2011; Mavrouli and Corominas, 2010; Negulescu and Foerster, 2010). The main idea was to adapt the standard push-over analysis performed in seismic vulnerability assessment, which consists in setting a lateral force on a building in a push down analysis by imposing displacement on a building. The fragility and vulnerability curves derived up to now are referred to single building and they combine the results of numerical analyses with those deriving from the use of damageability criteria adopted in the geotechnical practice. In 2010 Negulescu and Foerster proposed some preliminary fragility curves with respect to the magnitude of differential ground displacement due to landslides. The proposed methodology consisted in using 2-D parametric nonlinear static time history uncoupled analyses for a simple one bay - one storey cast in-place RC frame, 4 m long (bay) and 3 m high (floor). Referring to subsidence phenomena, Saeidi et al. (2012) developed vulnerability and fragility curves based on the use of analytical methods, tested and validated with a set of three cases that occurred in Lorraine between 1990 and 1996. They referred to two building types that are typical of a large number of countries: unreinforced masonry buildings and reinforced masonry buildings with lengths between 10 and 20 m and heights between 7 and 10 m.

The development of fragility and vulnerability curves at different scale are not available in scientific literature. The proposed procedure for the

construction of fragility and vulnerability curves will be addressed in Chapter 5 referring to slow-moving landslides and its application will be shown in Chapter 7.

4   THE DInSAR TECHNIQUES

"Ordinary men look at new things with old eyes. The creative man observes the old things with new eyes."

Gian Piero Bona

Remote sensing is a valuable tool to observe the earth surface or the atmosphere from out of space using satellites (space borne) or from the air using aircrafts (airborne).

Synthetic Aperture Radar (SAR) interferometry is an important branch of remote sensing. One of the major applications of the SAR technology is represented by the SAR Interferometry (InSAR) technique which exploits, in its basic form, the phase difference of (at least) two complex-valued SAR images. This contribution is further enhanced via the development of innovative algorithms such as those adopted for multipass Differential Interferometric Synthetic Aperture Radar (DInSAR) image processing which allows, even over large areas, the retrieval of around 20-year displacements of the topographic surface at fairly affordable costs. The potential of the use of DInSAR data is testified by their increasing diffusion, as recently recorded worldwide with several different applications (e.g. European Space Agency's (ESA) projects MASMOV, ALPS, SLAM, TERRAFIRMA, etc.). This growth is remarkable in Italy, where a pioneering project (Piano Straordinario di Telerilevamento Ambientale) was launched in 2002 (Italian Law 179/2002) to promote their use in the field of land management.

4.1   BASICS OF REMOTE SENSING

Remote sensing is the science (and to some extent, art) of acquiring information about the Earth's surface without actually being in contact with it. This is done by sensing and recording reflected or emitted energy

and processing, analyzing, and applying that information (Lillesand and Kiefer,1987).

As Natural Resource Canada (2002) reported in much of remote sensing, the process involves an interaction between incident radiation (from an energy source or illumination) and the targets of interest, after being interacted with the atmosphere. The energy is in the form of electromagnetic radiation, whose main characteristics are wavelength or equivalently frequency. The wavelength is the length of one wave cycle, which can be measured as the distance between successive wave crests. Frequency refers to the number of cycles of a wave passing a fixed point per unit of time. Therefore, the two are inversely related to each other. The shorter the wavelength, the higher the frequency. The longer the wavelength, the lower the frequency. Before radiation used for remote sensing reaches the Earth's surface it has to travel through some distance of the Earth's atmosphere. Particles and gases in the atmosphere can affect the incoming light and radiation. The main effects are caused by the mechanisms of scattering and absorption.

Scattering occurs when particles or large gas molecules present in the atmosphere interact with and cause the electromagnetic radiation to be redirected from its original path. How much scattering takes place depends on several factors including the wavelength of the radiation, the abundance of particles or gases, and the distance the radiation travels through the atmosphere. In contrast to scattering, the absorbation causes molecules in the atmosphere to absorb energy at various wavelengths. Ozone, carbon dioxide, and water vapour are the three main atmospheric constituents which absorb radiation. Radiation that is not absorbed or scattered in the atmosphere can reach and interact with the target. There are three forms of interaction that can take place when energy strikes, or is incident upon the surface. These are: absorption; transmission; and reflection The proportions of each will depend on the wavelength of the energy and the material and condition of the feature. Radiation that is not absorbed or scattered in the atmosphere can reach and interact with the target on Earth surface. Absorption (A) occurs when radiation energy is absorbed into the target while transmission occurs when radiation passes through a target. Reflection occurs when radiation "bounces" off the target and is redirected. In remote sensing, measuring the radiation reflected from targets is one of the most important task. Two types of reflection can be mentioned, which represent the two extreme ends of the way in which energy is reflected

from a target: specular reflection and diffuse reflection. When a surface is smooth we get specular or mirror-like reflection where all (or almost all) of the energy is directed away from the surface in a single direction. Diffuse reflection occurs when the surface is rough and the energy is reflected almost uniformly in all directions. Most earth surface features lie somewhere between perfectly specular or perfectly diffuse reflectors. Whether a particular target reflects specularly or diffusely, or somewhere in between, depends on the surface roughness of the feature in comparison to the wavelength of the incoming radiation.

The instruments used to measure the electromagnetic radiation reflected/emitted by the target under study are usually referred to as remote sensors.

There are two classes of Remote Sensor:

1. Passive remote sensor;
2. Active remote sensor.

Remote sensing systems which measure energy that is naturally available are called passive sensors. On the other hand, active sensor provide their own energy source for illumination. The sensor emits radiation which is directed toward the target to be investigated. The radiation reflected from that target is detected and measured by the sensor.

Advantages for active sensors include the ability to obtain measurements anytime, regardless of the time of day or season. A valuable active sensor is Synthetic Aperture Radar (SAR).

4.2 SYNTHETIC APERTURE RADAR (SAR)

Synthetic Aperture Radar (SAR) is a day–night, all-weather monitoring active microwave remote sensing imaging system. It is able to perform accurate distance measurements between the sensor platform and the target on the ground, monted on-board to an aircraft and/or a satellite.

The concept of Synthetic Aperture Radar is based on the observation that a given target is imaged in a certain number of echoes during the passage of the sensor. This is illustrated in Figure 4.1, where Q is the target, while P_1 and P_2 are the radar positions when Q is imaged for the first and for the last time respectively. The echoes received from Q as the sensor moves between P_1 and P_2 have undergone different Doppler

shifts due to the sensor movement. These Doppler shifts can be used to discriminate the different echoes from Q and to combine them into one single image, with the same resolution which would be given by an antenna with **length Ls=(P$_2$-P$_1$)**. The important result is that the azimuth resolution of a SAR system is independent from the antenna distance from the surface and that a smaller antenna gives a better resolution.

The antenna size is chosen as a trade off between the resolution and physical implementation constraints such as thermal dissipation and transmitted power.
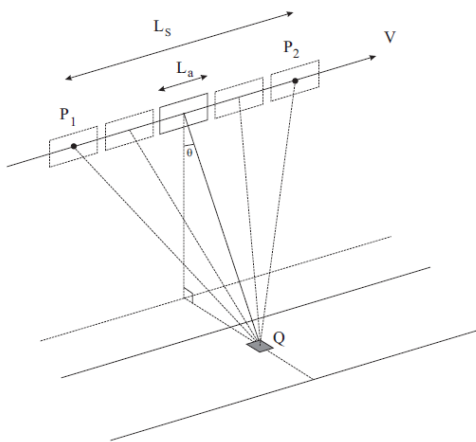
Figure 4.1 The principle of Synthetic Aperture Radar (Usai, 2001).

All satellites equipped with SAR sensors orbit the Earth on a near-polar orbit at an altitude ranging from 500 to 800 km above the Earth's surface, depending on the satellite platform hosting the SAR sensor. The time taken for a satellite to re-pass over the same area is called the 'revisiting time'.

Amongst different SAR sensors, the most used sensors are:

- ERS-1,ERS-2 and Envisat satellites operated by the European Space Agency (ESA);
- Radarsat-1 and Radarsat-2 operated by the Canadian Space Agency
- JERS-1 and Alos operated by the National Space Development Agency of Japan;
- COSMO-SkyMed operated by Italian Space Agency (ASI)
- TerraSAR-X operated by German Aerospace Center (DLR).

The earlier satellites (ERS, Envisat and Radarsat-1) were all right-looking satellites, meaning that microwave beam transmits and receives on the right side only of the satellite, relative to its orbital path, i.e. the system cannot rotate. Newer satellites (Radarsat-2, COSMO-SkyMed and TerraSAR-X) have both right-looking and left-looking capabilities, thus they can 'look' to the right or the left of the craft, but not both directions simultaneously.

The angle at which the sensor is pointed toward the earth's surface is referred to as the off-nadir angle (or look angle). The off-nadir angle of the ERS satellites was fixed at about 23°, but all subsequent satellites were fitted with the means to vary the viewing angle of the sensors, ranging from values of 20 to 50 degrees. This ability to vary the off-nadir angle is important in that it is possible to adjust for hilly or mountainous terrain if the relationship between viewing geometry and terrain slope is not optimal. As the satellite circumnavigates the Earth, it continuously emits millions of radar signals toward the Earth's surface along the radar beam's line of sight (LOS). The direction along the Line of Sight sensor-target is usually called the slant-range direction. The footprint trace has a swath 100 km wide in ground range on the Earth's surface, with the capability of imaging a strip 445 long every minute (strip map mode). The circumpolar orbits of all SAR satellites mean that for half of their trajectory they are travelling from the north pole towards the south pole and viceversa. When the scene is imaged with the sensor travelling from north to south the acquisition is referred to as descending; the opposite is referred to as ascending orbit.Currently, operational satellite SAR systems work in one of the following microwave bands:

• C band – 5.3 GHz (ESA's ERS and Envisat, the Canadian Radarsat, and the US shuttle missions)

• L band – 1.2 GHz (the Japanese J-ERS and ALOS)

• X band – 9.6 GHz (the German-Italian X-SAR on the shuttle missions).

L-band data, despite of a lower ground resolution than X and C band, are however advantageous for monitoring ground movement in vegetated areas, due to its vegetation-penetrating capabilities.

At the end the sensors are different mainly for band, maximum measurable displacement, revisiting time, period of acquisition, resolution, as synthesized in table 4.1.

Table 4.1 Main characteristics of most used SAR sensors

Sensor	Band	Maximum measurable desplacement [cm/year ca.]	Incidence angle [°]	Revisiting time [days]	Archive	Resolution [m x m]
ERS	C	15	23	35	1992-2001	20x5
RADARSAT-1	C	21	10-59	24	1995- -	10x5
RADARSAT-2	C	21	10-59	24	1997 up to now	10x5
J-ERS1	L	50	35	44	1992-1998	18x18
ALOS	L	47	18-43	46	2006-2011	16x16
ENVISAT	C	15	15-33	35	2002-2011	20x5
TerraSAR-X	X	35	___	8	2008- -	Up to 1x1
COSMOSky - Med	X	25	___	11	2008- -	Up to 1x1

SAR satellites acquire images of the Earth's surface by emitting radar signals and analyzing the reflected signal. A typical SAR image is 100 x 100 km and is regularly acquired over the same area (Figure 4.2).
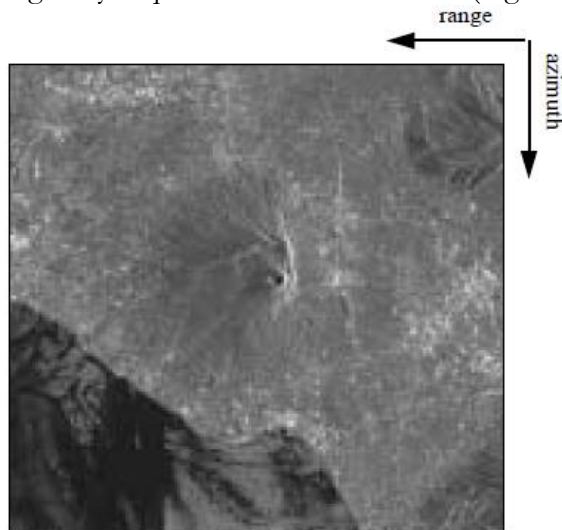
Figure 4.2 ERS image of Vesuvius (Italy) (Usai, 2001)

A digital SAR image can be seen as a mosaic (i.e. a two-dimensional array formed by columns and rows) of small picture elements (pixels). Each pixel is associated with a small area of the Earth's surface (called a resolution cell). More precisely, the resolution (depending on the sensor characteristics) is typically slightly smaller than the pixel dimension (depending on the sampling of the received signals) to guarantee the correct signal sampling. Each pixel gives a complex number that carries amplitude and phase information about the microwave field backscattered by all the scatterers (rocks, vegetation, buildings etc.) within the corresponding resolution cell projected on the ground.

This amplitude depends more on the roughness than on the chemical composition of the scatterers on the terrain. The detected SAR image is generally visualised by means of grey scale levels. Bright pixels correspond to areas of strong backscattered radiation (e.g. urban areas), whereas dark pixels correspond to low backscattered radiation (e.g. a quiet water basin) (ESA, 2013). So, texture and patterns, such as drainage ridges, fault lineaments and other morphologically features, are generally well visible in SAR images, thus they proved to provide complementary information for geological hazard mapping (Koopmans, 1993, Singhroy, 1995, Czuchlewski et al., 2003, Singhroy et al., 2004). Other studies have focused on the contribution of high-resolution stereo SAR and optical images, combined with topographic and geological information, in the production of landslide inventory maps (Singhroy et al., 1998; Singhroy and Mattar, 2000).

As well as amplitude values, radar systems record phase values, the key element in any interferometric measurement, given that it is related to the sensor-to-target distance.

The radiation transmitted from the radar has to reach the scatterers on the ground and then come back to the radar in order to form the SAR image (two-way travel). Scatterers at different distances from the radar (different slant ranges) introduce different delays between transmission and reception of the radiation. In real scenarios the SAR sensors transmit appropriate signals (modulated pulses) to lower the peak power; however, in order to simplify the discussion without loosing the rationale of the analysis, we assume to transmit purely sinusoidal signals. The above mentioned sensor-target distance introduces delay τ which is equivalent to a phase change $\Delta\varphi$ between transmitted and received signals. The phase change is thus proportional to the two-way travel distance 2R of the radiation divided by the transmitted wavelength λ.

However, due to the periodic nature of the signal, travel distances that differ by an integer multiple of the wavelength introduce exactly the same phase change. In other words, the phase of the SAR signal is a measure of just the last fraction of the two-way travel distance that is smaller than the transmitted wavelength.

Furthermore, exploiting differences of phases (Interferometric SAR, acronym InSAR) between two or more SAR observations from different orbits (spatial baseline) it is possible to derive digital elevation models (DEMs) (Madsen et al.,1993, Mora et al., 2003), while using also observation acquired at different times (temporal baseline) is possible to estimate surface displacements.

4.3   PRINCIPLES OF SAR INTERFEROMETRY

The basic principle of interferometry relies on the fact that the phase of SAR images is an ambiguous measure of the sensor-target distance. Therefore, distance variations can be determined by computing, on a pixel by pixel basis, the phase difference (interferometric phase) relative to two SAR images (standard two-pass interferometry) (Figure 4.3).
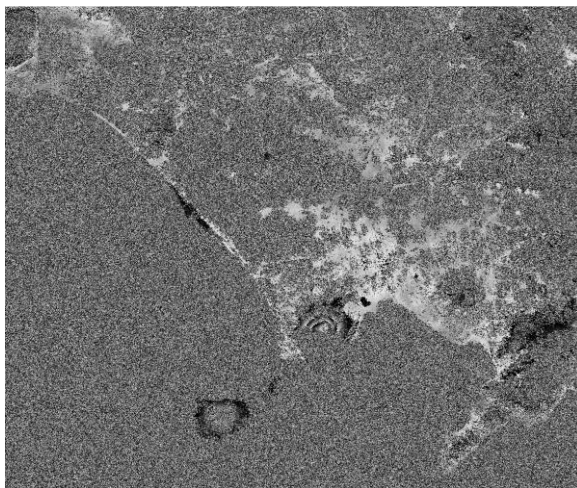
Figure 4.3 Interferogram derived by two ERS-2 acquisitions dated 18 December 1997 and 23 December 1999; the complete grayscale range corresponds to about 2,8 cm of sensor-target distance variation, (Data courtesy of IREA-CNR, Naples).

This is actually performed as pixel by pixel product of the reference image (master) times the complex conjugated secondary (slave) image. As already mentioned, each SAR image pixel represents the coherent sum of all scattering elements within a resolution cell.

Moreover, each element contributes both with its own complex reflectivity (amplitude and phase) and with its individual distance from the sensor. The coherent image formation mechanism coupled with the high phase sensitivity prevents the phase value relative to an individual pixel of a single SAR image from being directly exploitable. On the other hand, as long as the complex reflectivity of the pixel as a whole (i.e. the reflectivity of the elementary scatterers and their differential sensor-target path) does not change in the time span between successive radar acquisitions, it is cancelled out from the interferometric phase, thus allowing the measurement of the variation of the range path to the scatterers within the resolution cell. This is the basic assumption for carrying out interferometric measurements and is referred to as absence of decorrelation (or full coherence).

In reality, a residual differential reflectivity term always affects the interferometric phase and is referred to as decorrelation noise. In particular, vegetated areas are often afflicted by temporal decorrelation because of a complex reflectivity varying with time and/or position of the elementary scatterers within the sampling cell (e.g. leaves and small branches of a tree). Conversely, geometric decorrelation is due to a complex reflectivity that changes with the acquisition geometry [6]. Geometric decorrelation is mainly due to the presence of plural comparable (in terms of the backscattered radiation) scatterers within a single sampling cell. Their differential travel path varies with the acquisition geometry. The key orbital parameter controlling this effect is the so-called normal baseline b, i.e. the projection perpendicular to the line-of-sight (LOS) direction of the distance of the satellite orbits relative to the two images involved in the interferogram.

Briefly, the interferometric phase is the combination of several terms that can be classified in two main categories:
- geometric (deterministic) terms associated to the target-to-radar path difference;
- stochastic phase shift (noise) terms.
Mathematically, the phase difference $\Delta\varphi$, related to a generic pixel can be expressed as follows:

$$\Delta\varphi = \Delta_{\varphi geo} + \Delta_n \qquad (4.1)$$

wherein, $\Delta_{\varphi geo}$ is the geometric term and Δ_n the stochastic one.

Geometric terms are induced by the target topography in association with the presence of an angular view difference due to the spatial baseline, and a possible target displacement occurring between the passes:

$$\Delta_{\varphi geo} = \Delta_{\varphi}^{topo} + \frac{4\pi}{\lambda} d \qquad (4.2)$$

with λ the transmitted signal wavelength equal to 5.6 cm for sensor operating at C-band (ERS, Envisat, etc.).

The Stochastic contributions in equation are due to:

- changes of the scattering properties due to temporal modification (temporal decorrelation) and/or to the different interaction mechanisms between the electromagnetic wave and the ground surface associated to the angular view difference (spatial decorrelation).

- propagation delay variation due to the presence of the atmosphere (Atmospheric Phase Screen, or briefly APS).

Although SAR systems are capable of penetrating the cloud cover, the SAR phase signal is significantly influenced by the atmospheric conditions, in particular by the water vapour distribution in the troposphere. The atmospheric phase distortion (atmospheric phase screen, APS) is strongly correlated in space within each individual SAR image (i.e. it varies smoothly as a function of range and azimuth).

- receiver noise contributions (thermal noise decorrelation).

- processing artifacts and orbital information inaccuracies.

These latter (in particular baseline errors) translate into a further spatially correlated phase term (a low order phase polynomial).

The stochastic terms can be expressed as follows:

$\Delta n = \Delta n\_low + \Delta n\_high$

wherein Δn_low is mainly associated with the APS and to the orbital errors and Δn_high to the decorrelation effects, the thermal noise and processing artefacts. The former is a spatially correlated and temporally uncorrelated contribution and, as consequence, can be reliably estimated only by using a set of interferograms, rather than a single acquisition pair. Accordingly, if stochastic contributions are "low", or "kept low" via averages or ad-hoc filtering procedures, by knowing the target height from an external Digital Elevation Model (DEM), the topography

contribution can be subtracted from the interferogram (differential interferogram generation) thus accessing to the deformation measure.

Processing artifacts can be limited by using accurate algorithms for focusing and, particularly for the alignment (registration) of the two images before compare the phase difference.

Orbital information inaccuracies can be controlled because they appear as low order spatial contributions on images covering 80x80 km, such as those associated to a frame of ERS and Envisat-ASAR (ERS-like mode) data.

Thermal noise decorrelation is generally negligible, unless target backscattering is somewhat low (weak targets or targets in shadow). On the other hand, spatial decorrelation is relevant only at large spatial baseline (let's say 150 m for ERS and Envisat case) over homogeneous scenes. This noise contribution can be tackled, by limiting the baseline, or reduced by ad-hoc filtering techniques.

Temporal decorrelation is a much more critical issue that strongly impacts the final monitoring in terms of spatial coverage. Qualitatively arid is much better than forest, dry conditions are better than wet, and long radar wavelengths are better than short ones. With respect to this aspect, application of the DInSAR technique to urban areas is particularly favourable. In such a case, due to the presence of stable and bright (manmade) targets, high correlation may be observed even at temporal separation of several years.

Atmospheric contribution shows correlation lengths on the order of 0.5-1 km spatial separation and together with DEM inaccuracy, which introduces errors in the topographic contribution cancellation for the generation of the differential interferogram especially at large baseline, represents a major limitation for the accuracy of standard two-pass DInSAR

APS mitigation and the possibility to track the deformation $d(t)$, i.e. not only to determine its variation d between two time instants, and the retrieval of the residual topography Δz in (1.4), are the fundamental advances offered by recent multi-temporal DInSAR techniques over standard two-pass differential interferometry.

The first studies based on the InSAR technique were based on single interferograms (i.e. using an image pair) or a few interferograms, and provided only qualitative information on deformations (Fruneau et al.,1996, 2003, Rott et al., 1999, Kimura, 2000). However, InSAR is limited by the presence of at least two error sources: variations in the

Atmospheric Phase Delay (APD) and the inaccuracies of the external Digital Elevation Model (DEM) involved in the cancellation of the topography component from the signal interferences (Massonnet et al., 1993, 1995, Zebker, 1997). These limits were overcome with the development of Multipass Differential SAR Interferometry (MP-DInSAR), consisting of the processing of at least 30 images.

4.4 DInSAR MULTIPASS ALGHORITMS

Since early 2000s several multi-pass DInSAR algorithms have been widely used to retrieve information on displacements of the topographic surface, among them: the Small Baseline Subset (SBAS) technique (Berardino et al., 2002), the Coherent Point Target Analysis (CPTA) (Mora et al., 2003), the Interferometric Point Target Analysis (IPTA) (Wegmuller, 2005), the Spatio-Temporal Unwrapping Network (STUN) (Kampes and Adam, 2005) and the Enhanced Spatial Differences (ESD) (Fornaro et al., 2007). The available techniques for the analysis of phase signals in interferometric stacks can be grouped in two classes: persistent scatterers interferometry (PSI) (Ferretti et al., 2000, 2001; Costantini et al., 2008; Crosetto et al., 2008) and Small-Baseline (SBAS) approaches (Berardino et al., 2002; Fornaro et al., 2009). The Persistent Scatterers Interferometry (PSI) (Ferretti et al 2000) methods operates at full spatial resolution and identify reliable scatterers by measuring their multitemporal coherence related to the phase stability. Monitored scatterers correspond to man-made structures (buildings, roads, bridges) or bare rocks whose size is lower than the system resolution.

Conversely, the SBAS approach is aimed at monitoring distributed scatterers (i.e. scatterers distributed over a large number of pixels) in order to measure ground deformations over large areas (Berardino et al 2002). These techniques take benefit of a spatial averaging (multilook) operation to improve the quality of the phase signal thus performing a change of the scale of analysis. The interferograms are generated according to small, temporal and spatial, separation constraints in order to reduce decorrelation effects associated with distributed scattering mechanisms typically present on rural areas. The SBAS approach, allows investigating ground deformations at two distinct spatial scales referred

hereafter to as large and local scale, respectively. At the large scale, the technique exploits averaged (multi-look) interferograms and allows us to generate mean deformation velocity maps and associated time series for areas extending for some thousands of square kilometers (up to 100 x 100 km), with a ground resolution of the order of 80 x 80 m. The obtained products are particularly suited for regional scale displacement analysis, but can be conveniently used to outline individual and multiple distant sites affected by ground deformation. At the local scale, the technique exploits the single-look interferograms, i.e., generated at full spatial resolution (typically of the order of 10 x 10 m), and leads to detection and analysis of local deformation.

With reference to full resolution multitemporal DInSAR analysis, particularly suited for investigating single structures with high resolution sensors where angular decorrelation due to distributed scattering plays a marginal role, a recent advancement is represented by the introduction of tomography approaches (Fornaro et al 2005). More specifically, the Multi-Dimensional Imaging technique (MDI) (Lombardini 2005, Fornaro et al 2009) allows the identification, localization and monitoring of scatterers at full resolution with improved performances with respect to classical PSI approaches. Such an improvement of MDI is due to both the capability to "enter" within the SAR pixels to identify and monitor multiple scatterers (higher order analysis) and the enhanced detection and estimation performances in the identification and monitoring of displacements of the dominant scatterer in each pixel (first order nalysis). The former feature, particularly favourable for resolving layover onvertical structures (e.g. buildings) with very high (1m) resolution data,and the latter feature, evident also on high resolution (3m) data, are directly ascribed to the use, in MDI analysis, of both the amplitude and phaseinformation in the SAR stack, whereas PSI only exploits the phase information. The MDI is currently used at an operational level by the German Aerospace Center (DLR) for the analysis of urban areas (Zhu 2011, Wang et al. 2012) with TerraSAR-X data. Furthermore, the resolution improvement allows the capture of more details of singlefacilities under observation and hence their precise monitoring, astestified by the available literature mainly focused on the use ofTerraSAR-X data (Gernhardt et al 2010, Zhu and Bamler 2010, Reale et al 2011, Reale et al 2011a, Fornaro et al 2012, 2013).

As for the limits of DInSAR data, the principal ones are:

1) The time series of displacement are relative both in space, regards to a reference point assumed motionless, and in time referring to the first image available. The correct location of the reference point is fundamental in the quantitative detailed analysis. Considering this latter aspect, some techniques return (for example PSInSAR) information regarding the standard deviation [mm/year] which indicates the oscillation of estimated velocity with respect to the reference point in the analysis.

2) To overlay DInSAR data with other thematic maps it is necessary consider the error of location of DInSAR (in the case of PS is ± 2m to the north and east in the direction of ± 7m).

3) DInSAR data are returned with a precision of the order of mm/year on the velocity and of centimeter on the single displacement.

4) To each measure is associated a parameter of quality, named coherence. It measures the agreement between the data and the model used in the analysis and can take values between 0 and 1 (PST- MATTM, 2010) for all the algorithms, the value depends on the used algorithm of processing.

5) The images are acquired on ascending and descending orbit, and this question requires attention especially in the study of landslides where a shift along one side which exposes to the sensor can be viewed as lifts. An attempt to overcome this drawback is represented by the projection of the LOS measurement along the direction of maximum slope (Colesanti and Wasowski, 2006) for the production of advanced velocity DInSAR maps (Cascini et al., 2010a). In analysis of DInSAR data in flat areas (eg. subsidence in urban areas) the availability of data on both orbits allow to distinguish movements along the horizontal and vertical direction (Manzo et al., 2006).

6) Some of the available algorithms such as SBAS and PSInSAR, can return data with different resolutions: in the case of SBAS information is averaged over an area of 80 m x 80 m (Berardino et al., 2002) at low resolution while over an area 5 x 20m at full resolution (Lanari et al., 2004); in the case of technical PSInSAR ranging from information on the Permanent Scatterer (PS) to distributed scatteres provided by the new technique SqueeSAR (Tamburini et al., 2012). Examples of use of DInSAR data at different resolutions according to the scale of the analysis can be found in Peduto (2008) and Cascini et al. (2010a).

7) In the use of satellite data for buildings monitoring it is necessary consider that the measurements refer to the roof and not directly to

foundations. In this direction the so-called differential SAR tomography also known as 4D imaging(Fornaro et al. , 2012) can be particularly useful, promising to return, thanks to the use of sensors with very high resolution, 3D information on buildings over time.

4.5 STATE OF THE ART OF DInSAR APPLICATIONS

Since the first description of the technique, which was based on L-band SEASAT SAR data (Gabriel et al., 1989), the great potential of DInSAR for land deformation applications has been recognized. In the last twenty years many applications of DInSAR multipass technique have been developed in studying various natural phenomena in different fields of geosciences; Crosetto et al. (2003) distinguishes among them:
- *Seismology* probably represents the field where the major number of scientific achievements have been obtained, including different types of coseismic studies, (Massonnet et al., 1993; Peltzer and Rosen, 1995; Peltzer et al., 1999; Reilinger et al., 2000; Pedersen et al., 2001, Reale et al., 2011); postseismic deformation studies (Peltzer et al., 1996; Massonnet et al., 1996; Jónsson et al., 2003), and the monitoring of aseismic (Rosen et al., 1998) and interseismic tectonic events (Chorowicz et al., 1995; Wright et al., 2001; Colesanti et al., 2003).
- *Vulcanology* represents another relevant application field, with several studies of volcanic deflation and uplift, e.g. see (Massonnet et al., 1995; Amelung et al., 2000; Lu et al., 2000; Salvi et al., 2004).
- *Glaciology.* Different researches have been conducted in this domain, mainly on the ice sheets of Greenland and Antarctica. They included InSAR ice topography measurements (Kwok and Fahnestock, 1996; Joughin et al., 1996); ice velocity measurements (Goldstein et al., 1993; Joughin et al., 1995; Joughin et al., 1998; Mohr et al., 1998); and other glaciological applications, like the determination of the discharge of glaciers (Rignot et al., 1997; Joughin et al., 1999).

Other applications are related to subsidence and slow-moving landslides, on which this section focuses, distinguishing the analyses carried out at different scales.

4.5.1 Application to subsidence phenomena

The number of applications of DInSAR techniques to detect and monitor subsiding area at different scales[1] has been rapidly increased during the last decade (Table 4.2).

For instance, at *small scale* Meisina et al. (2008) developed a methodological approach for the geological interpretation of the PS data via the preliminary detection of the so called "anomalous areas" wherein significant movements are recorded (cluster of minimum 3 Ps with a maximum distance of 50 m and a rate of displacement exceeding ± 2 mm/year); then the interpretation is firstly carried out via the overlap, in a GIS environment, of anomalous areas with other layers (topographic map, geological map, orthophoto) that might have relevance in explaining the patterns of motions of PS points and finally a large investigation is carried out via geomorphological, geological and geotechnical field surveys.

At *small scale*, Vilardo et al. (2009) discriminated the vertical and east–west displacement components in Campania region thanks to the availability of datasets referring to both ascending and descending orbits of ERS-1 and ERS-2 satellites.

At *medium scale*, Cascini et al. (2007) preliminary detected the most critical zones of the Campanian Plain where the highest ground surface settlements occur, in terms of both magnitude and rate.

At *large scale*, Herrera et al. (2009, 2010) used DInSAR data to successfully detect and monitor recent subsidence affecting Murcia City (Spain) via the exploitation and the comparison of both C- and X-band satellite radars.

Cascini et al. (2007a, 2011a) derived, at *large scale*, the map of settlements and the deformation gradient map, while at *detailed scale* (Cascini et al.,2007b, 2011a) they derived relevant parameters (e.g. deflection ratio, relative rotation) widely adopted in engineering practice to assess building damageability.

Arangio et al. (2013) integrated, at *detailed scale* the results of a DInSAR analysis with an intermediate semi-empirical model to investigate three buildings located in the southern part of the city of Rome. The model, originally proposed by Finno et al. (2005).considers each building as an

---

[1] According to Fell et al. (2008), in this Thesis, the scales of analysis can be differentiated among: small scale (< 1:100,000), medium scale (1:100,000 to 1:25,000), large scale (1:25,000 to 1:5000) and detailed scale (<1:5.000).

equivalent laminated beam, where the layers represent the floors and the core material reproduces the infill walls. The results obtained by the model have been compared to the damages observed on the buildings, showing a good agreement .

Table 4.2 Applications of DInSAR technique to subsidence in analysis at different scale (modified after Peduto, 2008).

Case study	Causes	Scale of analysis	Author
Piemonte Region, Italy	Consolidation of recent sediments and construction of buildings	Small scale	Meisina et al. (2008)
Campania Region, Italy	Tectonic structures	Small scale	Milone et al. (2011)
	Water withdrawls	Small scale	Vilardo et al. (2009), Milone et al. (2011)
Su-Xi-Chang area and Shanghai City, China	Water withdrawals	Small scale	Shi et al. (2008)
Arno River Basin	Water withdrawals and compactation of soft soils	Medium scale	Canuti et al. (2006)
Barcellona province, Spain	Salt mine	Medium scale	Crosetto et al. (2005)
Toluca Valley basin, Mexico	Water withdrawals	Medium scale	Calderhead et al., (2010)
Campanian Plain, Italy	Water withdrawals	Medium scale	Cascini et al., 2007b
Rome	Consolidation process	Large scale	Stramondo et al., 2008
Murcia metropolitan area, Spain	Water withdrawals	Large scale	Herrera et al. (2009, 2010) Tomas et al. (2010)

Bologna, Italy	Water withdrawals and active tectonics.	Large scale	Stramondo et al., (2007)
Sarno, Italy	Water withdrawals	Large scale	Cascini et al., (2006: 2007), Peduto, (2008)
Manfredonia Gulf, Italy		Large scale	Triggiani et al., (2011)
Shanghai, Tianjin, Badong, and Three Gorges Dam (China)	Water withdrawals	Large scale	Perissin et al.,(2011)
Mexico City, Mexico	Water withdrawals	Large scale	Lopez-Quiroz et al. (2009), Osmanǧglu et al. (2011)
Mokpo City, Korea	Soil Compaction	Large scale	Kim et al. (2008)
Calcutta City, India	Water withdrawals	Large scale	Chatterjee et al., 2006
Vauvert salt mine (France).	Mining	Large scale	Raucoles et al., 2003
Bangkok, Thailand	Water withdrawals	Large scale	Worawattanamateekul et al, 2003),
Venice, Italy	Natural and anthropic	Large scale	Strozzi et al., 2001
Campi Flegrei Caldera, Italy	Bradism	Large scale	Lundgren et al., 2001
			Berardino et al., 2003
Los Angeles USA	Active faults, petroleum and water pumping	Large scale	Berardino et al., 2003
Paris, St.Lazare, France	Water pumping for underground construction.	Large scale	Fruneau et al., 2003

			Berardino et al., 2002
Vomero quarter, Naples (Italy)	Underground construction	Large scale	Lanari et al., 2004a
			Cascini et al., (2007b).
Sarno, Italy	Water withdrawals	Large scale	Cascini et al., (2007a, 2011), Peduto, (2008)
La Union, Spain	Collapse of an abandoned underground mine gallery	Large scale	Herrera et al. 2012
Rovigo, Italy	Underground construction	Detailed	Jurina et al., 2004
Sarno, Italy	Water withdrawals	Detailed	Cascini et al., 2007b, 2011a
Rome	Consolidation process	Detailed	Arangio et al., 2013

4.5.2 Application to slow-moving landslides

As for the application of multipass DInSAR data to slow-moving landslides, the scientific literature (i.e. Colesanti and Wasowski, 2006) has widely discussed the current limits:

1) Displacement data represent the one dimensional projection in the Line Of Sight (1D LOS projection) of a deformation that can actually occur in all three dimensions (Rocca, 2003; Manzo et al., 2006).

2) The ambiguity of phase measurements implies the impossibility to track correctly (i.e., unambiguously) the relative LOS displacement between two scatterers exceeding $\lambda/4$ (=1.4 cm for ERS) within one revisiting time interval (35 days for ERS), i.e. approximately 14.5 cm/yr. In practice it is extremely difficult to detect LOS displacement rates exceeding 8–10 cm/yr in the presence of low density of stable scatterers, such as in the case of landslides where topography and vegetation introduce a limitation in the number of detected scatterers. This limits cause the use of DInSAR data only to landslides ranging from extremely to very slow phenomena according to the velocity classification of Cruden and Varnes (1996).

3) Limited versatility in terms of (a) positioning of the measurement points and (b) revisiting time. Both factors (a) and (b) cannot be optimised as degrees of freedom while planning an analysis.

Despite of the above limits, the usefulness of DInSAR data for landslide characterization and mapping has been investigated in several studies, carried out at different scale of analysis (Table 4.3). Some of these studies at small and medium scales resulted in original procedures to update the landslide inventory map by combining conventional thematic data (e.g., topographic, geological, land use maps, and optical images) and on-site investigations with DInSAR data. As for the interpretation of the PSInSAR data at *small scale*, an interesting example is provided by Meisina et al. (2008) with reference to Piemonte region (25,000 km^2); in such a case, the adopted approach is quite similar to the one already synthesized for subsidence phenomena.

Cascini et al. (2009, 2010) carried out preliminary tests at *medium scale* with DInSAR data with the purpose of validating and/or updating landslide inventory maps with reference to both the state of activity of the mapped phenomena, and the detection of evidence of movements in landslide-prone areas in a test area (489 km^2) belonging to the northern portion of the territory of the National Basin Authority of Liri-Garigliano and Volturno rivers (NBA LGV) in central-southern Italy. In particular, they developed procedures for the generation of the a priori landslide DInSAR visibility map (which can be used to identify areas where a good DInSAR data coverage is expected) on ascending and descending orbits; moreover, the Authors implemented an original procedure for DInSAR data projection along the slope so as to generate an advanced DInSAR landslide velocity map.

At *medium scale*, Lu et al. (2012) developed a spatial statistic approach to automatically highlight areas preferentially affected by extremely slow-moving landslides, named Permanent Scatterers Interferometry Hotspot and Cluster Analysis (PSI-HCA) in the Arno River Basin Authority, Central Italy. This approach is based on two statistical steps: the Getis–Ord Gi* and Kernel density estimation. The Getis-Ord Gi* allows to the association of Ps at a certain distance, while Kernel density estimation converts a large amount of PSs into several hotspots for an easier and straightforward visualization.

At *large scale*, Colesanti et al. (2003) analyzed the evolution of the Ancona landslide (central Italy) by processing 61 ERS images acquired in the time span between June 1992 and December 2000 and then they compared

the obtained results with displacement values detected during optical leveling.

Cascini et al. (2010) using full-resolution DInSAR data pursued two main goals at *large scale*,: the preliminary analysis of landslide features (i.e. check of mapped boundaries; detection of ground displacement out of mapped areas) and an insight into different kinematic behaviour characterizing different portions of the same phenomenon.

However, the full integration of DInSAR data in current practices of Authorities in charge of land use planning and management and technicians and engineers engaged in design activities is not yet adequately supported by standardized procedures both for updating of inventory map and analysis of consequence. This issue will be addressed in Section 5.

Table 4.3 Application of DInSAR technique to landslide in analysis at different scale (modified after Peduto, 2008).

Case of study	Scale of analysis	Author
Umbria Region, Italy	Small scale	Guzzetti et al.,2009
Piemonte Region, Italy	Small scale	Meisina et al.,2008
Liri-Garigliano e Volturno River Basin, Italy	Medium scale	Cascini et al.,2009, 2010, 2013
Arno River Basin, Italy	Medium scale	Catani et al.,2005 Farina et al., 2006 Lu et al., 2012, 2013
Maratea, Italy	Large scale	Berardino et al, 2003
Ancona, Italy	Large scale	Colesanti et al,2003
Torrice and Frosinone, Italy	Large scale	Cascini et al.,2010
Naro, Italy	Large scale	Cigna et al., 2011
Shuping landslide, China	Large scale	Fu et al., 2010
La Clapiere, France	Large scale	Fruneau et al., 1996
La Vallette, France	Large scale	Squarzoni et al., 2003
Corvara landslide	Large scale	Strozzi et al., 2005
Costa della Gaveta, Italy	Large scale	Di Martire et al., 2013

5 THE PROPOSED PROCEDURE AT DIFFERENT SCALES

"Everything should be made as simple as possible,
but not simpler."

Albert Einstein

Nowadays the growing interest of scientists and technicians in DInSAR data currently available through National and Regional projects together with the complexity of remote sensed data and the continuous research in the field of interferometry call for procedures pursuing the proper use of DInSAR data and their validation with reference to well documented case studies.

To this end, after an in-depth review of the limits and potentialities of DInSAR data as well as the most relevant applications, this Section provides original procedures at different scales for both the characterization of the phenomena of interest and the prediction of the consequences to buildings interacting with them.

5.1 GENERAL FRAMEWORK

Innovative technologies have always represented and are expected to play roles of primary importance in all Engineering branches, and among these, in Geotechnical Engineering. The ways in which technologies are employed deeply affect the results. As for remote sensing data they represent a valuable tool, although shared standardized procedures are still lacking and the potential of this kind of data has not been fully exploited. As described in Crosetto et al. (2005) due to complex nature of the DInSAR data, the more advanced applications and the best results are usually achieved through a close cooperation between the DInSAR specialists and the people able to interpret, analyze and model the DInSAR. In this context the SAR specialists can play a fundamental

role in helping the users of the DInSAR products to fully understand their limits and potentialities.

In Figure 5.1 it is proposed a general framework involving experts in both the phenomenon (specific activities are framed in blue) and radar image processing (specific activities are framed in red).
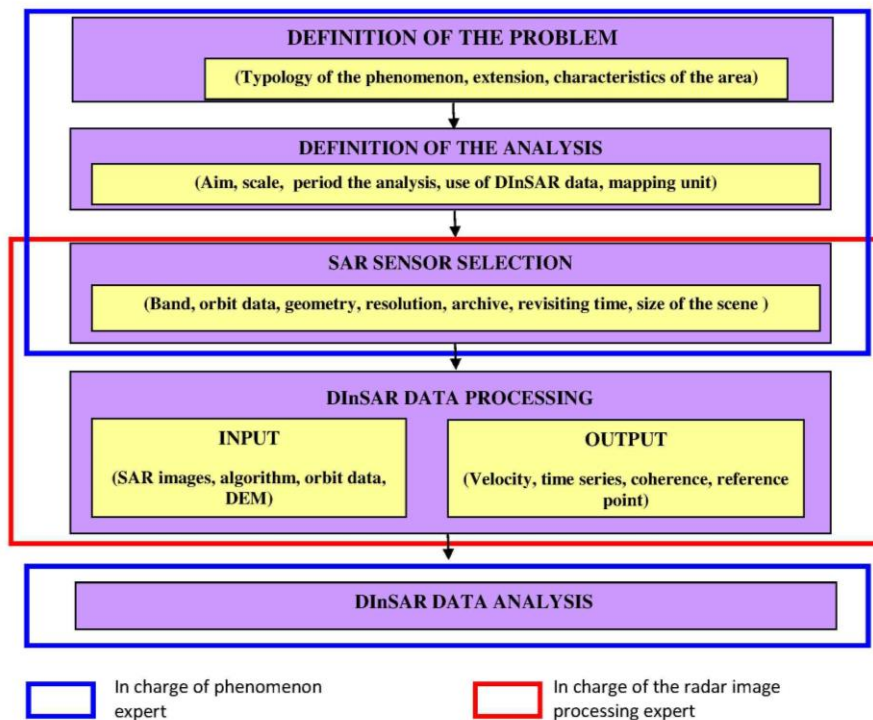
Figure 5.1 General framework for use of DInSAR data (modified after Cascini et al., 2012).

In particular, the first stage includes the definition of the problem at hand: the type of the phenomenon (e.g. subsidence, slow-moving landslide, etc.); the extension of the area to investigate and the description of the characteristics of the area that most directly can influence the use of satellite data (i.e. vegetation cover, presence of

urbanized area, topographical and historical information about any changes occurred in the area during the period of observation, etc.).

Once the problem is defined, it is necessary to set the analyses to be performed by identifying: the aim and the scale of the analysis; the period of the analysis; the mapping unit (Guzzetti et al., 2005) - e.g. grid cell for subsidence phenomena (see Section 5.2) and terrain units for landslides (see Section 5.3) - on which to carry out the analysis in GIS environment.

At this stage it is important to decide whether DInSAR data will be used in a standard (the most common in current applications involving the use of: velocity, time series, the accuracy of the measurement, the reference point) or sophisticated (taking into account the range of coherence related to the used algorithm and the localization error) way (Table 5.1).

Table 5.1 DInSAR data use as input for the analyses

DInSAR DATA	STANDARD USE	SOPHISTICATED USE
VELOCITY	**X**	**X**
TIME SERIES	**X**	**X**
MEASUREMENTS PRECISION	**X**	**X**
REFERENCE POINT	**X**	**X**
LOCALIZATION ERROR		**X**
COHERENCE		**X**

Then, with the contribution of both experts it is possible to identify, the selected image dataset according to the characteristics of the used sensor such as: band, orbital data, geometry of acquisition, data resolution, stacks of available images on the study area, revisiting time and size of the scene.

Once SAR images are selected they are processed through a well-determined algorithm (see Section 4.4) whose selection must be preferably carried out with the contribution of both experts depending on the available input data and the expected outputs (velocity, time series, coherence, reference point).

Finally, the analysis of the DInSAR data can be carried out at different scales pursuing different aims as it will be shown in Section 6 for subsidence phenomena and in Section 7 for slow-moving landslides.

5.2 PROCEDURES AT DIFFERENT SCALES FOR SUBSIDENCE PHENOMENA

As for the analysis of DInSAR data in subsidence studies, in this Thesis innovative multi-scalar procedures have been developed and validated with reference to well documented case studies (Figure 5.2). The scheme of figure 5.2 shows that in general at different scales of analysis different mapping units (i.e. cell size) need to be set on test areas of different extension and different objectives can be pursued as well.

SCALE	RANGE OF SCALES	SIZE OF CELL	PURPOSES / EXAMPLES OF APPLICATION	TEST AREA
SMALL	< 1:100,000	≥ 100 X 100 m	Critical area zoning	Campania Region
MEDIUM	1:100,000 to 1:25,000	25x25 m ≤ size of cell ≤100 x 100 m	Inventory of affected municipalities	Campanian Plane
LARGE	1:25,000 to 1:5,000	5 x 5 m ≤ size of cell ≤ 25 x 25 m	Zoning of built up areas where damage occurred or is likely to occur and analysis damage severity	Baronissi Municipalty (SA)
DETAILED	>1:5,000	≤ 5 x 5 m	Detection of damaged /likely damaged buildings	Buildings within Baronissi Municipality

Figure 5.2 Proposed procedure at different scale (modified after Cascini et al., 2011e).

The defined mapping unit to study subsidence phenomena is a grid cell dividing the territory into regular areas ("cells") of pre-defined size,

which are assumed as reference mapping unit (e.g., Carrara, 1983; vanWesten, 1993; Guzzetti, 2005).

In this Thesis the cell size is defined as equal to 1/1000 * the value of the scale; the use of DInSAR data according to table 5.1 is sophisticated.

As far as the analysis at small scale is concerned, it poses the problem of managing massive data over large area. The main objective is to detect critical areas in order to inform policy makers and dwellers. The test area is the Campania Region.

The results obtained at small scale address the analyses at medium scale just within the detected critical areas, thus avoiding both time consuming and expensive studies. At this scale, the aim of the analysis is to draw the inventory of affected municipalities as well as their ranking to be used in land use planning and management activities such as the evaluation of possible constraints in the development of large engineering projects (see Appendix D). At medium scale the analysis is carried out with reference to the most affected Plain of Campania Region, i.e. Campanian Plain, as shown by analysis at small scale.

At large scale the aim of the analysis is to zone built up areas where damage occurred or is likely to occur; moreover a preliminary analysis of damage severity which can turn out to be useful to plan more suitable zones to be urbanized or to detect damaged/likely damaged urbanized areas can be carried out

At detailed scale the analysis allows the application of damageability criteria and can be suited to Engineers engaged in design activities.

It is worth stressing that there is not an official Plan for subsiding areas in Italy; as a result these procedures can provide valuable benefits for scientists, practitioners and authorities in charge of land management for both subsidence mapping and the analysis of consequence to elements at risk.

5.2.1 Small scale

At small scale the aim of the analysis is to detect area affect by subsidence to inform policy makers and dwellers. The typical area of zoning is higher than 10.000 km² and the scale of analysis is lower than 1:100.000 according to Fell et. al. (2008), consequentially the adopted grid of analysis has a cell size superior of 100x100 m. As it is shown in Figure 5.3 the proposed procedure at small scale is subdivided in three working phases plus a preliminary one; the input data, the procedure and

the output, generally furnished as map, are also reported for each phase of analysis. The preliminary phase is preparatory for DInSAR data and for operative grid of analysis. In particular, in this phase the input data are Digital Terrain Model (DTM) and DInSAR data. Flat area are extracted from the slope angle map (derived by the DTM). Then, an operative grid of analysis is set on the flat area according to scale of analysis. The DInSAR data are treated to take into account the localization error (e.g. drawing of a buffer around DInSAR information on the ground). In the first phase the aim is the individuation of covered cells. In particular, each cell is defined covered if at least one PS falls within its perimeter. Cells covered by DInSAR data acquired on ascending orbit, descending orbit and (by their combination) covered by both ascending and descending orbit are distinguished.
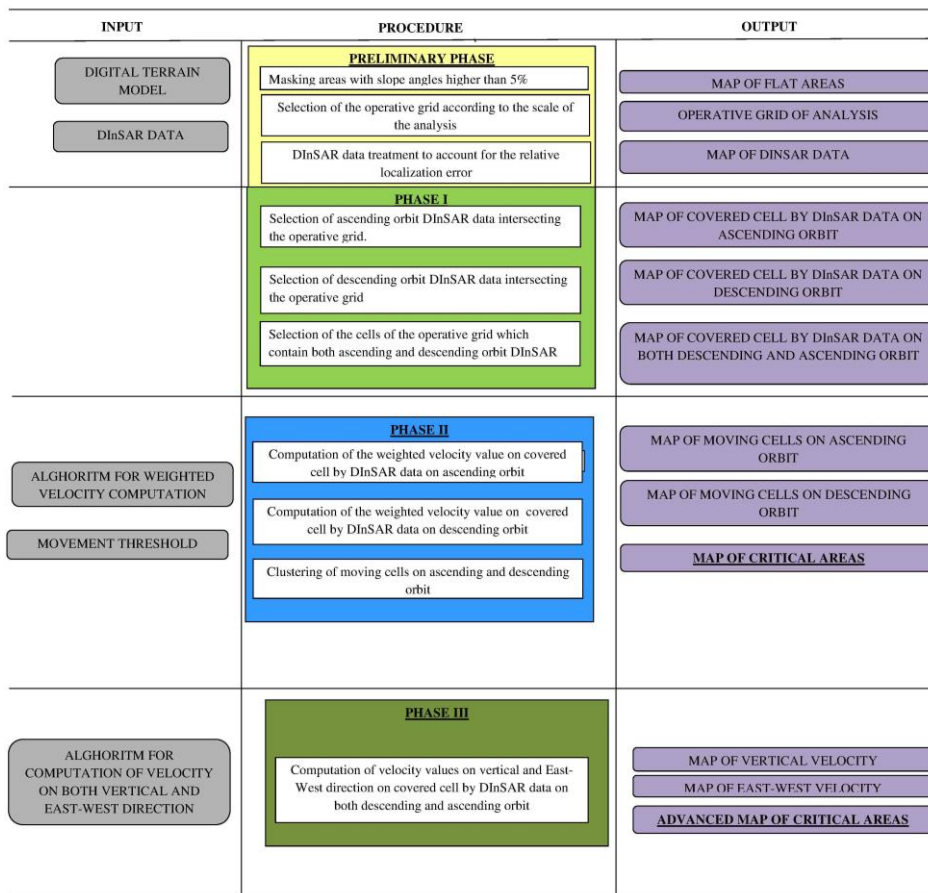
Figure 5.3 Flow chart of analysis to be carried out at small scale.

The aim pursued in the Second phase is the detection of critical areas.

With reference to DInSAR data acquired on ascending and descending orbit, the average velocity value is computed for each covered cell according to equation 5.1. In particular the equation provide the computation of average velocity modulus along LOS direction weighting PS LOS velocity values on their coherence values. This allows to take into account the coherence values which, although computed in different ways by currently used algorithms, can be considered as a reliability parameter to be associated with each PS velocity/displacement value (Cascini et al., 2013a).

$$\text{vel}_{a,C} = \frac{\sum_{i=1}^{N} w_{ci}\, V_i}{\sum_{i=1}^{N} w_{ci}} = \sum_{i=1}^{I} \frac{w_{ci}}{w_{cN}} V_i \ , \quad w_{ci} = \frac{(1-\varepsilon_{min})}{(C_{max} - C_{min})}(C_i - C_{min}) + \varepsilon_{min}$$

(5.1)

Where:

i refers to the ith PS within the grid cell;

N is the total number of PS within the grid cell;

w_{ci} is the weight computed on coherence of the velocity of the ith PS within the grid cell;

w_{cN} is the sum of w_{ci};

V_i is the velocity of ith PS;

C_{max} is the maximum coherence value of the used dataset;

C_{min} is the minimum coherence value of the used dataset;

C_i is the coherence value of the ith PS within the grid cell;

ε_{min} is a given very small number used in order to not discard the i-th PS with $C_i = C_{min}$

Once the weighted average LOS velocity values for each grid cell are computed a velocity threshold equal to 1.5 mm/year (Cascini et al 2010) is introduced, thus allowing each cell to be appointed as moving (average velocity value over 1.5 mm/year), not moving (average velocity value lower than 1.5 mm/year) and not covered (if no PS were found in the singular grid cell), the corresponding output is the map of critical areas.

The Third phase pursues the individuation of prevailing moving direction of critical areas detected in the second phase. In particular, focusing on the critical area only those cells with data on both orbits are selected in order to apply a procedure for the ascending and descending data combination which allows extracting the Vertical (V) and East-West (EW) velocities. In particular, by referring to Cascini et. al (2010), where it is outlined a general procedure that allows converting the measured ascending and descending velocity components (V $_{Los\_A}$ and V $_{Los\_D}$ respectively) to the displacement velocity along a direction selected according to a model, suited to the specific application, and by implementing reasonable approximations it is possible to derive a simple relation that relates the V $_{Los\_A}$ and V $_{Los\_D}$ to the vertical and horizontal velocity components (V_z and V_E, respectively), see also Manzo et al. (2006). In particular, with reference to Cascini et. al (2010, 2013a) and the mathematical formalism therein adopted, by assuming the orbits along the South-North direction (i.e., r_{AE}=- r_{DE}, r_{AZ}=- r_{DZ}), and by neglecting hence the NS velocity component of the displacement r_{AN}= r_{DN}=0, i.e. by letting u_N=0, we have that the EW and V velocity components can be simply derived as:

$$v_Z = \left(v_{LOS\_A} + v_{LOS\_D}\right)/\left(2r_{AZ}\right) \quad v_E = \left(v_{LOS\_A} - v_{LOS\_D}\right)/\left(2r_{AE}\right) \tag{5.2}$$

wherein, the relations between the ascending and descending line of sight unit vector components r_{AE}=- r_{DE}=sin(α) and r_{AZ}= r_{DZ}=cos(α) with α being the incidence angle, have been exploited for the derivation of equation 5.2. As a result, once considered the ratio between horizontal and vertical velocity modulus ($|V_E/V_Z|$**)** in each cell, the prevailing movement is assumed as horizontal for ratio values greater than 1.73 (corresponding to the value of the tangent of an angle of 60° between the movement direction and the vertical axis), horizontal/vertical for ratio values between 1.73 and 0.57 (corresponding to the value of the tangent of an angle of 30° between the movement direction and the vertical axis) and vertical for ratio values lower than 0.57 (Cascini et al., 2013a). The output of the analysis performed at the Third phase is the advanced map of critical areas.

5.2.2   Medium scale

At medium scale the aim of the analysis is the inventory of affected municipalities and their relative ranking, useful in land-use planning and management. The typical area of zoning, according to Fell et al. (2008) is between 1000 and 10.000 km^2 and the scale ranges from 1:25.000 to 1:100.000, consequentially the operative grid is among 25x25 m and 100x100m.

As for analysis at medium scale the flow-chart of Figure 5.4 is proposed, subdivided in two working phases besides a preliminary one. The input data, procedures and outputs, generally furnished as map, are reported for each phase of analysis.

Figure 5.4 Flow chart of the analysis to be carried out at medium scale.

At the preliminary phase the operative grid of analysis is set, according to the scale of analysis, on critical area detected at small scale.

In the first phase the aim is to detect critical urbanized area, to this aim cells covered by ascending and descending data are selected and, for each of them, weighted velocity values are computed (equation 5.1). Then, a velocity threshold equal to 1.5 mm/year (Cascini et al 2010) is introduced, thus allowing each cell to be appointed as moving (average velocity value over 1.5 mm/year), not moving (average velocity value

71

lower than 1.5 mm/year) and not covered (if no PS were found in the singular grid cell), the corresponding output is the map of moving ("critical") areas. The map of critical areas is intersected with the urbanized area in order to derive the map of the urbanised area with indication of evidence of movement. This latter output is used, in the second phase, to map the subsiding municipalities and to rank them, according to the Subsiding Municipality Index, I_{sm}:

$$I_{sm} = \frac{\left(\dfrac{\dfrac{U_m}{U_c}}{U_{tot}}\right)_{Mi}}{\displaystyle\sum_{Mi=1}^{n}\left(\dfrac{\dfrac{U_m}{U_c}}{U_{tot}}\right)_{Mi}} \tag{5.3}$$

Where:

U_m is urbanized area with evidence of movement;

U_c is covered urbanized area;

U_{tot} is urbanized area

M_i refers to the ith Municipalities within Campanian Plain.

The ranking of the affected municipalities is based on Subsiding Municipality Index. Accordingly, higher values are associated to most affected municipalities in which more detailed analyses are required.

5.2.3 Large scale

The aim of the analysis to be pursued at large scale is to zone built up areas where damage occurred or is likely to occur. The typical area of zoning, according to Fell et al.(2008) is between 10 and 1000 km^2 and the scale ranges from 1:5,000 to 1:25,000, consequentially the operative grid ranges from 5x5 m and 25x25 m. With reference to the use of DInSAR data for analyses at large scale, the flow-chart of Figure 5.5 is proposed.
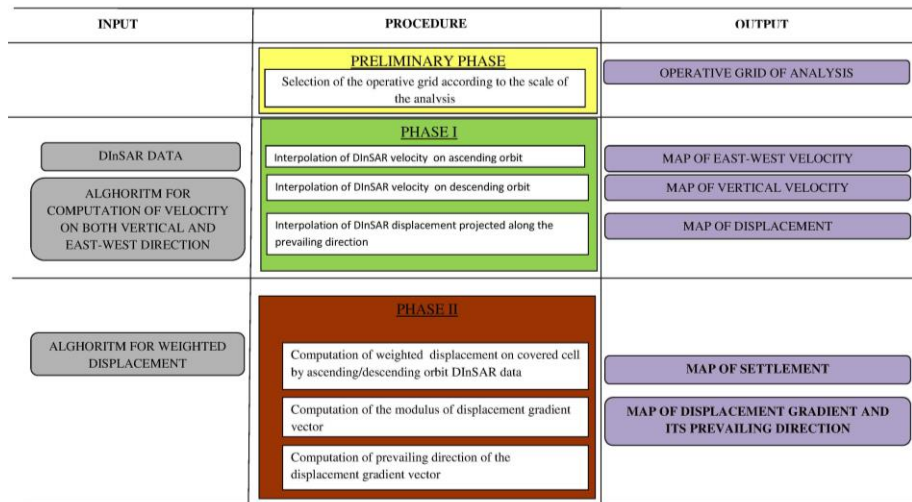
Figure 5.5 Flow chart of analysis to be carried out at large scale.

In the preliminary phase an operative grid according to the scale of the analysis is set. Then, the map of east-west/vertical velocity equation 5.2) and the map of settlements are derived through the interpolation of DInSAR data. In the second phase, the analysis are focused only on the areas in which the prevailing direction is vertical and only on DInSAR covered cells. The output of second phase are the map of settlements and the map of displacement gradients and their prevailing directions. These results allow to zone the area where damage occurred or is likely to occur within the municipal territory. In particular the value 1/500 is recommended in order to avoid cracking (DM 14/01/2008), the value of 1/300 is assumed by Skempton and MacDonald (1956) as the angular distortion threshold for first cracking in a panel walls and load-bearing walls, while the value of 1/150 is considered as a threshold for severe cracking and structural damage.

5.2.4 Detailed scale

Detailed scale studies are suitable for the analysis of single structures/infrastructures. With reference to the use of DInSAR data for analyses at detailed scale, the flow-chart of Figure 5.6 is proposed.

The analyses are carried out with reference to those buildings - covered by DInSAR data - reaching the highest value of gradient displacement at large scale (Preliminary Phase).

In the first phase DInSAR similarly to Cascini et al (2007b, 2011), the computed settlements are obtained assuming a pure shear mode of deformation of the building, without any strain (either of compressive or tensile type) in the vertical direction; as a consequence, the horizontal displacements are disregarded and the building settlements are computed referring to the DInSAR data located on its roof. As result multi-temporal profiles of building settlements and of relative rotations are derived in order to apply damageability criteria.
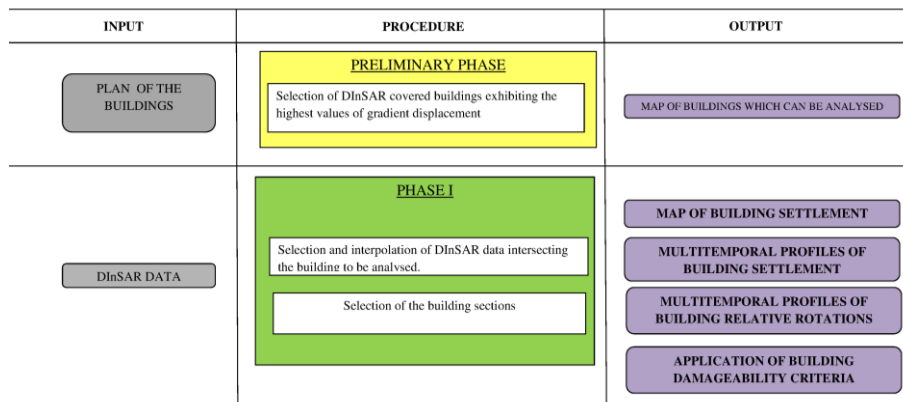
Figure 5.6 Flow chart of analysis to be carried out at detailed scale

5.3 PROCEDURES AT DIFFERENT SCALES FOR LANDSLIDE PHENOMENA

In this Section innovative procedures are proposed and described in detail both for update landslide inventory map and analyze the consequences.

5.3.1 Updating of landslide inventory map

A fundamental step in the landslide risk analysis and, more generally, in the landslide risk management process (Fell et al., 2008a) is represented by landslide inventory mapping which usually includes location, classification, volume, state of activity, date of occurrence (if available) and other characteristics of landslides. Accordingly, the obtained maps need to be not only accurate but also updated on a regular basis. Testing innovative procedures and techniques to update landslide inventory maps is a timely topic widely discussed in the scientific literature.

The framework sketched in Figure 5.7 describes the proposed procedure for DInSAR data interpretation at different scales in the analysis of landslides.

The preliminary phase consists of selection of SAR images according to visibility map (Peduto, 2008, Cascini et al., 2010a) and in their processing through a well defined algorithm (see Section 4.4).

Once SAR images have been processed, if an adequate knowledge of landslide phenomena is available, a procedure for 1D-LOS DInSAR data projection (Cascini et al., 2010a) can be implemented to assess the modulus of velocity according to simplified geomorphological scheme.

As far as the scale of the study is concerned, DInSAR data can be used for landslide analyses at 1:25,000 scale for checking/updating of landslide inventory map, whereas an insight into the main features and kinematics of a single phenomenon, as well as into the behaviour of DInSAR covered buildings/infrastructures interacting with active landslide-affected areas, can be achieved at large scale.

PRELIMINARY PHASE

DATA SELECTION	DATA ANALISYS
A Priori Visibility Map	Image processing
Choice of image dataset	DInSAR velocity assessment

LANDSLIDE ANALYSIS

SCALE	RANGE OF SCALE	OUTPUT	STUDY AREA
MEDIUM	From 1:100,000 to 1:25,000	Checking/updating of Landslide Inventory Map	21 Municipalities (Benevento Province)
LARGE	From 1:25,000 to 1:5,000	Kinematic zoning of landslide	Ascea municipality (SA)

5.7 Proposed procedure at different scale (modified after Cascini et al., 2011d).

Focusing on the updating of the available inventory maps Cascini et al. (2008) discussed the possibility of integrating remote sensing data, thematic maps and damage surveys to structures/infrastructures. Indeed, landslide induced damages – whether available – can be considered as movement indicators and, thus, can be used to validate DInSAR data where both datasets are available (e.g. in urbanised areas) as well as to overcome any lacks of remote sensing data availability (e.g. over vegetated areas).

Figure 5.8 presents a new procedure - also described in Cascini et al.(2013b) - which improves the exploitation of the abovementioned

datasets for the updating of slow-moving landslide inventory maps at medium scale (1:25,000) with reference to both the state of activity and the detection of unmapped phenomena. The adopted approach, although suited for the available datasets, can be valuably exported in different geological contexts using similar data. It consists of four phases to be carried out separately for the analysis of DInSAR and damage data which both play as ground movement indicators. After these phases, the two analysed datasets are merged into a DInSAR-Damage matrix which provides the updated state of activity as output. As far as the mapping unit is concerned, terrain units (Guzzetti et al., 2005) corresponding to landslide and hollow are used.
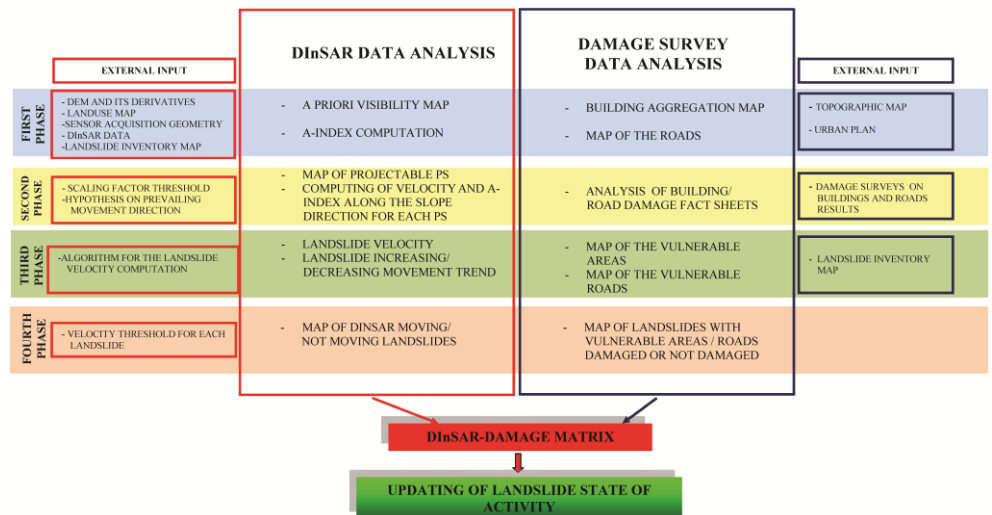
Figure 5.8 Flow-chart describing the procedure adopted for the updating of the state of activity of slow-moving landslides (Cascini et al., 2013b).

As for DInSAR data analysis the first phase includes the generation of the a priori landslide visibility map introduced by Cascini et al. (2009) (see also Plank et al., 2010), allowing the identification of the landslide affected areas for which radar ground targets can be detected prior to the SAR image processing. To this aim, the map is generated through the joint use of a digital elevation model (DEM) of the area and its derivatives (slope and aspect angle) as well as the land-use map and the sensor acquisition geometry. In the a priori landslide visibility map the nonlinear effects related to topography (i.e. shadowing) are disregarded,

thus visible areas may be overestimated. This map is especially useful when DInSAR data are not available for free, in order not to avoid waste of money and time in processing SAR image in areas where a bad DInSAR data coverage is expected on ascending and/or descending orbits.

Then, a new index is introduced, referred to as A-Index, which can be computed for each PS time series in order to complement with the velocity value for the definition of landslide state of activity. In particular, the A-Index represents the second order derivative of the second order polynomial curve best fitting the PS displacement time series (Figure 5.9 a). Combination of the velocity value and the A-Index of each PS can provide useful information on the trend of measured displacements (Figure 5.9 b).
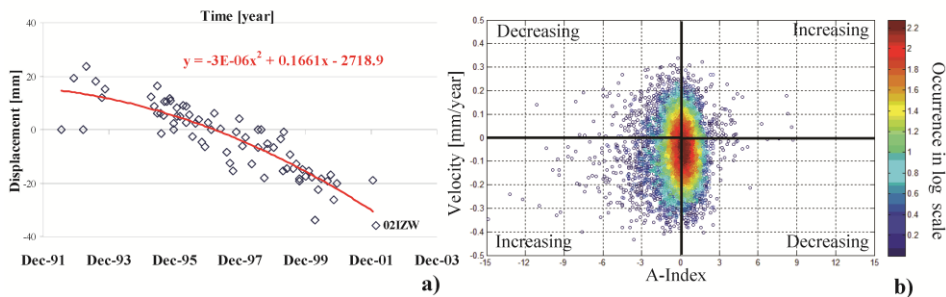
Figure 5.9 a) A-index value represents the coefficient of x squared in the second order polynomial equation fitting the time series; b) A-index vs. LOS-velocity diagram for the ERS ascending (45 images acquired from September 1992 – September 2000) PSI data; the colour bar shows the occurrence in log-scale (Cascini et al., 2013b).

In particular, as it is shown in Figure 5.9 b for a sample dataset, when the signs of the A-Index and the velocity are concordant (i.e. both negative or positive) the trend of the time series can be considered as increasing; on the other hand, discordant signs of A-index and velocity values (i.e. positive and negative) represents decreasing displacement trends. In the same figure the occurrence in log-scale of the couples velocity A-Index is shown.

The quantitative analysis and interpretation of 1D-LOS DInSAR data is closely related to the value of velocity/displacement along a given movement direction. To address this issue in the second phase, due to the scale of the analysis, firstly a prevalent translational movement along the steepest slope direction is assumed for each PS according to Cascini

et al. (2010a). Considering that the LOS projection on the along-slope direction can be biased by errors related to the projection operation (Colesanti and Wasowski, 2006; Cascini et al., 2010a), the map of projectable DInSAR data is introduced (Plank et al., 2010). This map distinguishes each PS according to the own scaling factor, namely the constant value by which the modulus of the LOS velocity (V_{LOS}) must be multiplied in order to obtain the modulus of the along slope velocity (V_{slope}). This issue was already addressed by Cascini et al. (2010a) through the adoption of the condition number of the inversion matrix solving the algebraic system used for the projection operation (i.e. from ascending, or descending, or ascending-descending LOS to slope direction). Indeed, the condition number is a measure of the instability of the inversion process and, in particular, of the accuracy of the solution after the inversion process. As shown by the authors, values of the condition number not exceeding 15 could be an acceptable threshold to select the most reliable projected PS velocity values. Figure 5.10 shows that the abovementioned threshold also corresponds, in the case of data acquired on single orbits (either ascending or descending), to those values of the scaling factor not exceeding 3.3 for the selected study area.
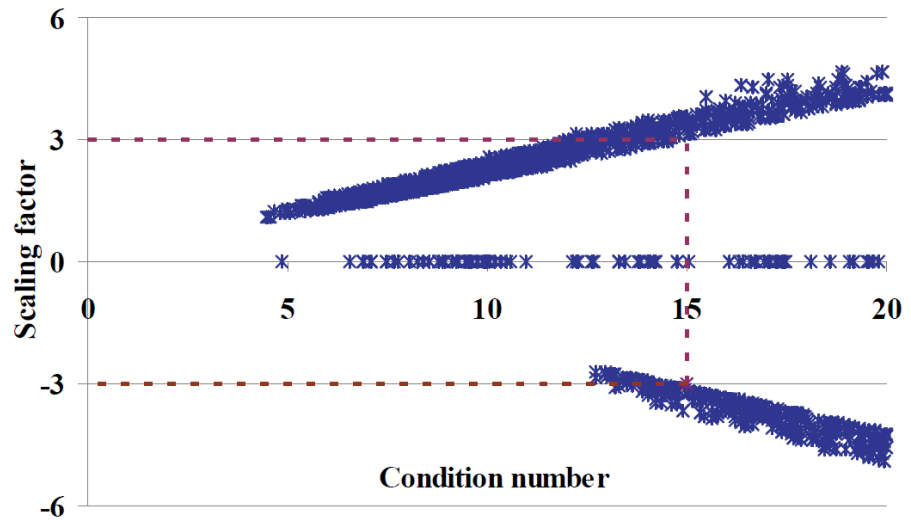
Figure 5.10 The condition number vs. the scaling factor of the PS velocity modulus relevant to the ENVISAT ascending dataset (November 2002 – July 2010) (Cascini et al., 2013b).

This threshold, which avoids the use of unreliable PS velocity, also matches with those assumed in other published researches (Plank et al.,

2010; Herrera et al., 2013) and derived by inverting only single, i.e. ascending or descending, projection. It is worth stressing that the principles and the input data, on which the map of projectable PS – or more generally DInSAR – data is based, are similar to those of the a priori visibility map in which visible, not visible, visible with difficulty area are distinguished. In particular the most of not projectable PS are within visible with difficulties areas. However, whereas the visibility map provides qualitative information by clustering landslide affected areas according to three visibility classes, the map of projectable PS data provides a quantitative visibility evaluation of the single PS measured velocity/displacement. Once the control on the condition number has been carried out, only those PS whose condition number (or scaling factor) is less than 15 (or 3.3) are assumed as "projectable" and, then, used for the following quantitative analyses; the remaining PS are discarded from the following phases and are appointed as "not projectable". The second phase includes two other operations consisting of the projection of both PS displacement time series and PS LOS velocity along the steepest slope direction, the latter carried out according to the procedures described in Cascini et al. (2010). Subsequently, V_{slope} modulus and the A-Index value relevant to the projected PS time series are computed.

In the third phase, via the joint use of the available landslide inventory map and the information on both V_{slope} and the A-index, each landslide is associated with a velocity value and an increasing/decreasing trend. The landslide velocity is assumed by some authors (Cigna et al., 2012) as either a simple average on PS velocity values within each landslide or as the maximum recorded value. In this work only those landslides exhibiting a minimum density of about 20 projectable PS km^2 or at least 3 projectable PS (Meisina et al., 2008; Notti et al., 2010) are considered in order to discard displacements more likely associated with single targets (e.g. single building structural settlements, etc.) rather than to landslides. Then the landslide velocity (Figure 5.11) is computed as the root mean square PS velocity along the slope according to the equation 5.4:

$$V_{slope\_rms} = \left(\frac{\sum_{i=1}^{N} w_{ci} V_{slope\_i}^2}{\sum_{i=1}^{N} w_{ci}} \right)^{1/2} = \left(\sum_{i=1}^{N} \frac{w_{ci}}{w_{cN}} V_{slope\_i}^2 \right)^{1/2}, \quad w_{ci} = \frac{(1 - \varepsilon_{min})}{(C_{max} - C_{min})}(C_i - C_{min}) + \varepsilon_{min}$$

$$(5.4)$$

in which weight values are established on the basis of the PS coherence (i.e. the higher the PS coherence the higher the weight value).

In equation 5.4:

i refers to the ith PS within the boundary of the landslide;

N is the total number of PS within the boundary of the landslide;

w_{ci} is the coherence weight of the ith PS within the landslide boundary;

w_{cN} is the sum of w_{ci};

V_{slope_i} is the velocity along the slope of ith PS;

C_{max} is the maximum coherence value of the used dataset;

C_{min} is the minimum coherence value of the used dataset;

C_i is the coherence value of the ith PS within the boundary of the landslide;

ε_{min} is a positive number not greater than 1 defining the weight of the PS with the smallest coherence. In the analyses, ε_{min} value was fixed equal to 0.2 thus assigning a weight of 20% to the smallest coherence value.
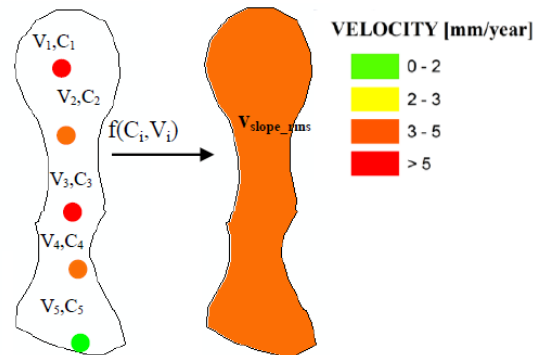
Figure 5.11 Example of the landslide velocity computation as a function of both the along-slope velocity (V_{slope}) and the coherence of the PS included in the boundary of the landslide (Cascini et al., 2013b)

The trend of each single covered landslide is conservatively assumed as increasing if at least 30% of the PS found within the landslide boundary exhibit "increasing" time series.

In the fourth phase, differently from other proposals recoverable in the scientific literature (Cigna et al., 2012; Bianchini et al., 2012; Righini et al., 2012), the velocity threshold is set for a given landslide taking into account the inaccuracy of DInSAR measurements and the scaling factor pertaining to the landslide (derived as root mean square of the scaling factor of the PS in the landslide) as it is described in detail in the

Appendix B. Subsequently, the mapped landslides are distinguished as "moving" (if their velocity exceeds the threshold), "not moving" (if their velocity is lower than the threshold) or "no data" (if less than 20 projectable PS/km^2 or less than 3 projectable PS are found within the landslide boundary).

The information achieved in the fourth phase is ready to be merged with the results of damage survey data analysis via the matrix

In order to use the damage dataset for a joint analysis with DInSAR data, facilities (buildings and roads) interacting with landslide affected areas must be identified (Cascini et al., 2008, Pisciotta, 2008). To this aim, with reference to each municipal territory of the study area, the existing buildings are firstly identified on the basis of the available digital topographic map at large scale (1:5,000); then, homogeneous building aggregations are defined considering that, at medium scale, the identification of a single building (van Westen, 2004) is impracticable and not significant. In particular, building aggregations are sketched as planar figures (Figure 5.12) whose geometry is convex-outwards and, therefore, do not present any cusps on their perimeters. Around each structure, a buffer of 25 m is considered in order to take into account the graphical error related to the working scale (1:25,000) as well as the possibility to have additional constructions in the property; moreover, the maximum allowable distance between each building is assumed lower than 100 m so that urbanized zones prevail on non-urbanized areas within each unit (Ferlisi and Pisciotta, 2007; Cascini et al., 2008).
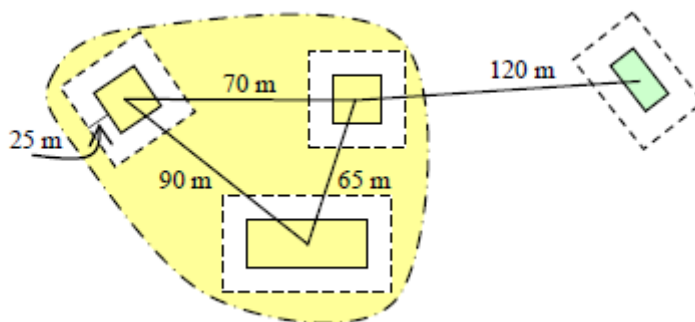
Figure 5.12 Scheme for the determination of building aggregations (Ferlisi and Pisciotta, 2007, Pisciotta, 2008)

Finally, building aggregations are further distinguished as homogeneous units – in terms of occupancy type – thanks to the information gathered from the available urban plans.

The intersection of the obtained building aggregations with the landslide inventory map allows the identification of the so-called "vulnerable areas", i.e. a potentially damageable built-up area. These latter, in turn, are classified as vulnerable areas with or without damage whether at least one damaged building within their perimeter is recorded. The roads are considered as single damaged or not damaged elements according to the information provided by the damage surveys.

At this point of analysis DInSAR data and damage survey data analysis are ready to be merged in the DInSAR-damage matrix.

The matrix-based approach was already tested in the scientific literature concerning the use of PSI data for the evaluation of the landslide state of activity (MATTM, 2010; Cigna et al., 2012; Bianchini et al., 2012; Righini et al.. 2012). This work adopts a new matrix whose innovation relies on the introduction of data concerning survey-recorded damage to facilities as indicators of movement, in addition to PSI (or more generally DInSAR) data and available landslide inventory maps. In particular, once the two datasets (i.e. DInSAR and facility damage data) have been separately analyzed, the DInSAR-Damage matrix is applied to those landslides for which DInSAR datasets, referred to different time periods (e.g. ERS and ENVISAT), are available.

As shown in Figure 5.13, the input data to the matrix are: the state of activity (i.e. active or dormant) provided by the landslide inventory map; the information gathered from the damage survey (i.e. landslide with damage, landslide with no damage, landslide with no damage survey); the condition of movement derived from DInSAR data (i.e. moving or not moving landslide) referring to time in the past (t1) (e.g. ERS 1992-2001). Of course, with reference to the latter information, only the landslides for which the velocity can be computed are considered. The above data are then cross-checked with the evidence of movement derived from DInSAR data at the time required for the updating of landslide inventory map (e.g. ENVISAT 2003-2010). The increasing/decreasing trend exhibited by a given landslide according to ERS data (displacement time series and velocity) represents an additional information, which is used when ERS and ENVISAT data provide different movement conditions of the landslide in order to support the definition of the updated state of activity. The updated state of activity can be distinguished between active or dormant; moreover, in-situ surveys are recommended when the available information is not sufficient to assign the new state of activity. In two cases the state of activity can be more confidently assumed as

active (dark red cell in Figure 5.13) or dormant (light yellow cell in Figure 5.13) corresponding to the concordant combination of all available indicators: active mapped landslide with damage and both ERS and ENVISAT moving evidences, for the former case; dormant mapped landslide with no damage recorded and both ERS and ENVISAT not moving evidences, for the latter case. In the other cases the state of activity derives from the information provided by the majority of the indicators (mapped landslide activity, damage, ERS and ENVISAT data) giving more weight to the most recent data (ENVISAT data). As for the cells divided in two triangles (Figure 5.13), the state of activity is determined using the additional information provided by the sign of the trend (i.e. increasing +; decreasing -). For instance, once all the other indicators were taken into account, if for an ERS moving landslide the assumed trend is decreasing and for ENVISAT the landslide is not moving it can be argued that during the ERS period (1992-2000) the landslide was decelerating and it stopped during the ENVISAT period (2003-2010); thus the current state of activity can be set to dormant. On the contrary, if for an ERS moving landslide the assumed trend is increasing and according to ENVISAT the landslide is not moving, it can be inferred that the landslide was accelerating during 1992-2000 and it stopped during 2003-2010, thus the current state of activity can not be easily defined and in-situ investigations are necessary.

Figure 5.13 The DInSAR-Damage matrix (modified after Cascini et al., 2013b, 2014).

As for the automated detection and mapping of slow-moving landslide phenomena via remote sensing techniques (radar and optical) over wide areas, in the present study the availability of the geomorphological map (1:25,000 scale) of the NBA LGV suggested to focus the analyses on the portions of the study area mapped as hollows.

As described in Cascini et al. (2009) these areas are characterized by geomorphological settings similar to landslide affected areas. The focus is on hollows for which DInSAR datasets, referred to different time periods (e.g. ERS and ENVISAT) and damage survey are available.

In particular both PS displacement time series and PS LOS velocity along the steepest slope direction are projected, according to the procedures described in Cascini et al. (2010). Then the hollow velocity is computed as the root mean square PS velocity along the slope according to the equation 5.4. Subsequently, the mapped hollows are distinguished as "moving" (if their velocity exceeds the threshold), "not moving" (if their velocity is lower than the threshold) or "no data" (if less than 20 projectable PS km² or less than 3 projectable PS are found within the

landslide boundary). The information achieved is ready to be merged with the results of damage survey data analysis; in particular if the hollow is moving according to both ERS and ENVISAT satellite and damages are recorded, hollows are likely to be landslides.

5.3.2 Analysis of consequences

As described is Section 3.3.2 only few contributions to the generation of fragility or vulnerability curves are available for slow-moving landslides in the scientific literature. This lack is even larger enhanced referring to standardized procedure over large area due to both the complexity of the topic and the inadequacy of databases that allow to establish relation between damage occurrence and intensity parameter. As a consequence, in this Section an original joint use of DInSAR data and damage survey data is proposed to derive fragility/vulnerability curve by empirical methods at 1:25,000 scale.
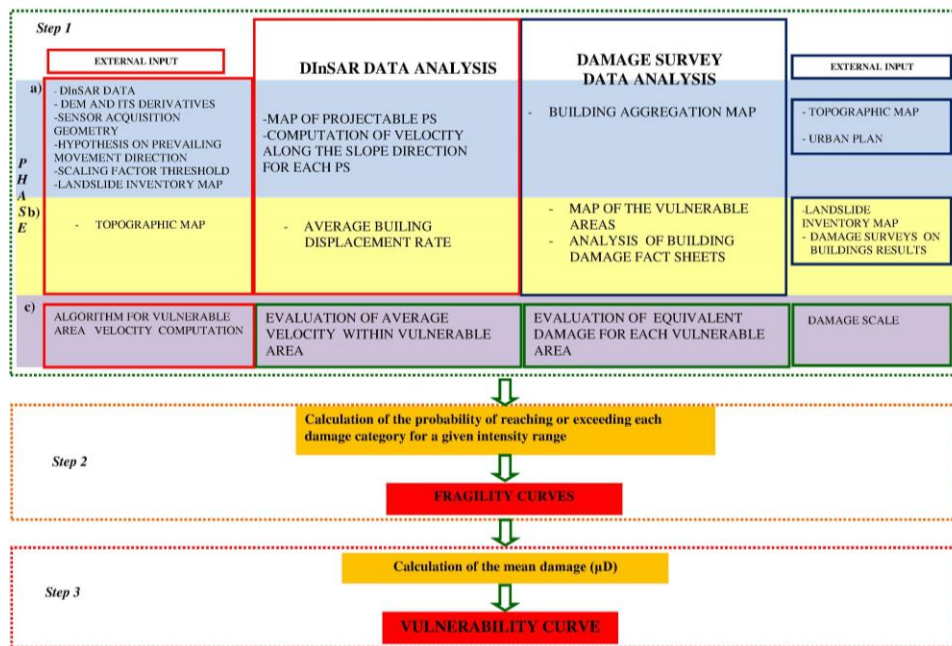
Figure 5.14 Procedure for generation of vulnerability curve at medium scale.

These graphical relations are useful both to update the existing official maps within the "Hydrogeological Setting Plans" (Italian Law 365/2000)

and in municipal land use planning to select more suitable zones to be urbanised. The adopted approach consists of 3 sequential steps (Figure 5.14) to be carried out in parallel and valuably exported in different contexts using similar data.

As for DInSAR data analysis the first step includes at the a) phase the generation of the projectability map (see Section 5.3.1). Via the joint use of the topographic map and the information on both V_{slope}, each building is associated with a displacement rate. The average building displacement rate is computed as the root mean square PS velocity along the slope according to the equation:

$$V_{a\_build} = \left(\frac{\sum_{i=1}^{N} w_{ci} V_{slope\_i}^2}{\sum_{i=1}^{N} w_{ci}} \right)^{1/2} = \left(\sum_{i=1}^{N} \frac{w_{ci}}{w_{cN}} V_{slope\_i}^2 \right)^{1/2} , \qquad w_{ci} = \frac{(1-\varepsilon_{min})}{(C_{max}-C_{min})}(C_i - C_{min}) + \varepsilon_{min}$$

(5.5)

in which weight values are established on the basis of the PS coherence (i.e. the higher the PS coherence the higher the weight value).

In equation (5.5):

- i refers to the ith PS within the boundary of the building;
- N is the total number of PS within the boundary of the building;
- w_{ci} is the coherence weight of the ith PS within the building boundary;
- w_{cN} is the sum of w_{ci};
- V_{slope_i} is the velocity along the slope of ith PS;
- C_{max} is the maximum coherence value of the used dataset;
- C_{min} is the minimum coherence value of the used dataset;
- C_i is the coherence value of the ith PS within the boundary of the building;
- ε_{min} is a positive number not greater than 1 defining the weight of the PS with the smallest coherence. In the analyses, ε_{min} value was fixed equal to 0.2 thus assigning a weight of 20% to the smallest coherence value.

Around each PS a buffer of 5 m is set in order to take into account the localization error.

As for Damage survey data analysis the first phase includes the identification of building aggregation map - on the basis of topographic map and urban plans following the same procedure described in Section

5.3.1- and then the identification of the "vulnerable areas" (Pisciotta, 2008).

As for DInSAR data analysis the first step includes (phase b) the computation of the vulnerable area velocity. This latter is computed on the basis of the average of building displacement rate within the vulnerable area, weighted on the number of PS covering each building (equation 5.6).

$$V_{a\_v\_a} = \frac{\sum_i N_i . V_{a\_build_i}}{\sum_i N_i} \qquad (5.6)$$

Where:

- N_i is the number of PS on i^{th} building within vulnerable area;
- $V_{a\_build_i}$ is the average velocity of ith building within vulnerable area.

In the same phase with reference to damage survey data, both the identification of the so-called "vulnerable areas" and the analysis of damage fact sheets are carried out. In this regard, the information reported in the available database of damage survey mainly regards: the occupancy type; the geometric description of the element at risk; the date of damage occurrence; the description of the damage, specifying the structural or no-structural damaged elements, the state of maintenance and any possible additional information.

The fact sheets are analyzed classifying the damage by considering the severity of the visible damage whose effects on buildings range from loss of serviceability to ultimate limit states (Ministerial Decree 14/02/2008).

The last phase of the first step consists of the evaluation of the average velocity for each vulnerable area weighted on the number of PS on each building (equation 5.6) and the evaluation of equivalent damage for each vulnerable area (equation 5.7).

According to Pisciotta (2008) equivalent damage ED of a given vulnerable area is computed as the weighted average of the individual damages suffered by the buildings included in the vulnerable area.

That is:

$$ED = \frac{\sum_i di.fi}{\sum_i fi} \qquad (5.7)$$

where di is the damage value suffered by a i-building and fi is the relative frequency of the ith class of damage value within the vulnerable area.

In the second step fragility curves are derived. Each curve, according to Negulescu et al.(2010), gives the conditional probability of exceeding a specific level of damage over a range of ground motion intensity (velocity in this case). Each fragility curve is obtained by counting, for different values of the imposed velocity, the number of situations over the total that reached or exceeded the considered level of damage.

In the third step the vulnerability curve is derived computing the mean damage for each class of intensity according to the following equation (Saeidi et al., 2009):

$$\mu D(\varepsilon) = \sum_{i=1}^{3} P(Di) * Di \qquad (5.8)$$

where $\mu D(\varepsilon)$ is the mean of damages for each class of intensity ε.

Finally it is worth stressing that the same procedures can be applied at both large and detailed scales by changing: the intensity parameters, the element at risk and the damage scale.

6 APPLICATIONS TO SUBSIDENCE PHENOMENA

"Facts do not cease to exist because they are ignored".

Aldous Huxley

This Section focuses on the applications of DInSAR data to study subsidence phenomena at different scales of analysis for both the characterization of the phenomena and the analysis of the related damage to urbanized area interacting with them.

6.1 SMALL SCALE ANALYSIS

The selected test area for the analysis at small scale is the Campania Region (Southern Italy) which includes the Southern Apennines chain and Plio-Quaternary structural depressions over an area of about 13,600 km². Campania region has a complex geological structure, characterized by an intense urbanization and by interplay of several geodynamic processes related to presence of active volcanoes (Vesuvius, Phlegraean Fields and Ischia), seismic structure by high magnitude earthquake, widespread landslides and geological instability, sinkhole, subsidence and from long to short term tectonic warping, which produce ground deformation pattern (Milone et al., 2001, Vilardo et al., 2009). These factors make the studied region particularly complex.

The aim of the analysis is the detection of subsiding area. For this purpose the dataset of the Italian 'Piano Straordinario di Telerilevamento' (PST project, 2010), resulting from the processing of medium resolution ERS and ENVISAT data acquired from 1992 to 2010, has been exploited for the Province of Avellino, Benevento, Caserta and Naples: moreover, ERS and Radarsat datasets (provided by Podis project) were used for Salerno Province. In Table 1 the number of

PS and the recorded values of minimum and maximum coherence (i.e. Cmin and Cmax) are reported with reference to each dataset.

6.1 The used DInSAR dataset

	Nr.	$\mathbf{C_{min}}$	$\mathbf{C_{max}}$
Ers asc.	43871	0.56	1
Ers disc.	349302	0.52	1
Env asc.	1182624	0.54	0.97
Env disc.	901514	0.59	0.97
Radarsat asc.	97491	0.65	0.99
Radarsat disc.	91781	0.66	0.99

As it shown in Cascini et al., 2011a, the first step of the analysis dealt with the validation of DInSAR data thanks to the availability of ground measurements. In this regard, after having verified the prevalence of vertical movement in the area (Cascini et al., 2011a), Figure 6.1a-b shows two examples of this cross validation with reference to available benchmarks located in Sarno Municipality (Salerno Province). The diagrams show a good fitting among remote sensed data (PInSAR and full-resolution SBAS data), projected along the vertical direction, and the ground measurements achieved via a topographic levelling technique.

a)

BENCHMARK 522

b)
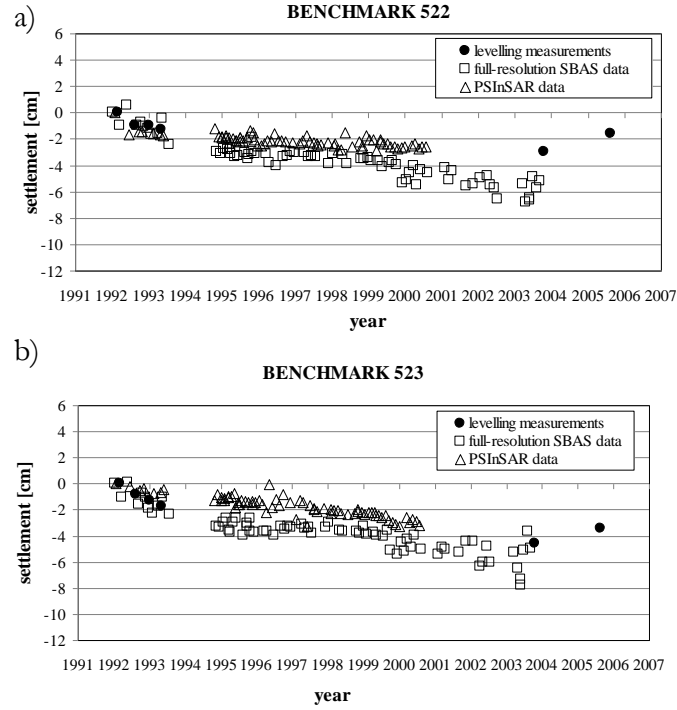
BENCHMARK 523

Figure 6.1 Cumulative settlements obtained, for two benchmarks (a,b) selected within Sarno town area via the use of data and topographic levelling measurements (modified after Cascini et al., 2011a).

Following the proposed flowchart shown in Section 5.2.1, the analysis are at small scale focused only on flat areas (Figure 6.1 c), for this purpose at preliminary phase (Figure 5.3, Figure 6.2) slope map is derived from DEM (Figure 6.1 a) and, according to Trigila and Iadanza (2007), a threshold equal to 3° is introduced to select flat area.

Then, owing to the huge amount of available point-wise PS data an operational grid (Figure 6.2 d, e) with a spacing of 250 m × 250 m was preliminarily set. DInSAR data derived on both orbit from ERS, ENVISAT and RADARSAT were treated in GIS environment (buffer of 10 meters) in order to take into account localization error (see Section 4.4).
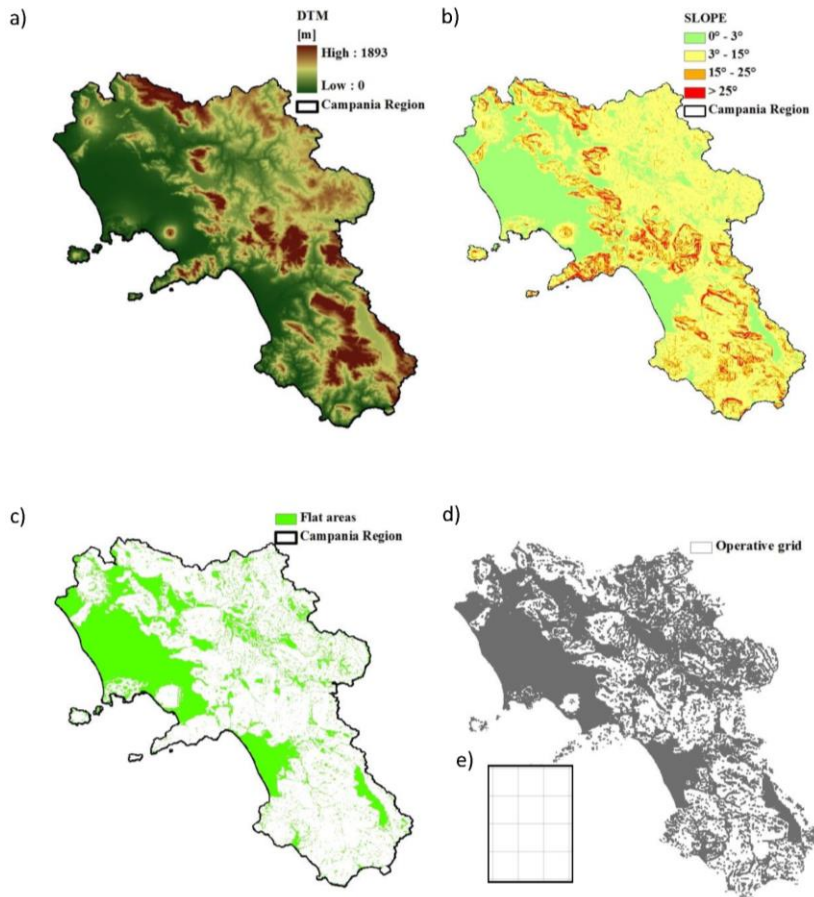
Figure 6.2 Preliminary phase of analysis: a) digital terrain model, b) slope map, c) flat area, d) operative grid of analysis.

In the first phase (Figure 5.3) the cell covered by DInSAR data - for each sensor and acquired on either ascending or descending orbit or by their combination - were selected. Accordingly, over a total of 105,286 cells covering the flat area of Campania Region: 46,696 (44 %) are covered by ERS ascending; 43,833 (42%) by ERS descending while 55,212 (52%) by ERS ascending and descending; 55,717 (53%) are covered by ENVISAT ascending; 46,833 (44%) by ENVISAT descending while 58% by ENVISAT ascending and descending. Referring to Salerno Province over a total of 30,457 cell: 14,830 (48%) are covered by RADARSAT ascending; 14983 (49%) by RADARSAT

descending while 17070 (56%) by RADARSAT ascending and descending.

In the second phase (Figure 5.3), within each grid cell, and referring separately to ERS, ENVISAT and RADARSAT on both orbits, the average velocity modulus along the LOS direction is computed by weighting PS LOS velocity, according to equation 5.1. Once the weighted average LOS velocity values for each grid cell are computed, a velocity threshold equal to 1.5 mm/year (Cascini et al 2010) is introduced, thus allowing each cell to be appointed as moving (an average velocity value over 1.5 mm/year), not moving (an average velocity value lower than 1.5mm/year) and not covered (if no PS were found in the singular grid cell). For ERS (Figures 6.3a-b), ENVISAT (Figures 6.3c-d) and RADARSAT (Figures 6.3 e-f) datasets, this procedure is firstly carried out separately for ascending and descending orbit, then the retrieved moving cells are merged in a single map for each sensor deriving critical area (red in Figures 6.4).

Consequently, although suffering from a lack of information in rural areas, the analysis of PSInSAR data reveals that a percentage of Campania Region ranging from 19% up to 25%, is affected by ground displacement according, respectively, to ENVISAT and ERS data.
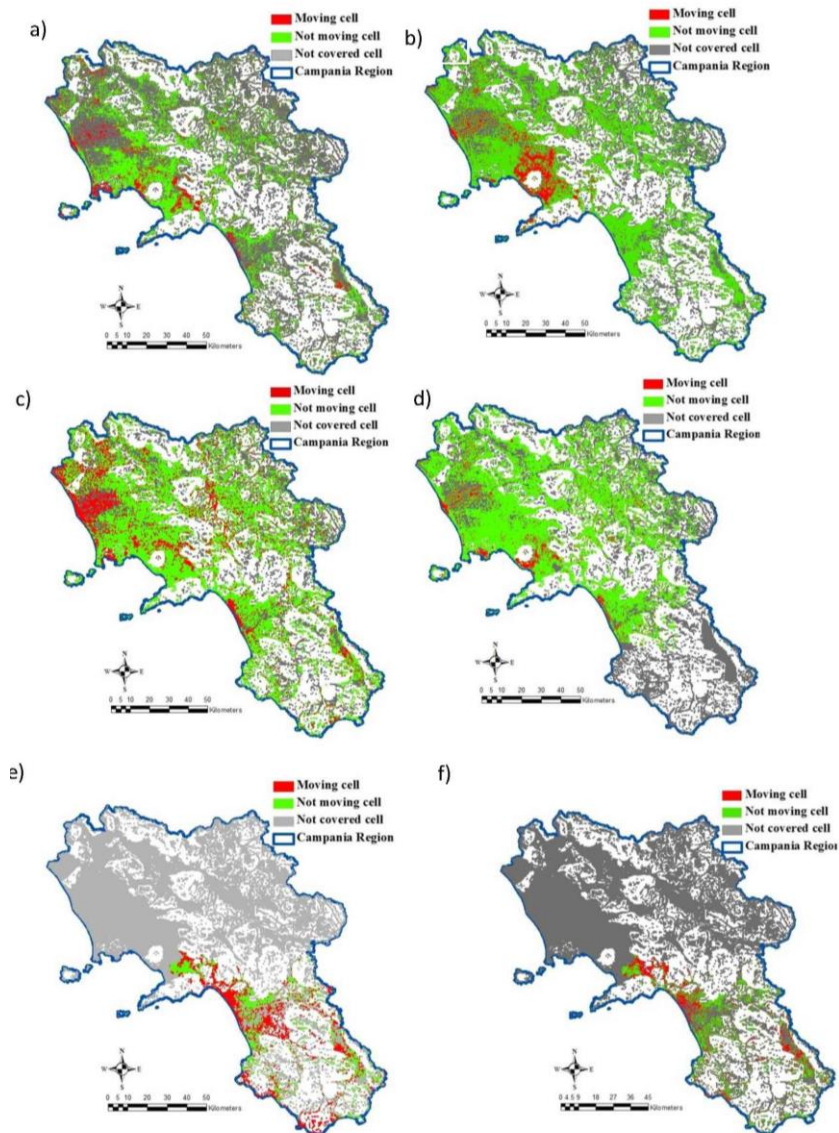
Figure 6.3 Map of moving cell: ERS ascending (a), ERS descending (b), ENVISAT ascending (a), ENVISAT descending (c), RADARSAT ascending (e); RADARSAT descending.

In order to select those areas exhibiting conditions of movement over the whole period of observation (about 20 years), the cells appointed as moving in figures 6.3(a-f) are selected (Figure 6.4 d). The analysis shows

that 4,283 cells are moving, corresponding to 9% of those covered by ERS, ENVISAT and RADARSAT datasets. These cells clearly concentrate on the most important plains of Campania Region: Campanian Plain, Sele Plain and Val Diano Plain (Figure 6.4 d).
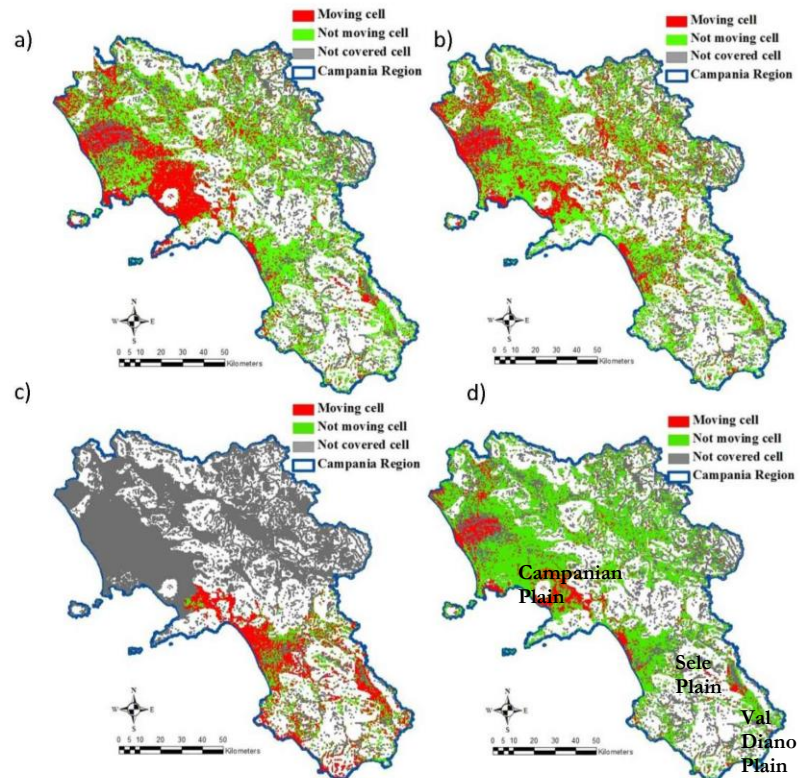
Figure 6.4 Map of critical area: ERS (a), Envisat (b), Radarsat (c), whole period of observation (d).

In the third phase, since DInSAR data were acquired on different orbits by different sensors (with different LOS angles: 23∘ for ERS-ENVISAT and 35∘ for RADARSAT), it was necessary to compute the prevailing movement direction for each cell in order to proceed with their joint use. In particular, focusing on the moving cells detected in Figure 6.4, only those cells with data on both orbits are selected in order to apply the procedure shown (Manzo et al., 2006, Cascini et al., 2010) for the ascending and descending data combination which allows extracting the vertical (V) and east–west (EW) velocities (equation 5.2).
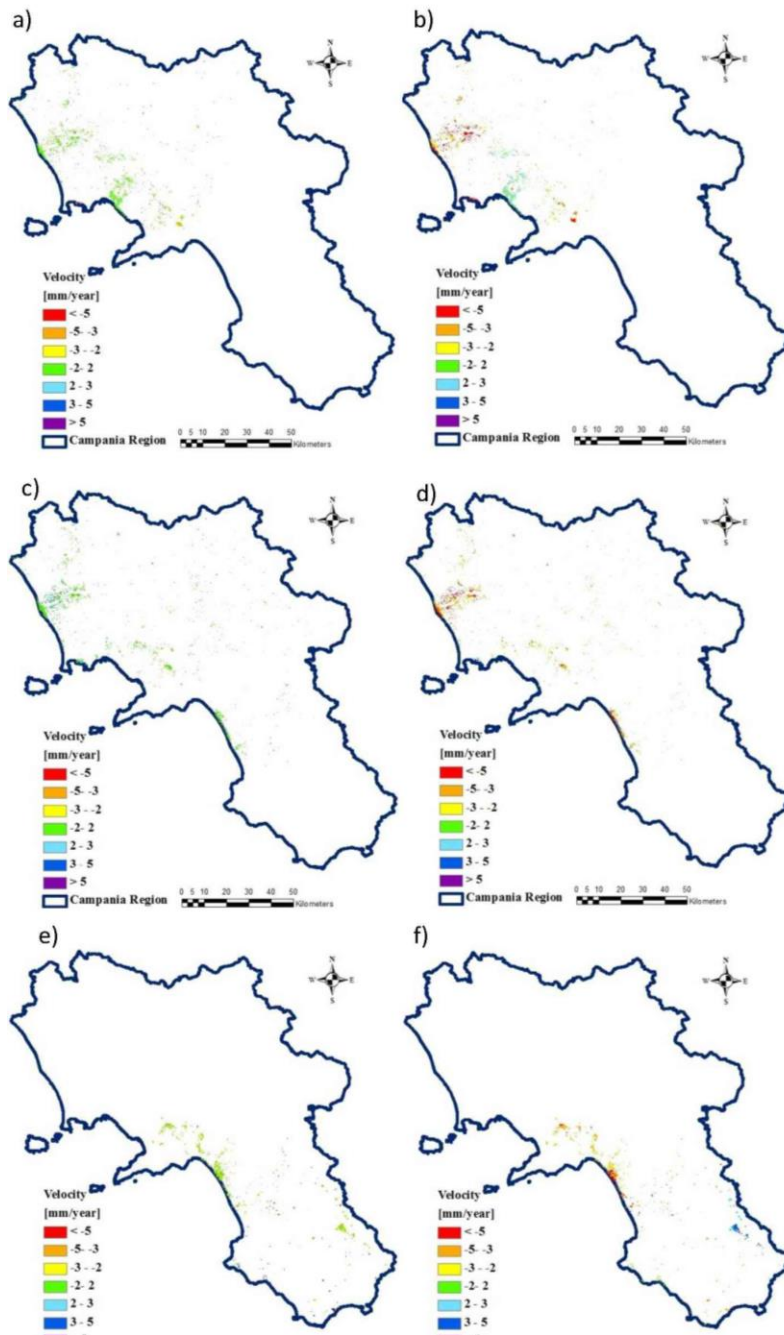
Figure 6.5 Map of East-West velocity (a) ERS; c) Envisat; e) Radarsat) and Map of vertical velocity (b) ERS; d) Envisat; f) Radarsat).

Finally, once considered the ratio between horizontal and vertical velocity modulus in each cell, the prevailing movement is assumed as horizontal for ratio values greater than 1.73 (corresponding to the value of the tangent of an angle of $60°$ between the movement direction and the vertical axis), horizontal/vertical for ratio values between 1.73 and 0.57 (corresponding to the value of the tangent of an angle of $30°$ between the movement direction and the vertical axis), and vertical for ratio values lower than 0.57 (Figure 6.6).
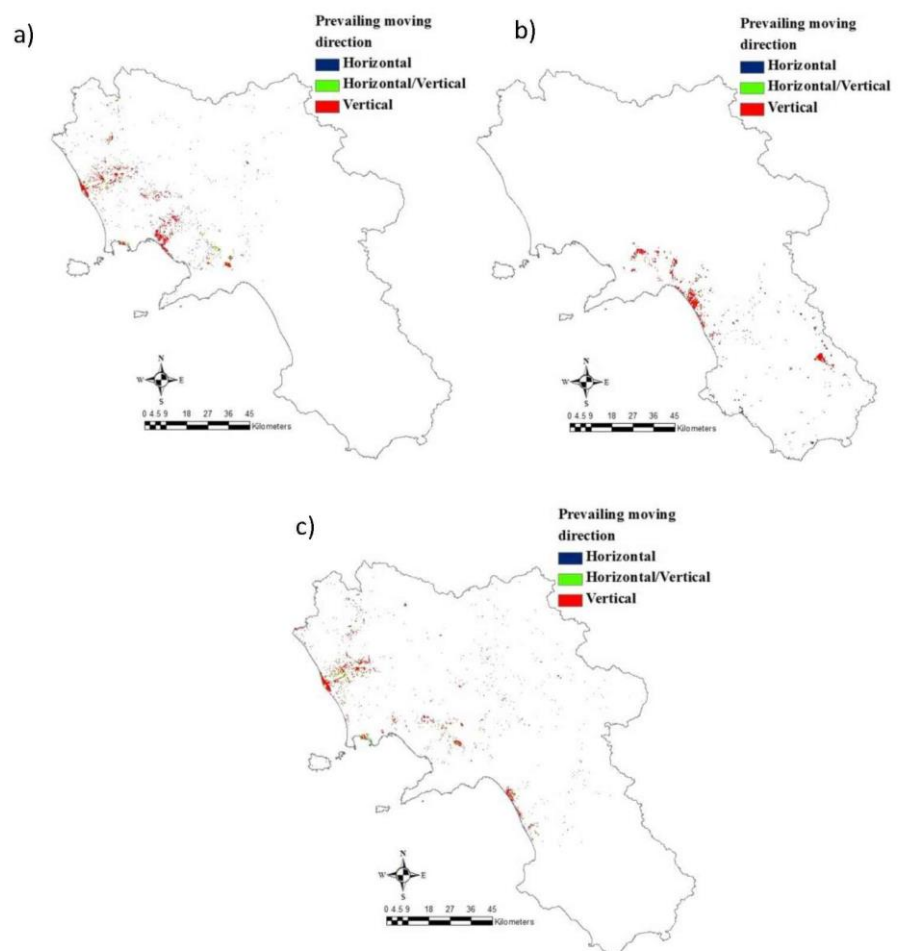
Figure 6.6 Map of the advanced critical area according to ERS (a); RADARSAT (b) and ENVISAT (c) for covered cells by both ascending and descending DInSAR data.

In the last step of the analysis, ranking of the Campanian Plains affected by subsidence was carried out according to the definition and computing of the Subsiding Plain Index. This latter (equation 6.1) is given by the ratio between the extension of the urbanized areas with evidence of movement (U_m), the covered urbanized (U_c) and urbanized area of the i-th Plain (P_i) of Campania Region normalized to the same terms referred to the whole Campania Region. The results (Figure 6.7) show that the most affected area is the Campanian Plain whose I_{SUP} reaches 91%. In particular where about 12% of the total urbanized area have evidence of movement.

$$I_{SUP} = \frac{\left(\dfrac{\dfrac{U_m}{U_c}}{U_{tot}}\right)_{Pi}}{\displaystyle\sum_{Pi=1}^{n}\left(\dfrac{\dfrac{U_m}{U_c}}{U_{tot}}\right)_{Pi}} \tag{6.1}$$
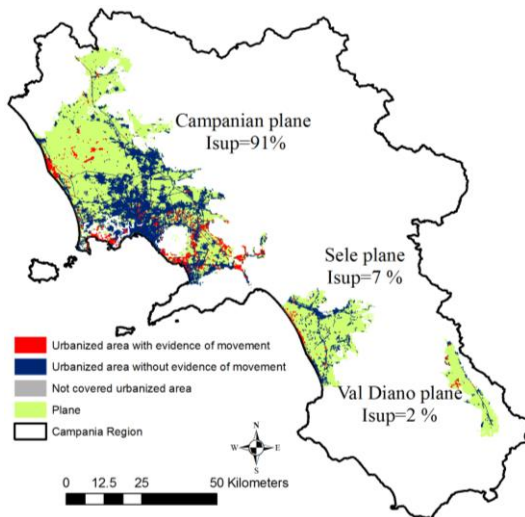
Figure 6.7 Map of Subsiding Plain Index.

100

6.2 MEDIUM SCALE ANALYSIS

Following the results achieved at small scale the selected area for the analysis at medium scale was Campanian Plain, the most critical plain of Campania Region. The Campanian Plain is the largest coastal plain along the Tyrrhenian Coast in Central-Southern Italy, extending for about 2,000 km^2. Owing to its rich environmental resources and its proximity to Naples town the whole territory of the Campanian Plain was highly exploited by intensive anthropogenic activities (e.g. groundwater withdrawals, huge urban development, etc) since the end of the Second World War As a result, several areas within Campanian Plain were affected by ground settlements of either natural or anthropogenic origins, as it is testified by a number of studies (Cascini et al., 2007a; Vilardo et al., 2009; ISPRA 2012).

Except for the north-western part, which still has a predominant agricultural use, the built up environment is almost uniformly distributed, especially in a ring-like zone bordering the Vesuvius volcano.

On the whole, the area plays a strategic role due to its about 3 million inhabitants, a rich cultural and natural heritage as well as a dense infrastructural network (national highways, high speed railways, international hubs) potentially exposed to ground surface displacements.

The distribution of ERS and ENVISAT data over the Campanian Plain with the indication of the recorded velocity along the LOS is shown in Figure 6.8 In particular, over the test area 454,644 ERS-PS and 1,090,623 ENVISAT-PS are available on both ascending and descending orbit with a density equal to 230 PS/km^2 for ERS-PS data and 550PS/km^2 for ENVISAT-PS data.
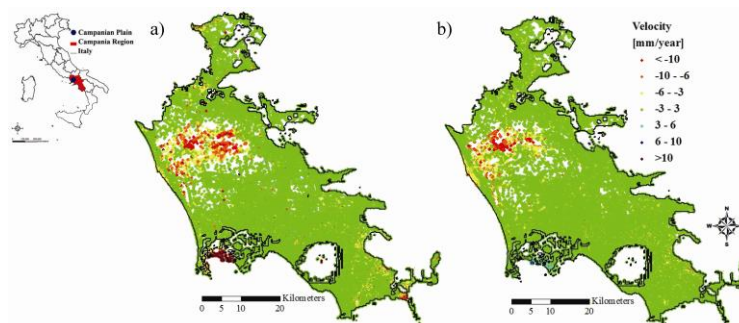
Figure 6.8 Distribution of PSInSAR data over the Campanian Plain according to: a) ascending/descending ERS and b) ascending/descending ENVISAT dataset. Values of velocity are computed along the LOS.

The analysis was carried out according to the procedure of Figure 5.4. Particularly, at the preliminary phase an operational grid with a spacing of 100m x 100m was set.

In the first phase, within each grid cell, and referring separately to ERS and ENVISAT on both orbits, the average velocity modulus along LOS direction is computed by weighting PS LOS velocity values on their coherence values according to equation (5.1). Once computed the weighted average LOS velocity values for each grid cell, a velocity threshold equal to 1.5 mm/year (Cascini et al 2010) was introduced, thus allowing each cell to be appointed as moving (average velocity value over 1.5 mm/year), not moving (average velocity value lower than 1.5 mm/year) and not covered (if no PS were found in the singular grid cell). For both ERS and ENVISAT datasets this procedure was firstly carried out separately for ascending and descending orbits, then the retrieved moving cells were merged in a single map for each sensor (Figure 6.9 a and 6.9 b). As a result, over a total of 191,894 cells covering the whole Campanian Plain: 32,940 cells resulted moving for ERS (44% of the covered ones) and 19,054 cells resulted moving for ENVISAT (22% of the covered ones). Consequently, although suffering from a lack of information in rural areas, the analysis of PSInSAR data revealed that a percentage of Campanian Plain territory - ranging from 10% up to 17% - is affected by ground displacements according, respectively, to ENVISAT and ERS data.
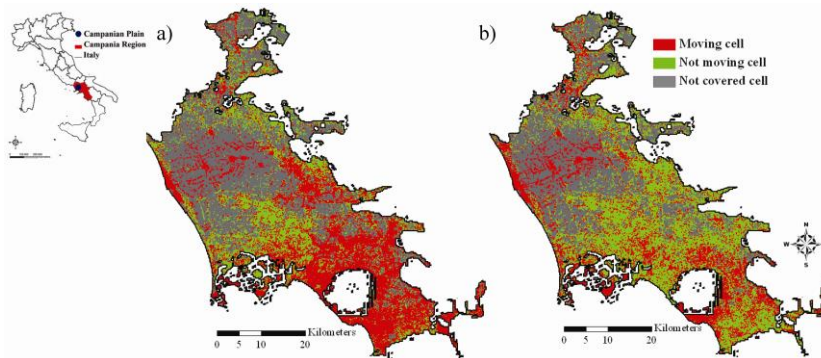
Figure 6.9 Distribution of moving/not moving cells over the Campanian Plain according to ERS (a) and ENVISAT (b) dataset (Cascini et al., 2013a).

In order to select those areas exhibiting conditions of movement over the whole period 1992-2010 the cells appointed as moving in both maps (Figure 6.9a-b) were selected (Figure 6.10). The analysis shows that 8,685

cells result as moving corresponding to 13% out of those covered by both datasets. These cells clearly concentrate on the Volturno river outlet, the Phlegrean Fields and a ring-like zone bordering the Vesuvius volcano (Figure 6.10).
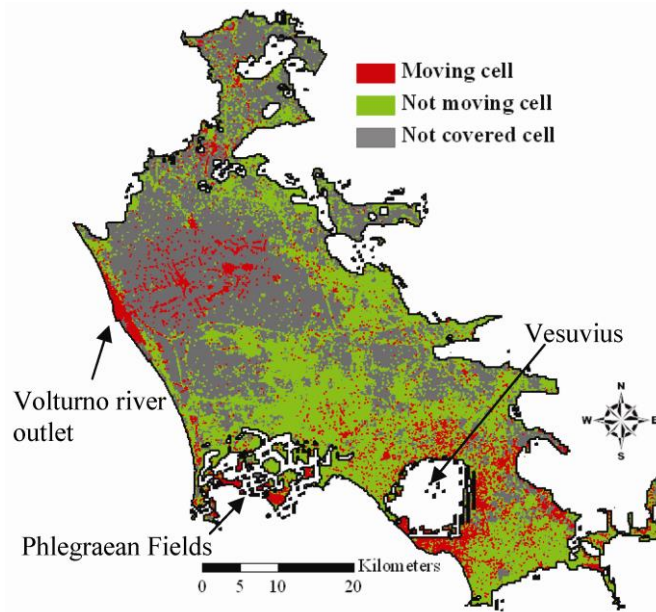
Figure 6.10. Distribution of moving/not moving cells over the Campanian Plain during the period 1992-2010. (Cascini et al., 2013a).

Furthermore, since in the case study at hand the available data were acquired on different orbits by different sensors (with different LOS angles: 23° for ERS-ENVISAT and 35° for COSMO-SkyMed) it was necessary to compute the prevailing movement direction for each cell in order to proceed with their joint use. In particular, focusing on the moving cells detected in Figure 6.9 a and 6.9 b only those cells with data on both orbits were selected in order to apply a procedure for the ascending and descending data combination which allows extracting the Vertical (V) and Est-West (EW) velocities.

As a result, once considered the ratio between horizontal and vertical velocity modulus in each cell following the procedure already shown at small scale, the prevailing movement was assumed as horizontal for ratio values greater than 1.73 (corresponding to the value of the tangent of an angle of 60° between the movement direction and the vertical axis),

103

horizontal/vertical for ratio values between 1.73 and 0.57 (corresponding to the value of the tangent of an angle of 30° between the movement direction and the vertical axis) and vertical for ratio values lower than 0.57. In figure 6.11 only those cells which exhibit the same prevailing movement throughout the period 1992-2010 are reported.
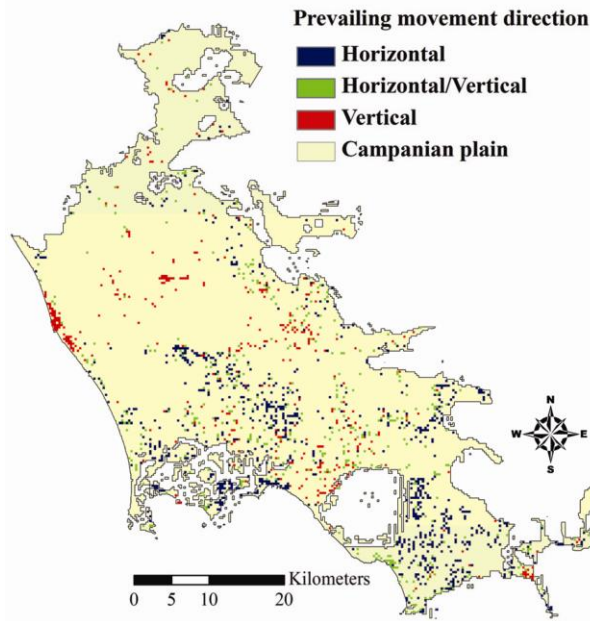
Figure 6.11 Map of the prevailing movement direction computed according to ERS-ENVISAT data for the cells for which both ascending and descending data were available (Cascini et al., 2013a).

The following step of the analysis was aimed at detecting and mapping the elements interacting with subsiding areas over the Campanian Plain in order to identify and rank the affected municipalities. To this end, two additional inputs data were used: the "Map of land-use" – CUAS-produced by Regione Campania and dated 2001 and 2009. From these two maps it was possible to extract the urbanized area, thus highlighting that in 2001 an extension of about 460 km^2 (corresponding to 23%) of the Campanian plain was built up; this percentage raises up to 25% in 2009.

Via the superimposition of the moving/not moving cells according to ERS data (Figure 6.9 a) over the map of the urbanized area dated 2001 it was possible to map the built up areas exceeding the moving threshold over the period 1992-2001 (Figure 6.12a). Consequently, 88% of the

urbanized area resulted covered by ERS-PS cells and 43% out of the covered urbanized area result as moving.

Similarly, the intersection of the map of moving cells according to ENVISAT data (figure 6.9 b) with the map of urbanized area dated 2009 allowed the detection of the portions of urbanized area (covered for 89% of its total extension) which resulted as moving (18%) during the period 2003-2010 (Figure 6.12b).
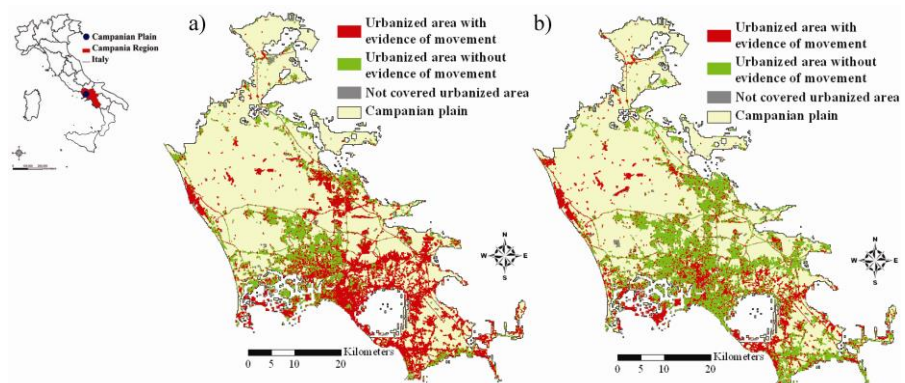
Figure 6.12 a) Map of the urbanised area dated 2001 with indication of evidence of movement for the period 1992-2001; b) map of the urbanised area dated 2009 with indication of evidence of movement for the period 2003-2010(Cascini et al., 2013a).

Furthermore, the results obtained in figure 6.10, merged with the urbanized area map, shows that around 11% out of the covered urbanized areas exceed the moving threshold over the period 1992-2010 (Figure 6.13). In particular, some of the most affected municipalities are Castel Volturno (located at the outlet of the Volturno river); Pozzuoli town in Phlegraean Fields area; Naples city with reference to both Vomero quarter and an area neighbouring the airport; some of the municipalities included in the ring-like area bordering Vesuvius volcano.

The final step focused on mapping those portions of urban areas developed between 2001 and 2009 (identified by comparing the two land-use maps) which exhibit movements during the years 2003-2010. Among the zones which resulted as moving two strategic infrastructures can be mentioned: the high speed railway track in proximity of Naples central station; the area of Grazzanise airport in the territory of Caserta Province.
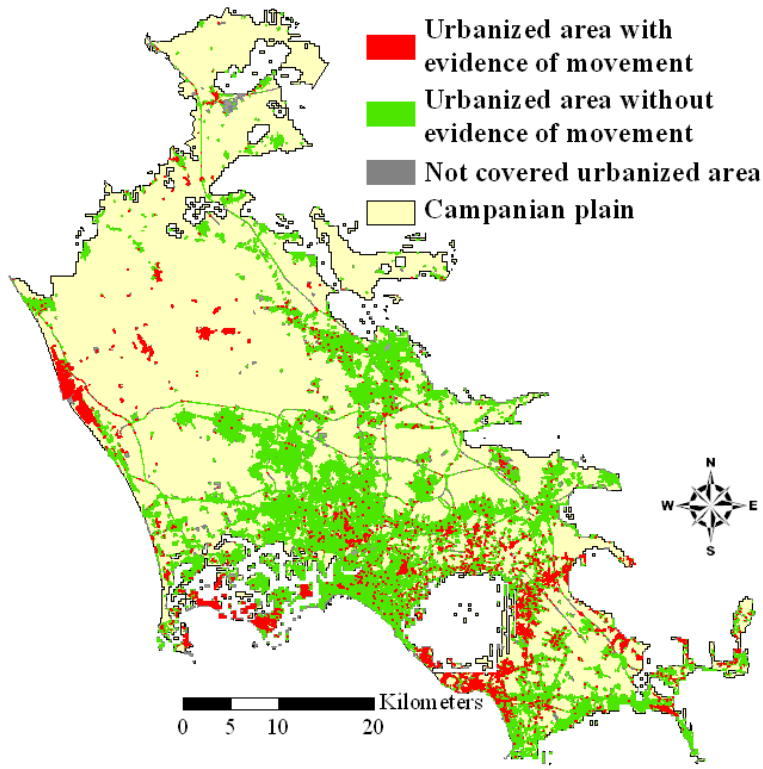
Figure 6.13 Map of the urbanised area dated 2001 with indication of evidence of movement for the whole period 1992-2010 (Cascini et al., 2013a).

In the last step of the analysis, inventory and ranking of affected municipalities were carried out according to the Subsiding Municipality Index referring either to the moving cells during the period of observation 1992-2010 where a prevailing natural subsidence was expected to be detected or to those moving cells during a shorter period of observation coinciding with ENVISAT time series (2003-2010).

Referring to the map of the urbanised area dated 2001 with indication of evidence of movement for the whole period 1992-2010 (Figure 6.12 a) the Map of subsiding Municipalities is reported in Figure 6.14. Then, the most affected municipalities, ranked in Figure 6.14 include some well documented cases of subsidence, such as Castelvolturno and Sarno. This can be considered a sort of preliminary validation of the developed analysis.
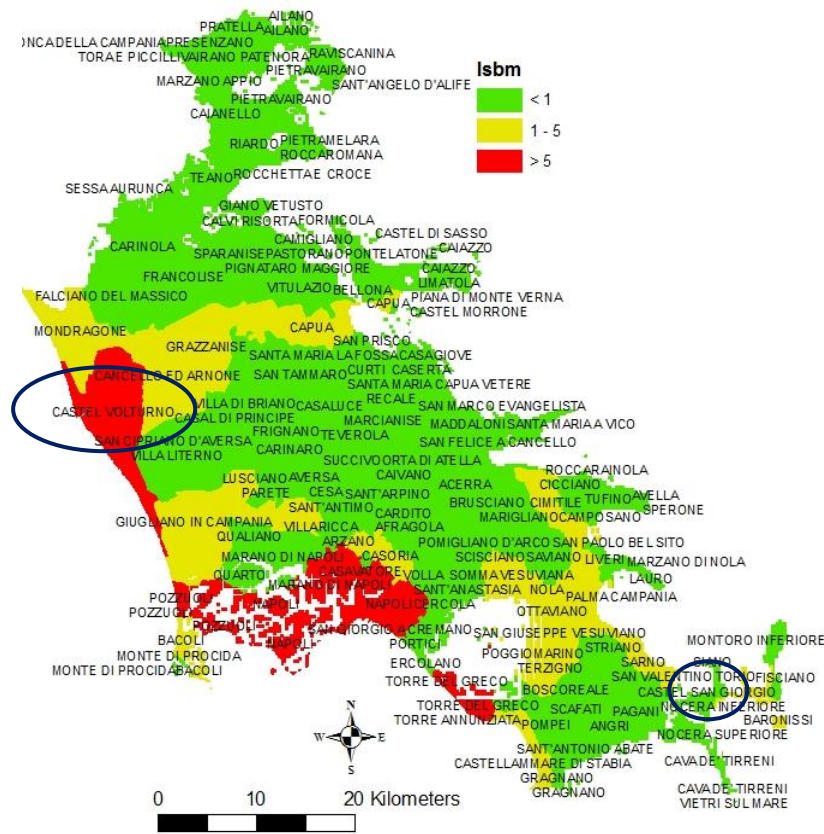
Figure 6.14 Map of Subsiding Municipalities referring to the period 1992-2010.

With reference to Castel Volturno area (Figure 6.15) it is affected by both a complex dynamic erosion processes affecting the whole coastline (Cocco, 1993).and a widespread subsidence phenomena (Corniello et al., 2010). This latter, in turn, can be associated with the huge groundwater withdrawals which also caused the sea ingression into land (salt-wedge) (Cascini et al., 2007).
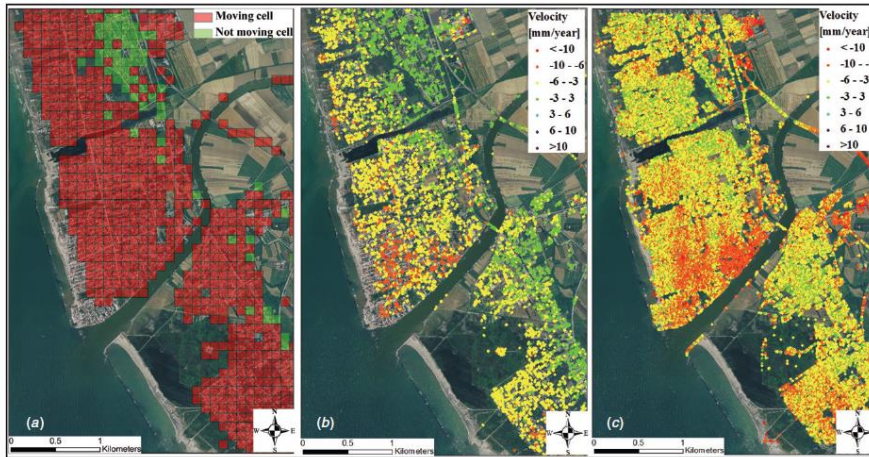
Figure 6.15 Castel Volturno (Campania region, Italy): map of the Volturno river outlet with: (*a*) indication of the grid of ERS-ENVISAT covered cells; (*b*) the distribution of ENVISAT data on both the ascending and descending orbit projected along the vertical direction; (*c*) the distribution of COSMO-SkyMed data on the descending orbit projected along the vertical direction (Cascini et al., 2013a).

As far as Sarno town is concerned, it is affected by a subsidence phenomenon (Cascini and Di Maio, 1994, Cascini et al 2006, 2007a, 2007b, 2011) induced by huge groundwater withdrawals causing damage of different severity to both masonry and reinforced concrete buildings by the end of 1980's (Figure 6.16).

Figure 6.16 (*a*) Close view map of moving cells and damaged buildings in the municipality of Sarno (Campania region, southern Italy); (*b*) a damaged masonry building with a sketch of surveyed cracks (*d*); (*c*) a damaged reinforced concrete building with a sketch of surveyed cracks (*e*) (Cascini et al., 2013a).

Some examples of the analyses at detailed scale both for Sarno and Castel Volturno municipalities are reported in the Appendix C.
Then turning our attention on the map of the urbanized area dated 2009 with indication of evidence of movement for the period 2003-2010 the municipality of Baronissi in Salerno Province results among the most subsidence-affected municipality (Figure 6.17).
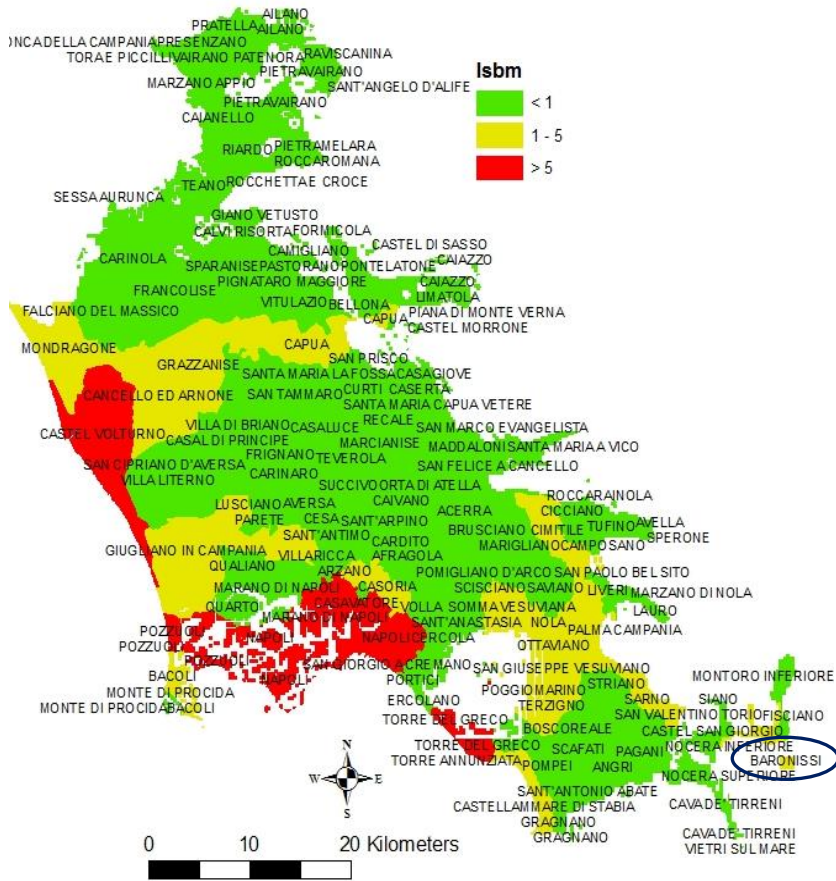
Figure 6.17 Map of Subsiding Municipalities referring to period (2003-2010).

The result concerning Baronissi was validated by in-situ surveys recently carried out showing the occurrence of damages induced by settlements (Figure 6.18). More details on this case study are provided in the next Sections concerning the large and detailed scale.

Figure 6.18 (*a*) Close view map of moving ENVISAT cells and damaged buildings in the municipality of Baronissi (Campania region, southern Italy); (*b*) damage recorded to infill walls and pavements; (*c*) damage recorded in the underground floor of a reinforced concrete building (Cascini et al., 2013a).

6.3   LARGE SCALE ANALYSIS

According to the results obtained at medium scale Baronissi municipality was selected for the analysis at large scale.

The area is located in Salerno Province (Figure 6.19a) in a flood plain, bordered by carbonatic ridge of Southern Apennines. The subsoil is mainly constituted by superficial deposits originated by soil degradation and washout of surrounding reliefs and by pyroclastic deposits originated by the volcanic activity of Campi Flegrei and Somma – Vesuvius (Santoro, 2001).

The contents of Section 6.3 and 6.4 are published in:

L. Ascione, L. Cascini, G. Sorbino, D. Peduto, L. Arena, A. Giordano, S. Spadea (2011) Sull'analisi geotecnica e strutturale degli edifici afferenti al Piano PEEP in località Cariti nel Comune di Baronissi''. Relazione Tecnica.

D. Peduto , L. Cascini, L. Arena, G. Sorbino (2012). L'impiego dei dati PSInSAR per l'analisi dei cedimenti di edifici in area urbana: un caso di studio.. In: Incontro Annuale dei Ricercatori di Geotecnica - IARG Padova 2-4 luglio 2012 RUBANO (PD) Grafiche Turato Edizioni Pag.1-6 ISBN:9788889524671

The typical stratigraphy is constituted by three main horizons (Di Rosario, 2002). The more shallow one (until 8.5 metres) is constituted by alternation of silty sand and sandy clayey silt.

Underneath, there is a layer of pyroclastic sand, called "grey tuff" with thickness ranging from 2 up to 3.5 m. The third deeper horizon is constituted by alternation of clayey silt and silty clay.In the study area 14 buildings were realized in the period between 2002 and 2003 (6.19 b). The buildings have a basement used as garage, a colonnade at ground floor devoted to commercial use and three or four floors for residential use.The used typology is reinforced concrete frames with rectangular Section columns and concrete slab. The foundations are shallow, in particular grade beam or grade slab (Ascione at al., 2011).
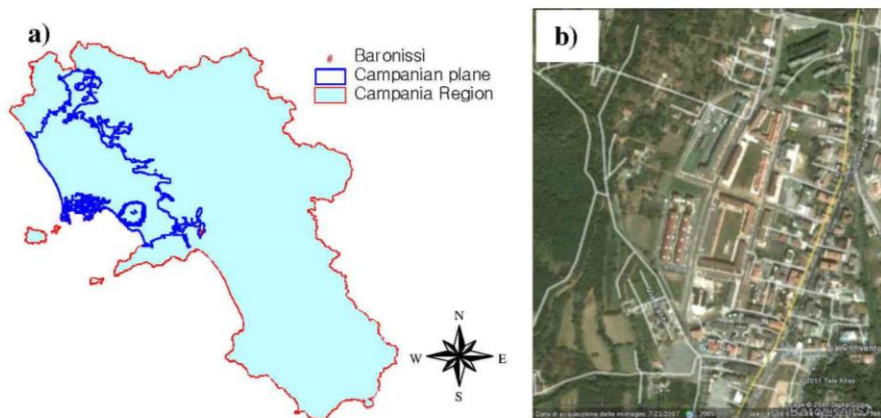
Figure 6.19 a) The study area; b) orthophoto covering a portion of Baronissi town (modified after Peduto et al., 2012)

In the study area, starting from May 2011, damages to the buildings were recorded affecting, in some cases, the functionality of underground garages and, in others, compromising building aesthetics due to the opening of significant cracks at the joints between contiguous buildings. According to the framework of Figure 5.5, after selecting the cell size of the operative grid (i.e. 10x10), in the preliminary phase the extent of the subsiding area was investigated by deriving the map of east-west and vertical velocity as a result of the combination of DInSAR data acquired on ascending and descending orbit (Manzo et al., 2006, Cascini et al., 2011). As it can be observed in Figures 6.20a and 6.20 b in the study area

during the period 1992 - 2000, velocity exceeded - both in the horizontal direction and vertical direction - the movement threshold equal to 2 mm/anno (Cascini et al., 2009) only in very limited portions of the territory. With reference to the period 2003 – 2007 (Figure 6.20 c-d), which, as above mentioned, coincides with the completion of the construction works of almost all of the buildings in the area, the average velocity recorded by PS data increased considerably, reaching values higher than 5mm/year.
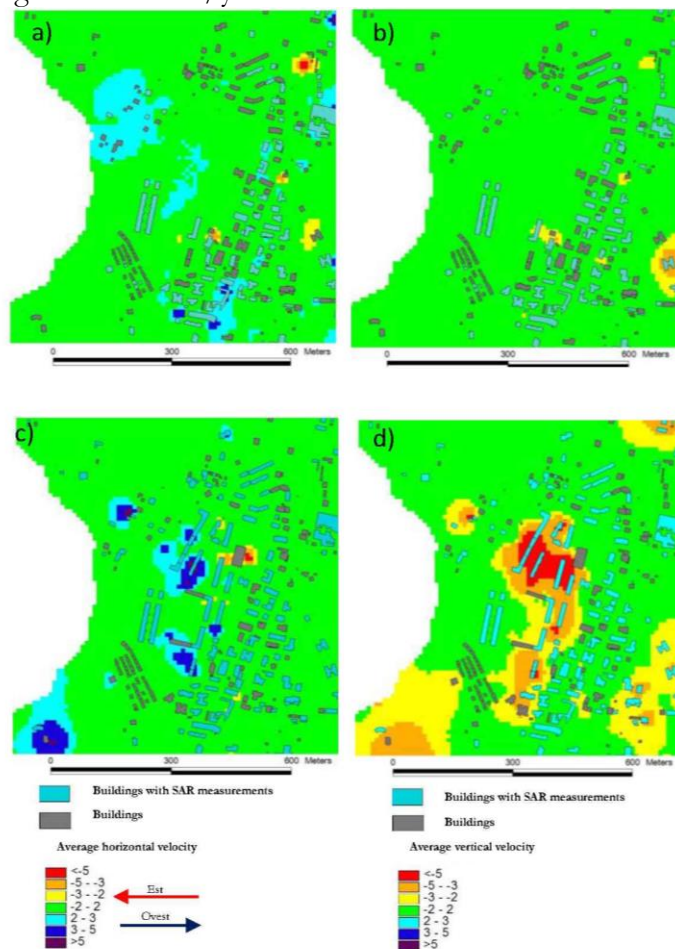
Figure 6.20 Map of horizontal and vertical velocity in the period 1993-2000 (a,b) and 2003-2007 (c,d).

After having verified that in the area of interest displacements mainly

occur along the vertical direction, maps of cumulative settlements relevant to different periods were computed (Figure 6.21).

Cumulated settlements [mm]

■	< -50
■	-50 - -30
■	-30 - -10
■	-10 - 10

■ Buildings with SAR measurements
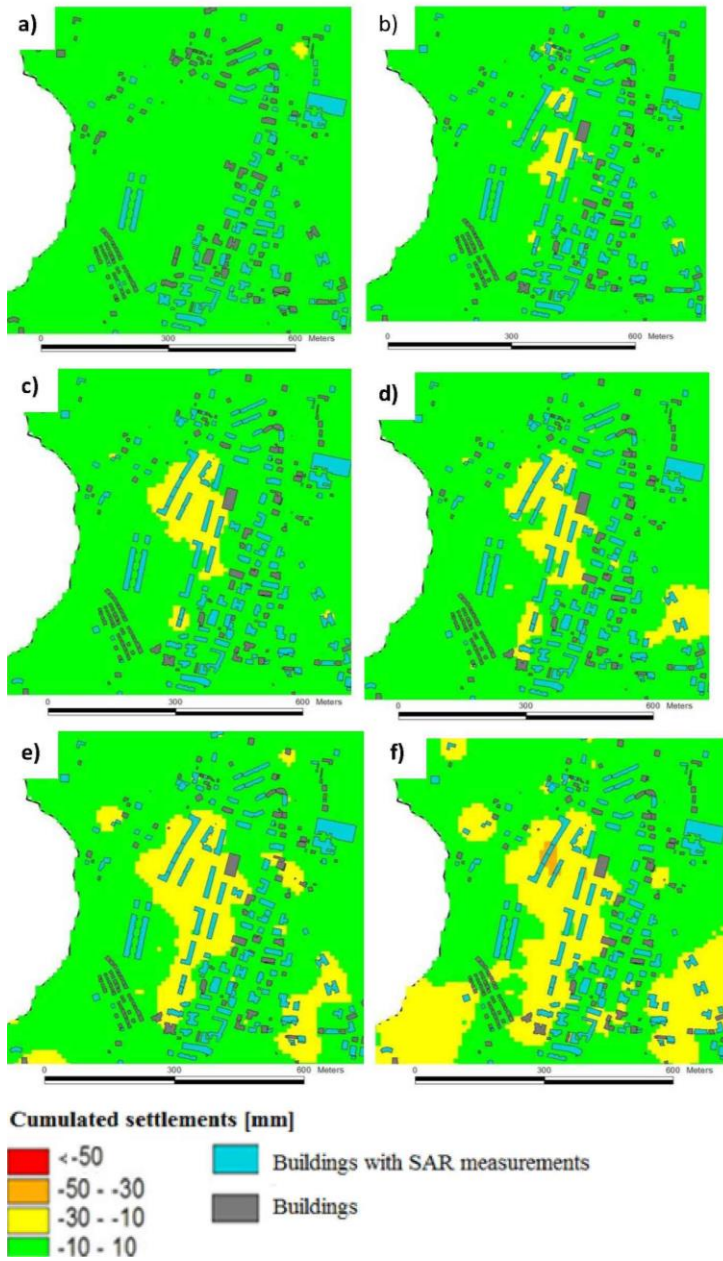
■ Buildings

Figure 6.21 Map of cumulated settlement period 1992-2000 (a), 1992-2003 (b); 1992-2004 (c); 1992-2005 (d); 1992-2006 (e) 1992-2007; 1992-2010 (f).

In order to investigate the relationship between the magnitude of settlement and the building damage occurrence, in the second phase the analysis was focused only on PSInSAR covered cell in the subsiding area. In particular, for each covered cell the average displacement - computed along its prevailing direction (vertical in this case) and weighted on the coherence of PSInSAR data - and was derived (Figure 6.22) using Envisat data.
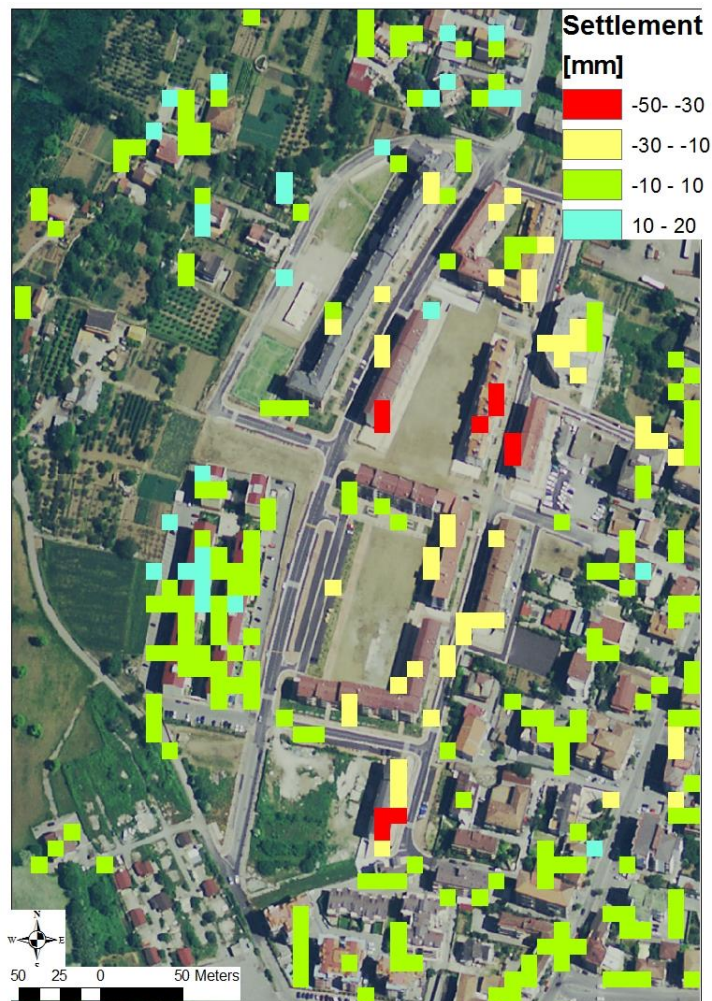
Figure 6.22 Map of cumulative settlement (period 2003-2010) using Envisat data.

Since damage occurrence and severity is usually related in the scientific literature to the magnitude of differential footing settlements (Burland

and Wroth 1974), a further step towards the analysis of consequences required the generation of the map of displacement gradients and their prevailing directions (Figure 6.23).
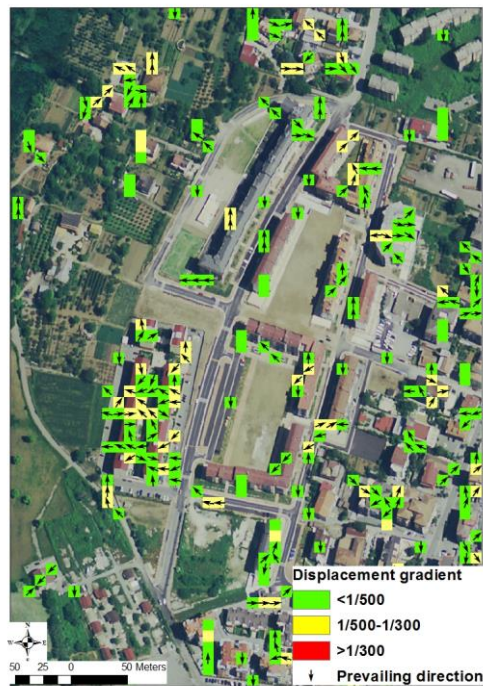
Figure 6.23 Map of displacement gradient and its prevailing direction (period 2003-2010).

The gradient of displacements was computed on the cell grid starting from the PSInSAR measured settlements.

The limit values in the legend of Figure 6.23 are referred to structures settling under their own weight: the value 1/500 is recommended in order to avoid cracking (DM 14/01/2008); the value of 1/300 is assumed by Skempton and MacDonald (1956) as the angular distortion threshold for first cracking in a panel wall and load-bearing walls; the value of 1/150 is considered as a threshold for severe cracking and structural damage.

The vector has the direction of the maximum rate of change of settlement. The result of Figure 6.23 was validated by in-situ surveys recently carried out (Figure 6.24) showing that, since the limitation due

to DInSAR coverage, damage occurred where the highest displacement gradient were reached.

Figure 6.24 a) Map of displacement gradient and its prevailing direction, a)-c)occurred damages.

The current limits to the application of the described methodology to derive map of displacement gradient are mainly related to the density of measurements points. In this regard, it is worth stressing that improvements concerning both ground resolution and reduced revisiting time allow an increased coverage (Figure 6.25, 6.26).
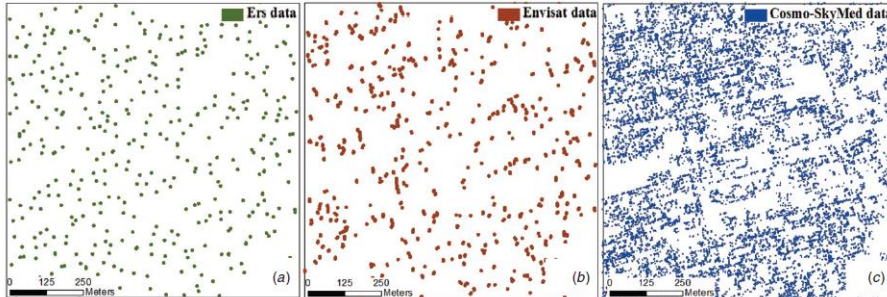
Figure 6.25 An example of the different distributions of targeted ground points achieved via ERS (*a*) and ENVISAT (*b*) data processed with PSInSAR (Ferretti *et al* 2001, Costantini *et al* 2008) and COSMO-SkyMed (*c*) data processed via MDI technique (Lombardini 2005, Fornaro *et al* 2009) over a sample urbanized area extending for 1 km² (Cascini et al., 2013).

Figure 6.27 shows an example of map of displacement gradient with reference to Naples city airport and its surrounding area for which COSMO-SkyMED data were provided by IREA-CNR for 1 year period. In particular, the density of detected points in the analysed area (extending for 18 km²) is about 16,100 PS km² for COSMO-SkyMed data and only 1078 PS km² for the ENVISAT data.
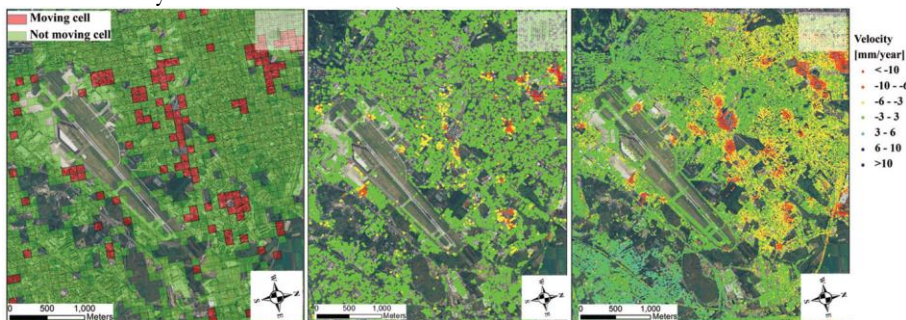
Figure 6.26 Naples city airport and its surrounding area: (*a*) map of moving ⁄ not moving cells according to ERS-ENVISAT dataset (period1992–2010); (*b*) map of ENVISAT PS velocity (November 2002 to July 2010); and (*c*) map of COSMO-SkyMed PS velocity (period February 2010 to February 2011).

With the purpose of showing how these analyses can be used to forecast the areas in which damage is likely to occur the map of displacement gradients was derived for the period 2010-2011 (Figure 6.27 a) - assuming a constant the rate of displacement - as well as for the period (2011-2021) (Figure 6.27 b). In Figure 6.27b it is interesting to observe that some buildings (coloured in green in Figure 6.27a) with the passing

of time exceed the threshold value of 1/500 related to severe cracking and structural damage to structures.

Figure 6.27. Map of displacement gradients in the surrounding area of Naples Airport with reference to: a) period 2010-2011; b) period 2011-2021.

6.4 DETAILED SCALE ANALYSIS

The analysis at detailed scale was focused on the building within Baronissi town that reached the highest values of displacement gradient at large scale (Figure 6.28). The building under examination consists of three blocks structurally separated by 20 cm wide joints. The used typology is reinforced concrete with rectangular Section columns and concrete slab. The foundation are shallow, in particular grade beam. According to the structural report and the static testing of the building the construction works started on November 2002 and finished on March 2003 (Ascione at al., 2011).

According to figure 6.28 the available PS were projected along the vertical direction and, then interpolated on a grid of 1 x 1 m at different dates. Once the direction of profile was chosen according to the maximum settlement change direction (Figure 6.23) profiles of settlements along the cross-Sections were retrieved. According to the settlements computed along the longitudinal cross-Section an increase with time of the absolute vertical settlements can be noticed. These latter reach their maximum (6 cm) in correspondence of the North limit of the building. Further interesting information was gathered by the trends exhibited by the relative rotation β (used by Skempton and McDonald's in their damageability criteria as a measure of the building distortion) . In particular, the values of the relative rotations, though low, reach the maximum values in the sections close to the northern limits of the building. The obtained results were validated via an in situ damage survey recently carried out in Baronissi. In particular, the building under examination recorded widespread cracks to the outside pavement and to infill walls and to the structural joint in correspondence of the section where maximum relative rotation were reached (1/450); conversely, the absence of significant cracks was recorded in the other sections thus confirming the results of the application of Skempton and McDonald's damageability criteria.
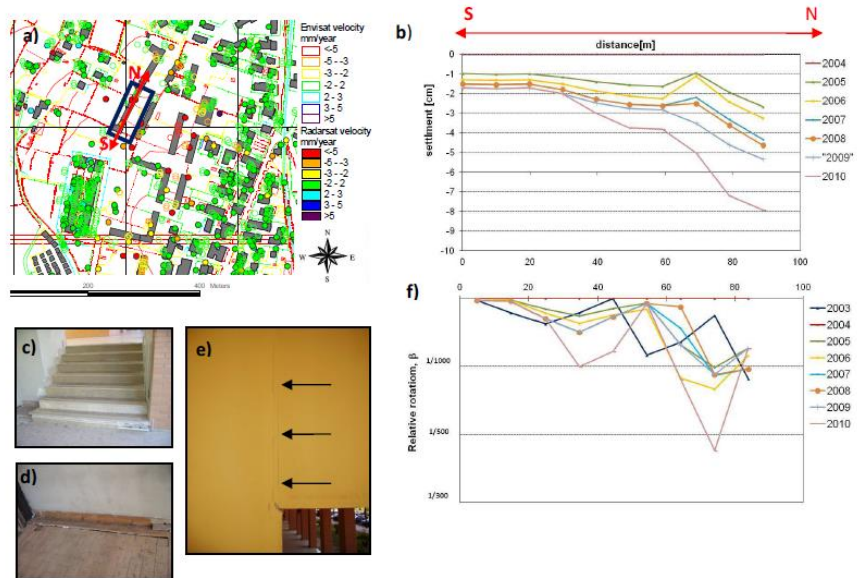
Figure 6.28. a) Distribution of PSInSAR data; b) vertical cumulative settlements at different dates starting from 2003; f) relative rotations computed along the sample longitudinal cross-Section at different dates starting from 2003; c) cracks to external stairs; d) cracks to outside pavement; e) cracks to infilled walls.

Other examples of analyses carried out at detailed scale are reported in the Appendix D.

7 APPLICATIONS TO SLOW-MOVING LANDSLIDE

"If you have to forecast, forecast often. "

E. Fiedler

This Section focuses on the applications of the procedures at different scales (see Section 5) based on the combination of DInSAR data and damage surveys to study slow-moving landslides.

7.1 ANALYSIS AT MEDIUM SCALE

7.1.1 Study area

The procedures, described in Section 5.3, were tested in an area (557 km^2) choosen within the territory of the National Basin Authority of Liri-Garigliano and Volturno rivers, including 21 Municipalities and 2 Provinces (Benevento and Avellino). This area was selected due to the widespread distribution of slow-moving landslides (covering around 25% of the total extension) which caused losses to structures/infrastructures

The contents of Section 7.1. and 7.2 are published in:

L. Cascini, S. Ferlisi, D. Peduto, L. Arena(2011d). L'impiego di dati DInSAR nella caratterizzazione a scala di bacino di fenomeni franosi a cinematica lenta. In: Incontro Annuale dei Ricercatori di Geotecnica Torino 4-6 luglio 2011 Pag.1-6

L. Cascini, D. Peduto, G. Pisciotta, L. Arena, S. Ferlisi, G. Fornaro(2013b).The combination of DInSAR and facility damage data for the updating of slow-moving landslide inventory maps at medium scale. Natural Hazards and Earth System Sciences, Vol. 13. Pag.1527-1549 issn:1561-8633.

D. Peduto , L. Cascini , L. Arena , S. Ferlisi , G. Pisciotta , G. Fornaro (2013).Uso congiunto dei dati DInSAR e dei danni al costruito per l'aggiornamento delle carte inventario dei fenomeni franosi a cinematica lenta. In: Incontro Annuale dei Ricercatori di Geotecnica Perugia 16-18 settembre 2013 Perugia Università degli Studi di Perugia Pag.1-6 ISBN:9788890642135
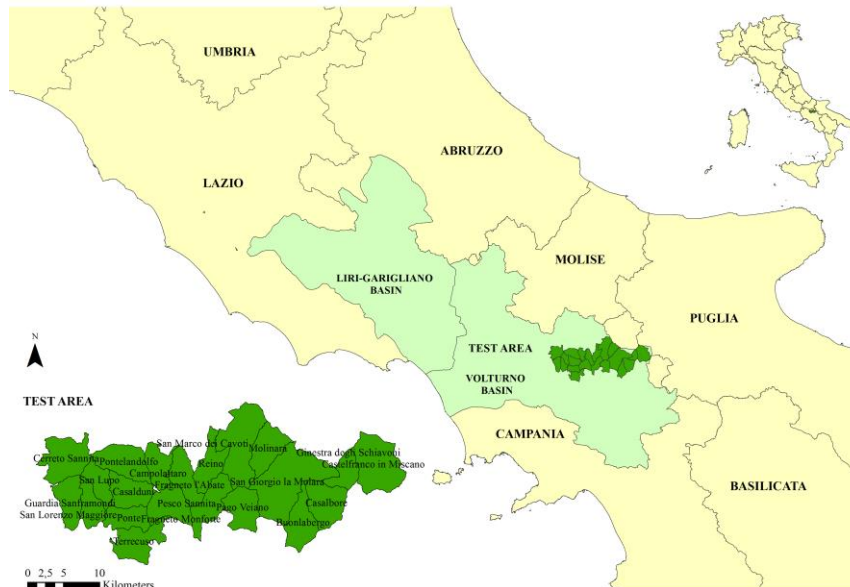
Figure 7.1 The study area (Cascini et al.,2013b).

interacting with them (Melidoro, 1971; D'Elia et al., 1985; APAT, 2007; Cascini et al. 2008).For the study area, base (topographic) maps at 1 : 5000 scale and thematic (geological, geomorphological, landslide inventory) maps at 1 : 25 000 scale are available. These maps were developed during the activities carried out by the NBA-LGV within the PsAI-Rf (Hydrogeological Setting Plans – Landslide Risk excerpt) project (Italian Law 365/2000). In particular, the geological map of the area highlights the existence of Mesozoic-Tertiary lithological units mainly consisting of clayey-sandy-arenaceous and clayey-calcareous-siliceous strata covered by marly-calcareous, arenaceous and arenaceous-conglomeratic units (Rapolla et al, 2012). These latter units together with the geo-structural setting mainly control the geomorphological features of the area.

As for landslide inventory (Figure 7.2 Distribution and types of slow-moving landslides over the study area (Cascini et al., 2013b)), the available map – developed at 1:25,000 scale on the basis of geomorphological criteria supported by field survey data and aerial photo interpretation – furnishes detailed information for each mapped phenomenon with reference to location, type, state of activity and areal extension.
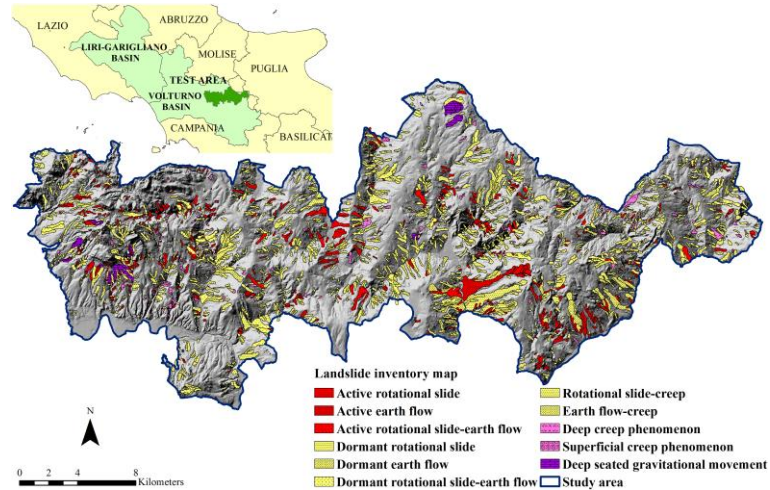
Figure 7.2 Distribution and types of slow-moving landslides over the study area (Cascini et al., 2013b)

As far as the type of phenomenon is concerned, over a total number of 2,180 slow-moving landslides, the inventory map distinguishes: 766 rotational slides; 267 rotational slide–earth flows; 1,117 earth-flows; 30 deep seated gravitational movements (dsgm); moreover, 158 creep phenomena, 65 earth flow-creeps and 2 rotational-creeps were also inventoried (Figure 7.3a-b). Furthermore, according to the adopted approach for landslide inventory mapping, two possible states of activity for rotational slides, rotational slide-earth flows and earth flows were considered (Figure 7.3a): "dormant" landslides and "active" landslides, the latter including active, reactivated and suspended phenomena (Cruden and Varnes, 1996). On these bases, Figure 7.3a shows a predominance of dormant phenomena (1562) on active ones (588) with size ranging from around 0.1 hectares up to around 200 hectares (Figure 7.3b).
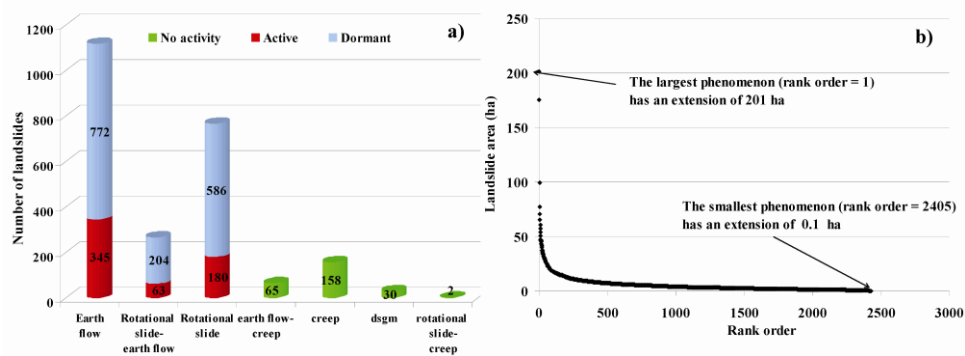
Figure 7.3 a) Number and state of activity of mapped phenomena distinguished per types within the test area; b) distribution of slow-moving landslide extension within the test area (Cascini et al., 2013b).

The PSI data used for the present study were collected within the Piano Straordinario di Telerilevamento (MATTM, 2010) which is a project supported by the Italian Ministry of Environment, Land and Sea covering all the Italian territory with an ERS-ENVISAT sensor database of almost 20 years since 1992. In particular, for the study area the following data are available: 208 ERS images on ascending orbit (period September 1992 – September 2000) and 134 on descending orbit (period November 1992 – December 2000); 52 ENVISAT images on ascending orbit (period November 2002 – July 2010) and 49 on descending orbit (period March 2003 – June 2010). The distribution and the recorded velocity of both ERS and ENVISAT PS over the study area are shown, respectively, in Figures 7.4a and 7.4b. ERS data exhibit a density of 43.4 PS/km^2, whereas a density equal to 91.4 PS/km^2 is recorded for ENVISAT data.
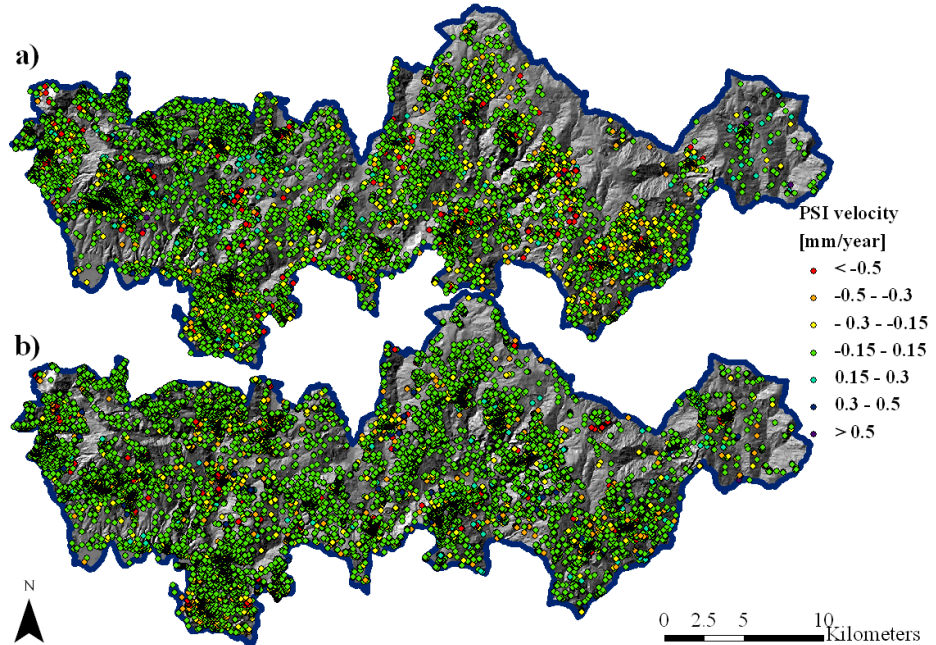
Figure 7.4 Distribution of PSI data over the study area according to a) ERS and b) ENVISAT sensor (Cascini et al., 2013b).

As far as dataset on landslide-induced damage to buildings, infrastructures and other facilities is concerned, damage survey was carried out inside PSAI project (2001). These data were achieved compiling damage-recording sheets. In each sheet, several information are reported, such as typology of the phenomenon, the characteristics and relative location of vulnerable element within landslide-affected area, the date of induced damage (if available), the structural or no-structural element damaged, the state of maintenance and other possible addition information.

7.1.2   Updating of landslide inventory map

With reference to the study area, the a-priori landslide visibility map was firstly generated according to the adopted methodological approach (Figure 5.8). The obtained map (Figure 7.5 a,b) highlights that the areas visible with difficulty on both orbits – namely slopes facing north or south (Cascini et al. 2009) – correspond to 23.6% of the total landslide

affected areas; the visible areas on ascending orbit (Figure 7.5b) correspond to 33.5%; whereas on descending orbit (Figure 13a) the percentage raises up to 42.8%. This is confirmed by the higher number of PS on descending orbit datasets (5,024 PS of which 60% in visible areas, 25% in areas visible with difficulty and 15% in not visible areas) than on ascending orbit datasets (4,882 PS of which 53% in visible areas, 25% in areas visible with difficulty and 22% in not visible areas) which are found within landslide affected areas. Moreover, the percentage of PS-covered (by at least 3 PS or with more than 20 PS/km^2) landslides is equal to 16% for ERS sensor and 20% for ENVISAT.
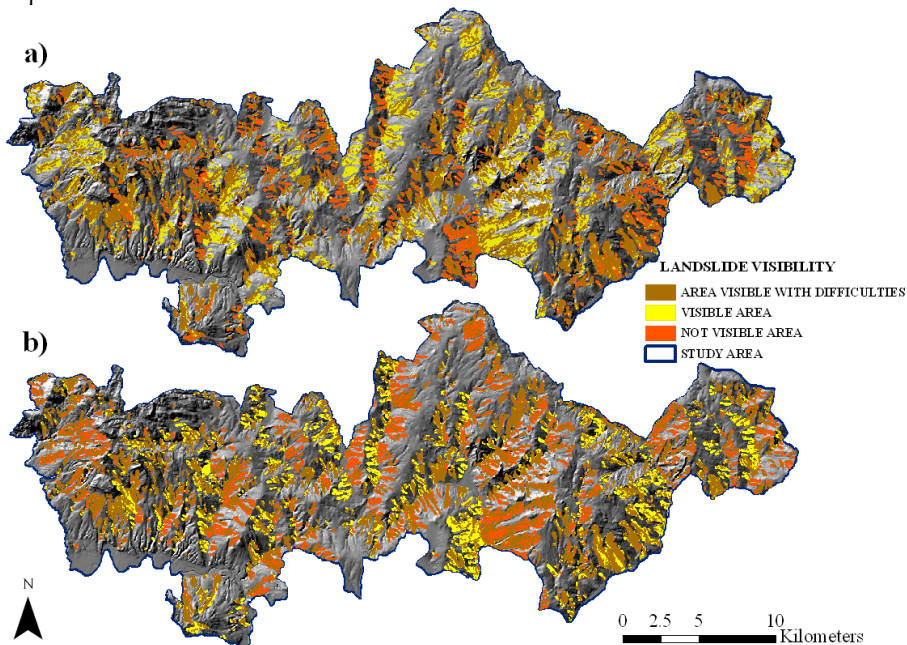
Figure 7.5 The A-priori landslide visibility map for the study area on descending (a) and ascending (b) orbit (Cascini et al., 2013b).

In this first phase of activities the A-Index was also computed for each available PS of the ERS dataset.

Through the map of projectable PS (Figure 7.7 a,b) the available PS were distinguished as projectable and not projectable depending on the value of the scaling factor (lower or higher than 3.3). In particular, around 53% out of the total ERS-PS (Figure 7.7a) and 47% of the ENVISAT-PS (Figure 7.7b) resulted projectable.
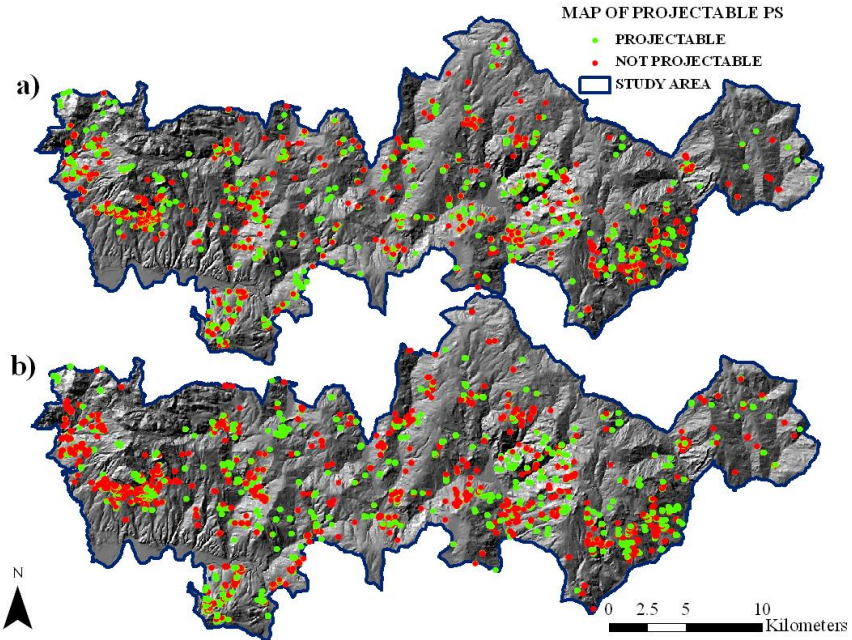
Figure 7.6 The map of projectable PS for ERS (a) and ENVISAT (b) datasets (Cascini et al., 2013b)

Focusing on the projectable PS, firstly the V_{slope} value was calculated for each PS; after that, the landslide velocity was computed for each covered phenomenon according to ERS (Figure 7.6 a) and ENVISAT (Figure 7.6 b) data. The achieved results, grouped for the different landslide types (i.e. earth flows, rotational slides and rotational slide – earth flows), show that the computed landslide velocities attain comparable values not exceeding a limit of 25 mm/year (Figure 7.7c) that is slightly over the velocity value of 16 mm/year discriminating extremely slow against very slow phenomena (Cruden and Varnes, 1996). With respect to creep phenomena, earth flow – creeps and deep seated gravitational movements the computed velocity values do not exceed 7 mm/year thus falling within the range of extremely slow phenomena (Cruden and Varnes, 1996). However, as already pointed out by Cascini et al. (2010) the computed landslide velocities refer to values averaged in time (period of observation of PSI dataset) and in space (amongst the velocities of the PS included in the boundary of the same landslide) whereas Cruden and Varnes (1996) reasonably refer to the maximum velocity value attained by a given – superficial or internal – point of a landslide displaced mass during its paroxysmal phase of movement.
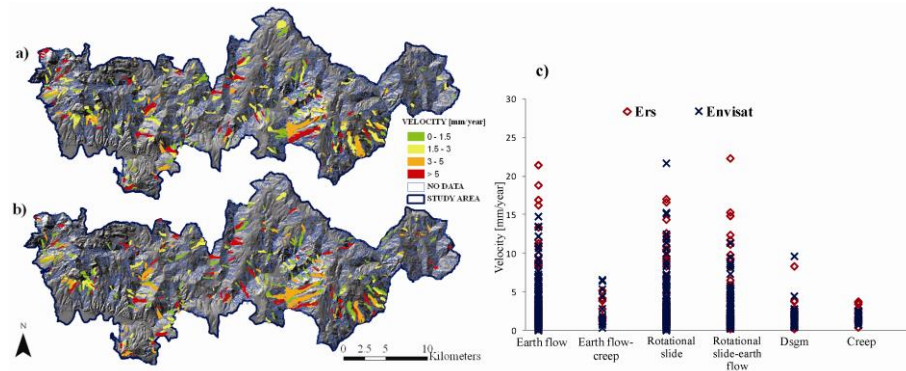
Figure 7.7 The PSI landslide velocity map for ERS (a) and ENVISAT (b) data; c) the computed landslide velocities per different landslide types (Cascini et al., 2013b).

The landslide velocity maps (Figure 7.7 a,b) are preparatory to the generation of the map in Figure 7.8 where PS-covered landslides are appointed as moving, not moving or no data according to the corresponding velocity thresholds (see the Appendix C). The results highlight that out of a total of 288 landslides covered by projectable ERS data (Figure 16a) 30% are moving and 70% are not moving. With reference to ENVISAT dataset (Figure 7.8b) out of 376 landslides covered by projectable ENVISAT data 38% are moving and 62% are not moving.

The condition of movement / no movement derived from ERS-PSI data (period 1992-2000) was compared with the state of activity reported in the landslide inventory map (2001) with reference to 249 landslides (53 active and 196 dormant) classified as earth flows, rotational slides or rotational slide – earth flows. In Figure 7.8 c it can be noticed that over 53 active landslides 36% are moving according to ERS landslide velocities; whereas 89% of 196 dormant phenomena are not moving. Finally, an increasing/decreasing trend was assumed for each landslide according to the previously described procedure (Sect.5.3.1) using ERS projected time-series.

This latter information together with the abovementioned data plays as input data to the DInSAR-Damage matrix.
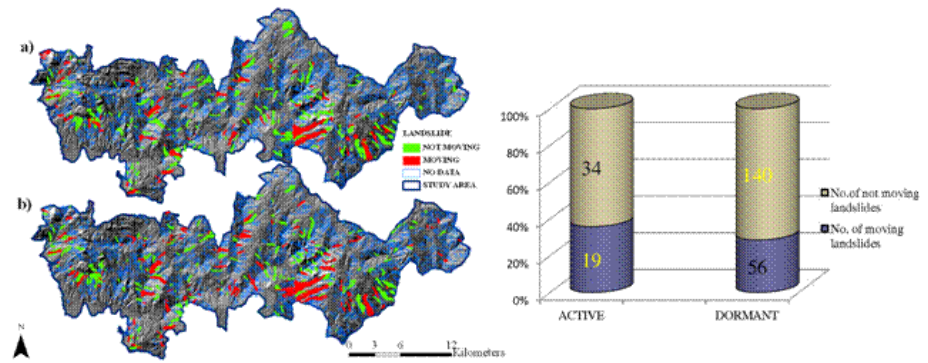
Figure 7.8 Map of moving/not moving landslide according to both ERS (a) and ENVISAT PSI (b) data; c) comparison among the state of activity derived from either the landslide inventory map or the indication of movement derived from ERS-PSI data (Cascini et al., 2013b).

With reference to all 21 urbanized municipal territories of the study area and according to the methodology described in Section 5.3., the homogeneous aggregations of existing buildings were firstly generated. Then, they were intersected with the mapped slow-moving landslide affected areas obtaining the so-called vulnerable areas distinguished on the basis of the buildings' occupancy type. On the other hand, the portions of single roads interacting with the inventoried landslides were detected. Once identified, vulnerable areas and roads were classified as damaged or not damaged whether at least either one damaged building within their perimeter or damage evidences along the road track interacting with the landslides were recorded. As a result, a total number of 190 vulnerable areas with damage survey (45% of them damaged and 55% not damaged) and 228 roads with damage surveys (60% of them damaged and 40% not damaged) was recorded.

Then, focusing on landslides interacting with damaged vulnerable areas and/or roads, out of a total of 147 censored phenomena – 94 (64%) of them involved only vulnerable roads, 35 (24%) only vulnerable areas and the remaining 18 (12%) both vulnerable areas and roads. On the other hand, the landslides interacting with not damaged vulnerable areas and/or roads are 247; these, in turn, can be distinguished among those involving *i)* only vulnerable roads (116 corresponding to 47%), *ii)* only vulnerable areas (101 corresponding to 41%), *iii)* both vulnerable areas and roads (30 corresponding to 12%). Furthermore, the highest number of slow-moving landslides interacting with damaged vulnerable areas

and/or roads pertains to the earth flow type, immediately followed by rotational slide type.

Over 352 (94 active and 258 dormant) landslides – for which the state of activity is reported in the inventory map (i.e. earth flows, rotational slides and rotational slide – earth flows) and detailed damage surveys are available – a good agreement is attained between dormant landslides and not damaged vulnerable areas/roads (about 70%), while the percentage of active landslides on which damages to vulnerable areas/roads were recorded is around 51%.

PSI-derived evidences of movement and the results of damage survey dataset were compared showing that over 44 PSImoving landslides, for which damage survey results are available, 57% of surveyed facilities recorded damage; whereas for landslides appointed as not moving (85), 58% of the total did not exhibit damage during surveys (Figure 7.9).
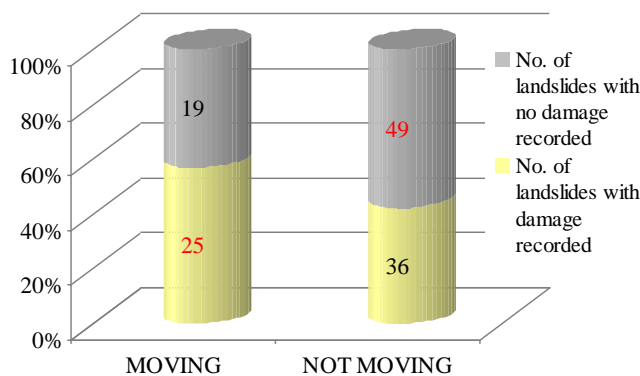
Figure 7.9 Comparison among PS-derived evidence of movement on landslides and the results of damage survey (Cascini et al., 2013b).

This may be related to the constraints arising from the adopted scale of work. Indeed, at medium scale (1:25 000), the role played by some relevant factors in influencing the damageability of facilities interacting with slow moving landslide bodies cannot be clearly highlighted, e.g. the relative position of facilities within the landslide affected areas. In the study area, nine not damaged building aggregations interacting with ERS-PSI moving earth flows were found to be in the middle portion of the landslide, usually affected by translational movements (Cascini et al., 2010). Therefore, the involved buildings may have not suffered damages because foundations were mainly subjected to absolute (not differential) displacements which can be tolerated by the superstructures.

The DInSAR-Damage matrix was applied to update the state of activity of 167 landslides (29 active and 138 dormant, see Figure 7.10a), for which both ERS and ENVISAT-PSInSAR data are available. As a result, 33 active and 83 dormant landslides are distinguished (Figure 7.10 b) and for 51 landslides further in-situ surveys are necessary since the available information is not enough to define the state of activity (Figure 7.10b).

A cross-check with the available pre-existing landslide inventory map (Figure 7.11a) reveals that 91 landslides confirm their previous state of activity, whereas for 25 it changes. In particular, 19 landslides pass from dormant to active and 6 from active to dormant.
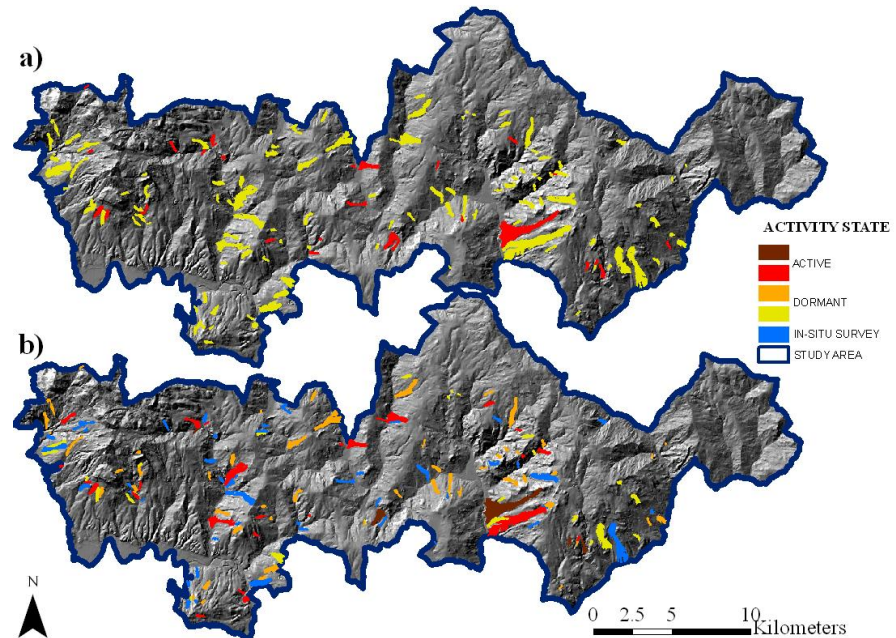
Figure 7.10 Results of the application of the DInSAR-Damage matrix: the pre-existing (a) and the updated (b) landslide state of activity (Cascini et al., 2013b).

A field validation test of the outcomes of the DInSAR-Damage matrix over such an extended area was carried out by randomly selecting 10% out of the total number of active and dormant landslides whose state of activity was either confirmed or changed with respect to the available landslide inventory. In 2012, field surveys were carried out on these areas to detect evidences of movement in structures and infrastructures. These surveys highlighted that, over 19 investigated landslides, the matrix-based state of activity was confirmed for 15 of them, being not confirmed for the remaining 4 landslides. Some examples are reported hereafter.

133

The first example refers to a rotational slide – earth flow located in the municipality of Pesco Sannita in Benevento Province (Figure 7.11 a-g). This landslide (Figure 7.11a) reported as active on the landslide inventory map showed a velocity around 8 mm/year (Figure 7.11b,c) from the analysis of PSI-ERS data. As for the damage, the survey carried out in 2000 (Figure 7.11d) recorded the presence of significant cracks in the elements of one masonry building (on the right in Figure 7.11d) and the tilting of another masonry building (on the left in Figure 7.11d), whose stability and serviceability were seriously affected, both located in the head of the landslide body (Figure 7.11a). The availability of ENVISAT-PSI dataset allowed to classify the landslide as moving – with a computed velocity of_5 mm/year (Figure 7.11c) – and according to the DInSAR-Damage matrix the assumed state of activity was confirmed as active (dark red in the matrix, first cell of the first column).
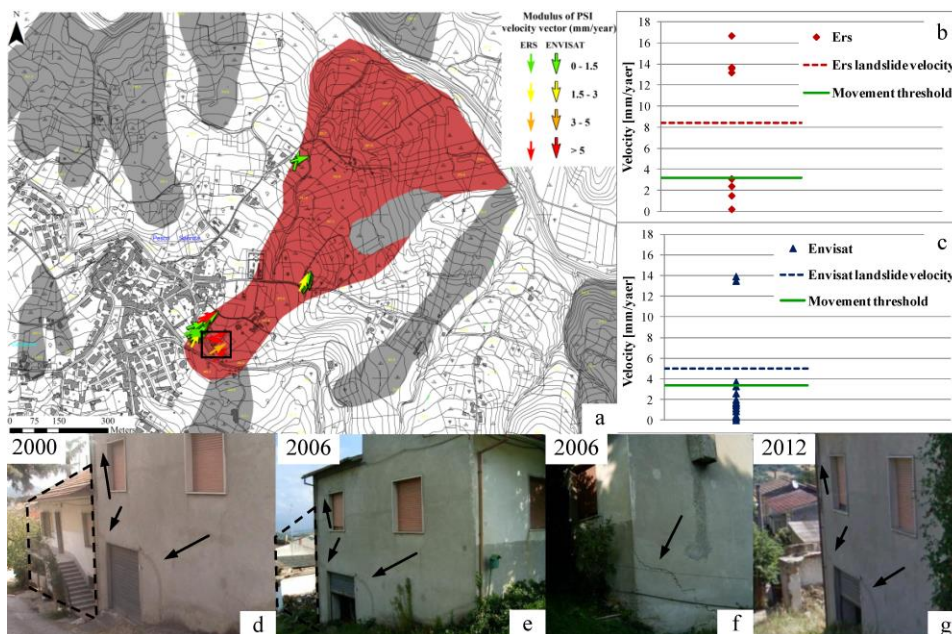
Figure 7.11 An active rotational slide – earth flow in the municipality of Pesco Sannita (Benevento Province): a) the inventory map with ERS/ENVISAT PS velocity vectors; b-c) diagrams of the ERS/ENVISAT velocity values for the PS located within the landslide boundaries and indication of both the computed landslide velocity and the computed movement threshold; d-g) photos of two buildings located in the head of the landslide with highlight on the damage recorded during the survey dated 2000, 2006, 2012 (Cascini et al., 2013b).

To check the reliability of this assumption two damage surveys were performed, as it is shown in Figures 7.11e-g, in 2006 and 2012 both showing the presence of cracks on the building on the right. Moreover, during the survey of 2012 the building on the left resulted to have been demolished.

A second example is shown in Figure 7.12 (a-h) with reference to an earth flow (Figure 7.12a), in the municipal territory of Reino (Benevento Province), reported as dormant in the landslide inventory. According to the analysis of both ERS and ENVISAT computed velocities (respectively equal to 9.8 mm/year and to_5 mm/year) the landslide resulted as moving. Moreover, during the damage survey carried out in year 2000 (Figure 7.12c-e) cracks were recorded on masonry row houses located along the boundary of the landslide body. The implementation of the DInSAR-Damage matrix allowed the classification of this landslide as active (seventh cell of the first column, Figure 5.13).
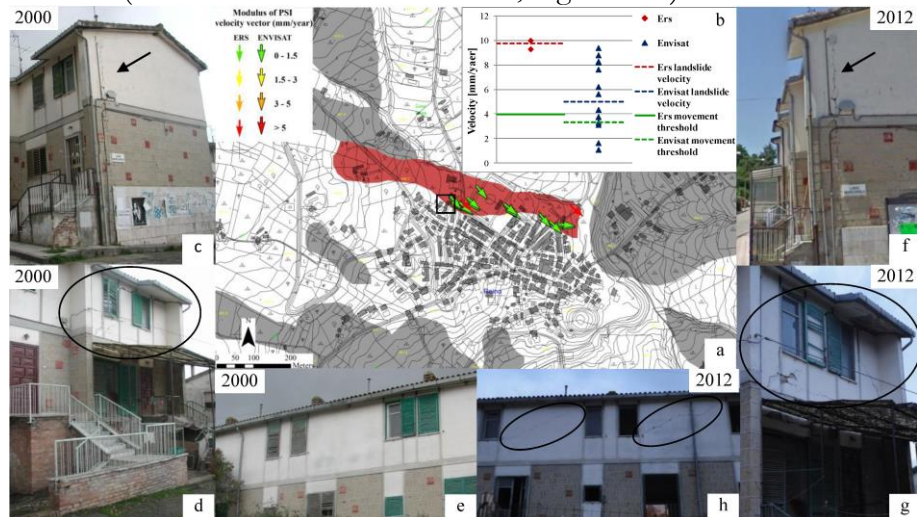
Figure 7.12 A dormant earth flow in the municipality of Reino (Benevento Province): a) the inventory map with ERS/ENVISAT PS velocity vectors; b) diagrams of the ERS/ENVISAT velocity values for the PS located within the landslide boundaries and indication of both the computed landslide velocity and the computed movement threshold; three different views of row-houses located on the middle boundary of the landslide (see the black square in Figure 23a) with highlight on the damage recorded in the surveys dated 2000 (c-e) and 2012 (f-h) (Cascini et al., 2013b).

To validate this assumption the results of a damage survey carried out in 2012 were used (Figure 7.12 f-h). In particular, Figure 7.11f shows a wall where the width of the vertical cracks recorded in year 2000 (Figure 7.12 c) increased (Figure 7.12f) as well as the occurrence of some inclined cracks (Figure 7.13h) on a wall which during the previous survey did not exhibit any cracks (Figure 7.12e). Moreover, with reference to the same group of structures during the survey dated 2012 some cracks on recently restored building façades were recorded.

The last example in Figures 7.13 (a-g) concerns a dormant rotational slide located in the municipality of San Giorgio la Molara (Benevento Province). In particular, Figure 7.13a shows that the head of the landslide involves some buildings and the ERS velocity vectors exhibit mostly (5 out of 6 PS) decreasing trends. The computation of the ERS landslide velocity (3.6 mm/year) exceeding the ERS velocity threshold (3.4 mm/year) allows defining the landslide as moving and, according to the majority of PS-derived trends, a decreasing trend is associated with the landslide. The analysis of ENVISAT data (Figure 7.13c-d) highlights that the landslide is not moving since the landslide velocity (0.9 mm/year) is lower than the computed velocity threshold (3.8 mm/year). For this landslide no damage survey data is available so entering the DInSAR-Damage matrix (eighth cell of the second column) and considering the ERS decreasing trend (sign -) the state of activity should be set to dormant. This result was validated by a damage survey carried out in 207.13 showing that the buildings located in the head of the rotational slide (Figure 7.13 e-g), mainly consisting of reinforced concrete structures, did not exhibited any cracks or damages.
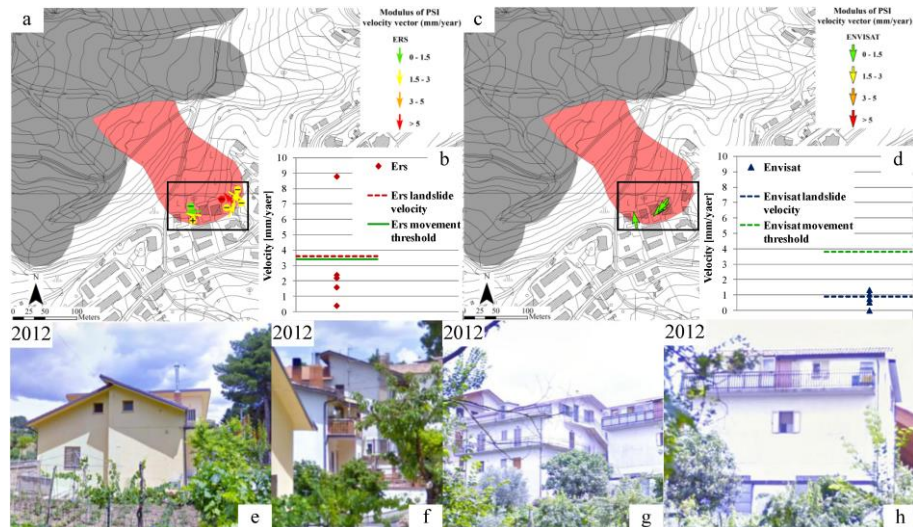
Figure 7.13 A dormant rotational slide in the municipality of San Giorgio La Molara (Benevento Province): a) the inventory map with ERS PS velocity vectors and indication of the increasing (+) or decreasing (-) trend of the displacement time series; b) diagrams of the ERS velocity values for the PS located within the landslide boundaries and indication of both the computed landslide velocity and the computed landslide movement threshold; c) the inventory map with ENVISAT PS velocity vectors; d) diagrams of the ENVISAT velocity values for the PS located within the landslide boundaries and indication of both the computed landslide velocity and the landslide movement threshold; e,f,g,h) different views of buildings located in the head of the landslide referring to the survey carried out in 2012 (Cascini et al., 2013b).

The automated detection and mapping of slow-moving landslide phenomena via remote sensing techniques (radar and optical) over wide areas is a challenging topic. In the present study the availability of the geomorphological map (1:25,000 scale) of the NBA LGV suggested to focus the analyses on the portions of the study area mapped as hollows. As described in Cascini et al. (2009) these areas are characterized by geomorphological settings similar to landslide affected areas; therefore, they can be preliminarily analysed prior to proceeding to the updating of a given inventory map. In the study area over a total of 1,580 hollows, 189 resulted covered by projectable ERS-PSI data. Focusing on the hollows covered by at least three PS or with a density higher than 20 PS/km^2, the velocities were computed and 33 hollows resulted moving (Figure 7.14). For 8 of these hollows the damage survey results dated

2000 were available and within the boundaries of 3 of them damages to facilities were recorded.

A similar comparison was then carried out with ENVISAT-PSI data whose information covered 233 hollows, 40 of which resulted as moving.
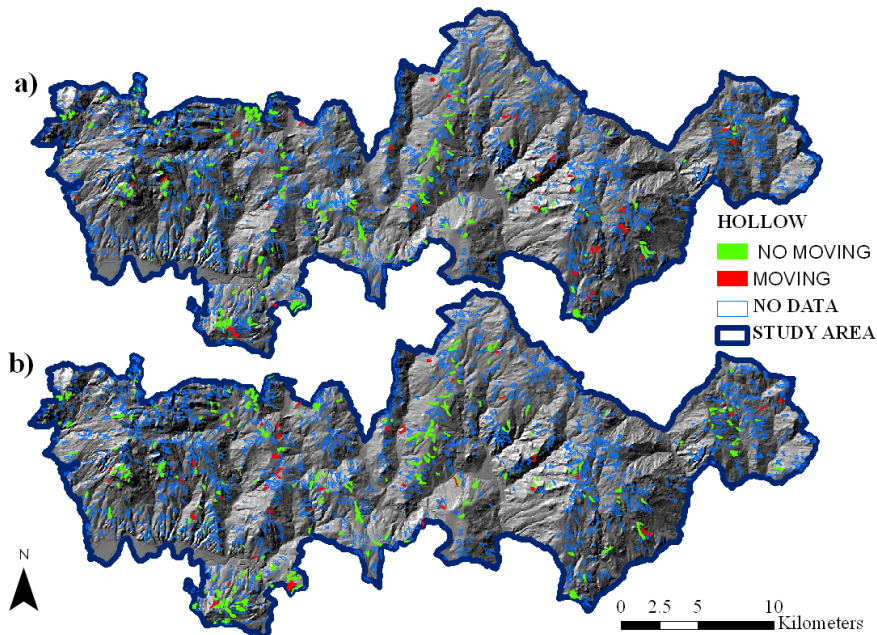
Figure 7.14 Map of the hollows in the study area distinguished according to ERS (a) and ENVISAT (b) PSI data analysis (Cascini et al., 2013b).

One of these is reported in Figures 7.15 a-g which show a moving hollow (in red in Figure 7.15 a) located at the head of a rotational slide earth flow (in gray in Figure 7.15 a) in the municipality of Campolattaro (Benevento Province). The computed velocity (1.7 mm/year) for ERS data (Figure 7.15 b) approaches the movement threshold (2 mm/year), whereas for ENVISAT data the threshold (2.8 mm/year) is exceeded by the velocity value (4.8 mm/year) with some PS velocity reaching up to about than 10 mm/year. In this area damage surveys were also carried out. The results of both the surveys in 2000 (Figure 7.15 c-d) and 2012 (Figure 7.15 e-g) show the tilting of a masonry building whose serviceability is definitively compromised. Moreover, the vertical crack pattern recorded in correspondence of the joint between the building and its entry structure (Figure 7.15 f and Figure 7.15 g) exhibits an

overall increase during the period 2000-2012. These evidences could be related to either the activation of a landslide phenomenon or to a retrogressive movement starting from the head of the rotational slide located downslope.
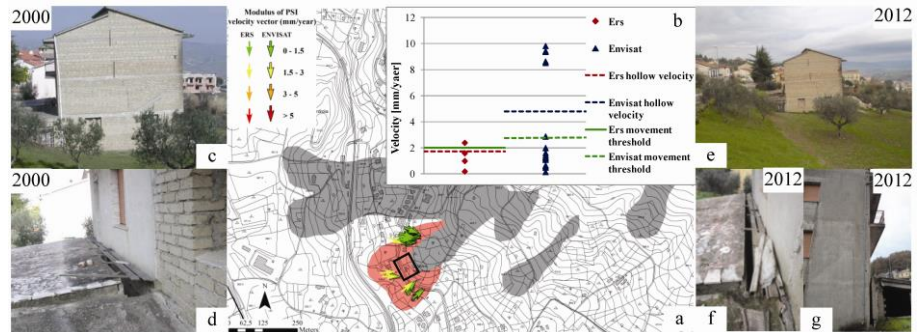
Figure 7.15 A hollow located in the municipality of Castelpagano (Benevento, Province): a) map the hollow (in red) located at the head of a rotational slide-earth flow (in gray) with ERS/ENVISAT PS velocity vectors; b) diagrams of the ERS/ENVISAT velocity values for the PS located within the hollow boundaries and indication of both the computed hollow velocity and the movement threshold; tilting of a masonry building and highlights on the crack pattern recorded during the surveys of 2000 (c-d) and 2012 (e-g) (Cascini et al., 2013b).

7.1.3 Analysis of consequences

The proposed methodological approach to derive fragility/vulnerability curves (Figure 5.14) at medium scale was applied with reference to 65 masonry buildings within the study area.

In particular, according to the scale of analysis, 27 vulnerable areas (see Section 5.3) were chosen because of the availability of both DInSAR data and damage survey on buildings belonging to them.

The recorded damages were classified, in this Thesis, into four classes of building damage severity from D0 to D3-D4 (Table 5.2); then, the equivalent damage for each vulnerable area was calculated via the equation 5.7.

Table 7.1 Damage classes for buildings (modified after Ferlisi and Pisciotta, 2007, Pisciotta, 2008).

Damage typology	Loss range [%]	Damage class
No damage	0	D0
Non structural, light damage. Stability not compromised.	1 to 25	D1
Cracks in the walls, but the stability is not compromised. The repairs are not urgent (critical).	26 to 50	D2
Important deformation, fracture in the elements of the structure. Stability compromised. Unstable doors and windows. Necessary evacuation.	51 to 75	D3-D4
Collapse of building, from partial to total, that necessitates the evacuation of the site. The recovery is compromised.	76 to 100	

The used intensity parameter is PSInSAR projected velocity. In particular, four classes of intensity were distinguished considering the mean range of velocity for each level of damage related to a sample of 50 masonry buildings in the study area (Table 7.2).

The contents of Section 7.3 are published in:

D. Peduto, G. Pisciotta, S. Ferlisi, L. Arena , G. Fornaro , L. Cascini (2014). Il ruolo delle tecniche DInSAR nell'analisi del rischio da frana a cinematica lenta. In: La geotecnica nella difesa del territorio e delle infrastrutture dai rischi naturali Associazione Geotecnica Italiana, XXV - Convegno Nazionale di Geotecnica - Milano - Stresa (submitted).

The first class of intensity range from 0 to 1.5 mm/year, the second one up to 3 mm/year, the third one up to 6 mm/year and the forth greater than 0.

Tabella 7.2 Class of damage and average velocity of considered sample buildings within the study area.

Class of damage	Average velocity [mm/year]	Municipality
D2	3.00	Cerreto Sannita
D2	1.00	Cerreto Sannita
D2	1.70	Cerreto Sannita
D1	2.70	Cerreto Sannita
D2	2.70	Cerreto Sannita
D1	2.70	Cerreto Sannita
D1	2.70	Cerreto Sannita
D2	3.10	Guardia Sanframondi
D2	1.30	Guardia Sanframondi
D2	1.30	Guardia Sanframondi
D2	1.20	Guardia Sanframondi
D1	1.30	Guardia Sanframondi
D1	1.20	Guardia Sanframondi
D2	3.10	Guardia Sanframondi
D1	2.70	Guardia Sanframondi
D1	0.40	Guardia Sanframondi
D1	2.70	Guardia Sanframondi
D1	0.90	Guardia Sanframondi
D1	3.10	Guardia Sanframondi
D1	0.20	Guardia Sanframondi
D1	1.30	Guardia Sanframondi
D1	0.80	Guardia Sanframondi
D1	0.80	Guardia Sanframondi
D2	0.40	Guardia Sanframondi
D2	4.10	Guardia Sanframondi
D1	2.80	Guardia Sanframondi
D1	4.20	Guardia Sanframondi
D2	3.60	Guardia Sanframondi
D2	0.20	Guardia Sanframondi
D2	1.20	Guardia Sanframondi
D2	1.30	Guardia Sanframondi

D3-D4	7.00	Guardia Sanframondi
D1	0.20	San Lorenzo Maggiore
D2	1.00	Torrecuso
D2	0.90	Torrecuso
D3-D4	13.60	Pesco Sannita
D3-D4	3.10	Pesco Sannita
D3-D4	13.60	Pesco Sannita
D3-D4	3.10	Pesco Sannita
D3-D4	16.70	Pesco Sannita
D3-D4	16.70	Pesco Sannita
D1	1.50	Pesco Sannita
D1	2.00	Pesco Sannita
D2	2.70	San Giorgio La Molara
D2	1.00	San Giorgio La Molara
D2	1.20	San Giorgio La Molara
D2	0.90	San Giorgio La Molara
D2	2.00	San Giorgio La Molara
D1	1.70	Casalbore
D3-D4	4.20	Campolattaro

Following the procedure for the generation of fragility and vulnerability curves at medium scale (Figure 5.14), average velocity for each vulnerable area was computed according to equation 5.6 and then related to the relevant damage class. Figure 7.16 shows the average velocity reached for each level of damage. The average velocities of vulnerable areas increase as level of damage increases, even if a dispersion of the obtained values can be observed due to different reasons (e.g. the complexity of soil-structure interaction, different building characteristics, the relative position of vulnerable area within the landslide affected area as well as the subjectivity in drawing damage-recording sheets by different technicians).
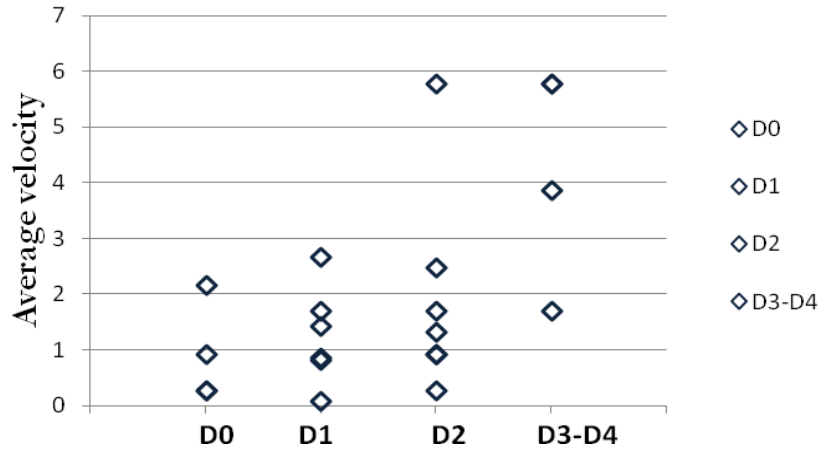
Figure 7.16 Average velocity of DInSAR data for each vulnerable area and related equivalent damage (modified after Cascini et al., 2014).

In the second phase, each fragility curve (Figure 7.18) was obtained by counting, for different values of computed class of intensity the number of vulnerable area out of the 27, that reached or exceeded a given damage level (Table 7.1 and Figure 7.17 a-d) and the relative cumulative probability (Figure 7.17 e-h).

Table 7.3 Number of vulnerable areas reaching a given damage class for each class of intensity.

Class of Intensity[mm/year]	Damage class (Di)	nr. of vulnerable area
I [up 1.5]	D1	9
	D2	4
	D3-D4	0
II [up to 3]	D1	14
	D2	7
	D3-D4	1
III [up to 6]	D1	18
	D2	11
	D3-D4	4
IV [up to >6]	D1	18
	D2	11
	D3-D4	4
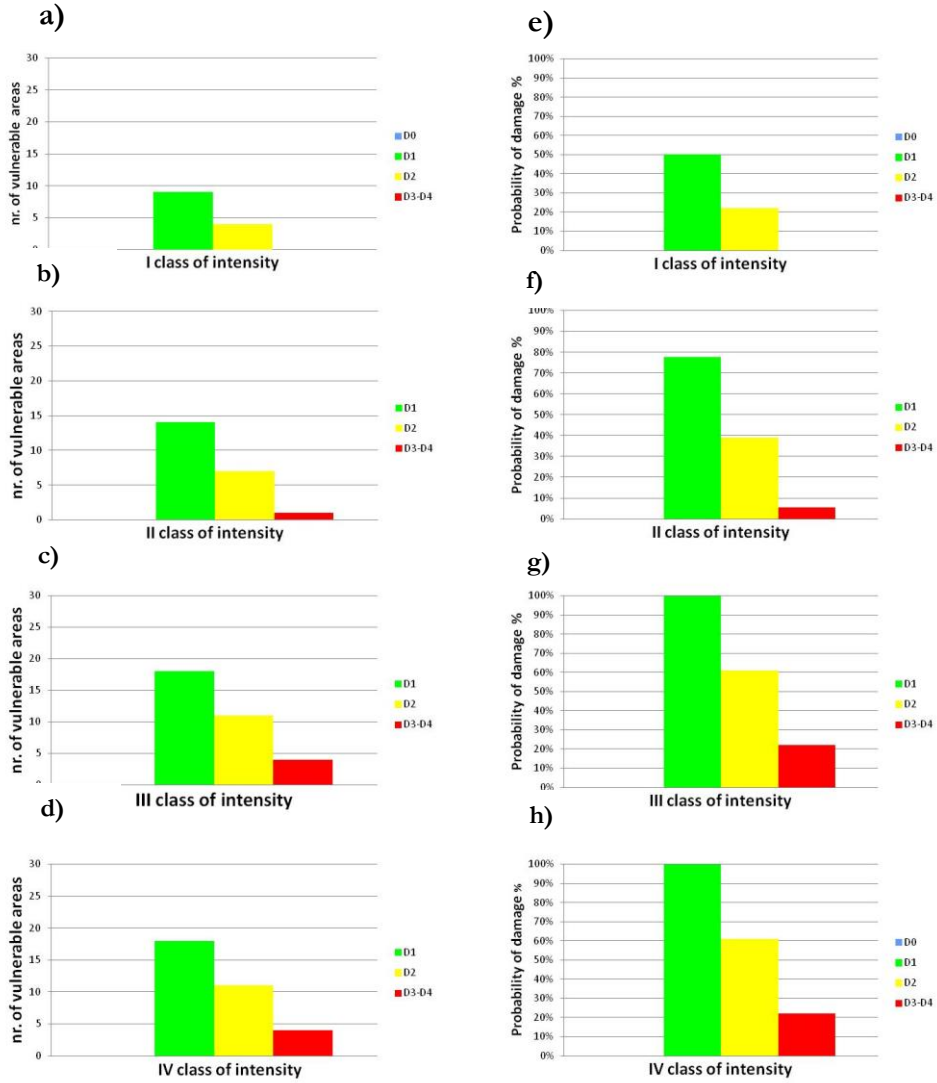
Figure 7.17 Number of vulnerable areas reaching damage class for each class of intensity and related probability.

144
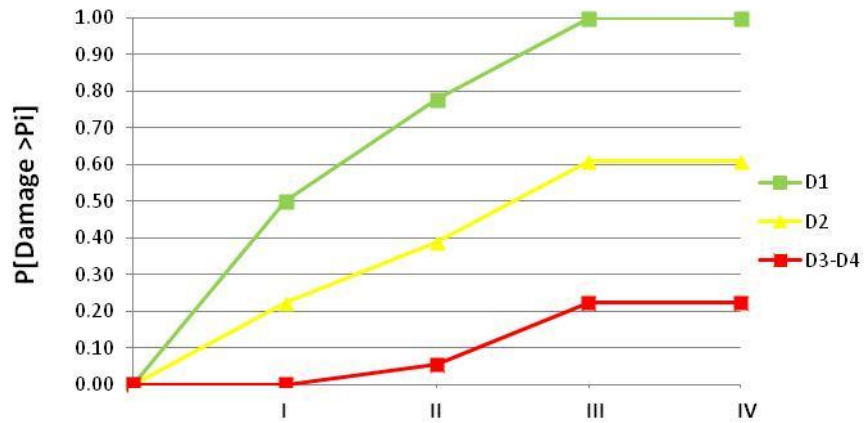
Figure 7.18 Fragility curves obtained for vulnerable area.

In the third step the vulnerability curve (Figure 7.20) was derived by computing the mean value of the damage for each intensity class, assumed as the most probable damage.
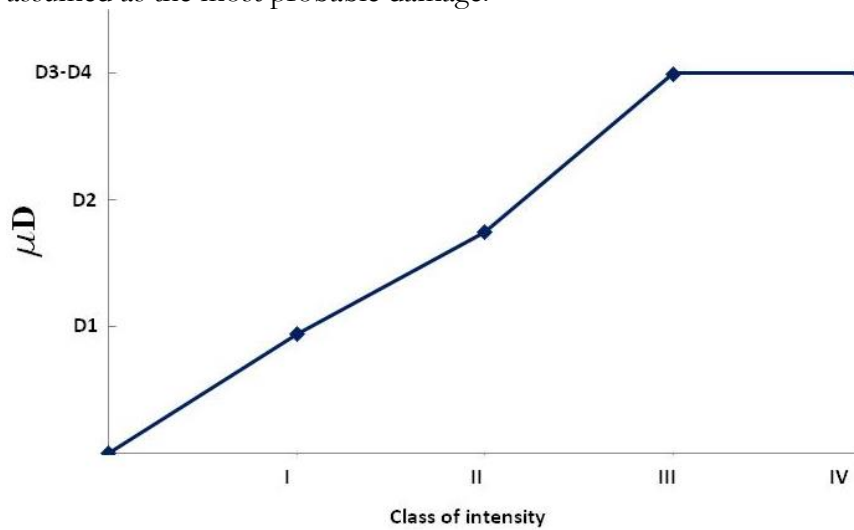
Figure 7.19 Vulnerability curve for vulnerable area.

The derived fragility and vulnerability curves can be used to predict the expected equivalent damage induced by slow-moving landslides to vulnerable areas. More precisely, once the average velocity of a given vulnerable area is computed, the fragility curves can be used to estimate

the probability of reaching or exceeding a given level of equivalent damage; on the other hand, the vulnerability curve (Figure 7.19) is useful to relate each class of intensity to the mean value of the equivalent damage. It is worth observing that the obtained curves are empirical, so the obtained results markedly depend on the quality and quantity of available data.

7.2 ANALYSIS AT LARGE SCALE

The selected test site for the analysis at large scale is an area located in the municipality of Ascea (Figure 7.20), extending for about 0.3 km^2, within Salerno Province (Campania region). In this area three active complex landslides (rotational slide – earthflow) and one creep zone were mapped at 1:5,000 scale on the basis of geomorphological criteria and in-situ investigations.

The preliminary phase, described in the framework of Figure 5.6, highlighted a full visibility of the area and a good coverage of DInSAR data. In particular, the PSInSAR data were derived from 46 and 79 ERS1/ERS2 images respectively acquired on ascending (September 1992 – September 2000) and descending (July 1992- January 2001) orbits. As a result, the number of available PS on ascending (9) and descending (43) orbits is quite different due to the aspect angle of the slope mainly facing South-West (Colesanti and Wasowski, 2006; Cascini et al., 2009).

As it is shown in Figure 5.7 the analysis at large scale can provide an insight into kinematics of the observed phenomenon. To this end, first of all, the prevailing movement direction was investigated via the

generation of two different maps derived from the interpolation of along-LOS velocity data on both orbits. These maps were, then, combined (Manzo et al., 2006) in order to compute the velocity along the up/down and east-west directions (Figures 7.21b and 7.21a).

Figure 7.20 The landsliding area within the municipal territory of Ascea (Salerno Province, southern Italy) and available PS data (modified after Cascini et al., 2011a,b).

The obtained results show that east-west displacement velocity values are fairly higher than up/down ones; these latter, on the other hand, attain the highest values in the heads of both the landslide phenomena and the creep zones. Moreover, the predominance of westbound (positive values stands for eastbound movements and negative values for westbound movements) can be related to the mainly translational movement of the landslide displaced masses, also taking into account the average slope angle lower than 45° (Cascini et al., 2010).

Following the same procedure and exploiting the available PSInSAR average velocity values derived from the RADARSAT1 satellite image dataset the analysis was then extended to 2003-2007 interval. For this period, both Figures 7.21e and 7.21f highlight, on the whole, an increase of the extension of the landslide affected areas with velocity values exceeding the movement threshold (2mm/year). As for up/down velocity values the increase is higher in the uphill zones.

With reference to the monitoring of facilities in landslide affected area, the knowledge acquired via the analysis of PSInSAR data was integrated with a damage survey. As a result, damages were recorded all over the investigated area. In this work the attention is focused on two buildings located, respectively, in the accumulation zone of the A-

labelled landslide (building nr. 1) and in the head of the B-labelled landslide (building nr. 2) which exhibited damages of different severity.

As for building nr. 1 (Figure 7.21 g), cracks were recorded starting from the corner of the building just in proximity of the windows. For the period 1992-2001 PSInSAR data on the building exhibit a cumulative settlement equal to 3 cm (Figure 7.21c). With reference to building nr. 2, which is currently abandoned, the PSInSAR-derived cumulative settlement, within the same period, equals 6 cm (Figure 7.21d). In this case the damage survey showed a far higher level of damage severity characterized by cracks distributed all over the structure and a tilted retaining wall near by the building.

These results point out that, all factors being equal, the position of the building within a given landslide-affected area can play a relevant role on physical vulnerability (Cascini et al., 2005; Pisciotta, 2008). In particular, in the portions of the landslide where the highest values of vertical velocity are usually recorded (i.e. upper portion of the displaced mass), the vulnerability of exposed buildings is higher than for those located in the landslide accumulation zone where the horizontal component of velocity vectors usually prevails.
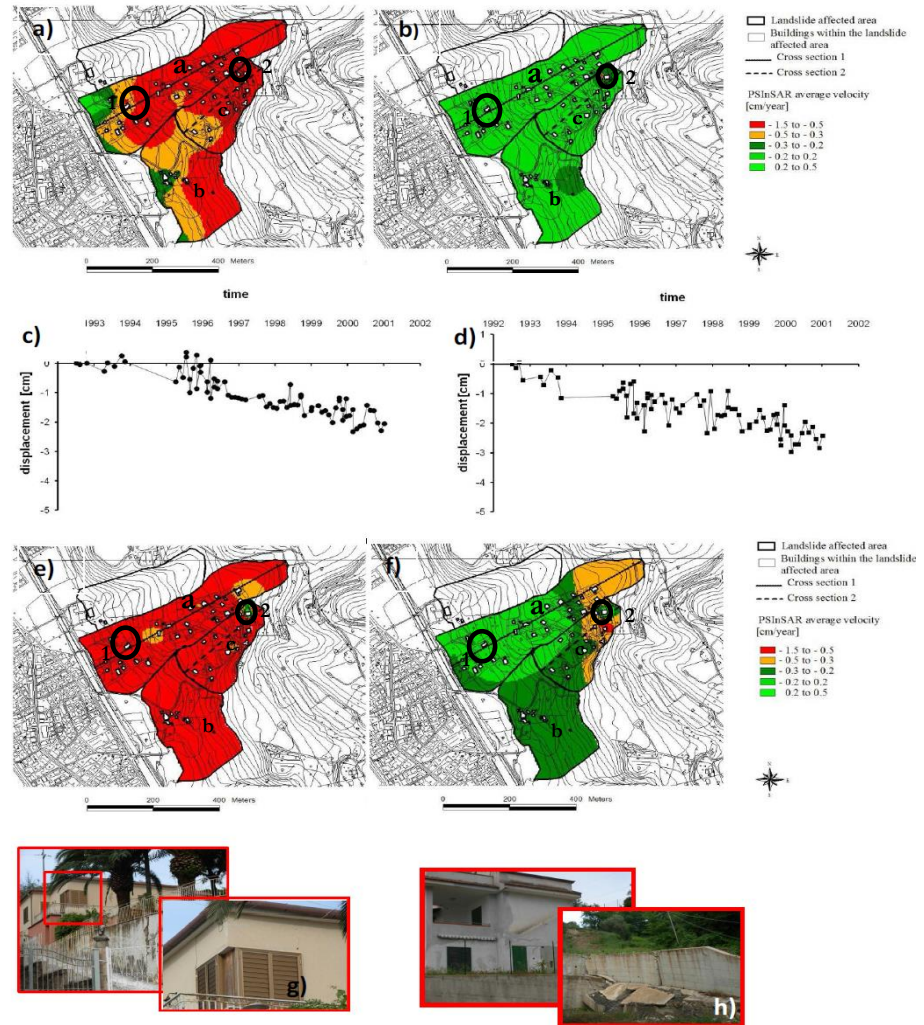
Figure 7.21 PSInSAR average velocities from ERS 1 and ERS2 data (time period spanning from July 1992 to January 2001) computed: a) in the horizontal direction (positive values stands for eastbound movements and negative values for westbound movements), b) in the vertical direction; c) PSInSAR-derived cumulative settlements of building nr. 1; d) PSInSAR-derived cumulative settlements of building nr. 2; e) PSInSAR average velocities from RADARSAT1 data computed, over the period 2003-2007, in the horizontal direction (positive values stands for eastbound movements and negative values for westbound movement); f) PSInSAR average velocities from RADARSAT1 data computed, over the period 2003-2007, in the vertical direction; g) photo of the building nr. 1 (dated May 2010); h) photo of the building nr. 2 (dated May 2010) (modified after Cascini et al., 2011).

8   CONCLUDING REMARKS

"Learn from yesterday, live for today, hope for tomorrow.
The important thing is not to stop questioning".
Albert Einstein

This PhD Thesis focused on the exploitation of DInSAR techniques to develop analyses in urban areas affected by subsidence or slow-moving landslides. The work started from a review of: the main features of the phenomena at hand (see Chapter 2); the related induced consequences to structures and infrastructures (see Chapter 3); the DInSAR techniques (see Chapter 4), stressing potentialities and limitations.
The complexity and inter-disciplinary character of the Thesis required the development of innovative methodological approaches (see Chapter 5), taking into account the appropriate management and interpretation of DInSAR data at different scales, so allowing the pursuit of different goals for both slow-moving landslides and subsidence phenomena (and associated effects). In particular, the conceived procedures were tested in different study areas of Campania Region in southern Italy (see Chapters 6 and 7, Appendix D) with the main aims of: characterizing slow-moving landslides and subsidence phenomena at different scales; predicting the consequences on the buildings with them interacting.

As far as the analysis of subsidence phenomena at small scale is concerned (Section 6.1), once validated DInSAR (high resolution) data were used to detect – by using computational grids of 250 m spacing – the subsiding areas of the Campania region with reference to a time frame spanning from 1992 up to 2010. The end-product of this activity (i.e., a map at 1:250.000 scale) can be useful to inform policy makers and general public since, in Italy, official Plan of subsiding areas (as a matter of fact, at every scale) are not yet available.
At the medium scale (Section 6.2) the analyses were carried out with reference to one of the most subsidence-affected areas of the Campania region, i.e. Campanian Plain, as highlighted by the analysis at small scale. In such a case, the analyses were mainly aimed at detecting and ranking –

on the basis of the Subsiding Municipality Index – the subsidence-affected municipalities of the Campania Plain that primarily need further in-depth analyses (at large scale) in order to predict and prevent damage to the exposed buildings. The results obtained – by using computational grids of 100 m spacing – can be used by regional and provincial Authorities in charge of the land resource management as well as by technicians for evaluating possible constraints in the development of large engineering projects (see Appendix D).

At large scale (Section 6.3) the analyses dealing with the urbanized areas of two Municipalities (i.e., Sarno and Baronissi, both in Salerno Province) where devoted to generate – by using computational grids of 10 m spacing – newly conceived relative rotation maps able to detect critical zones, i.e. where damage to buildings are most likely to occur. The obtained results were validated on the basis of information gathered via field surveys. The above maps are useful for urban planning purposes (e.g. to select the zones suitable for developments) or to individuate the most appropriate countermeasures to mitigate the subsidence risk to properties.

At detailed scale (Section 6.4 and Appendix D) the analyses allowed the investigation of the building response to ground movements via deriving the maximum values attained by some relevant parameters to be used in damageability criteria widely adopted in engineering practice. In this regard, it is worth remembering that these criteria (e.g. Skempton and MacDonald, 1956) are based on the observation of a limited number of case studies on real buildings; consequently, it seems possible that the current practice of building damageability forecasting could be valuably improved by taking advantage of the huge number of buildings for which settlement information can be derived from DInSAR data analysis.

With reference to slow-moving landslides the conceived procedures, based on the joint use of DInSAR data and damage survey, were developed in order to update the available inventory maps as well as to generate fragility/vulnerability curves. The procedures were tested in an area (557 km^2) chosen within the territory of the National Basin Authority of Liri-Garigliano and Volturno rivers, including 21 Municipalities and 2 Provinces (Benevento and Avellino).

As for the updating of slow-moving landslide inventory maps (Section 7.1.2), it must be preliminary observed that the scale of analysis

corresponds to that of the available landslide inventory maps (1:25,000). This scale called for some necessary pre-processing of both DInSAR and damage data prior to merging them into a so-called DInSAR-Damage matrix due to their point-wise characteristic.

The current limits to the application of the described methodology are mainly related to the availability of: DInSAR data on landslides (depending on vegetation, aspect, slope, the projected velocity value); thematic maps (geomorphological map, landslide inventory map); damage survey results. Therefore, the number of landslides whose state of activity can be updated can turn out to be limited. In this regard, it is worth stressing that future improvements concerning both ground resolution and reduced revisiting time will allow an increased DInSAR coverage over landslide affected areas. In addition, preliminary damage surveys carried out for the purpose of analyses at 1:25,000 scale could also benefit from the use of high resolution optical sensors, thus significantly reducing the number of facilities to be investigated. As for the updating of the inventory map the aforementioned enhancements could result in fostering the use of the DInSAR-Damage matrix since they will widen the sample of the landslides to which it can be applied. The validation tests of the matrix carried out up to now, although still limited due the extension of the study area, encourage future tests to better enquire about the reliability of the results. Moreover, the use of the matrix seems helpful in planning more expensive conventional surveys only with reference to around 30% of the analysed phenomena (i.e. those appointed as "in-situ surveys required"). Finally, the procedure adopted for the detection of unmapped phenomena tried to take advantage of the information contained in the available geomorphological map using remote sensing data. As a result, several areas which are likely to be affected by landslide phenomena were selected. In this regard, a further step will deal with the joint application of Object Based Image Analysis techniques which are currently considered as the most promising ones for the digital recognition of landslides especially when thematic maps are not available.

As for the analysis of consequences (Section 7.1.3), an innovative methodological approach to derive fragility and vulnerability curve at medium scale was proposed. The obtained result can integrate the current practice in land use planning and management in order to predict damages to buildings interacting with slow-moving landslide using the parameter of intensity derived by DInSAR data and to update the

existing official maps within the "Hydrogeological Setting Plans" (Italian Law 365/2000). In particular, once computed the velocity of vulnerable areas, the fragility curves can be used to assess the probability of reaching or exceeding a given class of damage; on the other hand, vulnerability curve are useful to relate the mean of equivalent damage to each class of intensity.

Finally, it is worth stressing that the ultimate higher resolution sensor data acquired with reduced revising time and the increasingly advanced image processing algorithms will provide end-users and scientists with a huge dataset which will foster the use of the procedure presented in this PhD Thesis.

REFERENCE

Agostini A., Tofani V., Nolesini T., Gigli G., Tanteri L., Rosi A., Cardellini S, Casagli N (2013). *A new appraisal of the Ancona landslide based on geotechnical investigations and stability modelling.* Quarterly Journal of Engineering Geology and Hydrogeology, pp. 1-10, ISSN:1470-9236.

Allen D. R. and Mayuga M. N. (1969). The mechanics of compaction and rebound, Wilmington oil field, Long Beach, California, USA.Land Subsidence, v. 2, Internat.Assoc. Sci. Hydrology Pub. 89, L. J. Tison, ed., pp. 410-422.

Amelung, F., Galloway, D.L., Bell, J.W., Zebker, H.A.,Laczniak, R.J. (1999). *Sensing the ups and downs of Las Vegas:InSAR reveals structural control of land subsidence and aquifersystemdeformation.* Geology, 27 (6), pp. 483-486.

Angeli M.G., Gasparetto P., Pasuto A. and Silvano S. (1989)-Examples of landslides instrumentation (Italy). Proceesings of the 12th International Conference on Soil Mechanics and Foundation Engineering, Rio de Janiero, v.3., p. 1531-1534.

Antronico L., Ferrari E., Gullà G., Sorriso-Valvo M., Tansi C., Terranova o, ACeto L., Niceforo D. (2003). *Linee guida per interventi di stabilizzazione di pendii in aree urbane da riqualificare.* Regione Calabrisa-P.O.P. 1994/99.

Arangio S., Calò F., Di Mauro M., Bonano M., Marsella M. and Manunta M. (2013). An application of the SBAS-DInSAR technique for the assessment of structural damage in the city of Rome. Structure and Infrastructure Engineering, (ahead-of-print), 1-15.

Arena L., Cascini L., Ferlisi S., Galluccio F., Giulivo I., Matano F., Peduto D. (2012). Analisi di frane lente in area urbana con il contributo dei dati PS-InSAR: il caso di Castelpagano (BN). Incontro Annuale dei Ricercatori di Geotecnica - IARG Padova 2-4 luglio 2012 Rubano (PD) Grafiche Turato Edizioni Pag.1-6 ISBN:9788889524671.

Arena L., Peduto D., Ferlisi S., Cascini L., Fornaro G. (2013). Un esempio di impiego di dati DInSAR a media e alta risoluzione in aree urbanizzate subsidenti. Incontro Annuale dei Ricercatori di Geotecnica Perugia 16-18 settembre 2013

PERUGIA UNIVERSITÀ DEGLI STUDI DI PERUGIA PAG.1-6 ISBN:9788890642135.

ASCIONE L., CASCINI L, SORBINO G., PEDUTO D., ARENA L., GIORDANO A.,

SPADEA S. (2011) *SULL'ANALISI GEOTECNICA E STRUTTURALE DEGLI EDIFICI AFFERENTI AL PIANO PEEP IN LOCALITÀ CARITI NEL COMUNE DI BARONISSI*. RELAZIONE TECNICA.

AUDELL H.S.(1996). GEOTECHNICAL NOMENCLATURE AND CLASSIFICATION SYSTEM FOR CRACK PATTERNS IN BUILDINGS. ENVIRONMENTAL AND ENGINEERING GEOSCIENCE, 2, 225–248.

ANGELI M.G., GASPARETTO P., PASUTO A. AND SILVANO S. (1989). EXAMPLES OF LANDSLIDE INSTRUMENTATIONS (ITALY). PROCEEDINGS OF THE 12 TH INTERNATIONAL CONFERENCE ON SOIL MECHANISM AND FOUNDATION ENGINEERING. RIO DE JANIERO, v.3., PP. 1531-1534.

BEEBY A. W. AND MILES J. R. (1969). PROPOSALS FOR THE CONTROL OF DEFLECTION IN THE NEW UNIFIED CODE. CONCRETE, 3(3), 101–110.

BELL F.G. (1994). FUNDAMENTALS OF ENGINEERING GEOLOGY. BLACKIE ACADEMIC AND PROFESSIONAL.

BERARDINO P., FORNARO G., LANARI R. AND SANSOSTI E (2002) A NEW ALGORITHM FOR SURFACE DEFORMATION MONITORING BASED ON SMALL BASELINE DIFFERENTIAL SAR INTERFEROGRAMS.IEEE TRANS. GEOSCI. REMOTE SENS., 40(11),2375–2383.

BERARDINO P., COSTANTINI M, FRANCESCHETTI G., IODICE A, PIETRANERA, L, RIZZO V. (2003). *USE OF DIFFERENTIAL SAR INTERFEROMETRY IN MONITORING AND MODELLING LARGE SLOPE INSTABILITY AT MARATEA (BASILICATA,ITALY)*. ENGINEERING GEOLOGY , 68: 31-51

BERTINI T., CUGUSU F., D'ELIA B. AND ROSSI-DORIA M. (1986) .LENTI MOVIMENTI DI VERSANTE NELL'ABRUZZO ADRIATICO: CARATTERI E CRITERI DI STABILIZZAZIONE., XVI CONVEGNO NAZIONALE DI GEOTECNICA.

BERTOLINI G., GUIDA M. AND PIZZAIOLO M.(2005). LANDSLIDES IN EMILIA-ROMAGNA REGION (ITALY): STRATEGIES FOR HAZARD ASSESSMENT AND RISK MANAGEMENT. LANDSLIDES, 2, 302–312.

BIANCHINI S., CIGNA F., RIGHINI G., PROIETTI C. AND CASAGLI N. (2012). *LANDSLIDE HOTSPOT MAPPING BY MEANS OF PERSISTENT SCATTERER INTERFEROMETRY*.ENVIRON. EARTH SCI., 67, 1155–1172, 2012.

BIRD J. F., CROWLEY, H. PINHO, R. AND BROMMER J. J. (2005A). *ASSESSMENT OF BUILDING RESPONSE TO LIQUEFACTION-INDUCED DIFFERENTIAL GROUND DEFORMATIONS*. BULL. NEW ZEALAND SOC. EARTHQ. ENG.,38(4), 20 PP., 2005A.

BIRD J. F., BROMMER J. J., CROWLEY H., AND PINHO R. (2005B). *MODELLING LIQUEFACTION-INDUCED BUILDING DAMAGE IN EARTHQUAKE LOSS ESTIMATION*. SOIL DYN. EARTHQ. ENG., 26, 15–30.

BJERRUM L.(1963). ALLOWABLE SETTLEMENT OF STRUCTURES.PROCEEDINGS OF THE 3RD EUROPEAN CONF. ON SOIL MECH. AND FOUND. ENGNG, WIESBADEN, 2, BRIGHTON, ENGLAND, 135–137, 1963.

BONNARD CH, TACHER L, BENISTON M (2008) *PREDICTION OF LANDSLIDE MOVEMENTS CAUSED BY CLIMATE CHANGE: MODELLING THE BEHAVIOUR OF A MEAN ELEVATION LARGE SLIDE IN THE ALPS AND ASSESSING ITS UNCERTAINTIES*. CHEN ET AL (EDS) PROCEEDINGS,10TH INTERNATIONAL SYMPOSIUM ON LANDSLIDES AND ENGINEERED SLOPES, XI'AN,CHINA, 1:217–227.

BOOKER J.R., SMALL J.C. AND CARTER, J.P. (1985). PREDICTION OF SUBSIDENCE CAUSED BY PUMPING OF GROUNDWATER. 21ST CONGRESS OF THE INTERNATIONAL ASSOCIATION OF HYDRAULIC ENGINEERING AND RESEARCH, MELBOURNE P. 130-134.

BOONE S. J.(2006). GROUND-MOVEMENT-RELATED BUILDING DAMAGE. J.GEOTECH. ENG.-ASCE, 122(11), 886–896.

BOSCARDIN M. D. AND CORDING, E. G.(1989). BUILDING RESPONSE TO EXCAVATION INDUCED SETTLEMENT, J. GEOTECH. ENG.-ASCE, 115, 1–21.

BURD H. J., HOULSB G. T., AUGARDE C. E. AND LIU, G.(2000). *MODELLING TUNNELLING-INDUCED SETTLEMENT OF MASONRY BUILDINGS*. PROC. INSTITUTION OF CIVIL ENGINEERS, GEOTECH. ENGNG, PAPER 11831, 143,17–29.

BURLAND J.B. AND WROTH C.P. (1974). *SETTLEMENT OF BUILDINGS AND ASSOCIATED DAMAGE*. SOA REVIEW. PROC. CONF. SETTLEMENT OF STRUCTURES, CAMBRIDGE, PENTECH PRESS, LONDON, PP 611-654.

BURLAND J.B., BROMS B.B. AND DE MELLO V.F.B. (1977). *BEHAVIOUR OF FOUNDATIONS AND STRUCTURES*. SOA REPORT. PROC. 9TH INT. CONF. SMFE, TOKYO, VOL. 2; PP 495-546.

BURLAND, J. B. (1995). ASSESSMENT OF RISK OF DAMAGE TO BUILDINGS DUE TO TUNNELLING AND EXCAVATION. INVITED SPECIAL LECTURE. IN: 1ST INT. CONF. ON EARTHQUAKE GEOTECH. ENGINEERING, IS.TOKYO '95.

CALDERHEAD A. I., THERRIEN R., RIVERA A., MARTEL R. AND GARFIAS J. (2011). SIMULATING PUMPING-INDUCED REGIONAL LAND SUBSIDENCE WITH THE USE OF INSAR AND FIELD DATA IN THE TOLUCA VALLEY, MEXICO. ADVANCES IN WATER RESOURCES,34(1), 83-97.

CANUTI P., CASAGLI N., FARINA P., FERRETTI A., MARKS F., MENDUNI G.(2006). ANALISI DEI FENOMENI DI SUBSIDENZA NEL BACINO DEL FIUME ARNO MEDIANTE INTERFEROMETRIA RADAR. GIORNALE DI GEOLOGIA APPLICATA 4 (2006) 131-136, DOI: 10.1474/GGA.2006-04.0-17.0145.

CARRARA A. (1983). A MULTIVARIATE MODEL FOR LANDSLIDE HAZARD EVALUATION. MATHEMATICAL GEOLOGY, 15: 403-426.

CASCINI L., GULLÀ G. (1992A). ANALISI DI DETTAGLIO DELLE CARATTERISTICHE FISICO MECCANICHE DEI TERRENI PRODOTTI DALL'ALTERAZIONE DEGLI GNEISS DI S. PIETRO IN GUARANO (CS).GEOLOGI APPLICATA E IDROGEOLOGIA, VOL. XXVII, PP 49-76.

CASCINI L., GULLÀ G. (1992B). *GRADO DI ALTERAZIONE E MACCANISMI DI ROTTURA NEI TERRENI PRODOTTI DALL'ALTERAZIONE DEGLI GNEISS DI S. PIETRO IN GUARANO* (CS).RISULTATI PRELIMINARI. CNR-IRPI, RAPPORTO INTERNO N.363.

CASCINI L. AND DI MAIO C. (1994). *EMUNGIMENTO DELLE ACQUE SOTTERRANEE E CEDIMENTI NELL'ABITATO DI SARNO: ANALISI PRELIMINARE.* RIVISTA ITALIANA DI GEOTECNICA, N. 3, 217-231.

CASCINI L.(2002). IL RISCHIO DA FRANA IN AREE URBANE DELL'APPENNINO CENTRO-MERIDIONALE. XXI CONVEGNO NAZIONALE DI GEOTECNICA, L'AQUILA PP.127-134.

CASCINI L., GULLÀ G., SORBINO G. (2006). GROUNDWATER NODELLING OF A WEATHERED GNEISS COVER. CANADIAN GEOTHECNICAL JOURNAL 43 (11), PP. 1153-1166.

CASCINI L.; GULLA' G; SORBINO G. (2006A).*GROUNDWATER MODELLING OF A WEATHERED GNEISSIC COVER.* CANADIAN GEOTECHNICAL JOURNAL. VOL. 43(11). PAG.1153-1166 ISSN:0008-3674.

CASCINI, L., FERLISI, S., FORNARO, G., LANARI, R., PEDUTO D. AND ZENI G. (2006B). SUBSIDENCE MONITORING IN SARNO URBAN AREA VIA MULTITEMPORAL DINSAR TECHNIQUE. INTERNATIONAL JOURNAL OF REMOTE SENSING, 27 (8), 1709-1716.

CASCINI L., FERLISI S., PEDUTO D., DI NOCERA S., FORNARO G. AND SERAFINO F. (2007A). A LAND SUBSIDENCE STUDY VIA DINSAR TECHNIQUE OVER LARGE URBANISED AREAS. PROC. URBAN REMOTE SENSING JOINT EVENT. PARIS 11-13 APRIL (CD-ROM).

CASCINI L., FERLISI S., PEDUTO D., FORNARO G. AND MANUNTA M. (2007B). ANALYSIS OF A SUBSIDENCE PHENOMENON VIA DINSAR DATA AND GEOTECHNICAL CRITERIA. ITALIAN GEOTECHNICAL JOURNAL, 4, 50-67.

CASCINI L., FERLISI S., PEDUTO D., PISCIOTTA G., DI NOCERA S.AND FORNARO G. (2009) MULTITEMPORAL DINSAR DATA AND DAMAGE TO FACILITIESAS INDICATORS FOR THE STATE OF ACTIVITY OF SLOW-MOVING LANDSLIDES. LANDSLIDES AND ENGINEERED SLOPES – FROM THE PAST TOTHE FUTURE, EDITED BY: CHEN, Z., ZHANG, J., LI, Z., WU, F., ANDHO, K., PROCEEDINGS OF THE 10TH INTERNATIONAL SYMPOSIUM ON LANDSLIDES AND ENGINEERED SLOPES, 30 JUNE-4 JULY 2008, XI'AN(CHINA), CRC PRESS, 2, 1103–1109, 2008.

CASCINI L., FORNARO G. AND PEDUTO D.(2009). ANALYSIS AT MEDIUM SCALE OF LOW-RESOLUTION DInSAR DATA IN SLOW-MOVING LANDSLIDE AFFECTED AREAS. ISPRS J. PHOTOGRAM. REMOTE SENS., 64, 598–611.

CASCINI L., FORNARO G. AND PEDUTO, D.(2010A). ADVANCED LOW- AND FULLRESOLUTION DInSAR MAP GENERATION FOR SLOW-MOVING LANDSLIDE ANALYSIS AT DIFFERENT SCALES. ENG. GEOL., 112, 29–42.

CASCINI L., CALVELLO M., GRIMALDI G.M. (2010B). GROUNDWATER MODELING FOR THE ANALYSIS OF ACTIVE SLOW-MOVING LANDSLIDES. JOURNAL OF GEOTECHNICAL AND GEOENVIRONMENTAL ENGINEERING. VOL. 136. PAG.1220-1230 ISSN:1090-0241.

CASCINI L., FERLISI S., PEDUTO D., ARENA L., FORNARO G. (2011A).MONITORAGGIO CON TECNICHE SATELLITARI DI AREE URBANIZZATE IN SUBSIDENZA. INNOVAZIONE TECNOLOGICA NELL'INGEGNERIA GEOTECNICA NAPOLI 22-24 GIUGNO 2011 ROMA ASSOCIAZIONE GEOTECNICA ITALIANA VOL.2, PAG.657-664 ISBN:9788897517047.

CASCINI L., FERLISI S., PEDUTO D., ARENA L.(2011B). TECNICHE INNOVATIVE SATELLITARI NEL MONITORAGGIO DI OPERE INTERAGENTI CON FRANE A CINEMATICA LENTA. INNOVAZIONE TECNOLOGICA NELL'INGEGNERIA GEOTECNICA NAPOLI 22-24 GIUGNO 2011 ROMA ASSOCIAZIONE GEOTECNICA ITALIANA VOL.2, PAG.665-672 ISBN:9788897517047.

CASCINI L., FERLISI S., PEDUTO D., FORNARO G. (2011C). THE USE OF DINSAR TECHNIQUES TO ANALYSE GROUND DEFORMATIONS AND RELATED EFFECTS TO BUILDINGS. IN: FIFTH INTERNATIONAL SYMPOSIUM ON DEFORMATION CHARACTERISTICS OF GEOMATERIALS SEOUL (COREA DEL SUD) 1-3 SETTEMBRE 2011 HANRIMWON CO., LTD. EDITION. VOL.2, PAG.1239-1246 ISBN:9788957082065.

CASCINI L., FERLISI S., PEDUTO D., ARENA L. (2011D). L'IMPIEGO DI DATI DInSAR NELLA CARATTERIZZAZIONE A SCALA DI BACINO DI FENOMENI FRANOSI A CINEMATICA LENTA. INCONTRO ANNUALE DEI RICERCATORI DI GEOTECNICA 2011 - IARG 2011 TORINO, 4 -6 LUGLIO 2011.

CASCINI L., FERLISI S., PEDUTO D., ARENA L., FORNARO G. (2011E). UN APPROCCIO MULTISCALARE PER L'USO DEI DATI DInSAR NELL'ANALISI DI FENOMENI DI SUBSIDENZA IN AREE URBANE. INCONTRO ANNUALE DEI RICERCATORI DI GEOTECNICA - IARG TORINO 4-6 LUGLIO 2012 PAG.1-6.

CASCINI L. (2012).CURATORE/I DI CRITERI DI ZONAZIONE DELLA SUSCETTIBILITÀ E DELLA PERICOLOSITÀ DA FRANE INNESCATE DA

EVENTI ESTREMI (PIOGGE E SISMA). DI PADOVA. COMPOSERVICE S.R.L. PAG.1-439 ISBN:9788890687334.

CASCINI L., PEDUTO D., REALE D., ARENA L., FERLISI S., VERDE S., FORNARO G., (2013A). DETECTION AND MONITORING OF FACILITIES EXPOSED TO SUBSIDENCE PHENOMENA VIA PAST AND CURRENT GENERATION SAR SENSORS. JOURNAL OF GEOPHYSICS AND ENGINEERING, 10.6 (2013): 064001.

CASCINI L., PEDUTO D., PISCIOTTA G., ARENA L., FERLISI S. AND FORNARO G. (2013B). THE COMBINATION OF DINSAR AND FACILITY DAMAGE DATA FOR THE UPDATING OF SLOW-MOVING LANDSLIDE INVENTORY MAPS AT MEDIUM SCALE. NAT. HAZARDS EARTH SYST. SCI., 13, 1527-1549, DOI:10.5194/NHESS-13-1527-2013.

CATANI F., CASAGLI N., ERMINI L., RIGHINI G. AND MENDUNI G. (2005). *LANDSLIDE HAZARD AND RISK MAPPING AT CATCHMENT SCALE 2005 ARNORIVER BASIN*. LANDSLIDES, 2, 329–342, 2005.

CHATTERJEE RS, FRUNEAU B, RUNDANT JP, ROY PS, FRISON P-L, LAKHERA RC, DADHWAL VK, SAHA R (2006). SUBSIDENCE OF KOLKATA (CALCUTTA) CITY. INDIA DURING THE 1990S AS OBSERVED FROM SPACE BY DIFFERENTIAL SYNTHETIC APERTURE RADAR INTERFEROMETRY(D-INSAR) TECHNIQUE. REMOTE SENS ENVIRON 102:176–185.

CHOROWICZ, J., LUXEY, P., RUDANT, J. P., LYBERIS, N., YÜRÜR, T.,GÜNDOGDU, N. (1995). *SLIP-MOTION ESTIMATION ALONG THE OVACIKFAULT NEAR ERZINCAN (TURKEY) USING ERS-1 RADAR IMAGE:EVIDENCE OF IMPORTANT DEFORMATION INSIDE THE TURKISH PLATE*. REMOTE SENSING OF ENVIRONMENT, 52, PP. 66-70.

CIGNA F., DEL VENTISETTE C., LIGUORI V. AND CASAGLI N. *ADVANCED RADAR-INTERPRETATION OF INSAR TIME SERIES FOR MAPPING AND CHARACTERIZATION OF GEOLOGICAL PROCESSES*. NAT. HAZARDS EARTH SYST.SCI., 11, 865—881, DOI:10.5194/NHESS-11-865-2011, 2011.

CIGNA F., BIANCHINI S., CASAGLI N. (2012).HOW TO ASSESS LANDSLIDE ACTIVITY AND INTENSITY WITH PERSISTENT SCATTERER INTERFEROMETRY (PSI): THE PSI-BASED MATRIX APPROACH. LANDSLIDES, DOI: 10.1007/S10346-012-0335-7.

CLEMENTINO RV, PROUDFOOT DW, LAW DJ, SKIRROW R (2008) *EMBANKMENT SLOPE STABILIZATION USING SUBHORIZONTAL DRAINS AT HIGHWAY 39 NEAR DRAYTON VALLEY*. ALBERTA PROCEEDINGS, 4TH CANADIAN CONFERENCE ON GEOHAZARDS, QUEBEC, CANADA:511–517.

COCCO E., DE MAGISTRIS M. A., BENTIVOGLIO C., IACONE Y., SERPICO M. (1993). *PROCESSI EROSIVI, OPERE DI DIFESA E RIEQUILIBRIO DEI LITORALI IN CAMPANIA*. LA DIFESA DEI LITORALI IN ITALIA, 34, 175 - 194. EDIZIONI DELLE AUTONOMIE.

COLESANTI, C., FERRETTI, A., NOVALI, F., PRATI, C., ROCCA, F. (2003). SAR MONITORING OF PROGRESSIVE AND SEASONAL GROUNDDEFORMATION USING THE PERMANENT SCATTERERS TECHNIQUE. IEEETRANSACTIONS ON GEOSCIENCE AND REMOTE SENSING, 41 (7), PP.1685-1701.

COLESANTI C. AND WASOWSKI J. (2006). INVESTIGATING LANDSLIDES WITH SPACEBORNESYNTHETIC APERTURE RADAR (SAR) INTERFEROMETRY. ENG.GEOL., 88, 173–199.

COOPER A.H., (2008). THE CLASSIFICATION, RECORDING, DATABASING AND USE OF INFORMATION ABOUT BUILDING DAMAGE CAUSED BY SUBSIDENCE AND LANDSLIDES. QUARTERLY JOURNAL OF ENGINEERING GEOLOGY AND HYDROGEOLOGY, 41(3), 409-424.

CORNIELLO, DUCCI, TRIFUOGGI (2010). *HYDROLOGY AND HYDROGEOCHEMISTRY OF THE PLAIN BETWEEN MT. MASSICO AND THE RIVER VOLTURNO.* ITALIAN JOURNAL OF ENGINEERING GEOLOGY AND ENVIRONMENT, 1.

COSTANTINI M., FALCO S., MALVAROSA F., MINATI F. (2008). A NEW METHOD FOR IDENTIFICATION AND ANALYSIS OF PERSISTENT SCATTERERS IN SERIES OF SAR IMAGES. IEEE INTERNATIONAL GEOSCIENCE & REMOTE SENSING SYMPOSIUM, JULY 6-11, 2008, BOSTON, MASSACHUSETTS, U.S.A, PP. 449-452.

COTECCHIA F. (1989). STUDIO DI UN MOVIMENTO FRANOSO NELLE UNITÀ IRPINE DELL'ALTA VALLE DELL'OFANTO. RIVISTA ITALIANA DI GEOTENICA, 2, 57-84.

COTECCHIA, V., (2006). THE SECOND HANS CLOOS LECTURE. EXPERIENCE DRAWN FROM THE GREAT ANCONA LANDSLIDE OF 1982. BULLETIN OF ENGINEERING GEOLOGY AND THE ENVIRONMENT, 65, 1–41.

CRESCENTI U., CIANCETTI G.F., COLTORTI M., DRAMIS F, GENTILI B., MELIDORO G., NANNI T., PAMBIANCHI G., RAINONE M.L., SEMENZA E., SORRISO-VALVO M, TAZIOLI G.S. (1983) - *LA GRANDE FRANA DI ANCONA DEL 1982* - ATTI XV CONVEGNO NAZIONALE DI GEOTECNICA. SPOLETO. ATTI CONGR. VOL. III.

CROSETTO, M., M. CASTILLO AND R. ARBIOL (2003). *URBAN SUBSIDENCE MONITORING USING RADAR INTERFEROMETRY: ALGORITHMS AND VALIDATION.* PHOTOGRAMMETRIC ENGINEERING AND REMOTE SENSING.

CROSETTO M, CRIPPA B AND BIESCAS E (2005). EARLY DETECTION AND IN-DEPTH ANALYSIS OF DEFORMATION PHENOMENA BY RADAR INTERFEROMETRY. ENGINEERING GEOLOGY, 79, 81-91.

CRUDEN D.M., VARNES D.J. (1996). LANDSLIDE TYPES AND PROCESSES. LANDSLIDES: INVESTIGATION AND MITIGATION. TRANSPORTATION

RESEARCH BOARD, SPECIAL REPORT NO. 247, NATIONAL RESEARCH COUNCIL, NATIONAL ACADEMY PRESS, WASHINGTON DC, USA 36-75.

CZUCHLEWSKI K., WEISSEL J. AND KIM Y. (2003). *POLARIMETRIC SYNTHETIC APERTURE RADAR STUDY OF THE TSAOLING LANDSLIDE GENERATED BY THE 1999 CHI-CHI EARTHQUAKE, TAIWAN*. JOURNAL OF GEOPHYSICAL RESEARCH 108: DOI: 10.1029/2003JF000037. ISSN: 0148-0227.

D'ELIA B., ESU F., PELLEGRINO A., AND PESCATORE T. S. (1985). *SOME EFFECTSON NATURAL SLOPE STABILITY INDUCED BY 1980 ITALIAN EARTHQUAKE*. PROCEEDINGS OF THE 11TH INTERNATIONAL CONFERENCE ON SOILMECHANICS AND FOUNDATION ENGINEERING, SAN FRANCISCO, 4, 1943–1949.

DI MARTIRE D., RAMONDINI M., CALCATERRA D., NIRCHIO F. (2013). *RISULTATI PRELIMINARI DEL MONITORAGGIO INTERFEROMETRICO DI UNA FRANA A CINEMATICA LENTA MEDIANTE DIFFERENTI SENSORI SAR IN BANDA X* . INCONTRO ANNUALE DEI RICERCATORI DI GEOTECNICA PERUGIA 16-18 SETTEMBRE 2013 PERUGIA UNIVERSITÀ DEGLI STUDI DI PERUGIA PAG.1-6 ISBN:9788890642135.

DI ROSARIO A. (2002). RELAZIONE GEOLOGICA-TECNICA.

DLUGOLECKI A. (2004). A CHANGING CLIMATE FOR INSURANCE. A SUMMARY REPORT FOR CHIEF EXECUTIVES AND POLICYMAKERS. ASSOCIATION OF BRITISH INSURERS.

DUMOVA-JOVANOSKA, E. (2004) *FRAGILITY CURVES FOR RC STRUCTURES IN SKOPJE REGION*. PROCEEDINGS OF THE 13TH WORLD CONFERENCE ON EARTHQUAKE ENGINEERING, VANCOUVER, CANADA, PAPER NO. 3.

EEA, EUROPEAN ENVIROMENTAL AGENCY, (2012). CLIMATE CHANGE, IMPACTS AND VULNERABILITY IN EUROPE 2012. AVAILABLE ON LINE, LAST ACCESS: 25/01/2013.

ESA, EUROPEAN SPACE AGENCY (2013). EDUSPACE. HTTP://WWW.ESA.INT/SPECIALS/Eduspace_EN/, LAST ACCESS: 25/01/2013.

ESSER AJ (2000). *CASE OF A SLOPE FAILURE IN LACUSTRINE DEPOSITS. LANDSLIDES IN RESEARCH, THEORY AND PRACTICE*. IN BROMHEAD ET AL (EDS) PROCEEDINGS, 8TH INTERNATIONAL SYMPOSIUM ON LANDSLIDES, CARDIFF, UK, 1:531–536.

FARINA P., COLOMBO D., FUMAGALLI A., MARKS F., MORETTI S. (2006). *PERMANENT SCATTERERS FOR LANDSLIDE INVESTIGATIONS: OUTCOMES FROM THE ESA-SLAM PROJECT*. ENGINEERING GEOLOGY 88, 200–217.

FELL R., COROMINAS J., BONNARD CH., CASCINI L., LEROI E., SAVAGE W. Z. ON BEHALF OF THE JTC-1 JOINT TECHNICAL COMMITTEE ON LANDSLIDES AND ENGINEERED SLOPES (2008). GUIDELINES FOR

LANDSLIDE SUSCEPTIBILITY,HAZARD AND RISK ZONING FOR LAND-USE PLANNING, COMMENTARY. ENG. GEOL., 102, 99–111.

FENG Q. Y., LIU G. J., MENG, L., FU, E. J., ZHANG, H. R. AND ZHANG, K. F. (2008). LAND SUBSIDENCE INDUCED BY GROUNDWATER EXTRACTION AND BUILDING DAMAGE LEVEL ASSESSMENT—A CASE STUDY OF DATUN, CHINA. JOURNAL OF CHINA UNIVERSITY OF MINING AND TECHNOLOGY, 18(4), 556-560.

FERLISI S. AND PISCIOTTA, G. (2007). A PRELIMINARY STUDY OF LANDSLIDE INDUCED PROPERTY DAMAGES TOWARDS CONSEQUENCE ANALYSIS. PROCEEDINGS OF THE FIRST NORTH AMERICAN LANDSLIDE CONFERENCE, EDITED BY: SCHUSTER, V. R., SCHUSTER, R. L., TURNER, A. K., VAIL (COLORADO), 3–9 JUNE 2007, AEG PUBLICATION N. 23, ISBN 978-0-975-4295-3-2, (ON CD-ROM).

FERRETTI A, PRATI C, ROCCA F (2000). NONLINEAR SUBSIDENCE RATE ESTIMATION USING PERMANENT SCATTERERS IN DIFFERENTIAL SAR INTERFEROMETRY. IEEE TRANS. GEOSCI. REMOTE SENS., 38, 5, 2202-22127.

FERRETTI A., PRATI C., ROCCA F. (2001) PERMANENT SCATTERERS IN SAR INTERFEROMETRY. IEEE TRANSACTIONS ON GEOSCIENCE AND REMOTE SENSING 39 (1), 8–20.

FINNO R. J., VOSS F. T., ROSSOW E. AND BLACKBURN J. T.(2005) EVALUATING DAMAGE POTENTIAL IN BUILDINGS AFFECTED BY EXCAVATIONS. J.GEOTECH. GEOENVIRON., 131(10), 1199–1210.

FORNARO G., SERAFINO F. AND LOMBARDINI F. (2005). 3D MULTIPASS SAR FOCUSING: EXPERIMENTS WITH LONG-TERM SPACEBORNE DATA. IEEE TRANS. GEOSCI. REMOTE SENS. 43 (4), 702–712.

FORNARO, G. PAUCIULLO A., SERAFINO F., (2007). MULTIPASS SAR PROCESSING FOR URBANIZED AREAS IMAGING AND DEFORMATION MONITORING AT SMALL AND LARGE SCALES. URBANREMOTE SENSING JOINT EVENT URS 2007 PARIS, 11_13 APRIL. IEEE CATALOG NUMBER:07EX1577. ISBN: 1-4244-0712-5.

FORNARO G, REALE D AND SERAFINO F. (2009). FOUR-DIMENSIONAL SAR IMAGING FOR HEIGHT ESTIMATION AND MONITORING OF SINGLE AND DOUBLE SCATTERERS. IEEE TRANS. GEOSCI. REMOTE SENS., 47 (1), 212–237.

FORNARO G, REALE D AND VERDE S (2012). *POTENTIAL OF SAR FOR MONITORING TRANSPORTATION INFRASTRUCTURES: AN ANALYSIS WITH THE MULTI-DIMENSIONAL IMAGING TECHNIQUE.* J. GEOPHYS. ENG. 9 S1

FORNARO G, REALE D AND VERDE S (2013). *BRIDGE THERMAL DILATION MONITORING WITH MILLIMETER SENSITIVITY VIA MULTIDIMENSIONAL SAR IMAGING.* IEEE GEOSCI. REMOTE SENS. LETT. 10 677–81.

FOTOPOULOU S., PITILAKIS K. (2011). AN ANALYTICAL APPROACH FOR THE VULNERABILITY ASSESSMENT OF RC BUILDINGS SUBJECTED TO EARTHQUAKE INDUCED GROUND DISPLACEMENTS", COMPDYN 2011, III ECCOMAS THEMATIC CONFERENCE ON COMPUTATIONAL METHODS IN STRUCTURAL DYNAMICS AND EARTHQUAKE ENGINEERING, M. PAPADRAKAKIS, M. FRAGIADAKIS, V. PLEVRIS (EDS.) CORFU, GREECE, 26–28 MAY.

FRUNEAU B., ACHACHE J., DELACOURT C.(1996).OBSERVATION AND MODELING OF THE SAINT-ETIENNE-DE-TINÉE LANDSLIDE USING SAR INTERFEROMETRY. TECTONOPHYSICS, 265, 181–190.

FRUNEAU B., CARNEC C., COLESANTI C., DEFFONTAINES B., FERRETTI A., MOUELIC S., LE PARMENTIER A. M., RUDANT J.P., (2003).CONVENTIONAL AND PS DIFFERENTIAL SAR INTERFEROMETRY FOR MONITORING VERTICAL DEFORMATION DUE TO WATER PUMPING: THE HAUSSMANN-ST-LAZARE CASE EXAMPLE (PARIS, FRANCE). PROC. FRINGE 2003, 1-5 DECEMBER 2003, FRASCATI, (ITALY).

FRUZZETTI V.M.E, G. SCARPELLI (2004). *IL CONSOLIDAMENTO DI EDIFICI FONDATI SUPERFICIALMENTE, IN PENDICI INSTABILI: PROPOSTA DI UNA METODOLOGIA OPERATIVE.* PROGETTO DI RICERCA PRIN 2001-2003. ATTI DEL WORKSHOP INTERNAZIONALE DI ANACAPRI. A CURA DI L. PICARELLI, SPEDALGRAF SUD , PP. 95-106.

FU W., GUO H., TIAN Q. AND GUO, X. (2010). *LANDSLIDE MONITORING BY CORNER REFLECTORS DIFFERENTIAL INTERFEROMETRY SAR.* INTERNATIONAL JOURNAL OF REMOTE SENSING, 31(24), 6387-6400.

FUJISAWA K, HIGUCHI K, KODA A, HARADA T (2007). *LANDSLIDE DETECTION, MONITORING, PREDICTION, EMERGENCY MEASURES AND TECHNICAL INSTRUCTION IN A BUSY CITY, ATAMI, JAPAN.* PROCEEDINGS, FIRST NORTH AMERICAN LANDSLIDE CONFERENCE, VAIL, COLORADO:65–73.

GABRYSCH R.K. (1984). GROUND-WATER WITHDRAWALS AND LAND-SURFACE SUBSIDENCE IN THE HOUSTON GALVESTON REGION, TEXAS, 1906–80. TEXAS DEPARTMENT OF WATER RESOURCES REPORT 287, 64.

GALLOWAY D., JONES D.R., INGEBRITSEN (1999). LAND SUBSIDENCE IN THE UNITED STATES. CIRCULAR 1182. US GEOLOGICAL SURVEY.

GALLOWAY D L, BURGMANN R, FIELDING E, AMELUNG F, LACZIAK R J (2000). MAPPING RECOVERABLE AQUIFER-SYSTEM DEFORMATION AND LAND SUBSIDENCE IN SANTA CLARA VALLEY, CALIFORNIA, USA, USING SPACE-BORNE SYNTHETIC APERTURE RADAR. LAND SUBSIDENCE PROC. OF THE 6TH INTERNATIONAL SYMPOSIUM ON LAND SUBSIDENCE, CARBOGNIN, GAMBOLATI, JOHNSON (EDS.), VOL.1, 237-128, LA GARANGOLA (PADOVA, ITALY) EDITION.

Gernhardt S, Adam N, Eineder M and Bamler R (2010). Potential of very high resolution SAR for persistent scatterer interferometry in urban areas Ann. GIS 16 103–11

Gillon MD, Saul GJ (1996) *Stabilisation of Cairnmuir Landslide. Landslides*. Senneset (ed) Proceedings, 7th International Symposium on Landslides, Balkema, Rotterdam, 3:1693–1698.

Grimaldi G.M. (2008). Modelling the displacements of slow moving landslides. PhD Thesis, pp 214.

Guzzetti F. (2005). IRPI CNR, Perugia, Italy. Review and Selection of Optimal Geological Models Related to Spatial Information Available, Project RISK AWARE, Action 1.14 Report, 44pp.

Guzzetti F., Manunta M., Ardizzone F., Pepe A., Cardinali M., Zeni G. and Lanari R. (2009). *Analysis of ground deformation detected using the SBAS-DInSAR technique in Umbria*, Central Italy. Pure and .pplied Geophysics,166(8-9), 1425-1459.

Herrera G., Fernández J. A., Tomás R., Cooksley G. and Mulas J., (2009). Advanced interpretation of subsidence in Murcia (SE Spain) using A-DInSAR data – modelling and validation. Nat. Hazards Earth Syst. Sci., 9, 647-661, doi:10.5194/nhess-9-647-2009.

Herrera G., Tomás R., Monells D., Centolanza G., Mallorquí J. J., Vicente, F. and Mulas, J. (2010). Analysis of subsidence using TerraSAR-X data: Murcia case study. Engineering Geology, 116(3), 284-295.

Herrera G, Álvarez Fernández MI, Tomás R, González-Nicieza C, López-Sánchez JM, Álvarez Vigil AE. (2012). Forensic analysis of buildings affected by mining subsidence based on Differential Interferometry (Part III). Eng Fail Anal 24:67–76. doi:10.1016/j.engfailanal.2012.03.003.

Herrera G., Gutiérrez F., García-Davalillo J. C., Guerrero J., Notti D., Galve J. P. and Cooksley G. (2013). *Multi-sensor advanced DInSAR monitoring of very slow landslides: the Tena valley case study (central Spanish Pyrenees)*.Remote Sensing of Environment, 128, 31-43.

Hutchinson J.N. (1988). Morphological and Geotechnical parameters of Landslides in relation to Geology and Hydrogeology. State of the art Report. Proc. V Intl. Symposium on Landslides, Lausanne, Vol. 1, pp. 3 – 35.

Iaccarino G., Peduto F., Pellegrino A, Picarelli L. (1995). *Principal features of earthflows in part of Southern Apennine*. Proc. 11th Europ. Conf. on Soil Mechanics and Foundation Engineering, Copenhagen, 4: 354-359.

Iovine G., Petrucci O., Rizzo V. and Tansi C. The March 7th 2005 Cavallerizzo (Cerzeto) landslide in Calabria – SouthernItaly.Proceedings of the 10th IAEG Congress, Nottingham,Great Britain, 6–10 September 2006, 785, 1–12, 2006.

ISPRA (Istituto Superiore per la Protezione e la RicercaAmbientale) 2006 Pericolosità Di Origine Naturale. Annuale Dei Dati Ambientali pp 1023–7, http://annuario.isprambiente.it/, last access: 25/01/2014.

IFFI (2007). AAVV Rapporto sulle frane in Italia, il progetto IFFI-metodologia risultati e rapporti regionali.

Iovine G, O Petrucci, V Rizzo, C Tansi (2006). *The March 7th 2005 Cavallerizzo (Cerzeto) landslide in Calabria* - Southern Italy. Geol. Soc. of London . LONDON:Geol. Soc. of London, Spec. Publ.,Nottingham, UK, 06-10 settembre 2006

Ireland R. L., Poland J. F. and Riley F. S. (1984). Land subsidence in the San Joaquin Valley, California, as of 1980, U.S. Geol. Surv. Prof. Pap., 437-1, pp 93.

Jones C.J.F.P., Bellamy J.B. (1973). Computer prediction of ground movements due to mining subsidence. Geotechnique, 23: 515-530.

Jónsson S., Segall P., Pedersen R., Björnsson G. (2003). *Postearthquake ground movements correlated to pore-pressure transients*. Nature, 424, pp. 179-183.

Joughin I.R., Winebrenner D.P., Fahnestock M.A. (1995). *Observations of ice-sheet motion in Greenland using satellite radar interferometry*. Geophys. Res. Lett., 22 (5), pp. 571–574.

Joughin I., Winebrenner D., Fahnestock M., Kwok R.,Krabill W., 1996. *Measurement of ice-sheet topography usingsatellite radar interferometry*. J. Glaciology, 42 (140).

Joughin I.R., Kwok R., Fahnestock M.A. (1998). *Interferometric estimation of three-dimensional ice-flow usingascending and descending passes*. IEEE Transactions onGeoscience and Remote Sensing, 36 (1), pp. 25-37.

Jurina L., Ferretti A., (2004). Un caso emblematico di un parcheggio interrato: diagnosi di un dissesto. Progettare il sottosuolo, per un edificato sicuro Milano, 6 maggio 2004.

Kampes B.M., Adam N., (2005). The STUN algorithm for persistent scatterer interferometry. Fringe 2005 Workshop, Frascati, Italy.

Kim S. W., S. Wdowinski, T.H. Dixon, F. Amelung, Joong-Sun Won and Jeong Woo Kim, (2008). InSAR -based mapping of surface

SUBSIDENCE IN MOKPO CITY, KOREA, USING JERS-1 AND ENVISAT SAR DATA. EARTH PLANETS SPACE, V.60, P. 453-461.

KIMURA, H., AND Y. YAMAGUCHI (2000). *DETECTION OF LANDSLIDE AREAS USING SATELLITE RADAR INTERFEROMETRY*. PHOTOGRAMMETRIC ENGINEERING& REMOTE SENSING, 66(3):337–344.

KJEKSTAD O. AND L. HIGHLAND (2009). ECONOMIC AND SOCIAL IMPACTS OF LANDSLIDES. SASSA,K., CANUTI, P. (EDS.), DISASTER RISK REDUCTION. SPRINGER-VERLAG, BERLIN HEIDELBERG, PP. 573–588.

KOOPMANS B.N. AND FORERO R. (1993). AIRBORNE SAR AND LANDSAT MSS AS COMPLEMENTARY INFORMATION SOURCE FOR GEOLOGICAL HAZARD MAPPING, ISPRS JOURNAL OF PHOTOGRAMMETRY AND REMOTE SENSING, VOL. 48, NO. 6, PP.28-37.

KONAGAI K., ASAKURA T., SUYAMA S., KYOKAWA H., KIYOTA T., ETO C. AND SHIBUYA K. (2012).SOIL SUBSIDENCE MAP OF THE TOKYO BAY AREA LIQUEFIED IN THE MARCH 11TH GREAT EAST JAPAN EARTHQUAKE. PROCEEDINGS OF THE INTERNATIONAL SYMPOSIUM ON ENGINEERING LESSONS LEARNED FROM THE 2011 GREAT EAST JAPAN EARTHQUAKE, MARCH 1-4, 2012, TOKYO, JAPAN.

KWOK, R., FAHNESTOCK, M.A. (1996). *ICE SHEET MOTION AND TOPOGRAPHY FROM RADAR INTERFEROMETRY*. IEEE TRANSACTIONS ON GEOSCIENCE AND REMOTE SENSING, 34 (1), PP. 189-200.

LAGOMARSINO S, GIOVINAZZI S. MACROSEISMIC AND MECHANICAL MODELS FOR THE VULNERABILITY AND DAMAGE ASSESSMENT OF CURRENT BUILDINGS (2006). EARTHQ ENG 2006;4:415_43.

LANARI, R., MORA, O., MANUNTA, M., MALLORQUI, J.J., BERARDINO, P. AND SANSOSTI, E. (2004). *A SMALLBASELINE APPROACH FOR INVESTIGATING DEFORMATIONS ON FULL RESOLUTION DIFFERENTIAL SAR INTERFEROGRAMS*. IEEE TRANSACTION ON GEOSCIENCE AND REMOTE SENSING, 42 (7), 1377-1386.

LANZO G., D'ELIA B. (1997). EXPERIENCES ON SLOPE MOVEMENTS IN CLAYEY SOILS. RIVISTA ITALIANA DI GEOTECNICA. XXI, N. 2, 15-27.

LEONE F., ASTÉ J.P., LEROI, E., (1996). VULNERABILITY ASSESSMENT OF ELEMENTS EXPOSED TO MASS-MOVEMENT: WORKING TOWARD A BETTER RISK PERCEPTION. SENNESET, K. (ED.), LANDSLIDES-GLISSEMENTS DE TERRAIN, VOL. 1. BALKEMA, ROTTERDAM, PP. 263–269.

LEROUEIL S., LOCAT J., VAUNAT J., PICARELLI L., LEE H., FAURE R. (1996). GEOTECHNICAL CHARACTERIZATION OF SLOPE MOVEMENTS. SENNESET, K. (ED.), LANDSLIDES. BALKEMA, ROTTERDAM, PP. 53 – 74

LILLFSAND T. M. AND KIEFER R. W., (1979). REMOTE SENSING AND IMAGE INTERPRETATION. JOHN WILEY & SONS.

LUNDGREN P., USAI S., SANSOSTI E., LANARI R., TESAURO M., FORNARO G., BERARDINO P., (2001). MODELING SURFACE DEFORMATION OBSERVED WITH SYNTHETIC APERTURE RADAR INTERFEROMETRY AT CAMPI FLEGREI CALDERA. JOURNAL OF GEOPHYSICAL RESEARCH 106 (B9),19355– 19366.

LOMBARDINI F. (2005). *DIFFERENTIAL TOMOGRAPHY: A NEW FRAMEWORK FOR SAR INTERFEROMETRY.* IEEE TRANS. GEOSCI. REMOTE SENS. 43 37–44.

LOPEZ-QUIROZ P., DOING M.P. , TUPIN F., BRIOLE P. AND J.M. NICOLAS (2009). TIME SERIES ANALYSIS OF MEXICO CITY SUBSIDENCE CONSTRAINED BY RADAR INTERFEROMETRY. JOURNAL OF APPLIED GEOPHYSICS, 69(1).

LOSACCO NUNZIO, (2011). DEVELOPMENT AND TESTING OF A SIMPLIFIED BUILDING MODEL FOR THE STUDY OF SOIL-STRUCTURE INTERACTION DUE TO TUNNELLING IN SOFT GROUND. PHD THESIS,PP.231.

LU Z., MANN D., FREYMUELLER J.T., MEYER D.J. (2000). *SYNTHETIC APERTURE RADAR INTERFEROMETRY OF OKMOK VOLCANO,ALASKA: RADAR OBSERVATIONS.* JOURNAL OF GEOPHYSICAL RESEARCH,105 (B5), PP. 10791-10806.

LU P., CASAGLI, N., CATANI, F., AND TOFANI, V. (2012).*PERSISTENT SCATTERERS INTERFEROMETRY HOTSPOT AND CLUSTER ANALYSIS (PSI-HCA) FOR DETECTION OF EXTREMELY SLOW-MOVING LANDSLIDES.* INT. J. REMOTE SENS., 33, 466–489, 2012.

LU P., CATANI F., TOFANI, V. AND CASAGLI, N. (2013). *QUANTITATIVE HAZARD AND RISK ASSESSMENT FOR SLOW-MOVING LANDSLIDES FROM PERSISTENT SCATTERER INTERFEROMETRY.*LANDSLIDES, 1-12.

MADSEN, S. N., ZEBKER, H. A. AND MARTIN, J., (1993). *TOPOGRAPHIC MAPPING USING RADAR INTERFEROMETRY*: PROCESSING TECHNIQUES. IEEE TRANSACTIONS ON GEOSCIENCE AND REMOTE SENSING 31(1), PP. 246–256.

MALONE AW, HANSEN A, HENCHER SR, FLETCHER CJN (2008) *POST-FAILURE MOVEMENTS OF A LARGE SLOW ROCK SLIDE IN SCHIST NEAR POS SELIM, MALAYSIA.* IN: CHEN ET AL (EDS) PROCEEDINGS, 10TH INTERNATIONAL SYMPOSIUM ON LANDSLIDES AND ENGINEERED SLOPES,XI'AN, CHINA, 1:457–461

MANSOUR, M. F., MORGENSTERN, N. R., AND MARTIN, C. D. (2011). *EXPECTED DAMAGE FROM DISPLACEMENT OF SLOW-MOVING SLIDES.* LANDSLIDES, 7, 117–131, 2011.

MANZO M, RICCIARDI G P, CASU F, VENTURA G, ZENI G, BORGSTROM S,BERARDINO P, DEL GAUDIO C AND LANARI R (2006). *SURFACEDEFORMATION ANALYSIS IN THE ISCHIA ISLAND (ITALY)*

BASED ON SPACEBORNE RADAR INTERFEROMETRY. J. VOLCANOL. GEOTHERM. RES.151 399–416.

MASSONNET, D., M. ROSSI, C. CARMONA, F. ADRAGNA, G. PELTZER, K.FELGL, AND T. RABAUTE (1993). *THE DISPLACEMENT FIELD OF THE LANDERSEARTHQUAKE MAPPED BY RADAR INTERFEROMETRY.* NATURE, 364:138–142.

MASSONNET, D., P. BRIOLE, AND A. ARNAUD (1995). DEFLATION OF MOUNT ETNA MONITORED BY SPACEBORNE RADAR INTERFEROMETRY. NATURE,375:567–570.

MASSONNET, D., THATCHER, W., VADON, H. (1996). *DETECTION OFPOSTSEISMIC FAULT ZONE COLLAPSE FOLLOWING THE LANDERS EARTHQUAKE.* NATURE, 382, PP. 489-497.

MAVROULI O. AND COROMINAS J., (2010). *ROCKFALL VULNERABILITY ASSESSMENT FOR REINFORCED CONCRETE BUILDINGS.* NATURAL HAZARDS AND EARTH SYSTEM SCIENCES. VOL. 10, NO. 10, PP. 2055-2066.

MEISINA C., ZUCCA F. , NOTTI D, COLOMBO A., CUCCHI A.,SAVIO G., GIANNICO C. AND BIANCHI M.,(2008). *GEOLOGICAL INTERPRETATION OF PSINSAR DATA AT REGIONAL SCALE.* SENSORS 2008, 8, 7469-7492; DOI: 10.3390/S8117469.

MELIDORO G.(1971). *MOVIMENTI FRANOSI E ZONIZZAZIONE DEL BACINO DEL FIUME FORTORE.* GEOLOGIA APPLICATA E IDROGEOLOGIA, 6, 7–41.

MILONE G., SCEPI G.(2011). *A CLUSTERING APPROACH FOR STUDYING GROUND DEFORMATION TRENDS IN CAMPANIA REGION THROUGH PS-INSAR TIME SERIES ANALYSIS.* JOURNAL OF APPLIED SCIENCES, 2011 ISSN 1812/ DOI: 10. 3923/JAS.

MODONI G., DARINI G., SPACAGNA R.L., SAROLI M., RUSSO G., CROCE P. (2013). *SPATIAL ANALYSIS OF LAND SUBSIDENCE INDUCED BY GROUNDWATER WITHDRAWAL.* ENGINEERING GEOLOGY 01/2013; 167:59–71.

MOHR J.J., REEH N., MADSEN S.N. (1998). *THREE-DIMENSIONAL GLACIAL FLOW AND SURFACE ELEVATION MEASURED WITH RADAR INTERFEROMETRY.* NATURE, 391 (6664), PP. 273–276.

MOORE DP, WATSON AD, MARTIN CD (2006) *DEFORMATION MECHANISM OF A LARGE ROCKSLIDE INUNDATED BY A RESERVOIR.* WORKSHOP ON THE MECHANICS AND VELOCITY OF LARGE LANDSLIDES, TECHNICAL REPORT, ITALY.

MORA O., MALLORQUI´ J. J., AND BROQUETAS A. (2003). *LINEAR AND NONLINEAR TERRAIN DEFORMATION MAPS FROM A REDUCED SET OF INTERFEROMETRIC SAR IMAGES.* IEEE TRANSACTIONS ON GEOSCIENCE AND REMOTE SENSING, 41, 2243 – 2253.

NATIONAL COAL BOARD (1975). SUBSIDENCE ENGINEERS HANDBOOK. NATIONAL COAL BOARD PRODUCTION DEPT., U.K.

NEGULESCU C.AND FOERSTER, E. (2010). PARAMETRIC STUDIES AND QUANTITATIVE ASSESSMENT OF THE VULNERABILITY OF A RC FRAME BUILDING EXPOSED TO DIFFERENTIAL SETTLEMENTS. NATURAL HAZARDS AND EARTH SYSTEM SCIENCE, 10(9), 1781-1792.

NELSON (2012). SUBSIDENCE: DISSOLUTION & HUMAN RELATED CAUSES. HTTP://WWW.TULANE.EDU/~SANELSON/NATURAL_DISASTERS/SUBSIDENCE.HTM, LAST ACCESS: 15/01/2013.

NICHOL D. AND LOWMAN R. D. W. (2000). *STABILISATION AND REMEDIATION OF A MINOR LANDSLIDE AFFECTING THE A5 TRUNK ROAD AT LLANGOLLEN, NORTH WALES*. LANDSLIDES IN RESEARCH, THEORY AND PRACTICE. IN: BROMHEAD ET AL (EDS) PROCEEDINGS, 8TH INTERNATIONAL SYMPOSIUM ON LANDSLIDES, CARDIFF, UK, 3:1099–1104.

NOTTI D., DAVALILLO J. C., HERRERA G. AND MORA, O. (2010). *ASSESSMENT OF THE PERFORMANCE OF X-BAND SATELLITE RADAR DATA FOR LANDSLIDE MAPPING AND MONITORING: UPPER TENA VALLEY CASE STUDY*. NAT. HAZARDS EARTH SYST. SCI., 10, 1865–1875, DOI:10.5194/NHESS-10-1865-2010.

OKUMURA T. (1969). ANALYSIS OF LAND SUBSIDENCE IN NIIGATA. PROCEEDING OF THE INTERNATIONAL SYMPOSIUM ON LAND SUBSIDENCE, TOKYO, JAPAN, VOL. 1, 130–143.

OSMANOGLU, B., DIXON, T. H., WDOWINSKI, S., CABRAL-CANO, E., & JIANG, Y. (2011). MEXICO CITY SUBSIDENCE OBSERVED WITH PERSISTENT SCATTERER INSAR. INTERNATIONAL JOURNAL OF APPLIED EARTH OBSERVATION AND GEOINFORMATION, 13(1), 1–12.

OVANDO-SHELLEY E., ROMO M.P., CONTRERAS N. AND GIRALT A.(2003). EFFECTS ON SOIL PROPERTIES OF FUTURE SETTLEMENTS IN DOWNTOWN MEXICO CITY DUE TO GROUND WATER EXTRACTION. GEOFÍSICA INTERNACIONAL, VOL. 42, NÚM. 2, APRIL-JUNE, 2003, PP. 185-204.

PECK R.B. (1969). DEEP EXCAVATIONS AND TUNNELLING IN SOFT GROUND. A THICKNESS OF THE TAIL PIECE. PROCEEDINGS, 7TH INTERNATIONAL CONFERENCE ON SOIL MECHANICS AND FOUNDATION ENGINEERING, MEXICO CITY, PP. 225-290.

PEDERSEN R., SIGMUNDSSON F., FEIGL K.L., ÁRNADÓTTIR T. (2001). *COSEISMIC INTERFEROGRAMS OF TWO MS=6.6 EARTHQUAKES IN THE SOUTH ICELAND SEISMIC ZONE, JUNE 2000*. GEOPHYSICAL RESEARCH LETTERS, 28 (17), PP. 3341-3344

PEDUTO D. (2008). ANALYSIS OF GROUND DEFORMATIONS RELATED TO SUBSIDENCE AND LANDSLIDE PHENOMENA VIA DINSAR TECNIQUES. PHD THESIS, PP. 258.

PEDUTO D., CASCINI L., ARENA L., FERLISI S., PISCIOTTA G., FORNARO G. (2013).USO CONGIUNTO DEI DATI DINSAR E DEI DANNI AL COSTRUITO PER L'AGGIORNAMENTO DELLE CARTE INVENTARIO DEI FENOMENI FRANOSI A CINEMATICA LENTA. INCONTRO ANNUALE DEI RICERCATORI DI GEOTECNICA PERUGIA 16-18 SETTEMBRE 2013 PERUGIA UNIVERSITÀ DEGLI STUDI DI PERUGIA PAG.1-6 ISBN:9788890642135.

PEDUTO D., PISCIOTTA G., FERLISI S., ARENA L., FORNARO G., CASCINI L. (2014). IL RUOLO DELLE TECNICHE DINSAR NELL'ANALISI DEL RISCHIO DA FRANA A CINEMATICA LENTA. LA GEOTECNICA NELLA DIFESA DEL TERRITORIO E DELLE INFRASTRUTTURE DAI RISCHI NATURALI. ASSOCIAZIONE GEOTECNICA ITALIANA, XXV - CONVEGNO NAZIONALE DI GEOTECNICA - MILANO - STRESA (SUBMITTED).

PELLEGRINO A., RAMONDINI M., URCIOULI G. (2004). INTERPLAY BETWEEN THE MORPHOLOGY AND MECHANISM OF MUDSLIDES: FIELD EXPERIENCES FROM SOUTHERN ITALY. LACERDA W (ED.). PROCEEDINGS OF THE 9TH INTERNATIONAL SYMPHOSIUM ON LANDSLIDES, RIO DE JANEIRO, VOL.2 BALKEMA, ROTTERDAM, PP. 1403-1409.

PELTZER, G., ROSEN, P. (1995). *SURFACE DISPLACEMENT OF THE 17MAY 1993 EUREKA VALLEY, CALIFORNIA EARTHQUAKE OBSERVED BY SAR INTERFEROMETRY*. SCIENCE, 268, PP. 1333-1336.

PELTZER, G., ROSEN, P., ROGEZ, F., HUDNUT, K. (1996). *POSTSEISMICREBOUND IN FAULT STEP-OVERS CAUSED BY PORE FLUID FLOW*. SCIENCE,273, PP. 1202-1204.

PELTZER, G., CRAMPÉ, F., KING, G. (1999). *EVIDENCE OF THE NONLINEAR ELASTICITY OF THE CRUST FROM MW7.6 MANYI (TIBET)EARTHQUAKE*. SCIENCE, 286 (5438), PP. 272-276.

PERISSIN D. AND WANG T. (2011). TIME-SERIES INSAR APPLICATIONS OVER URBAN AREAS IN CHINA. SELECTED TOPICS IN APPLIED EARTH OBSERVATIONS AND REMOTE SENSING, IEEE JOURNAL OF, 4(1), 92-100.

PHIEN-WEJ N., GIAO P.H., NUTALAYA P., (2006). LAND SUBSIDENCE IN BANGKOK, THAILAND. ENGINEERING GEOLOGY 82, 187–201.

PITILAKIS K., ALEXOUDI M., ARGYROUDIS S., MONGE O., MARTIN C. (2006). *VULNERABILITY AND RISK ASSESSMENT OF LIFELINES*. ASSESSING AND MANAGING EARTHQUAKE RISK, VOL. 2, PP. 185-211.

PICARELLI L., RUSSO C. (2004). MECHANICS OF SLOW ACTIVE LANDSLIDES AND INTERACTION WITH MAN-MADE WORKS. KEY NOTE LECTURE, 9TH INTERNATIONAL SYMPOSIUM ON LANDSLIDES, RIO DE JANEIRO, VOL. 2.

PISCIOTTA, G.(2008). PHYSICAL VULNERABILITY OF ELEMENT AT RISK IN LANDSLIDE PRONE AREAS. PHD THESIS, UNIVERSITY OF SALERNO, ITALY, PP 270.

POLSHIN D.E. AND TOKAR R.A. (1957). MAXIMUM ALLOWABLE NON-UNIFORM SETTLEMENT OF STRUCTURES. PROC. 4TH INT. CONF. SMFE, LONDON, VOL. 1, P 402.

PLANK S., SINGER J., MINET CH. AND THURO K.(2010). GIS BASED SUITABILITY EVALUATION OF THE DIFFERENTIAL RADAR INTERFEROMETRY METHOD (DInSAR) FOR DETECTION AND DEFORMATION MONITORING OF LANDSLIDES. PROCEEDINGS OF FRINGE 2009 WORKSHOP, EDITED BY: LACOSTE-FRANCIS, H., 30 NOVEMBER–4 DECEMBER 2009, ESRIN, FRASCATI, ITALY (ESA SP-677, MARCH 2010), 8 PP., ISBN: 978-92-9221-241-4.

PROFESSIONAL BROKING, (2007). SUBSIDENCE COSTS SINKING. PROFESSIONAL BROKING, JANUARY 2007.

PROKOPOVICH N. P,. MARRIOTT M. J. (1983). COST OF SUBSIDENCE TO THE CENTRAL VALLEY PROJECT, CALIFORNIA. ASSOCIATION OF ENGINEERING GEOLOGISTS BULLETIN, 20, 3, 325–332.

RAPOLLA A., DI NOCERA S., MATANO F., PAOLETTI V. AND TARALLO D. (2012). *LE AREE DEI TERRENI COMPLESSI DEL SANNIO E DELL'IRPINIA. CRITERI DI ZONAZIONE DELLA SUSCETTIBILIT`A E DELLA PERICOLOSIT`A DA FRANE INNESCATE DA EVENTI ESTREMI (PIOGGE E SISMA). COMPOSERVICE S.R.L.,PADOVA, ITALY, 238–248, ISBN: 9788890687334, 2012. RAUCOLES D., MAISONS

REALE D, NITTI D O, PEDUTO D, NUTRICATO R, BOVENGA F AND FORNARO G (2011). *POST-SEISMIC DEFORMATION MONITORING WITH THE COSMO/SKYMED CONSTELLATION* IEEE GEOSCI. REMOTE SENS.LETT. 8 696–700.

REALE D, FORNARO G, PAUCIULLO A, ZHU X AND BAMLER R (2011A). *TOMOGRAPHIC IMAGING AND MONITORING OF BUILDINGS WITH VERY HIGH RESOLUTION SAR DATA. IEEE GEOSCI. REMOTE SENS. LETT.8 661–5.

REGIONE CAMPANIA, CUAS 2001/2009 LAST ACCESS 29/01/2014: HTTP://SIT.REGIONE.CAMPANIA.IT/PORTAL/PORTAL/DEFAULT/DOWN LOAD.

REILINGER, R.E., ERGINTAV, S., BÜRGMANN, S., MCCLUSKY, S.,LENK, O., BARKA, A., GURKAN, O., HEARN, L., FEIGL, K.L.,CAKMAK, R., AKTUG, B., OZENER, H., TÖKSOZ, M.N. (2000).*COSEISMIC AND POSTSEISMIC

FAULT SLIP FOR THE 17 AUGUST 1999, M=7.5, IZMIT, TURKEY EARTHQUAKE. SCIENCE, 289 (5484), PP.1519-1524.

RICCERI G. AND SORANZO M. (1985). AN ANALYSIS ON ALLOWABLE SETTLEMENTS OF STRUCTURES. ASSOCIAZIONE GEOTECNICA ITALIANA, N.4.

RICCERI G. (2007). IL FUTURO DI VENEZIA TRA SUBSIDENZA ED EUSTATISMO. RIVISTA ITALIANA DI GEOTECNICA, 3. PATRON EDITORE (BO).

RIGHINI G., PANCIOLI V. AND CASAGLI N. (2012). UPDATING LANDSLIDE INVENTORY MAPS USING PERSISTENT SCATTERER INTERFEROMETRY (PSI). INT. J.REMOTE SENS., 33, 2068–2096, 2012.

RIGNOT E.J., GOGINENI S.P., KRABILL W.B., EKHOLM S. (1997). NORTH AND NORTHEAST GREENLAND ICE DISCHARGES FROM SATELLITERADAR INTERFEROMETRY. SCIENCE, 276, PP. 934-937.

ROSEN, P., WERNER, C., FIELDING, E., HENSLEY, S., BUCKLEY, S., VINCENT, P. (1998). ASEISMIC CREEP ALONG THE SAN ANDREAS FAULT NORTHWEST OF PARKFIELD, CA MEASURED BY RADAR INTERFEROMETRY. GEOPHYSICAL RESEARCH LETTERS, 25 (6), PP. 825-828.

ROSSETTO T., ELNASHAI A. (2003) DERIVATION OF VULNERABILITY FUNCTIONS FOR EUROPEAN-TYPE RC STRUCTURES BASED ON OBSERVATIONAL DATA. ENGINEERING STRUCTURES 25 (2003) 1241–1263.

ROTA M. PENNA A. AND STROBBIA C. (2006). TYPOLOGICAL FRAGILITY CURVES FROM ITALIAN EARTHQUAKE DAMAGE DATA. PROCEEDINGS 1ST EUROPEAN CONFERENCE ON EARTHQUAKE ENGINEERING AND SEISMOLOGY, GENEVA, PAPER (NO. 386).

ROTT H., B. SCHEUCHL, A. SIEGEL, AND B. GRASEMANN, (1999). MONITORING VERY SLOW SLOPE MOVEMENTS BY MEANS OF SAR INTERFEROMETRY: A CASE STUDY FROM A MASS WASTE ABOVE A RESERVOIR IN THE ÖTZTAL ALPS, AUSTRIA. GEOPHYSICAL RESEARCH LETTERS, 26 (11), PP. 1629-1632.

RUSCH H. AND MAYER H(1964). BAUSCHADEN ALS FOLGE DER DUCHBIEGUNG VON STAHLBETON. BAUTEILEN, DEUTSCHER AUSSCHUSS FUR STAHLBETON, BERLIN, NO. 10, (IN GERMAN).

SABETTA F., GORETTI A. AND A. LUCANTONI (1998). EMPIRICAL FRAGILITY CURVES FROM DAMAGE SURVEYS AND ESTIMATED STRONG GROUND MOTION. 11TH EUROPEAN CONFERENCE ON EARTHQUAKE ENGINEERING, PARIS, CD-ROM, ISBN 90 5410 982 3, BALKEMA.

SAEIDI A., DECK O. AND VERDEL, T. (2009). DEVELOPMENT OF BUILDING VULNERABILITY FUNCTIONS IN SUBSIDENCE REGIONS FROM EMPIRICAL METHODS. ENGNG STRUCT. 31, NO. 10, 2275–2286.

SAEIDI A., DECK O. AND VERDEL, T . *DEVELOPMENT OF BUILDING VULNERABILITY FUNCTIONS IN SUBSIDENCE REGIONS FROM ANALYTICAL METHODS*. GEOTECHNIQUE 62, NO. 2, 107–120 HTTP://DX.DOI.ORG/10.1680/GEOT.9.P.028]

SAFELAND DELIVERABLE 2.5 (2011) PHYSICAL VULNERABILITY OF ELEMENTS AT RISK TO LANDSLIDES: METHODOLOGY FOR EVALUATION, FRAGILITY CURVES AND DAMAGE STATES FOR BUILDINGS AND LIFELINES. EDITED FOR THE SAFELAND EUROPEAN PROJECTBY: STUMPF, A., MALET, J.-P., AND KERLE, N., AVAILABLE AT: HTTP://WWW.SAFELAND-FP7.EU (LAST ACCESS: 23 MAY 2013).

SALVI S., ATZORI S., TOLOMEI C., ALLIEVI J., FERRETTI A., ROCCA F., PRATI, C., STRAMONDO, S., FEUILLET, N. (2004). *INFLATION RATE OF THE COLLI ALBANI VOLCANIC COMPLEX RETRIEVED BY THE PERMANENT SCATTERERS SAR INTERFEROMETRY TECHNIQUE*. GEOPHYSICAL RESEARCH LETTERS, 31 (12), L12606.

SANTORO U. (2011). RELAZIONE GEOLOGICA

SHARPE C.F.S. (1938). LANDSLIDES AND RELATED PHENOMENA : A STUDY OF MASS-MOVEMENTS OF SOIL AND ROCK. COLUMBIA UNIVERSITY PRESS. NEW "YORK.

SHI X., WU J., YE S., ZHANG,Y., XUE Y., WEI, Z. AND YU, J. (2008). REGIONAL LAND SUBSIDENCE SIMULATION IN SU-XI-CHANG AREA AND SHANGHAI CITY, CHINA. ENGINEERING GEOLOGY, 100(1), 27-42.

SINGHAL, A. AND KIREMIDJIAN, A.S. (1996). *METHOD FOR PROBABILISTIC EVALUATION OF SEISMIC STRUCTURAL DAMAGE*. JOURNAL OF STRUCTURAL ENGINEERING 122:12, 1459-1467.

SINGHROY, V. H.(1995) SAR INTEGRATED TECHNIQUES FOR GEOHAZARD ASSESSMENT. ADVANCES IN SPACE RESEARCH. VOL 15 #11 PP.67-78.

SINGHROY, V., MATTAR K.E. AND GRAY A.L. (1998). *LANDSLIDE CHARACTERISATION IN CANADA USING INTERFEROMETRIC SAR AND COMBINED SAR AND TM IMAGES*. ADVANCE SPACE RESEARCH. 21: 465-476.

SINGHROY, V. AND MOLCH, K. (2004). *CHARACTERIZING AND MONITORING ROCKSLIDES FROM SAR TECHNIQUES*. ADVANCES IN SPACE RESEARCH, VOLUME 33,ISSUE 3 (2004), P. 290-295. ISSN: 0273-1177 DOI: 10.1016/S0273-1177(03)00470-8.

SINGHROY, V.AND K. MATTAR. (2000). *SAR IMAGE TECHNIQUES FOR MAPPING AREAS OF LANDSLIDES*. ISPRS 2000. PROCEEDINGS. AMSTERDAM, P1395-1402.

SKEMPTON, A.W. (1953). THE COLLOIDAL "ACTIVITY" OF CLAYS. PROCEEDINGS OF THE 3RD INTERNATIONAL CONFERENCE OF SOIL MECHANICS AND FOUNDATION ENGINEERING, (1) 57-60.

SKEMPTON A.W. AND MACDONALD D.H. (1956). ALLOWABLE SETTLEMENT OF BUILDINGS. PROC. INSTN. CIV. ENGRS., PT. III, VOL. 5, PP 727-768.

STRAMONDO S., BOZZANO F., MARRA F., WEGMULLER U., CINTI F.R., MORO M., SAROLI M., (2008). SUBSIDENCE INDUCED BY URBANISATION IN THE CITY OF ROME DETECTED BY ADVANCED INSAR TECHNIQUE AND GEOTECHNICAL INVESTIGATIONS. REMOTE SENSING OF ENVIRONMENT 112 (2008) 3160–3172, DOI:10.1016/J.RSE.2008.03.008

STRAMONDO, S., M. SAROLI, C. TOLOMEI, M. MORO, F. DOUMAZ, A. PESCI, F. LODDO, P. BALDI, AND E. BOSCHI (2007).
SURFACE MOVEMENTS IN BOLOGNA (PO PLAIN-ITALY) DETECTED BY MULTITEMPORAL DINSAR. REMOTE SENS. ENVIRON., 110, 304–316.

STROZZI T., WEGMÜLLER U., TOSI L., BITELLI G. AND SPRECKELS V., (2001). LAND SUBSIDENCE MONITORING WITH DIFFERENTIAL SAR INTERFEROMETRY. PE&RS, 67(11):1261-1270.

SOWERS G. F.(1962) SHALLOW FOUNDATIONS. FOUNDATION ENGINEERING. EDITED BY: LEONARDS, G. A., MCGRAW-HILL BOOK CO., NEW YORK, NY, USA, 525–632.

SQUARZONI C.,DELACOURT C., ALLEMAND P. (2003). NINE YEARS OF SPATIAL AND TEMPORAL EVOLUTION OF THE LAVALLETTE LANDSLIDE OBSERVED BY SAR INTERFEROMETRY. ENGINEERINGGEOLOGY 68, 53–66.

SWISS RE (2011). THE HIDDEN RISKS OF CLIMATE CHANGE: AN INCREASE IN PROPERTY DAMAGE FROM SOIL SUBSIDENCE IN EUROPE. HTTP://MEDIA.SWISSRE.COM/DOCUMENTS/SOIL_SUBSIDENCE_PUBLICATION_EN_0718.PDF, LAST ACCESS: 15/01/2013.

TAMBURINI A., DEL CONTE S., LARINI G., LOPARDO L., MALAGUTI C., VESCOVI P. (2012). *APPLICATION OF SQUEESARTM TO THE CHARACTERIZATION OF DEEP SEATED GRAVITATIONAL SLOPE DEFORMATIONS:THE BERCETO CASE STUDY (PARMA, ITALY)*. ATTI DEL SECOND WORLD LANDSLIDE FORUM – 3-7 OTTOBRE 2011,ROMA.

TOMÁS R., HERRERA G., DELGADO J., LÓPEZ-SÁNCHEZ J.M., MALLORQUÍ J.J, MULAS (2010).A GROUND SUBSIDENCE STUDY BASE DON DINSAR DATA: CALIBRATION OF SOIL PARAMETERS AND SUBSIDENCE PREDICTION IN MURCIA CITY (SPAIN) ENGINEERING GEOLOGY, 111 (2010), PP. 19–30.

TOMMASI P., PELLEGRINI P., BOLDINI D., RIBACCHI R. (2006). INFLUENCE OF RAINFALL REGIME ON HYDRAULIC CONDITIONS AND MOVEMENT RATES IN THE OVERCONSOLIDATED CLAYEY SLOPE OF THE ORVIETO HILL (CENTRAL ITALY). CANADIAN GEOTECHNICAL JOURNAL, 43, PP. 70-86.

TOPAL T, AKIN M (2008) *INVESTIGATION OF A LANDSLIDE ALONG A NATURAL GAS PIPELINE (KARACABEY-TURKEY)*. CHEN ET AL (EDS)

PROCEEDINGS, 10TH INTERNATIONAL SYMPOSIUM ON LANDSLIDES AND ENGINEERED SLOPES, XI'AN, CHINA, 2:1647–1652.

TÖRNQVIST, T.E. ET AL. (2008). *MISSISSIPPI DELTA SUBSIDENCE PRIMARILY CAUSED BY COMPACTION OF HOLOCENE STRATA*. NAT. GEOSCI. 1, 173–176.

TRIGILA A., IADANZA C. (2007) *STATISTICHE NAZIONALI ED ELABORAZIONI DATI DEL PROGETTO IFFI*. APAT (2007). RAPPORTO SULLE FRANE IN ITALIA. IL PROGETTO IFFI – METODOLOGIA, RISULTATI E RAPPORTI REGIONALI, RAPPORTI 78/2007.

TRIGGIANI M. (2011). LE TECNICHE DI INTERFEROMETRIA RADAR APPLICATE ALLO STUDIO DELLA SUBSIDENZA NEL GOLFO DI MANFREDONIA. DIGILABS, 2011.,PP. 92, ISBN 8875220395, 9788875220396.

USAI S., (2001). A NEW APPROACH FOR LONG TERM MONITORING OF DEFORMATIONS BY DIFFERENTIAL SAR INTERFEROMETRY. PHD THESIS, PP 165.

VARNES D. J. (1978). SLOPE MOVEMENT TYPES AND PROCESSES. SPECIAL REPORT 176: LANDSLIDES: ANALYSIS AND CONTROL, EDITED BY: SCHUSTER, R. L. AND KRIZEK, R. J., TRB, NATIONAL RESEARCH COUNCIL, WASHINGTON, DC, 11–33, 1978.

VAN WESTEN, C.J. (1993). APPLICATION OF GEOGRAPHIC INFORMATION SYSTEMS TO LANDSLIDE HAZARD ZONATION. PHD DISSERTATION TECHNICAL UNIVERSITY DELFT. ITCPUBLICATION NUMBER 15, ITC, ENSCHEDE, THE NETHERLANDS, PP. 245.

VILARDO G., VENTURA G., TERRANOVA C., MATANO F. AND NARDO S. (2009). GROUND DEFORMATION DUE TO TECTONIC, HYDROTHERMAL, GRAVITY, HYDROGEOLOGICAL, AND ANTHROPIC PROCESSES IN THE CAMPANIA REGION (SOUTHERN ITALY) FROM PERMANENT SCATTERERS SYNTHETIC APERTURE RADAR INTERFEROMETRY. REMOTE SENS. ENVIRON. 113 197–212.

WANG Y, ZHU X, SHI Y AND BAMLER R (2012) *OPERATIONAL TOMOSARPROCESSING USING TERRASAR-X HIGH RESOLUTION SPOTLIGHT STACKS FROM MULTIPLE VIEW ANGLES* PROC. IEEE 2012 IGARSS CONF., (MUNICH, GERMANY) PP 7047–50.

WEGMÜLLER U., WERNER C., STROZZI T., WIESMAN, A. (2005). ERS _ ASAR INTEGRATION IN THE INTERFEROMETRIC POINT TARGET ANALYSIS. PROCEEDINGS FRINGE 2005 WORKSHOP, FRASCATI, ITALY, 28 NOVEMBER_2 DECEMBER.

WORAWATTANAMATEEKUL, J., HOFFMANN J., ADAM N., KAMPES B. (2003). URBAN DEFORMATION MONITORING IN BANGKOK METROPOLITAN (THAILAND) USING DIFFERENTIAL INTERFEROMETRY AND THE PERMANENT SCATTERER TECHNIQUE. FRINGE 2003 WORKSHOP, FRASCATI, ITALY.

Zebker, H. A., P. A. Rosen, and S. Hensley (1997). *Atmospheric effects in interferometric synthetic aperture radar surface deformation and topographic map*. J. Geophys. Res., 102(B4), 7547–7563.

Zischinsky, U.(1969).Uber Bergzerreißung und Talzuschub. Geol. Rundschau, 58(3), 974–983.

Zhou Y (2000) *Research and treatment of Shazhou Landslide, Sichuan. Landslides in research, theory and practice.* Bromhead et al (eds) Proceedings, 8th International Symposium on Landslides, Cardiff, UK, 3:1647–1652.

Zhu X and Bamler R (2010). *Very high resolution spaceborne SAR tomography in urban environment*. IEEE Trans. Geosci. Remote Sens. 48 4296–308.

APPENDIX A

LANDSLIDE CLASSIFICATION, STATE OF ACTIVITY AND INTENSITY

According to Cruden (1991) the term landslide refers to any "movements of a mass of rock, debris or earth down a slope".

Landslides could be activated or triggered by different factors.

Terzaghi (1950) divides the causes triggering the landslides in: external and internal causes. The external ones produce an increase of shear stresses; they could be either human causes such as excavations at the toe or surcharging at the crest, or natural phenomena such as erosion at the toe or earthquake. Internal causes are related to a decrease in strength of materials in the absence of changes in total stresses. Very frequently, the internal causes are related to the increase in pore water pressure or progressive decrease in the cohesion of the slope materials. Intermediate causes are for example the phenomena of rapid emptying of rivers and dams or sub-surface erosion and liquefaction.

Owing to the complexity and extreme variability of landslides, several landslide classifications have been proposed in the scientific literature, all based on the description of the mechanism of post-failure deformation and movement (Picarelli, 2000). Among them the most widely used are those proposed by Skempton (1953), Varnes (1958), Hutchinson (1968), Blong (1973), Varnes (1978), Hutchinson (1988), Cruden and Varnes (1996), Leroueil e Locat (1998), Hungr et al (2001), Hutchinson (2004).

This variety is due to many reasons; for instance Walker et al. (1987) stress that "the basic problem, and the reasons that there are so many different classifications, is that landslides form a continuum and there are an infinite number of ways dividing a continuum".

Among the landslide classification system that can be found in the international literature, the one adopted in this work to describe both the type of movement and the involved material is the system proposed by Varnes (1978). The author distinguishes five types of movements: Falls, Topples, Slides (rotational and translational), lateral Spreads and Flows.

An additional class, the Complex movements, is used to define any combination of more than one type of movement.

Table A.1 Landslide classification based on type of movements and involved materials (Varnes, 1978)

TYPE OF MOVEMENT		BEDROCK	ENGINEERING SOILS	
			Predominantly coarse	Predominantly fine
FALLS		Rock fall	Debris fall	Earth fall
TOPPLES		Rock topple	Debris topple	Earth topple
SLIDES	ROTATIONAL	Rock slide	Debris slide	Earth slide
	TRANSLATIONAL			
LATERAL SPREADS		Rock spread	Debris spread	Earth spread
FLOWS		Rock flow	Debris flow	Earth flow
		(deep creep)	(soil creep)	
COMPLEX		Combination of two or more principal types of movement		

Note: under "TYPE OF MATERIAL" heading, "ENGINEERING SOILS" spans "Predominantly coarse" and "Predominantly fine".

Falls are "detached masses of any size moving down steep slopes or cliffs with little or no shear displacement between the materials originally on contact, and descend mostly through the air by free fall, bouncing, or rolling". The term Topple refers to movements characterized by the forward rotation of soil units about some pivotal point, below or low in the unit, under the actions of gravity and forces exerted by adjacent units or by fluids in cracks. Lateral Spreads are translational movements resulting in the overall extension (spreading) of detached coherent masses, which move toward a free face on a basal shear surface or on subject material that has deformed by liquefaction or plastic flow. When the detached masses shears along the basal slip surface, remaining in contact with the stable slope material, a Slide phenomenon occurs. Slides can be further subdivided into Rotational Slides and Translational Slides respectively characterized by a concavely upward slip surface and a planar rupture surface. Finally, flows are landslides showing internal differential movements distributed throughout the moving mass. In earth and debris material these phenomena can show a clear slip surface when differential movements take place on closely spaced shear surface; however, a visible shear surface may not form when the differential movements act among the grains. Among flow phenomena, Varnes (1978) classifies Creep as imperceptibly slow, steady, downward movement of slope-forming soil or rock caused by shear stress sufficient

to produce permanent deformation, but too small to produce shear failure.
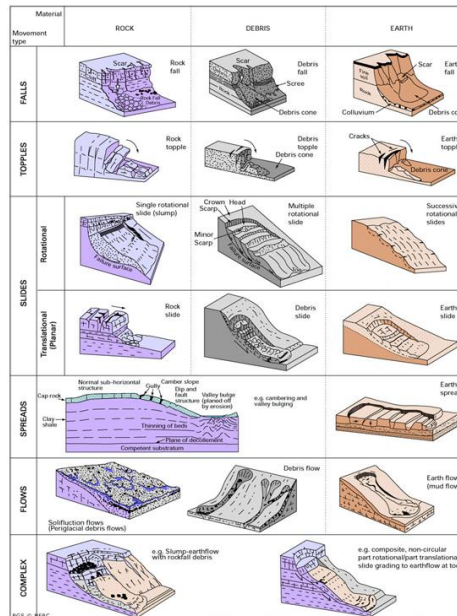

Figure A.1Schematic examples of some of the mass movements reported in the Varnes 'landslideclassification system (British Geological Survey, http://www.bgs.ac.uk: last access 06/11/2013).

In Varnes' classification the materials are distinguished as rock (a hard or firm mass that was intact and in its natural place before the initiation of movement), earth (material in which 80% or more of the particles are smaller than 2 mm) and debris (contains a significant proportion of coarse material, 20% to 80% of particles are greater than 2mm and the remainder are smaller than 2mm).

Leroueil et al. (1996) stressed the importance of an accurate geotechnical characterization" of slope movements for their appropriate classification, schematically it takes the form of a 3-D matrix, the three axes being types of movement, types of material and the four stages of movement (Figure A.2).
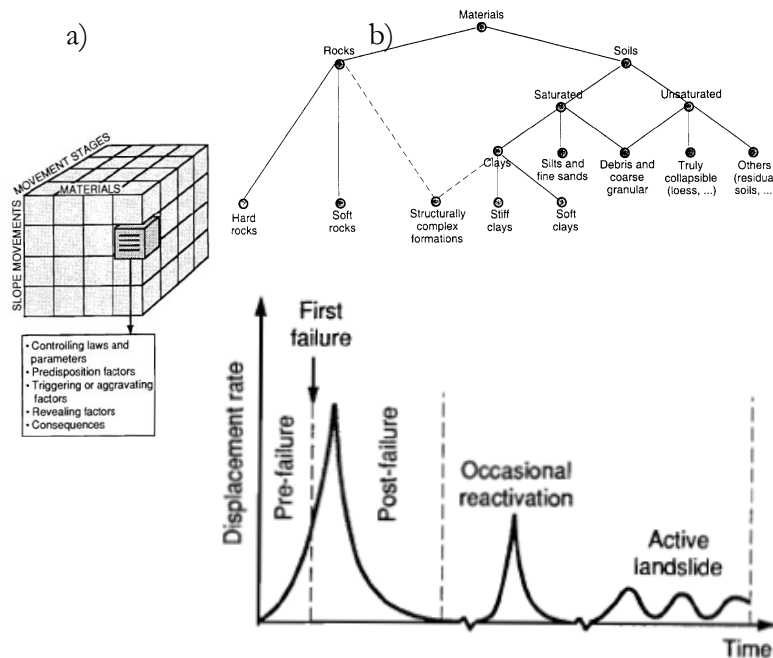
Figure A.2 Geotechnical schematization of landslide given by Leroueil et al., 1996: scheme for landslide characterization, (b) material involved and (c) different stages of slope movements.

Regarding the phases of the movements, the authors identify:

(a) pre-failure stage, including all the deformation processes leading to failure. This stage is controlled mostly by deformations due to changes in stresses, creep and progressive failure.

(b) The onset of failure, characterized by the formation of a continuous shear surface through the entire soil mass.

(c) The post-failure stage, which includes movement of the soil mass involved in the landslide, from just after failure until it essentially stops.

(d) The reactivation stage, when a soil mass slides along one or several pre-existing shear surfaces.

Among reactivations the Authors distinguish "active landslides" from "reactivated landslides". In active landslides, the rate of displacement varies with the seasonal changes in pore pressures. This is particularly true for translational landslides in which the driving forces do not change significantly with time. The rates of displacement are generally small, varying between some centimeters and some metres per year (Urciuoli,

1990). In contrast to active landslides, reactivated landslides may be associated with sudden and fairly rapid displacements (Hutchinson, 1987). These authors listed mechanisms that can produce such movements, among which the most common seem to be:

(i) rapid pore pressure increase due to filling of cracks or breaking of pipes;

(ii) stress change due to excavation;

(iii) rapid change in load distribution along the shear surface;

(iv) increase in strength along the shear surface due to cementation or chemical change that could give some brittleness to the soil at the time of failure;

(v) seismic forces.

With reference to the other two dimensions of the matrix, the Authors propose to use the classes of Varnes (1978) to describe the type of movement, while they suggest a classification of the type of material in 9 classes in order to provide a framework most exhaustive of the materials existing in nature it is associated with a specific mechanical behavior under the action of different load conditions.

Cruden and Varnes (1996), deepening the previous classification system provided by Varnes (1978), focused on landslide activity (e.g. state, distribution and style) and other feature such as landslide rate, water content, material and type. Specially, referring to the terms relating to landslide age and state of activity as defined by Varnes (1978), the terms defining the sequence or repetition of movement were regrouped under three headings, e.g.: **State of Activity**, which describes what is known about the timing of movements; **Distribution of Activity**, which broadly describes where the landslide is moving, **Style of Activity**, which indicates how different movements within the landslides contribute to its overall movement.

With regard to the state of activity, the Authors define as *active* landslide that are currently moving; they include first-time movements and reactivations. Landslides that have moved within the last annual cycle of seasons but which are not moving at the present are described as suspended. The term *inactive* covers landslides that last moved move more than one annual cycle of seasons ago. This state may be further subdivided. If the causes of movements appear to be remaining, landslide are dormant. If the river that had been eroding toe of the moving slope has itself changed course, the landslide is abandoned

183

(Hutchinson, 1973). If the toe of the slope has been protected against erosion by bank armouring or if other artificial remedial measures have stopped movement, the landslide can be described as stabilized. On the other hand, landslides that have clearly developed under geomorphological or climatic conditions, perhaps thousands of years ago, can be called relict. A landslide that is again active after being inactive may be called reactivates

Table A.2 Glossary for the formation of names of landslides (Cruden and Varnes, 1996).

Activity		
State	**Distribution**	**Style**
Active	Advancing	Complex
Reactivated	Retrogressing	Composite
Suspended	Widening	Multiple
Inactive:	Enlarging	Successive
Dormant	Confined	Single
Abandoned	Diminishing	
Stabilized	Moving	
Relict		

The limits of these classes are subsequently modified by Cruden & Varnes (1996) to ensure that each class of speed has a width of two orders of magnitude. The extreme values are represented by the value of 5 m/s representative of the speed of a person in the race, the limit between the phenomena classified as Very Rapid and Extremely Rapid, and from 15 mm/anno speed limit between classes Very Slow and Extremely Slow to below which the landslide, generally, does not cause damage to most of the structures (Table A.3).

Like other natural hazard, landslides can be characterized by their intensity that can be defined as a set of qualitative or quantitative spatially distributed parameters, which determine the potential of a given landslide phenomenon to cause the damage (Hungr, 1977).

Estimation of landslide intensity is one of the most difficult issues to be addresses, as it is strictly related, for instance, to the history of an existing landslide or to volumes of potentially unstable masses. Therefore, it is not surprising that this factor is defined in different ways by different Authors. According to Leone et al. (1996) intensity parameters of landslides can be grouped into three categories:

- dimensional ore geometric parameters (surface, volume, shape, depth, amplitude, distance, height and thickness);
- kinetic parameters (velocity, flow-rate, acceleration and deformation fields);
- other parameters such as viscosity, mass, sediment load and density.

The most used approach associates intensity to the velocity of the body mass, as Cruden and Varnes (1996) suggest. Similarly to the Mercalli's scale, which is based on the descriptions of the local effexts of an earthquake, the Authors define the probable destructive significance of the landslides associated with seven velocity class as shown in figure A.3.

Velocity Class	Description	Velocity (mm/sec)	Typical Velocity	Probable Destructive Significance
7	Extremely Rapid			Catastrophe of major violence; buildings destroyed by impact of displaced material; many deaths; escape unlikely
		5×10^3	5 m/sec	
6	Very Rapid			Some lives lost; velocity too great to permit all persons to escape
		5×10^1	3 m/min	
5	Rapid			Escape evacuation possible; structures; possessions, and equipment destroyed
		5×10^{-1}	1.8 m/hr	
4	Moderate			Some temporary and insensitive structures can be temporarily maintained
		5×10^{-3}	13 m/month	
3	Slow			Remedial construction can be undertaken during movement; insensitive structures can be maintained with frequent maintenance work if total movement is not large during a particular acceleration phase
		5×10^{-5}	1.6 m/year	
2	Very Slow			Some permanent structures undamaged by movement
		5×10^{-7}	15 mm/year	
	Extremely SLOW			Imperceptible without instruments; construction POSSIBLE WITH PRECAUTIONS

Figure A.3 Proposed landslide velocity scale and probable destructive significante (Cruden and Varnes, 1996).

Moreover, Sassa (1988) suggests to evaluate the landslide intensity through the estimation of its Kenetic energy using the so-called "sled-model".

References

BLONG R.J. (1973). A NUMERICAL CLASSIFICATION OF SELECTED LANDSLIDES OF THE DEBRIS SLIDEAVALANCHE-FLOW TYPE. ENGINEERING GEOLOGY, 7, PP. 99-144.

CRUDEN, D.M. (1991). A SIMPLE DEFINITION OF A LANDSLIDE. BULLETIN OF IAEG, 43, 27-29.

CRUDEN D.M., VARNES, D.J. (1996). LANDSLIDE TYPES AND PROCESSES. LANDSLIDES:INVESTIGATION AND MITIGATION. TRANSPORTATION RESEARCH BOARD, SPECIAL REPORTNO. 247, NATIONAL RESEARCH COUNCIL, NATIONAL ACADEMY PRESS,WASHINGTON DC, USA 36-75.

HUNGR, O. (1997). *SOME METHODS OF LANDSLIDE HAZARD INTENSITY MAPPING*. IN LANDSLIDE RISK ASSESSMENT D. CRUDEN AND R. FELL (EDITORS). 215-226. BALKEMA, ROTTERDAM.

HUNGR O., EVANS S.G., BOVIS M.J., HUTCHINSON J.N. (2001). *A REVIEW OF THE CLASSIFICATION OF LANDSLIDES OF THE FLOW TYPE*. ENVIRON. & ENG. GEOSCI., VII (3), PP.221 – 238.

HUTCHINSON J.N. (1968). MASS MOVEMENT. IN: THE ENCYCLOPEDIA OF GEOMORPHOLOGY, (ED) FAIRBRIDGE, R. W., REINHOLD BOOK CORPORATION,688–695.

HUTCHINSON J.N. (1973). *THE RESPONSE OF LONDON CLAY CLIFFS TO DIFFERING RATES OF TOE EROSION*. GEOLOGIA APPLICATA E IDROGEOLOGIA.

HUTCHINSON J.N. (1987). MECHANISM PRODUCING LARGE DISPLACEMENT IN LANDSLIDES ON PRE-EXISTING SHEARS. 1ST SINO-BRITISH GEOLOGICAL CONFERENCE , TAPEI, MEMOIR OF GEOLOGICAL SURVEY OF CHINA,9: 175-200.

HUTCHINSON J.N. (1988). MORPHOLOGICAL AND GEOTECHNICAL PARAMETERS OF LANDSLIDES IN RELATION TO GEOLOGY AND HYDROGEOLOGY. STATE OF THE ART REPORT. PROC. V INTL. SYMPOSIUM ON LANDSLIDES, LAUSANNE, VOL. 1, PP. 3 – 35.

HUTCHINSON J.N. (2004). *REVIEW OF FLOW-LIKE MASS MOVEMENTS IN GRANULAR AND FINEGRAINEDMATERIALS*. PROC. OF THE INT. WORKSHOP "FLOWS 2003 - OCCURRENCE ANDMECHANISMS OF FLOWS IN NATURAL SLOPES AND EARTHFILL", PP. 3 – 16.

LEROUEIL S., LOCAT J., VAUNAT J., PICARELLI L., LEE H., FAURE R.(1996). *GEOTECHNICAL CHARACTERIZATION OF SLOPE MOVEMENTS*. PROCEEDINGS 7TH INTERNATIONAL SYMPOSIUM LAND-SLIDES, TRONDHEIM, NORWAY 1: 53-74

LEROUEIL S., LOCAT J. (1998). SLOPE MOVEMENTS–GEOTECHNICAL CHARACTERIZATION, RISK ASSESSMENT AND MITIGATION.

GEOTECHNICAL HAZARD, MARIC, LISAC & SZAVITS-NOSSAN (EDS). BALKEMA, ROTTERDAM.

PICARELLI L (2000) *MECHANISMS AND RATES OF SLOPE MOVEMENTS IN FINE GRAINED SOILS*. PROCEEDINGS OF THE INTERNATIONAL CONFERENCE ON GEOTECHNICAL AND GEOLOGICAL ENGINEERING,GEOENG2000, MELBOURNE, PP 1618–1670.

SASSA K. SPECIAL LECTURE: GEOTECHNICAL MODEL FOR THE MOTION OF LANDSLIDES [A]. INT. PROC. 5TH INTERNATIONAL SYMPOSIUM ON LANDSLIDE,1C, ROTTERDAM, A. A. BALKEMA, 37–55, 1988.

SKEMPTON A.W. (1953). *THE COLLOIDAL ACTIVITY OF CLAYS*. PROC. 3RD INT. CONF. SOIL MECH. FOUND. ENGNG, 1, PP. 7-61, ZURICH.

TERZAGHI K. (1950). *MECHANISM OF LANDSLIDES*. PAIGE, S., EDITOR, 1950.APPLICATION OF GEOLOGY TO ENGINEERING PRACTICEGEOL. SOC. AM., BERKEY VOL., PP. 83–123.

URCIUOLI G (1990) *CONTRIBUTO ALLA CARATTERIZZAZIONE GEOTECNICA DELLE FRANE DELL' APPENNINO*.QUADERNI DELL' ISTITUTO DI TECNICA DELLE FONDAZIONI E COSTRUZIONI IN TERRA, UNIVERSITÀ DI NAPOLI FEDERICO II, 1.

VARNES D.J. (1958). LANDSLIDE TYPES AND PROCESSES. IN SPECIAL REPORT 29:LANDSLIDE AND ENGINEERING PRACTICE (E.B. ECKEL, ED.), HRB, NATIONAL RESEARH COUNCIL, WASHINGTON, D.C., 20-47.

VARNES D.J. (1978). SLOPE MOVEMENT TYPES AND PROCESSES. LANDSLIDE ANALYSIS AND CONTROL. TRANSPORTATION RESEARCH BOARD SPECIAL REPORT NO. 176, NATIONALACADEMY OF SCIENCES, WASHINGTON DC, USA 11-33.

WALKER B.F., BLONG R.J. AND MACGRE ,J.P. (1987). *SOIL SLOPE INSTABILITY AND STABILISATION*. A.A.BALKEMA, PP.2-52.

APPENDIX B

VALIDATION OF PSInSAR DATA

This Appendix concerns the validation of PSInSAR with ground measurements furnished by Campania Region during a training period. In particular, the PSInSAR data were validated with available inclinometer measurements acquired in the period from 04/09/2007 to 05/05/2008 in Castelpagano Municipality (BN).

In this period of time, the inclinometer I1 (see Figure B1) did not record any movements and, congruently, the closer PS did not exceed the threshold of movement equal to 2 mm/year. Conversely, the inclinometer I2 provides a cumulative horizontal movement in the direction of the azimuth of approximately 10 mm during eight months of observation. In order to carry out a quantitative comparison with the interferometric measurements, the LOS displacements of the moving PS closer to inclinometer I2, were projected along the direction defined by the azimuth of the inclinometer in the horizontal plane according to projection operations defined by Cascini et al. (2010). The result in Figure B.1 show a good agreement between the different measurements thus allowing DInSAR data to be more confidently used.
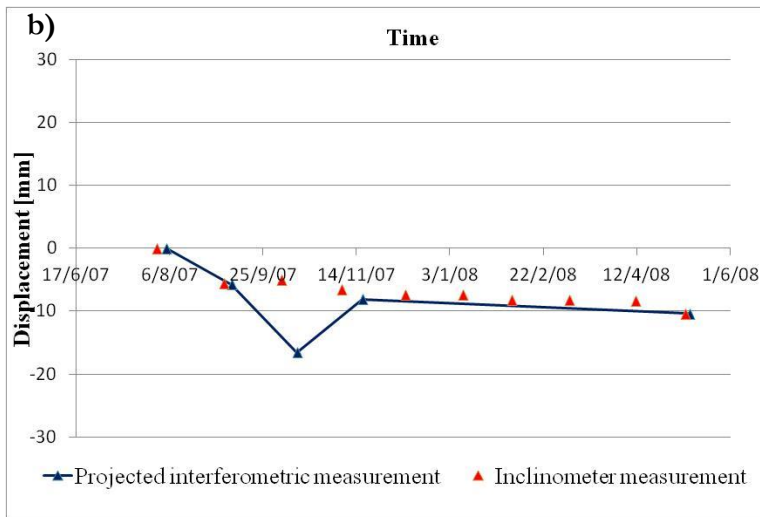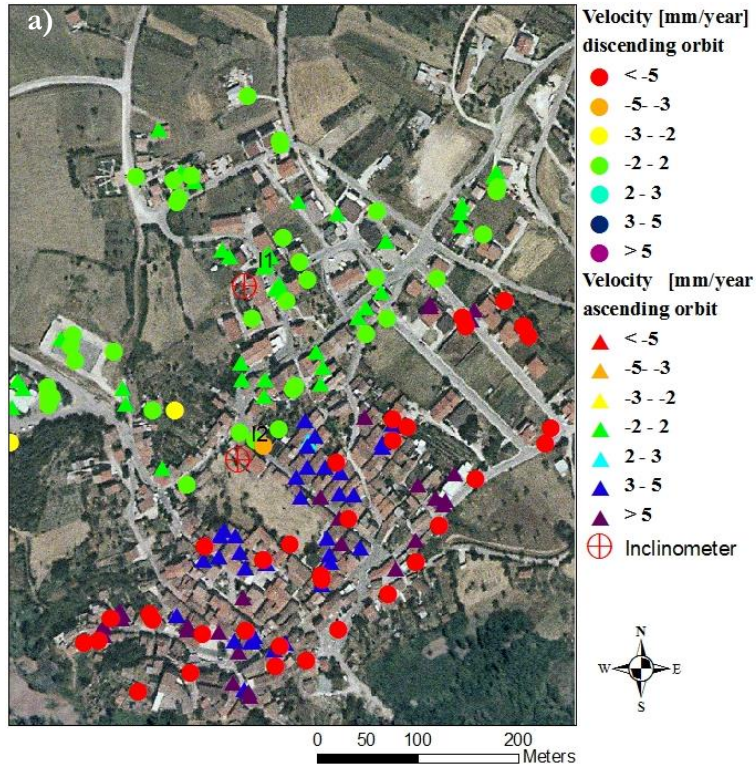
Figure B.1 a) Map of PS and inclinometer within Castelpagano (BN) urban area; b) Interferometric versus inclinometer measurements.

APPENDIX C

DEFINITION OF MOVING THRESHOLD FOR LANDSLIDE

This Appendix is devoted to explain the adopted method to establish if a given slow-moving landslide can be defined as moving according to Cascini et al., 2013. In particular, this method is based on the analysis of V_{slope} values pertaining to the projectable PS located within the landslide boundaries, taking account of both PS V_{LOS} inaccuracies and $V_{LOS} - V_{slope}$ scaling factor values. First of all it must be observed that a landslide is usually defined as *moving* when the velocity of its body (or of a part of it) is greater than zero. In order to verify the attainment of this condition on the basis of PSI-derived velocities, it must be considered that these values are characterized by inherent inaccuracies. As a consequence, the condition of landslide movement should imply the exceeding of a PS velocity threshold which takes into account the abovementioned inaccuracies.Assuming that a landslide affected area is covered by a number of PS equal to N, the generic i^{th} PS is characterized by a V_{LOS_i} value having an inaccuracy σ typically ranging from 1.5 to 2 mm/yr (Cascini et al., 2010; Cigna et al. 2012) depending on PS coherence. Accordingly, the portion of the landslide body referred to this PS can be assumed as moving if :

$$V_{los\_i}^2 > \sigma^2 \qquad\qquad\qquad C.1$$

Considering that coherence values may vary among different PS, a movement threshold representative of the whole landslide body can be individuated according to the equation:

$$\sum_{i=1}^{N} w_i \; \frac{V_{slope\_i}^2}{k_i^2} > \sigma^2 \qquad\qquad\qquad C.2$$

---

being $w_i = w_{ci}/w_{cN}$ the normalized weights based on the PS coherence and $k_i (\geq 1)$ the point-dependent scaling factor.

Letting V_{slope_rms} be

$$V_{slope\_rms} = \left(\sum_{i=1}^{N} w_i V_{slope\_i}^2 \right)^{1/2}$$ C.3

Therefore, equation C.2. can be rearranged as:

$$\frac{1}{k^2} V_{slope\_rms}^2 > \sigma^2$$ C.4

where $k = \left(\dfrac{1}{N} \sum_{i=1}^{N} k_i^{-2} \right)^{-1/2} > 1$ represents the root mean square (rms) scaling factor.

Finally, from equation C.4, the condition of landslide movement can be expressed as:

$$V_{slope\_rms} > k\sigma$$ C.5

It is worth to note that equations C.2 and C.4 are equivalent if and only if the scaling factors k_i have a constant value ($k_i = k$). Furthermore, the equation C.5 shows that the landslide moving threshold on the rms velocity along the slope (V_{slope_rms}) must take into account that the inaccuracies due to instrumental errors should be properly amplified according to the scaling factor k depending, in turn, on the landslide aspect and slope as well as on the sensor LOS.

References

CASCINI L., FORNARO G. AND PEDUTO, D.(2010). ADVANCED LOW- AND FULL RESOLUTION DINSAR MAP GENERATION FOR SLOW-MOVING LANDSLIDE ANALYSIS AT DIFFERENT SCALES. ENG. GEOL., 112, 29–42.

CASCINI L., PEDUTO D., PISCIOTTA G., ARENA L., FERLISI S. AND FORNARO G. (2013B). THE COMBINATION OF DINSAR AND FACILITY DAMAGE DATA FOR THE UPDATING OF SLOW-MOVING LANDSLIDE INVENTORY MAPS AT MEDIUM SCALE. NAT. HAZARDS EARTH SYST. SCI., 13, 1527-1549, DOI:10.5194/NHESS-13-1527-2013.

CIGNA F., BIANCHINI S., CASAGLI N. (2012).HOW TO ASSESS LANDSLIDE ACTIVITY AND INTENSITY WITH PERSISTENT SCATTERER INTERFEROMETRY (PSI): THE PSI-BASED MATRIX APPROACH. LANDSLIDES, DOI: 10.1007/S10346-012-0335-7.

APPENDIX D

EXAMPLES OF APPLICATION AT DETAILED SCALE FOR SUBSIDENCE

In this Appendix three examples of analyses at detailed scale are presented. The first one refers to the whole period of observation of interferometric measurements (1992-2011) using ERS, ENVISAT and COSMO-SkyMED satellites in Castelvolturno municipality; the second one refers to the period 1992-2000 using only ERS satellite in Sarno municipality; the third one refers to the period 2010-2011 using COSMO-SkyMED satellite data in an area near Naples central station. [11] The first selected application concerns the single-floored reinforced concrete row-house located within the territory of the Castel Volturno municipality (Figure D.1).
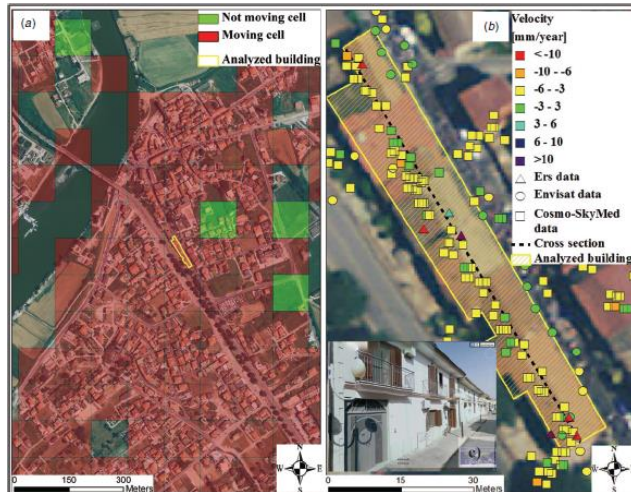
Figure D.1 Close view of the Castel Volturno area with an indication of the grid of ERS-ENVISAT covered cells and the analysed buildings; (b) zoom on the analysed buildings showing ERS-ENVISAT-COSMO-SkyMed coverage and the cross-Section used for the analyses; (c) a picture of the analysed buildings. Taken from Google Earth. © Google 2013 (Cascini et al., 2013).

In particular, Figure D.1 (a) shows that the test structure (framed in yellow) falls within a cell which was found to be moving over the whole period 1992–2010 according to ERS-ENVISAT data in the analysis at medium scale (Figure 6.12). In the close view of the building sketched in figure A.C.1 (b), all the available PS (6 for ERS, 21 for ENVISAT, 109 for COSMO-SkyMed) are shown, thus highlighting the huge increase of COSMO-SkyMed PS data, although this latter dataset refers only to the descending orbit. Moreover, since as it was shown in Figure 6.10 vertical movements seem to prevail in the area, LOS velocity and displacement data are projected along the vertical direction (Cascini et al, 2007).

With reference to close PS, the combination of three datasets can provide about 20-year monitoring period of a given zone. An example is shown in figure D.2, where the vertical displacement time series belonging to three PS located over the building in figure D.1(c) is put in a sequence and linked to the previous time series by assuming a linear trend for the periods for which no measurements are available.
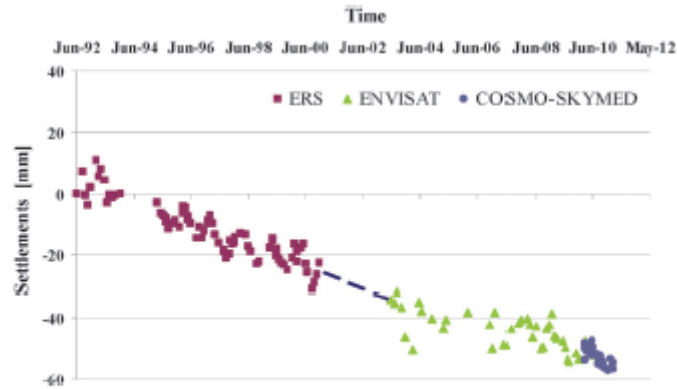
194

Figure D.2 An example of cumulative vertical settlement derived from three-dataset time series for three close PS over the analysed buildings (Cascini et al., 2013).

Accordingly, a 6 cm cumulative vertical settlement is computed for the analysed portion of the building. Then, by spatially interpolating the vertical cumulative settlements over the building - with a 1m × 1m cell grid - it is possible to retrieve the settlement profile (Figure D.3 (a)) corresponding to the longitudinal cross-Section shown in Figure D.1(b). Similarly to Cascini et al (2007), 2011a,b), the computed settlements are obtained assuming a pure shear mode of deformation of the building, without any strain in the vertical direction; as a consequence, the horizontal displacements are disregarded and the building settlements are computed referring to the PInSAR data located on its roof. It is worth stressing that this assumption matches the results concerning the prevailing movement direction (Figure 6.11) which reveals the presence of mostly vertical displacements in the area. According to the settlements computed along the longitudinal Section (Figure D.3 (a)), an increase with time of the absolute vertical settlements is clear, as well as of the sagging (upward concavity) and hogging (downward concavity) zones of the foundation. Further interesting information is gathered (Figure D.3 (b)) by the trends exhibited by the angular distortion β - the rotation of the line joining two reference points on the foundation relative to the rigid body rotation of the whole superstructure - adopted by Skempton and MacDonald (1956) in their damageability criterion as a measure of the building distortion. The diagram in Figure D.3 (b) highlights the presence of some sections for which β attains the highest relative values (not exceeding $0.0013 = 1/769$); these in turn, do not imply the occurrence of damage according to Skempton and MacDonald (1956).

195

The obtained results were validated via an in situ damage survey recently carried out in the Castel Volturno area. In particular, the analysed building recorded the absence of cracks, therefore confirming the results of the application of Skempton and McDonald's damageability criterion.
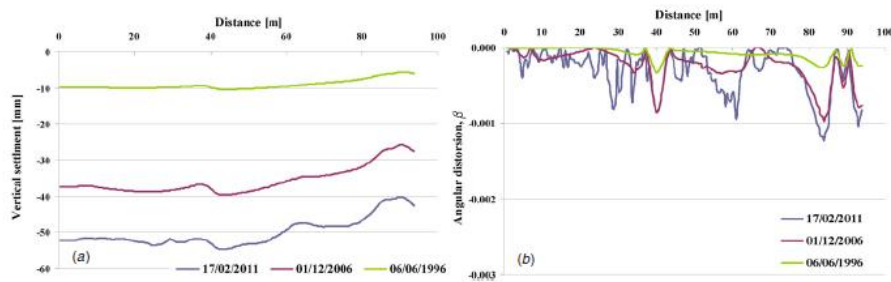

Figure D.3 (a) Vertical cumulative settlements and (b) relative rotations computed along the sample longitudinal cross-Section at three different dates starting from 1992 (Cascini et al., 2013).

With reference to a well documented case of subsidence occurred in Sarno town (Cascini et al 2007, 2011a,b,Peduto, 2008), once derived the map of cumulative settlement using both SBAS and PSInSAR data (Figure D.4), analysis at detailed scale, was carried out with reference to two buildings adequately covered by both coherent pixels SBAS full-resolution data) and PS.
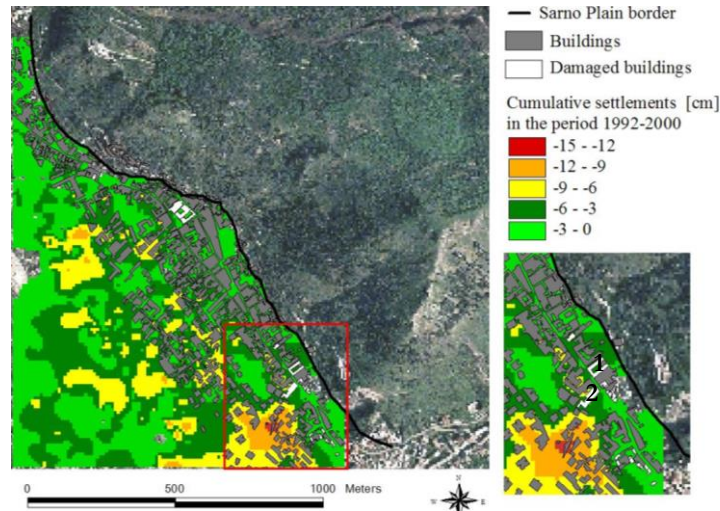
Figure D.4.Map of the cumulative settlements derived from the projection of both full-resolution SBAS and PSInSAR data along the vertical direction and, then, interpolated on a grid of 10 x 10 m (period 1992-2000) (Cascini et al., 2011a,b).

The first building (Figure D.5), was built at the beginning of 1900s and it is a 10 meter two floored masonry structure with shallow foundations.

The available DInSAR data on this building were interpolated on a regular square grid with 1meter side in order to compute the cumulative settlement trends (from June 1992 till November 2000) along the two cross Sections sketched in Figure D.5. The computed settlements were obtained assuming a pure shear mode of deformation of the building, without any strain (either of compressive or tensile type) in the vertical direction; as a consequence, the horizontal displacements were disregarded and the building settlements were computed referring to the DInSAR data located on its roof.

According to the diagrams of the settlements computed along the longitudinal Sections it is possible to distinguish the sagging and hogging zones of the foundation. Moreover, the same diagrams highlight that the building rotates around a longitudinal axis, similarly to what supposed by Nigro (1992) on the basis of the crack patterns recorded during damage surveys.

Further interesting information can be gathered by the trends exhibited by two others relevant parameters, namely the relative rotation β and the deflection ratio Δ/L, respectively adopted by Skempton and McDonald (1956) and Burland and Wroth (1974) in their damageability criteria as a

measure of the building distortion. The diagrams in Figure D.5 highlight the presence of some weak sections for which the abovementioned parameters attain the highest relative values. Moreover, taking into account that the building under examination was already damaged when DInSAR measurement started, on the basis of the recorded values of parameters β and Δ/L, both adopted damageability criteria substantiates the verified absence of damage severity increase during the period of building monitoring.

The second building (Figure D.6), built up in 1960s, is a three floored reinforced concrete (r.c.) structure on shallow foundations with a total height of about 14 meters. The analysis of DInSAR data highlights that the highest settlements are attained in correspondence of the main building façade; also in such a case the building behaves as a rigid body undergoing a rotational motion, accordingly to Nigro's (1992) observations. Finally, the damageability criterion given by Skempton and McDonald (1956) seems the most fitting since it allows the prediction of the damage occurrence in correspondence of the building stairs.
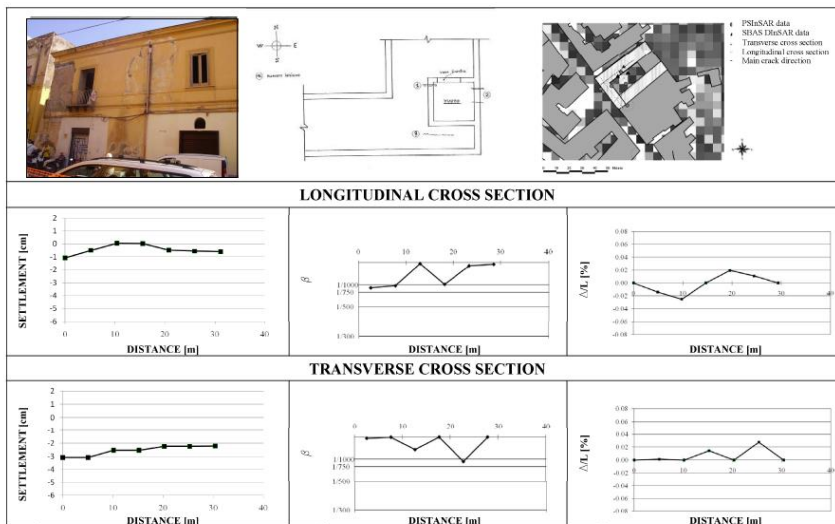

Figure D.5 Building n. 1: cumulative settlements, relative rotations and deflection ratios computed via DInSAR data along a selected cross Section for a time period spanning from June 1992 to November 2000 (Peduto,2008, Cascini et al., 2011a,b).
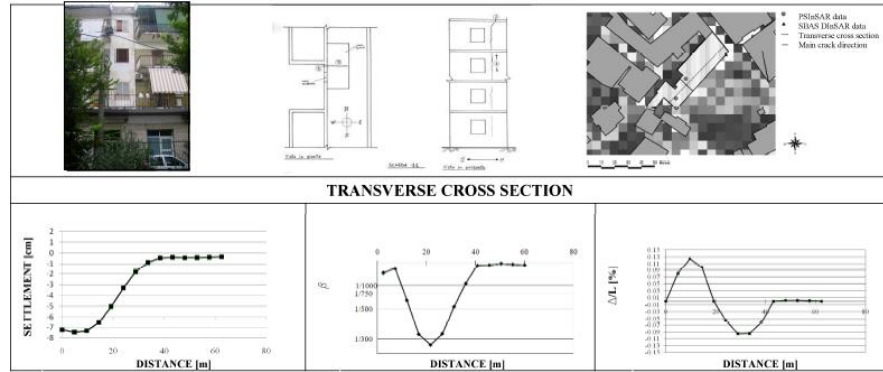
Figure D.6. Building n. 2: cumulative settlements, relative rotations and deflection ratios computed via DInSAR data along selected cross Sections for a time period spanning from June 1992 to November 2000 (modified after Peduto, 2008; Cascini et al., 2011a).

In addition to buildings, another valuable application of DInSAR data deals with the analysis and monitoring of infrastructures which can be pursued especially when high resolution remote sensing data are available. The third application refers to a crossing Section of two important infrastructures located not far from Naples central station: a high-speed railway line and a highway viaduct (Figures D.7 (a)–(c)).
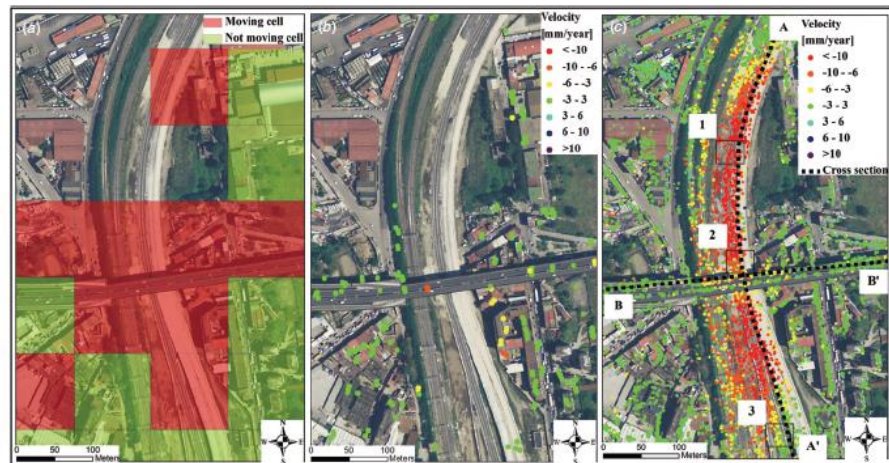

Figure D.7 A zoom over the railway lines near Naples central station with: (a) an indication of the grid of ENVISAT covered cells; (b) the distribution of ENVISAT data; and (c) the distribution of COSMO-SkyMed data (Cascini et al., 2013).

199

Figure D.7 (a) shows that the area is covered by moving cells according to ENVISAT data; in figures A.C.7 (b),(c) the different coverage provided by ENVISAT and COSMO-SkyMed data is highlighted. It is worth stressing the full coverage which COSMO-SkyMed data (although referring in this case only to descending orbit) can provide over almost linear features (roads, railways, airport runways, etc). In order to take into account the outcome of the analyses on the prevailing movement direction (Figure 6.11) which showed mainly vertical displacements in this area, both velocity and displacement values measured along the LOS are assumed as occurring along the vertical direction (Cascini et al 2007b). The diagram in figure D.8 shows one-year cumulative settlements computed along the vertical direction for some sample COSMO-SkyMed PS located in three different zones along the railway line. Furthermore, the available coverage provided by COSMO-SkyMed data allows the retrieval of two settlement profiles along the two sample cross-Sections shown in figures D.9 (a) and (b). In particular, the cumulative vertical settlements along the railway line sum up to about 20 mm(Figure D.9 (a)) in one year; whereas along the considered cross section on the viaduct they do not exceed 10mm (Figure D.9(b)).
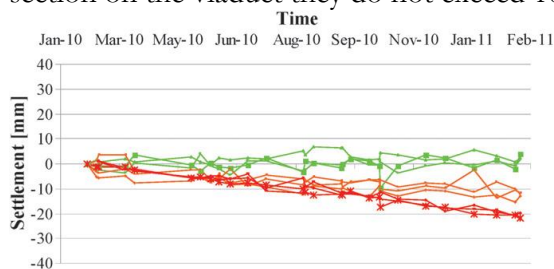

Figure D.8 A selection of COSMO-SkyMed PS recorded in the three different areas of the railway track: the green series is relevant to area 1; the orange series is relevant to area 2; and the red series is relevant to area 3. (Cascini et al., 2013)
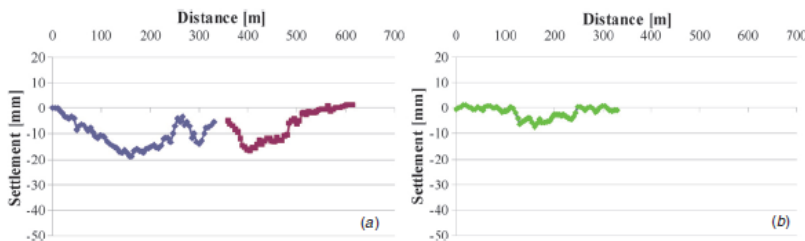

Figure D.9 The trend of cumulative vertical settlements recorded by COSMO-SkyMed data over: (a) the longitudinal cross-Section of the railway; and (b) the cross Section of the viaduct (Cascini et al., 2013).

References

BURLAND J.B. AND WROTH C.P. (1974). *SETTLEMENT OF BUILDINGS AND ASSOCIATED DAMAGE*. SOA REVIEW. PROC. CONF. SETTLEMENT OF STRUCTURES, CAMBRIDGE, PENTECH PRESS, LONDON, PP 611-654.

CASCINI L., FERLISI S., PEDUTO D., FORNARO G. AND MANUNTA M. (2007B). *ANALYSIS OF A SUBSIDENCE PHENOMENON VIA DINSAR DATA AND GEOTECHNICAL CRITERIA*. ITALIAN GEOTECHNICAL JOURNAL, 4, 50-67.

NIGRO E. (1992). *RELAZIONE SUL RILIEVO DELLO STATO FESSURATIVO DI EDIFICI DELL'AREA URBANA DEL COMUNE DI SARNO*.

PEDUTO D. (2008). *ANALYSIS OF GROUND DEFORMATIONS RELATED TO SUBSIDENCE AND LANDSLIDE PHENOMENA VIA DINSAR TECNIQUES*. PHD THESIS, PP. 258.

SKEMPTON A.W. AND MACDONALD D.H. (1956). *ALLOWABLE SETTLEMENT OF BUILDINGS*. PROC. INSTN. CIV. ENGRS., PT. III, VOL. 5, PP 727-768.